# Spectroscopic investigation of a high pressure $CO_2$ microwave discharge

## Dissertation

zur Erlangung des akademischen Grades

Dr. rer. nat.

eingereicht an der
Mathematisch-Naturwissenschaftlich-Technischen Fakultät
der Universität Augsburg

von

**Federico Antonio D'Isa**

Augsburg, 29 April 2021

Tag der mündlichen Prüfung 29.04.2021

Erste Gutachterin: Prof. Dr.-Ing. Ursel Fantz

Zweiter Gutachter: Prof. Dr. Dirk Volkmer

# Introduction

Carbon dioxide $CO_2$, a highly potent greenhouse gas, is produced in very large quantities from industrial processes but also for power generation. Reducing the $CO_2$ released in the atmosphere is of critical importance to mitigate the climate changes in the next decades, due to the greenhouse effect. For this reason, several strategies to increase the usage of $CO_2$, and consequently reduce its release to the atmosphere, are being investigated. A possible solution is $CO_2$ decomposition to form CO to be used as a primary building block for the synthesis of synthetic fuels such as methanol. In this thesis, the $CO_2$ dissociation using microwave plasmas is investigated as a possible technology for energy-efficient $CO_2$ valorization using renewable energies.

A comprehensive characterization of a 2.45 GHz microwave plasma torch in a vortex flow configuration operated in a large pressure range (30-1000 mbar) with pure $CO_2$ flow input is here presented. The main plasma characteristics are investigated by mass spectrometry ($CO_2$ decomposition), iCCD imaging (plasma volume) and optical emission spectroscopy (gas temperature). This work aims to investigate the dependence of the $CO_2$ dissociation on the external parameters (pressure, power, flow), to try to establish a correlation between the plasma volume and gas temperature, and to determine the main mechanisms of the $CO_2$ dissociation. The focus is to optimize both $CO_2$ conversion and energy efficiency.

The plasma is driven in both continuous and pulsed mode. In continuous mode, steady state values of $CO_2$ conversion, plasma volume and gas temperature are determined. In the pulsed mode, the typical temporal evolution time scales of the $CO_2$ conversion, plasma volume and gas temperature are investigated.

# Contents

# 1 The role of $CO_2$ in the energy and climate challenges

## 1.1 The importance of $CO_2$ utilization in the energy and climate challenges

The anthropic $CO_2$ emission in 2019 was *ca.* 33 Gt [1]. In May 2013, its concentration in the atmosphere exceeded 400 ppm in the atmosphere for the first time in modern history [2] a much higher value with respect to the typical concentration present before the industrial revolution, i.e. 280 ppm [2]. Scenario development of the average temperature increase predicts that complete decarbonization of the energy sector will be required by 2060 to achieve a target of 2 °C of maximum world average temperature increase, while an increase of 1.5 °C will require a substantial contribution of negative emission technologies. Figure 1.1 shows the $CO_2$ emission per year necessary to achieve a world average temperature increase between 0.9-2.3 °C or between 4-5 °C in 2100. The predicted curves are compared with the cumulative $CO_2$ emission. Net negative emission technologies provide a net reduction of the $CO_2$ concentration in

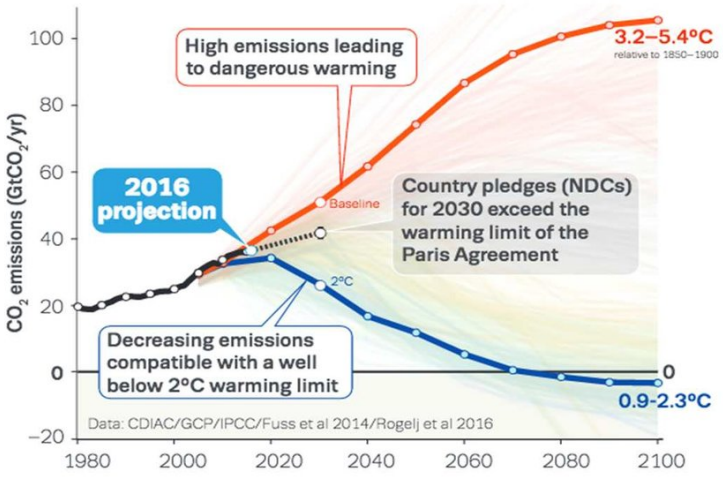


Figure 1.1: The anthropic $CO_2$ emission (black line), the $CO_2$ emission necessary to keep the average temperature increase between 0.9 and 2.3 °C (blue line) and the $CO_2$ emission that will lead to an average temperature increase of 4-5 °C (red line). Figure adopted from [3] and produced with data from [2].

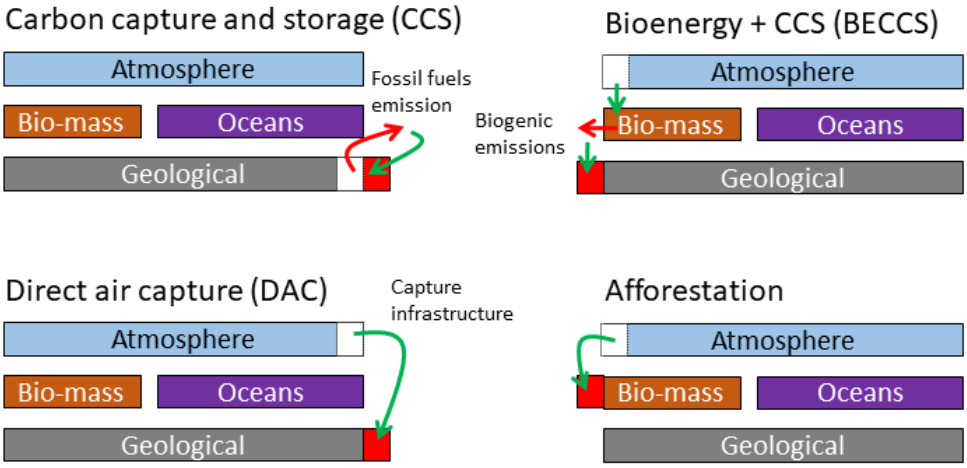


Figure 1.2: Principles of carbon capture and storage, direct air capture, reforestation and bio-energy with carbon capture and storage, as discussed in [5].

the atmosphere. Examples of negative emission technologies (typically included in the scenario development) are carbon capture and storage (CCS), direct air capture (DAC), re-forestation (and afforestation) and bio-energy production combined with carbon capture and storage (BECCS) [4]. Direct air capture foresees to capture the $CO_2$ in the atmosphere and store it in geological deposits or the oceans. In CCS technologies the $CO_2$ is captured where it is produced and then stored in long term deposits similarly to the DAC technologies. CCS and DAC technologies appear to be very similar, however, the additional step of capturing the $CO_2$ from the atmosphere is highly energy-intensive and it makes less favourable DAC technologies with respect to CCS. Reforestation and afforestation, as suggested by the name, focus on planting trees to increase the biological consumption of $CO_2$. BECCS technologies use biomasses to produce energy rather by direct combustion of the biomasses or through the production of fuels by fermentation. Such technologies foresee combined to capture the $CO_2$ produced in the energy production process. In such way, the $CO_2$ is captured (by the growing plants) from the atmosphere and not released, achieving a net negative emission. Figure 1.2 shows an overview of the $CO_2$ reduction schemes discussed. The application of BECCS to produce bio-fuels is particularly relevant to reduce the $CO_2$ from the sectors that cannot be de-carbonized (e.g. aviation, heavy-duty vehicles...). The total negative contribution from BECCS system is estimated to be 2-11 $GtCO_2\ yr^{-1}$ in 2050 and 15-70 $GtCO_2\ yr^{-1}$ in 2100 [6–8]. However, the large application of BECCS (as well as re-forestation) is limited by the land (and water) consumption [5]. Also, the creation of large scale mono-culture/forest would seriously harm the biodiversity and eventually it leads to land erosion. It has been

calculated by Smith et al. [5] that achieve a negative net emission between 1.1-3.3 $GtCO_2$ $yr^{-1}$ requires a land between 2-4 times larger than the world areas defined as abandoned or marginal. Thus, the cultivation to mitigate the $CO_2$ emission problem would compete with food production. This reduces the effective net negative emission achievable, via BECCS technologies and re-forestation.

## 1.2 Strategies for $CO_2$ utilization

In 2019 the worldwide $CO_2$ utilization sums up to 230 Mt, most of which, is used in urea production (130 Mt) and for enhanced oil recovery (80 Mt) [9]. $CO_2$ is used also in the food and beverage production, fire suppression and steel production [9]. Direct use of $CO_2$ is limited and the annual world consumption is small compared to the emission of $CO_2$ from burning fuels and the chemistry sector, hence new strategies are being currently investigated [10, 11].

The usage of $CO_2$ into the chemical industry can follow two routes: use of $CO_2$ preserving its oxidation state (+4) to form compounds such as poly-carbonates and polyurethanes, inorganic carbonates, hydrogen carbonates etc. or through a change in the oxidation of the carbon (+2 or lower) for the formation of hydrocarbons. The latter is more energy demanding, however, it allows the synthesis of fuels and hydrocarbons in general, whose demand is significantly larger (>10 times) than the chemicals that can be produced preserving the oxidation state of the carbon [11]. Fuel synthesis from $CO_2$ does not represent a negative emission technique since $CO_2$ used in the production is re-emitted in the atmosphere. However, the avoided $CO_2$ emission is larger if the fuels are produced with $CO_2$ captured from the air (similarly to DAC technologies).

The simplest way to use $CO_2$ as a primary building block of fuels is to de-oxygenate it forming CO, which is used directly in fuel and hydrocarbon synthesis in combination with hydrogen [15, 16]. The typical source of $H_2$ are hydrocarbons, and hydrogen production has $CO_2$ as byproduct [17]. Therefore, hydrogen that is combined with CO to produce fuels must be produced from water electrolysis or other $CO_2$ neutral sources to obtain an effective carbon reduction. The energy used to de-oxygenate $CO_2$ should come from the perennial energy sources (such as wind, sun etc.) to have a positive effect on the net $CO_2$ emission.

The $CO_2$ de-oxygenation process can fully adapt to an intermittent energy source, such as renewable energies sources. Such sources typically suffer from two problems: intermittency and mismatch between availability of (efficient) renewable energy and

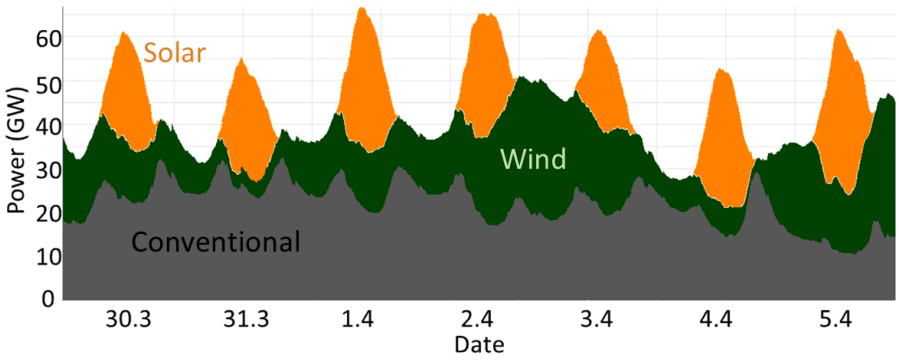


(a)

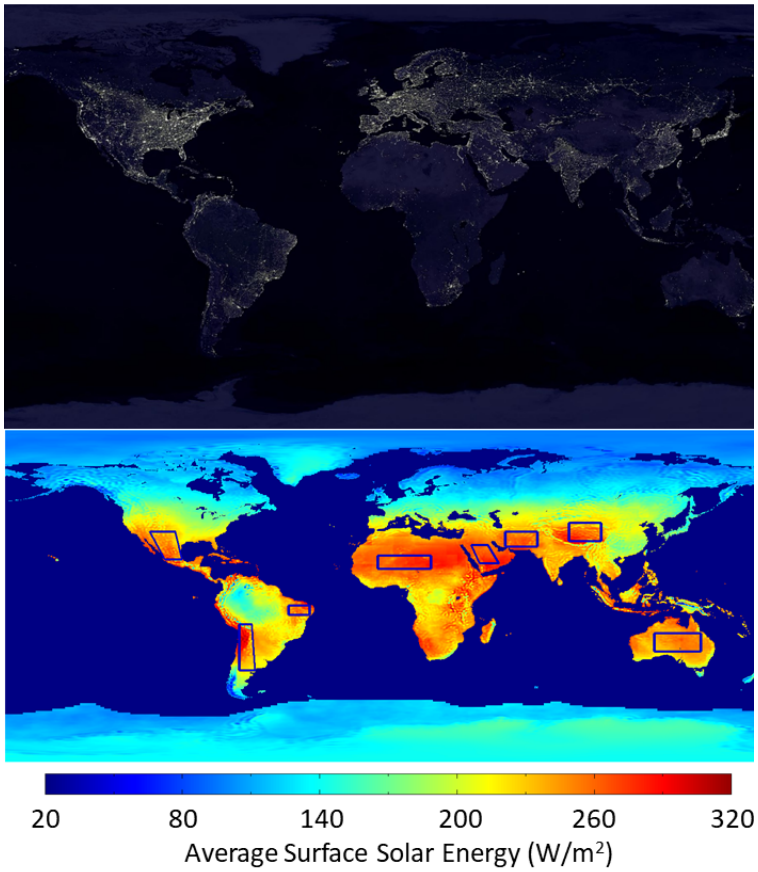


(b)

Figure 1.3: *(a)* oscillations of electric power produced in Germany by solar panels and wind mill in week 14 of 2020, data obtained from [12]; *(b)* solar energy density averaged over an year compared with the night illumination, figures adopted from [13] and [14].

energy demand. Both concepts are visually represented in figures 1.3 *(a)* and *(b)*. Figure *(a)* shows the electric energy produced in Germany from wind (green), sun (yellow) and from conventional (e.g. coal, oil etc.) sources (grey). Figure 1.3 *(b)* shows a comparison of the solar energy density on the earth and the light illumination at night (i.e. the energy demand distribution). If the excess of renewable energy is used to convert $CO_2$ into CO (but also to produce the necessary $H_2$) the $CO_2$ conversion into fuels and chemicals becomes also an attractive option to solve the problems of intermittency and geographical mismatch between availability of renewable energies and energy demand.

The current $CO_2$ valorization research focuses mainly on electro-catalytic processes and thermochemical processes [18], which are the most mature technologies. Plasma technology is also currently studied as a mean of $CO_2$ conversion into CO [19]. Plasma devices offer high flexibility in terms of response time (between seconds and minutes) compared to thermo-chemical reactions that require tens of minutes (e.g. [20]). Hence the plasma can follow the power oscillations. Additionally the plasma sources, contrary to electro-catalytic processes, typically do not require complex or rare materials (thus expensive), which makes them attractive for a large application. For example, microwave plasmas are based on readily available magnetrons or solid-state generators. The former is manufactured in large quantities for the microwave ovens and the latter is used in the telecommunication sector (although with limited power). Therefore, microwave plasma devices are attractive for large scale applications such as $CO_2$ conversion for fuel production.

Different types of plasma discharges are used for $CO_2$ conversion: dielectric barrier, microwave, radio-frequency, corona, gliding arc, and nanosecond pulsed high voltage discharges. In [21], the different discharges are compared in terms of maximum energy efficiency and $CO_2$ conversion. Dielectric barrier discharges have a maximum energy efficiency of 20% and a $CO_2$ conversion of about 40%. With gliding arcs on the other hand energy efficiency up to 60 % have been reported but with conversion typically limited to a maximum of 30 %. Microwave discharges and RF discharges are reported to achieve the highest conversion (up to 90 %) and energy efficiencies (up to 90%), albeit not simultaneously [21]. Although modern experiments are not able to reproduce such results, microwave discharges still represent the most promising technology for plasma-assisted $CO_2$ conversion.

# 2 Microwave plasma for $CO_2$ conversion

## 2.1 Definition of plasma

Plasma indicates a state of matter in which positively and negatively charged particles separately coexist and their density is sufficient to influence the collective motion. Plasma is sometimes identified as the fourth state of matter. Such epithet comes from the fact that by transferring energy to a solid, it becomes a liquid, then a gas and finally a plasma. A huge variety of systems from stars to sparks are in the plasma state. Generally, plasmas are divided into two categories laboratory plasmas and natural plasmas. In space plasmas are the form in which most of the visible matter can be found the stars, as well as the interstellar medium, solar wind, solar corona and many other common systems, are in the plasma state. Natural plasmas can be found also on earth examples are lightening and aurora. Plasmas that are generated artificially are typically called laboratory plasmas. Nowadays plasmas are widely used in many technological applications such as the electronic industry or waste treatment. Plasmas are significantly attractive for technological application since a significant concentration of radicals and chemically active components can be generated far from thermodynamic equilibrium [22].

To be classified as plasma a mixture of positively and negatively charged particles has to fulfil some conditions: *quasi-neutrality* the density of positive charges and the negative charges must be equal, on a scale larger than the Debye length. The size of the system (plasma) must be larger than the Debye length (L>> $\lambda_d$) and the particle density in a Debye length sphere must be large ($\frac{4}{3}\pi \mathrm{n}_e\ \lambda_d^3 >> 1$, where $n_e$ is the electron density). The Debye length is the characteristic distance in which the electrostatic interactions between the charges that constitute a plasma is not negligible. The Debye length can be written as:

$$\lambda_d = \sqrt{\frac{\epsilon_0\ K_b T_e}{n_e e^2}} \tag{2.1}$$

where $\epsilon_0$ is the vacuum dielectric constant, $T_e$ the electron temperature (in eV), $n_e$ the electron density and $e$ the electron charge.

By definition, a plasma exists for a time significantly longer than the charge density oscillation, so-called plasma frequency $\omega_{pe}/2\pi$. The angular plasma frequency ($\omega_{pe}$), defined as the characteristic oscillation frequency of a species in a plasma is:

$$\omega_{pe} = \sqrt{\frac{n_e e^2}{m_e \epsilon_0}} \tag{2.2}$$

where $m_e$ is the electron mass.

A plasma is often generated starting from a gas, which is ionized and becomes a plasma. The ionization processes are often in laboratory cases initiated by a strong electric field, which produces the energetic electrons needed to ionize the neutral particles in the gas. The plasma ignition (the generation of a plasma from another state of matter) is different from sustaining a plasma. A plasma can be sustained only when the ionization reactions are sufficient to compensate the recombination (losses of ions, e.g. $Ar^+ + e \leftrightarrow$ Ar). When the recombination processes are faster then the ionization all the charges of the system are lost and the plasma ceases to exist. The fraction of neutral particle that is ionized is called ionization degree ($=\frac{n_e}{n_n+n_e}$, where $n_n$ is the neutral density). Ionization processes require energetic electrons (the threshold depends on the ionized species), while recombinations are more likely to happen with low energy electrons, it follows that to sustain a plasma it is necessary to supply (continuously) energy to the system. The plasmas investigated in this work are called microwave plasmas since they are sustained by microwave.

### 2.1.1 Equilibrium in plasma

The zeroth principle of the thermodynamics defines the concept of thermal equilibrium: *"If two systems are in thermal equilibrium with a third system, then they are in thermal equilibrium with each other"* which implies that when two objects at thermal equilibrium are in contact, there is no net heat transfer between the objects [23]. A thermodynamic system is typically described using its temperature, which, despite being intuitive, is a rather complex quantity whose definition requires to define the concept of entropy and internal energy. Entropy (S) is a measure of the number of microscopic states a system ranges over when it is in a particular macroscopic state. The internal energy (U) is the energy contained within the system. The reciprocal of temperature than can be defined as *"The reciprocal temperature (1/T) corresponds to the relative change in the number of microscopic states a macroscopic system at*

*equilibrium ranges over, at constant volume and chemical composition, with a change in internal energy."* [24], i.e. $\frac{\partial S}{\partial U} = \frac{1}{T}$. In a system of known fixed total energy the temperature (T) can be used to describe the probability of a particle of having an energy E is p(E) = $Z^{-1}e^{-E/k_BT}$, where $k_B$ is the Boltzmann constant, Z a normalization constant. The distribution p(E) is called Boltzmann distribution. In a system where the particle energy distribution (namely the number of particles with energy E + $\delta$E) follows a Boltzmann distribution, it is possible to assign a temperature, which is the one describing the particle energy distribution.

The temperature is the minimum information needed to describe the energy distribution of the particles in a system at thermal equilibrium. However, in systems with many degrees of freedom a temperature can be used to describe the population distribution of the particles for each different degree of freedom. In a plasma there is always the coexistence of multiple degrees of freedom: electrons, ions and neutrals can be described by different energy distributions. The gas temperature can be used to describe the kinetic energy distribution of the neutral particles in a plasma, the electron temperature the kinetic energy distribution of the electrons, etc. In general for each molecular species in the plasma, there are 3N degrees of freedom (translational, rotational and vibrational). A temperature can be (although not necessarily) associated with each of these degrees of freedom to describe the energy distribution if thermally populated. Strictly, in a plasma there is a thermodynamic equilibrium only if all the species and all their degrees of freedom have the same temperature, i.e. there is 0 net energy transfer between them.

In naturally generated plasma (astrophysical plasma, auroras etc.) as well as plasma generated in laboratories, the energy is coupled non uniformly. In most laboratory cases (and the ones investigated in this thesis), plasmas are generated and sustained by a (strong) electric field, where the energy is at first transferred to the electrons. Electrons undergo elastic and inelastic collision with the other plasma species, transferring their energy to the different degrees of freedom (see equation 2.6). The equilibration of the system is driven by collisions, however very often there is not enough time (collision are too slow) or energy (not all the particles can be heated up) to reach a complete thermal equilibrium. An extension of the thermodynamics, that is a description in which space is not considered, is the local thermodynamic equilibrium (LTE). Thermal plasmas (i.e. plasma at thermal equilibrium) are plasma in which every point in space can be described by a single temperature at a given pressure and initial composition. The thermal equilibrium is fulfilled differently at different positions in space (namely there are density and temperature gradients).

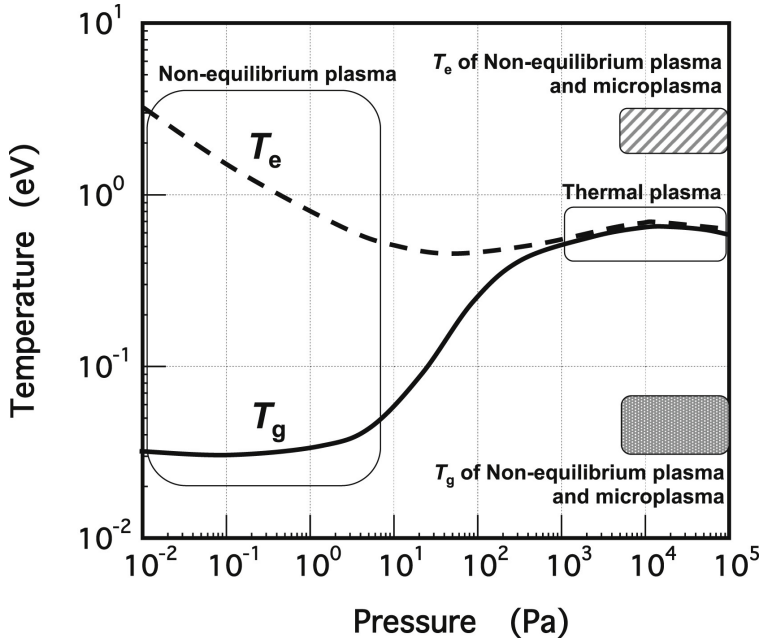


Figure 2.1: Typical evolution of the gas temperature and electron temperature as a function of the pressure. Image from [25].

Non-equilibrium plasma are characterized by the co-existence of several temperatures related to different plasma particles and the different degrees of freedom. In a molecular plasma, it is often found that $T_e > T_{ex} > T_{vib} > T_{rot} \approx T_{ions} \approx T_{gas}$ [26], where $T_e$ is the electron temperature. $T_{ex}$ is the so called excitation temperature, the temperature associated with the energy distribution of the electronic states of the species in the plasma. $T_{vib}$ is the temperature associated with the molecules vibration (for $CO_2$ it is often found $T_{v_3} > T_{v_1} \approx T_{v_2}$, where $T_{v_3}$ is the temperature associated with the asymmetric stretching, see section 2.3 for more discussion). $T_{rot}$ the temperature associated with the molecular rotation that, in high pressure plasmas, is often found in equilibrium with the gas ($T_{gas}$) and ion temperature ($T_{ions}$).

Figure 2.1 shows the typical evolution of the electron temperature and the gas temperature as a function of the pressure. In plasmas the equilibrium often depends on the gas pressure. As mentioned before, the energy is coupled to the electrons, and then transferred to the heavy species via collisions. The electron mass is much lower than the ion mass, thus the energy exchange is not efficient. The electrons-neutral collision frequency ($=n_e n_n \langle \sigma v \rangle$, where $\sigma$ indicates the collision cross section and $v$ the relative velocity) increases at increasing pressure, as consequence the gas temperature increases eventually reaching equilibrium. The latter behavior is a simplified picture, and in reality also high pressure plasma can be found out of equilibrium. For example, Dielectric Barrier Discharges and microplasmas are known to be outside of equilibrium at atmospheric pressure [25].

## 2.2 Microwave plasma

Among the several types of plasma, microwave plasma discharges are the most promising plasma route for $CO_2$ dissociation [21]. Microwave plasma discharges are widely used in industrial application including synthesis of inorganic compounds [27] and plasma deposition technologies [28]. Due to their intrinsic low electric fields and high average power densities, microwave plasmas allow generating molecular plasmas with relatively low electron temperatures, between 0.5 and 3 eV, in the pressure range between few mbar and atmospheric pressure [29]. The low electron temperature favours the power deposition to the asymmetric stretching of the $CO_2$ molecule that can favour vibrational dissociation in place of direct dissociation mechanisms by electron impact (see section 2.3).

### 2.2.1 Power coupling in microwave plasma

A microwave discharge is sustained by the electric field of the electromagnetic wave. The power is coupled to the electrons, which then transfer via collisions the power to the heavy particles. The energy absorbed by the electrons can be modelled as [30]:

$$Q_{ohm} = \frac{1}{2} Re(\sigma) |\vec{E}|^2 \tag{2.3}$$

where $\vec{E}$ the electric field and $\sigma$ is the complex conductivity:

$$\sigma = \frac{\epsilon_0 \omega_{pe}^2}{\nu_{en} + i\omega} \tag{2.4}$$

where $\omega_{pe}$ is the plasma frequency, $\nu_{en}$ the collision frequency between electrons and heavy particles for elastic momentum exchange, $\omega$ the frequency of the electromagnetic wave. The microwave power is absorbed in the plasma by the electrons with a characteristic absorption length (also called skin depth) of [31]:

$$\delta = \frac{c}{\omega_{pe}} \sqrt{\frac{2\nu_{en}}{\omega}} \tag{2.5}$$

where c is the speed of light in vacuum. The skin depth corresponds to a 1/e attenuation of the wave electric field under the condition $\nu_{en}/\omega > 1$.

### 2.2.2 Concept of plasma torch

One of the most common microwave plasma generator used in the pressure range from a few tens of mbar up to atmospheric pressure is the plasma torch. Although

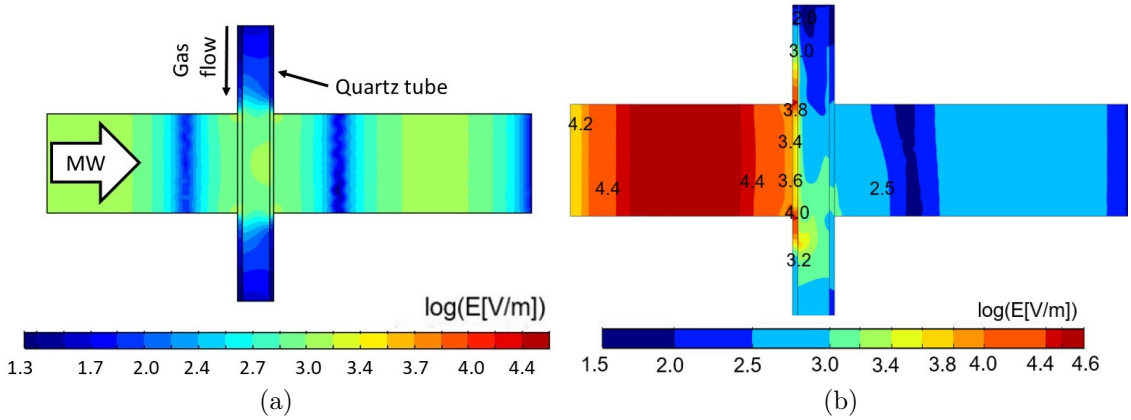


Figure 2.2: *(a)* simulated electric field sustained in a waveguide by the microwave without the plasma (M. Baeva private communication). *(b)* simulated electric field in an Ar plasma sustained in the microwave plasma torch with 1 kW power, a gas injection velocity of 2 m $s^{-1}$ in a 1 ion approximation model. Figure adopted from [32]

a few different designs of microwave plasma torches exist the working principle is the same. The most simple design of a microwave plasma torch consists of a microwave generator, a waveguide and a quartz tube placed inside it, where the plasma is sustained.

Figure 2.2 *(a)* shows electric field sustained by the microwave in the waveguide when there is no plasma. The reduced electric field sustained by the microwave is typically not sufficient to ignite a plasma at pressures higher than >100 mbar. The plasma ignition can be obtained without the aid of external igniters only at low pressure. Only at pressures below 100 mbar, the reduced electric field (the ratio between the electric field and the particle density) is sufficient to initiate the ionization reactions. Examples of external igniters are retractile metallic antennas inserted in the quartz tube by a pneumatic system to ignite the plasma or fix coaxial pin (see chapter 4 for a more complete description of the coaxial pin) that enhance the electric field to reach values that allow the plasma ignition [33].

After the plasma ignites the microwave power is transferred to the electrons. The microwaves are absorbed inside the skin depth and the electric field in the plasma, where the electrons are, is reduced. In figure 2.2 *(b)* the electric field simulated in an Ar plasma sustained in a microwave plasma torch is shown [32]. Since the microwave power is absorbed in a skin depth the electric field inside the quartz tube remains low. This allows keeping the electron temperature low from a fraction of eV up to a few eV.

### 2.2.3 Power transfer to heavy species

The electrons transfer the microwaves energy to the heavy particles through collisions. The energy gained by the heavy particle via collision with electrons can be written as [30]:

$$Q_{en}^{elastic} = \sum_{s \neq e} \frac{3}{2} n_e \nu_{es} \left(\frac{2m_e}{m_s}\right) k_b (T_e - T_n) \tag{2.6}$$

where s indicates the heavy particle in the plasma, $n_e$ the electron density, $m_e$ the electron mass, $m_s$ the heavy particle mass, $T_e$ the electron temperature and $T_n$ the temperature of the heavy particles (i.e. the gas temperature). The elastic collisions between the heavy species and the electrons are responsible for the equilibration of the electronic temperature with the heavy particle temperature(s). Along with the pure heating of the heavy species (i.e. elastic collision), inelastic collisions take place. Inelastic collisions result in an energy exchange of the kinetic energy of the electrons and the internal energy (electron energy, vibrational energy, rotational energy, etc) of the heavy species. The electron energy loss (or gain) due to inelastic collision can be written as [30]:

$$Q_{en}^{inelastic} = \sum_{l} R_l \Delta\epsilon_l \tag{2.7}$$

with l indicating the inelastic collision considered, $R_l$ the reaction rate and $\Delta\epsilon_l$ the average energy exchange in the reaction. An example of inelastic collision reaction is the ionization of the $CO_2$ molecule:

$$CO_2 + e \rightarrow CO_2^+ + e + e \tag{2.8}$$

### 2.2.4 Heavy particle collisions

A general discussion about the reactions that can occur in a plasma is beyond the purpose of this work, an overview can be found in Fridmann's book "Plasma chemistry" [22], here only the reactions relevant for this work will be discussed.

#### Two body reactions

A two body reaction involves the collision of two particles A and B, which generates two products C and D, generally can be written in the form:

$$A + B \rightarrow C + D \tag{2.9}$$

The reaction rate for a two body reaction A+B describes the number of reaction per unit of time that takes place in a unit of volume, and can be written as [22]:

$$R_{A+B} = n_A n_B \langle \sigma_{A+B} v \rangle = n_A n_B \int \sigma_{A+B}(v) v f(v) dv = n_A n_B k_{A+B} \tag{2.10}$$

where A and B are the reactant and n is their respective density, v is the relative velocity of the particle A with respect to B, $\sigma$ is the cross section for the reaction A+B. This is typically a parameter that depends on the relative velocity of the colliding partners, f(v) is the velocity distribution of the reactants, the integral $\int \sigma_{A+B}(v) v f(v) dv$ is the rate coefficient $k_{A+B}$ and it has the units $m^3 s^{-1} molecule^{-1}$.

Apart from chemical reactions, another group of reactions that is relevant in this work are energy transfer reactions. These are collisions between two species that result in an exchange of internal energy between the reactants. Type of energy transfer reactions are:

- Electronic excitation - vibrational energy transfer (V-E): a collision in which vibrational energy is transfer to an electronic excitation or vice versa.
- Vibrational-vibrational (V-V) energy transfer, in which the reactants exchange vibrational energy.
- Vibrational - rotational (V-R) energy transfer: a collision in which vibrational energy is transfer to rotational energy or vice versa.
- Vibrational - translational (V-T) energy transfer: a reaction in which vibrational energy is transfer to kinetic energy.

**Three body reaction**

A three-body reaction involves two species A and B and it yields one single product species AB. Three-body reactions are typically written in the form:

$$A + B + M \rightarrow AB + M \tag{2.11}$$

where M represents a collision partner. All the relevant three-body reactions considered in this work are chemical reactions. The reaction rate of a three-body reaction can be written as:

$$R_{A+B+M} = n_M n_A n_B k_{A+B+M} \tag{2.12}$$

where $k_{A+B+M}$ is the reaction rate for the three-body reaction and has the unit $m^6 s^{-1} molecule^{-2}$ and $n_M$ the density of the collision partner M. The three-body reactions rate are sensitive to the collision partner density. The ratio between a three-body

and a two-body reaction rate involving the same species A and B increases linearly with the third body density ($\propto$ pressure). It follows that at increasing pressure the importance of three-body processes with respect to the two-body processes increases. Typically three-body processes start to be relevant in $CO_2$ microwave plasma at pressures above 100 mbar.

**Quenching**

In plasmas, where (electronically/vibrationally) excited states are common, it is useful to define how quickly an excited state is lost through energy exchange reactions. The *quenching* rate is the number of reaction per unit of time that takes place in a unit of volume and results in a loss of that excitation. The quenching rate does not indicate a single reaction but rather a variety of processes such as energy transfer reactions or chemical reactions between excited states.

## 2.3 $CO_2$ dissociation

### 2.3.1 Conversion and energy efficiency definition

Before discussing the mechanism that leads to the $CO_2$ dissociation it is useful to define the conversion and energy efficiency. The former express the fraction of $CO_2$ converted, the latter the energy spent in the conversion. The $CO_2$ conversion obtained in a device can be quantified by looking to the concentration of $CO_2$, CO and $O_2$ in the output gas.

The conversion rate of the plasma can be determined by analyzing the gas composition as:

$$\chi = 1 - \frac{[CO_2]_{out}}{[CO_2]_{in}} = \frac{1 - \frac{[CO_2]_{out}}{[CO_2]_{out}+[CO]_{out}+[O_2]_{out}}}{1 + \frac{[CO_2]_{out}}{2\cdot([CO_2]_{out}+[CO]_{out}+[O_2]_{out})}} \tag{2.13}$$

where $\chi$ is the conversion efficiency (from now on conversion), [CO] and [$CO_2$] stand for the carbon monoxide and carbon dioxide concentrations. The more common form of the conversion $\frac{[CO]_{out}}{[CO_2]_{out}+[CO]_{out}}$ can be obtained under the assumption of 2 $[CO]_{out}$ = $[O_2]_{out}$, fulfilling the stoichiometry of the $CO_2$ dissociation (see equation 2.18). From the conversion the energy efficiency can be calculated:

$$\eta = \chi \frac{\Delta H}{SEI} \tag{2.14}$$

$\eta$ is the energy efficiency, $\Delta$H the enthalpy of the $CO_2$ dissociation (2.93 eV, see equation 2.18). The specific energy input in a plasma device describes the energy

available for each $CO_2$ molecule that cross the plasma. It is a global parameter that can characterize easily any kind of plasma discharge and can be expressed in electronvolt per molecule as the following:

$$SEI = 0.0138 \, \frac{power[W]}{flow[L/min]} \left[\frac{eV}{molecule}\right] \tag{2.15}$$

where the power is expressed in Watt and the flow in standard liter per minute, the overall constant has the proper units to obtain the SEI in eV/molecule [34].

### 2.3.2 $CO_2$ dissociation chemistry

The $CO_2$ molecule is (in its ground state) a symmetric three-atomic linear molecule. Figure 2.3 summarized the possible nuclei vibration in the $CO_2$ molecule: asymmetric stretching (first energy quantum=0.291 eV), symmetric stretching (first energy quantum=0.172 eV) and bending mode (first energy quantum=0.083 eV).

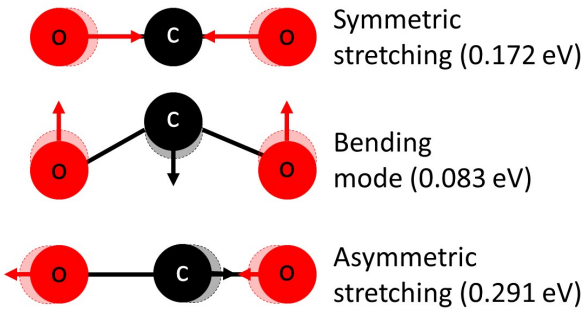


Figure 2.3: Illustration of vibrational modes in a $CO_2$ molecule. Figure adopted from [35].

From a chemical perspective the dissociation of the $CO_2$ molecule requires a minimum energy of 5.5 eV:

$$CO_2 + M \rightarrow CO + O + M \qquad \Delta H = 5.5 \, eV \tag{2.16}$$

where M is a collision partner. This reaction has a specific energy requirement of 5.5 eV per dissociated $CO_2$ molecule at 400 K and at atmospheric pressure. In presence of atomic oxygen additional dissociation of $CO_2$ can be obtained via:

$$CO_2^* + O \rightarrow CO + O_2 \qquad \Delta H = 0.3 \, eV \tag{2.17}$$

where $CO_2^*$ is a vibrationally excited $CO_2$ molecule. If the potential energy of the O atom produced in the first step (process 2.16) is not lost via its mutual recombination with another O atom to form an $O_2$ molecule via the reaction $O + O + M \rightarrow O_2 + M$

where M is a third particle or a wall, but it reacts with an excited $CO_2$ molecule and produces an additional CO molecule. In the latter scenario, the minimum energy requirement for one CO molecule production decreases to 2.93 eV/molecule.

$$CO_2 \rightarrow CO + \frac{1}{2}O_2 \quad \Delta H = 2.93\, eV \tag{2.18}$$

The difference between process 2.18 and 2.16 is due to the potential energy difference of the O atom in its free or bond state (i.e. $O_2$ molecule). The gain is equal to half the energy needed for splitting the $O_2$ bond.

### 2.3.3 $CO_2$ dissociation mechanism in microwave plasmas

In a plasma, the dissociation of $CO_2$ can be induced either by electron impact processes or thermal dissociation.

#### Electron impact dissociation

Electron driven dissociation of $CO_2$ hereby stands for the dissociation mechanism that needs an electron impact collision to be initiated. In presence of high energy electrons (7.5 eV and more) $CO_2$ dissociation can occur via electron impact:

$$CO_2 + e \rightarrow CO^* + O^* + e \tag{2.19}$$

accordingly to the energy of the electrons that dissociate $CO_2$, several electronically excited state of the CO molecule ($CO^*$) and oxygen atoms ($O^*$) can be formed in the process [36]. Electron impact dissociation cross-section of $CO_2$ has been recently discussed by Morillo Candas et al. [37], who found consistency between the reaction rate calculated starting from the cross-section given by Polak et al. [38] and the experimentally measured reaction rates. Two thresholds are found in the dissociation cross-section of the $CO_2$ one at 7.5 eV and a second at *ca.* 11.9 eV. The first corresponds to a dissociation through allowed and forbidden excitation of the electronically excited states of $CO_2$ with electron energy in range 7-9 eV and the second to dissociation via the generation of electronically excited fragments [39]. In particular, the dissociation channel: $CO_2 + e \rightarrow CO(a^3\Pi) + O(^3P)$ represent up to 40 % of the total cross-section [38], also all the other triplets state of CO (see chapter 5) can be formed in the dissociation process. The formation of the CO molecule in its excited states $CO(a^3\Pi)$ opens the possibility of another $CO_2$ dissociation channel [40]:

$$CO_2 + CO(a^3\Pi) \rightarrow CO + CO + O \tag{2.20}$$

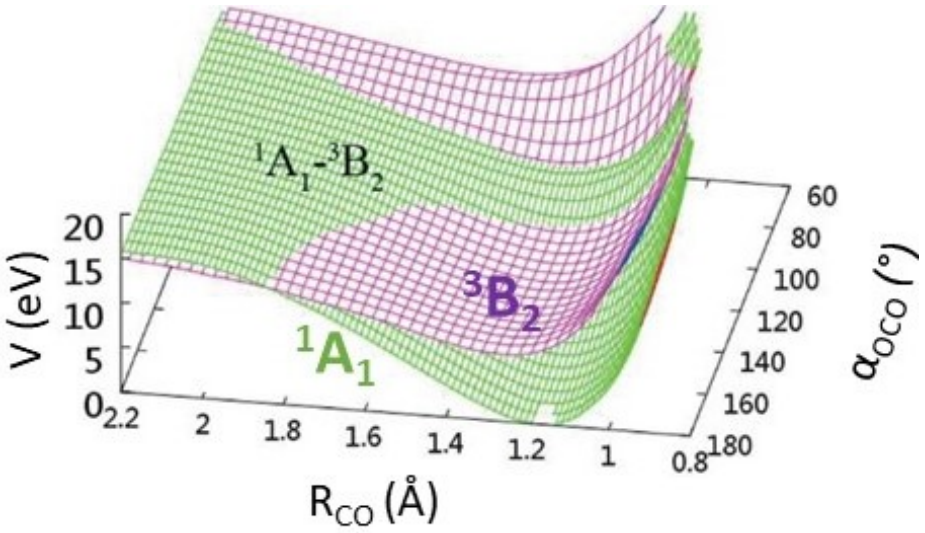


Figure 2.4: Potential energy surfaces of the $^1A_1$ and $^3B_2$ states of the $CO_2$ molecule. Figure adopted from [41].

The $CO(a^3\Pi)$ state has an energy of about 6 eV, thus it can promote efficient dissociation of the $CO_2$ via energy exchange. Effectively it can recover the energy spent on the electron impact dissociation of $CO_2$ with high energy electrons, thus increasing the energy efficiency.

### Vibrational dissociation

Another mechanism that leads to $CO_2$ dissociation is the dissociation via vibrational ladder climbing. The dissociation asymptote of the ground state of the $CO_2$ molecule ($^1A_1$) lays above 7 eV and corresponds to the dissociation of $CO_2$ into the $CO(X^1\Sigma^+)$ and $O(^1D)$ fragments [41]. The ground state of the $CO_2$ molecule has a strong interaction with the first excited bend state of the $CO_2$ molecule ($^3B_2$) which dissociate at *ca.* 5.5 eV in the $CO(X^1\Sigma^+)$ and $O(^3P)$ states [41]. If enough energy is stored in the vibrational excitation of the $CO_2$ molecule (namely when the CO bond in the $CO_2$ molecule is longer than 1.6 Å [41]) a crossing can occur between the two electronic states which lead to dissociation of the $CO_2$ molecule with lower energy. Figure 2.4 shows the intersection of the potential surfaces $^3B_2$ and $^1A_1$ of the $CO_2$ molecule. The potential energy surfaces are plotted as a function of the CO bond length and the OCO bond banding angle. The dissociation asymptote shown in the figure refers to the $CO_2$ dissociation into two oxygen atoms and a carbon atom.

The overall vibrational dissociation pathway can be written as:

$$CO_2(^1A_1, \nu) + M \rightarrow CO_2(^3B_2, \nu') + M \rightarrow CO(X^1\Sigma^+) + O(^3P) + M \qquad (2.21)$$

where the $CO_2(^1A_1, \nu)$ indicates the $CO_2$ molecule in the electronic ground state, with $\nu$ excitation of the asymmetric stretching and 0 excitation of the symmetric stretching and bending mode, M a collision partner. The same results can be obtained by pumping the other vibration modes of the $CO_2$ molecule to induce the electronic transition and dissociation.

To obtain (efficient) vibrational dissociation of the $CO_2$ molecule, the asymmetric stretching should be excited preferentially. The needed excitation can be obtained via several electron excitations or via heavy particle collisions.

It is known that the asymmetric stretching of $CO_2$ can be pumped via vibrational-vibrational (V-V) energy exchange [42]. At the same time, the losses of vibrational excitation into gas heating (V-T) should be minimized, however, the higher the gas temperature the faster are the losses of vibrational excitation into gas heating [22]. The V-T relaxation of the asymmetric stretching of $CO_2$ is known to be slow, while the V-T relaxation of the bending mode is known to be faster [34]. Moreover, the symmetric stretching and the bending mode of the $CO_2$ molecule are strongly coupled with each other [43]. It follows that to reduce the energy spend to dissociate a $CO_2$ molecule, the asymmetric stretching mode should be excited preferentially and the energy should not be spent into excitation of the other vibrational modes. Indeed in low pressure DC discharges (<30 mbar) it is observed that the asymmetric stretching does not equilibrate with the gas temperature, while the bending and the symmetric stretching do [43].

A crossing between the $^1A_1$ potential surface and the $^3B_2$ potential surface occurs also at bending angle of the OCO bounds of *ca.* 85-105° [41]. A vibrational dissociation, similar to the one that can be obtained via the asymmetric stretching, can also be obtained through the excitation of the vibrational bending mode of the $CO_2$ molecule. However, because the V-T relaxation of the vibrational banding is much faster than the asymmetric stretching relaxation such process is not energy efficient since the energy spent in the excitation of the banding mode is quickly lost into gas heating.

Vibrational dissociation of the $CO_2$ molecule through selective excitation of the asymmetric mode of the $CO_2$ molecule has been invoked (in the past) to justify measured $CO_2$ conversion efficiency in microwave plasma above 90 %. [44–47]. Indeed only a $CO_2$ dissociation happening because of vibrational ladder climbing can explain such high energy efficiency since both thermal dissociation (see below) and electron impact dissociation has lower energy efficiency.

### 2.3.4 Thermal equilibrium dissociation

At thermodynamic equilibrium, any system can be completely characterized by any of its fundamental relations. At known gas temperature and pressure and initial composition, the most appropriate relation to characterize the system is the Gibbs free energy. The chemical composition expected from a reaction at thermal equilibrium can be calculated by minimizing the Gibbs free energy. The equilibrium composition is independent of the "initial" mixture a $CO_2$ gas and a mixture of $C_2$ and $O_2$ in a ratio 1:2 are the same if considered at thermodynamic equilibrium at the same pressures and temperature.

The Gibbs free energy can be expressed as [48]:

$$G = \sum_j n_j \mu_j \tag{2.22}$$

where $n_j$ is the number of moles of the species j in the mixture and $\mu_j$ the chemical potential of the species j. The fraction of mass of each chemical element (e.g. C and O in pure $CO_2$) in the mixture is a constant independently of how it is distributed over the different chemical species. Therefore, for each chemical element i can be written [48]:

$$\sum_j a_{ij} n_j - b_i^0 = 0 \tag{2.23}$$

where j are the component of the mixture (e.g. in the $CO_2$ case all possible combination of C and O) and $a_{ij}$ represent the number of atoms of the i-th element in the j-th species (e.g. in $CO_2$ $a_{O,CO_2} = 2$ ). This set of equations represents the constrain on the variation of the $n_j$ of the system. Matematically the problem can be solved using the Lagrange moltiplicator, which allows to write (after derivation) [48]:

$$\sum_j \left(\mu_j + \lambda_i a_{ij}\right) \delta n_j + \sum_i \left( \sum_j a_{ij} n_j - b_i^0 \right) \delta \lambda_i = 0 \tag{2.24}$$

where $\lambda_i$ are the Lagrangian multiplier. In this work the chemical equilibrium is calculated using the program CEA [49]. The other relevant thermodynamic proprieties such as the enthalpy of the mixture can be obtained using the fundamentals thermodynamics relations [49].

The equilibrium composition for a mole of $CO_2$ (or a gaseous mixture of C and O with ratio 1:2) at atmospheric pressure at temperatures above 2000 K favours the formation of CO. In figure 2.5 is shown the composition of such gas mixture resulting from heating $CO_2$ at atmospheric pressure. Heating $CO_2$ gas at temperatures above

4000 K causes a complete dissociation into CO and O. The conversion and energy efficiency of the thermal decomposition of $CO_2$ can be obtained from the thermal equilibrium composition.

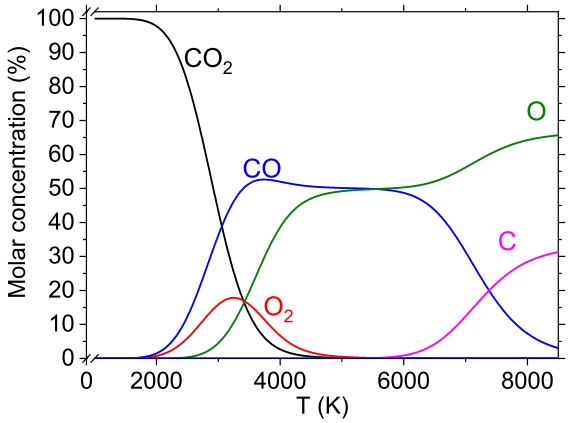


Figure 2.5: The molar fraction of $CO_2$ (red), CO (magenta), $O_2$ (orange), O (blue) and C (green) expected by heating a mole of $CO_2$ at atmospheric pressure as a function of temperature.

Figure 2.6 *(a)* shows the degree of conversion of $CO_2$ into CO as a function of the gas temperature for different pressures. Note that the conversion is calculated under the assumption that all the carbon atoms (that are formed at $T_{gas}$ >5500 K) recombine into CO. The pressure has only a weak effect on the conversion. For instance, the gas temperature required to convert 50% of the $CO_2$ into CO increases from 2700 to 3050 K (from 50 to 1000 mbar). The calculated conversion refers to the $CO_2$ dissociation fraction.

The energy spent to heat the $CO_2$ and used in the conversion of $CO_2$ into CO can be expressed as:

$$Q = \int_{T_0}^{T_{fin}} \left(\frac{\partial H}{\partial T}\right)_p dT = H(T_{fin}) - H(T_0) \tag{2.25}$$

where $T_0$ and $T_{fin}$ represent the initial temperature (298 K) and the final temperature, H is the enthalpy of the gas mixture at a given temperature. The enthalpy of the mixture is a result of the CEA calculation, from which the energy per molecule required to obtain a given temperature can be calculated:

$$SEI = \frac{Q[J/g] \cdot 44.07[g/mol]}{C_{eV}[J/eV] N_A[molecule/mol]} \tag{2.26}$$

where Q is given in J/g, 44.07 is the molar mass of $CO_2$, $N_A$ the Avogadro number and $C_{eV}$ the conversion factor between J and eV, hence the units of the SEI are eV/molecule. The latter is used to calculate the energy efficiency shown in figure 2.6

*(b)*. The energy efficiency of thermal dissociation for producing CO peaks at about 3000 K with a value of *ca.* 47 % and reduces at higher temperatures where energy is then spent not only for warming up the gas (i.e. via its heat capacity) but also for dissociating $O_2$ and CO (see figure 2.5).

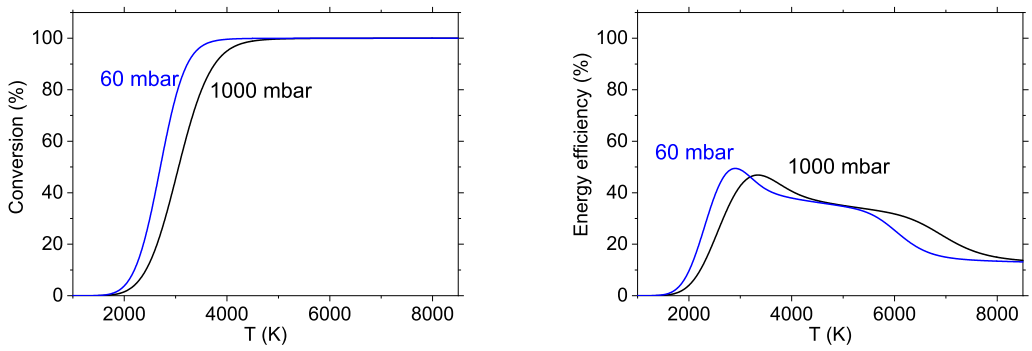


(a) (b)

Figure 2.6: *(a)* $CO_2$ dissociation expected at a given pressure as a function of the gas temperature, under the assumption of ideal quenching (no CO losses) and recombination of carbon atoms into CO. *(b)* energy efficiency at a given pressure as a function of the temperature under ideal quenching conditions.

### 2.3.5 Energy deposition $CO_2$ microwave plasma

Accordingly to the mean electron energy (that depends on the reduced electric field), different collision processes are dominant in a plasma, as a result, the electron energy (therefore microwave power) is transferred preferentially to certain degrees of freedom of the molecule (or atoms). Figure 2.7 shows the different energy deposition channel as a function of the reduced electric field at the corresponding mean electron energy in a $CO_2$ plasma. At low electron energy, the processes that are favoured are the excitation of the bending mode of the $CO_2$ molecule, the excitation of the rotational mode and elastic scattering. At *ca.* 1 eV the fraction of energy deposited into the asymmetric stretching of $CO_2$ is maximized. At increasing energy the electronic excitation (formation of electronically excited states via electron impact collisions) and the ionization becomes dominant. Electron energy between 0.5 eV and 3 eV is optimal for transferring the microwave power (through collision with electrons) to the asymmetric stretching of the $CO_2$ molecule. $CO_2$ microwave plasmas at pressures between 30 mbar and atmospheric pressure have electron energy between 0.5 eV and

2 eV, which is the optimal range to deposit the microwave energy into the asymmetric stretching of $CO_2$.

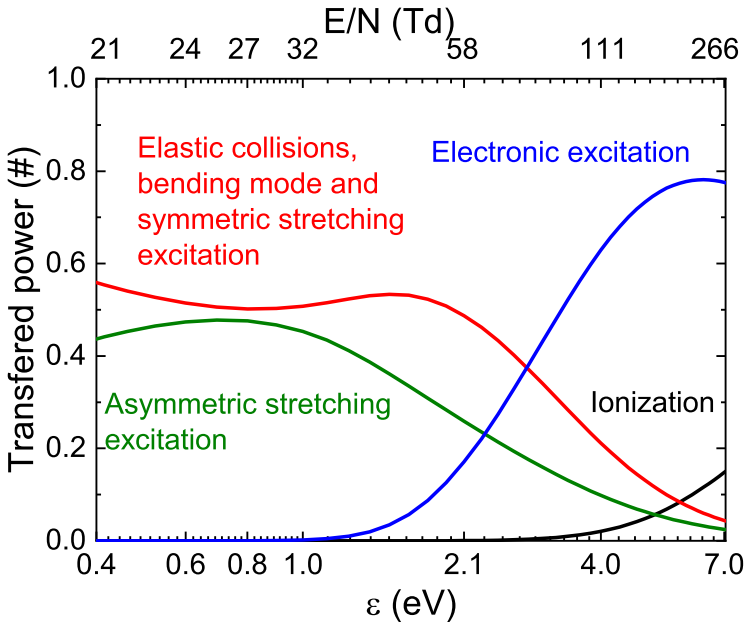


Figure 2.7: Energy deposition as function of the mean electron energy in $CO_2$ microwave plasma. Courtesy E. Carbone, the calculation of the mean electron energy is carried out with BOLSIG+ [50] with the Morgan cross section database from LxCat [51].

### 2.3.6 CO losses in microwave plasma

Avoiding recombination of CO into $CO_2$ is of significant importance to guarantee efficient $CO_2$ conversion. The mixture of $C/O/O_2/CO/CO_2$ (and other species of minor importance) needs to be quenched rapidly to avoid recombination of CO via:

$$CO + O + M \rightarrow CO_2 + M. \tag{2.27}$$

$$CO + O_2 \rightarrow CO_2 + O \tag{2.28}$$

The CO molecule can recombine via a three body process 2.27 or via a two body recombination 2.28. It has been shown that rapid cooling reduces the losses of CO in the plasma effluent. Den Harder et al. [52] modelled the evolution of the gas composition, at different initial gas temperature and cooling rates, using a 0D kinetic model. They show that the higher is the gas temperature the faster must be the

cooling to avoid significant $CO_2$ losses. To avoid high losses of CO a gas mixture at an initial temperature above 2000 K needs to be cooled faster then $10^6$ K/s [52].

# 3 Simulation of spectra of diatomic molecules

Optical emission spectroscopy (or emission spectroscopy in short) represents one of the most widely used diagnostics in plasma physics. It is a non-invasive diagnostic tool, which allows the direct measure of the population distribution (absolute or normalized, according to the calibration of the spectrometer) of the emitting species over the various degrees of freedom such as electronic excitation (in case of atoms and molecules) and ro-vibrational excitation in case of molecules.

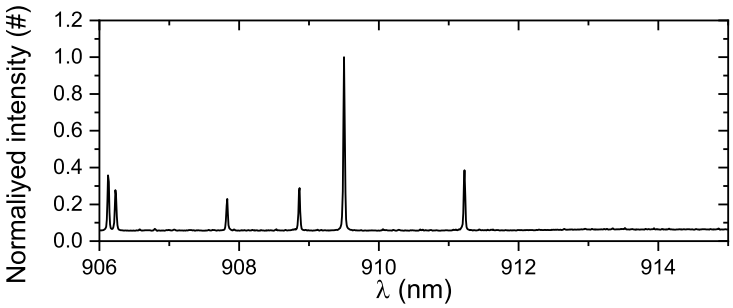


(a) *C emission*

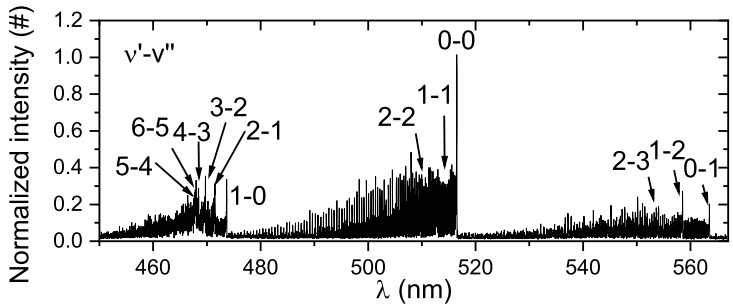


(b) *$C_2$ emission*

Figure 3.1: Typical atomic emission *(a)* carbon atoms and the typical molecular emission *(b)* $C_2$ emission. In the molecular spectrum also the vibrational levels that produce the transition are indicated.

In a molecule (or an atom) several electronic states are typically accessible, each of

them has different energy (i.e. $E_e$). The electronic state at lower energy is typically called ground state. An electronically excited state (whose energy is higher than the ground state) naturally tends to decay in a state with lower energy, the excess energy is carried away by a photon. The probability of decay from a state with higher energy to a state with lower energy is called Einstein coefficient (A). The Einstein coefficient is typically expressed in $s^{-1}$ and its reciprocal is the lifetime of the ro-vibrational energy level of the electronic state. If one electronic state can decay in another depends mostly on the electronic structure of the two states. Typical emission of atomic transitions consists of several lines, corresponding to the optically allowed electronic transitions. When a molecule is considered the typical emission is (much) more complex since the molecule can lose vibrational and rotational energy in a transition. Figure 3.1 shows a comparison between the atomic emission of carbon at *ca.* 910 nm and the emission from a $C_2$ molecule at *ca.* 440-570 nm.

This chapter is focused on explaining the theory of how the emission spectrum of a diatomic molecule can be simulated. The calculations performed in this work are presented in chapter 5. The problem of simulating an emission spectrum is divided into three sub-problems: find the energy level, find the transition probability, simulate the experimental spectra. Section 3.1 explains the structure of the energy levels of a diatomic molecule. The contribution of the electron energy and nuclear energy are first discussed. In section 3.1.6 the method used to calculate the energy level is presented. In section 3.2 the electronic transitions allowed in electric dipole approximation and the calculation of the transition probabilities are presented. In section 3.4 the simulation of a synthetic spectrum is discussed. A walk through example is presented in the text.

## 3.1 Molecular structure

The nuclei in a diatomic molecule are bound together by the electrons. Without the electrons the nuclei would repel each other because of their coulomb interaction. The electrons arrange themselves into the molecular orbitals which holds the molecule together. According to which orbitals are occupied by the electrons, different electronic states can be formed for each molecule (their classification according to their quantum numbers will be discussed later in this section). The sum of the electron energy and the Coulomb potential of the nuclei is typically called *potential curve* and represent the potential energy under whose the nuclei carry out their motion. The latter consist of vibration of the nuclei and rotation, which for a diatomic molecule

is not degenerate only with respect to the center of mass. The Schrödinger equation for the complete system is [53]:

$$\frac{1}{m_e}\sum_i\left(\frac{\partial^2\Psi}{\partial x_i^2}+\frac{\partial^2\Psi}{\partial y_i^2}+\frac{\partial^2\Psi}{\partial z_i^2}\right)+\sum_k\frac{1}{M_k}\left(\frac{\partial^2\Psi}{\partial k_i^2}+\frac{\partial^2\Psi}{\partial k_i^2}+\frac{\partial^2\Psi}{\partial z_k^2}\right)+\frac{2}{\hbar^2}(E-V)\Psi \;=\; 0 \tag{3.1}$$

where $m_e$ is the electron mass and the sum over i is a sum over all the electrons at their position $x_i$, $y_i$, $z_i$. The summation over k is a sum over the nuclei of mass $M_k$. Under the assumption of electrons moving much faster than the nuclei the eigenfunction ($\Psi$) that describes the motion can be separated an electronic part and a nuclear part [53]. E is the energy associated with $\Psi$ and V is the external potential (i.e. the potential curve after some approximation [53]). It follows that the problem can be separated in finding the energy of the nuclei rotation and vibrations and the energy of the electronic state. Thus, the eigenfunctions of a bi-atomic molecule (which are non-rigid rotators) can be factorized in a rotational part, that is only function of the molecular orientation in the space, and a vibrational part that does not depend on the orientation of the molecule, but only on the displacement of the nuclei from the equilibrium distance $r_e$ [53]. The total eigenfunction of the system then can be separated in its three components: the electronic eigenfunction ($\Psi_e$), the vibrational eigenfunction ($\frac{1}{r}\Psi_\nu$) and the rotational eigenfunction ($\Psi_r$), thus:

$$\Psi \;=\; \Psi_e\frac{1}{r}\Psi_\nu(r-r_e)\Psi_r(\theta,\phi) \tag{3.2}$$

where the molecule orientation in the space, in spherical coordinates, is described via 2 angles $\theta$ and $\phi$. $\Psi_\nu$ are the eigenfunction of the harmonic oscillator and $\Psi_r(\theta,\phi)$ the eigenfunction of the rigid rotator [53].

An electronic state can be classified into two groups: repulsive (or dissociative) states and bound states. The latter is characterized by the presence of (at least) one minimum in the potential curve, that is necessary for having a stable electronic state. In fact when a minimum is present the nuclei vibrate (and rotate) about an equilibrium position. When a minimum is not present the nuclei repel each other until the molecule dissociate, thus those states are called dissociative. Dissociative state are (typically) not observed in spectroscopy since their lifetime (the time the two nuclei need to separate completely) is shorter than the radiative lifetime, namely the inverse of the transition probability, that is the typical time required to have a decay with photon transition. A stable potential energy curve is always characterized by a vertical asymptote at short internuclear distances and a horizontal asymptote at long nuclear distances. The latter is the dissociation limit of the molecule, when the energy

stored in the motion of the nuclei (vibration and rotation) exceed the dissociation limit, the molecule breaks. The schematic of a typical dissociative potential curve is compared with a stable state in figure 3.2 for the example of the $C_2$ molecule.

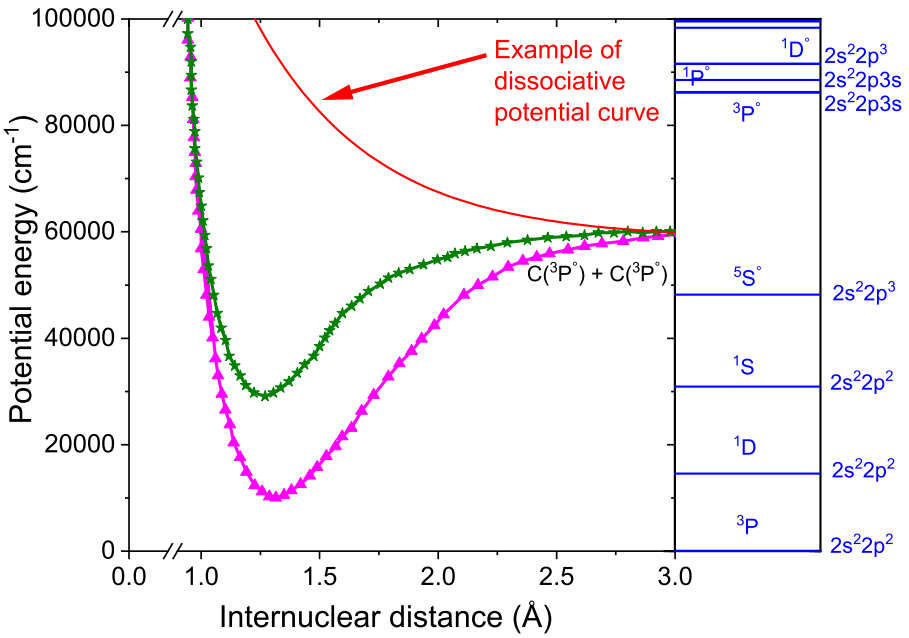


Figure 3.2: Potential curves of the $C_2(a^3\Pi_u)$ and $C_2(d^3\Pi_g)$ electronic levels [54] and energy levels of the carbon atom [55]. The red solid line is the schematic of a dissociative potential curve, note that it does not correspond to any real potential curve. The electronic orbital configuration of the C energy levels is indicated on the right side of the figure, the term symbols are indicated on top on the energy level. The dissociation fragment of the $C_2$ state corresponds to the ground state of the carbon atom.

The potential curve of a diatomic molecule can be in first approximation described analytically by a Morse potential [56], but also more sophisticated method have been developed such as the extended Hartree-Fock approximate correlation energy method [57]. The potential curve of a molecular state can also be derived from the spectroscopic constants using the so-called RKR method [58]. *Ab initio* calculation methods of the potential curves are also performed via computational methods, several of these have been combined in the program MolPro [59]. Figure 3.2 shows the potential curves of some electronic state of the $C_2$ molecules [54], and the energy level of the C atom [55], the fine structure of the atomic levels is not shown.

### 3.1.1 The nuclear motion

The motion of the nuclei of a diatomic molecule can be described as a vibrating rotator. The vibrational motion carried out by the nuclei under the potential energy of the electronics state is described by an anharmonic oscillator. The energy levels allowed in the potential well are labelled by the quantum number $\nu$ and have an energy [60]:

$$E_\nu = hc\left(\omega_e\left(\nu+\frac{1}{2}\right)-\omega_e\chi_e\left(\nu+\frac{1}{2}\right)^2+\omega_e y_e\left(\nu+\frac{1}{2}\right)^3+...\right) \tag{3.3}$$

where $\omega_e$ is the frequency of the oscillation and $\omega_e\chi_e$, $\omega_e y_e$ are anharmonicity factors. The parameters $\omega_e$, $\omega_e\chi_e$ etc. are called spectroscopic constants since they are typically obtained from spectroscopic investigations. The anharmonicity of the motion is originated from the shape of the potential energy curve, that is not a parabola (see figure 3.2), but deviates from it. The energy difference between the energy levels of an anharmonic oscillator is reducing at increasing energy. The energy levels close to the dissociation limit of the molecular state are so dense that this region is also called vibrational quasi-continuum. The effect can also be observed in the CO($b^3\Sigma^+$) state whose rotational levels are perturbed by several vibrational ($\nu$ >31) levels of the CO($a'^3\Sigma^+$) (see section 5.3.1). The vibration of the nuclei around the equilibrium position is only a function of the inter-nuclear distance r and its displacement from the equilibrium position $r_e$.

The vibration of the nuclei in the diatomic molecule is coupled with the rotation: the change of inter-nuclear distance due to the molecular vibration changes the moment of inertia, which affects the molecular rotation. However, since the typical period of vibration is small with respect to a period of rotation, a mean value of inertia can be used to describe the rotation of the nuclei in every vibrational level $\nu$. After account for the vibrational distortion of the moment of inertia, the rotation of the molecule can be described as a non-rigid rotator [53]. The energy levels of such rotator are labelled by the quantum number J and have an energy [60]:

$$E_J = B_\nu J(J+1)+D_\nu J^2(J+1)^2+H_\nu J^3(J+1)^3+L_\nu J^4(J+1)^4... \tag{3.4}$$

where $B_\nu$, $D_\nu$ etc. are average values for the vibrational state $\nu$, with a average inter-nuclear separation $r_\nu$. The parameter $B_\nu$ is a parameter connected with the

inertia of the molecule that can be expressed as:

$$B_\nu \;=\; B_e - \alpha_e \left(\nu + \frac{1}{2}\right) + ... \tag{3.5}$$

where the subscript $e$ indicates the equilibrium value. $B_e$ is the molecule inertia at the molecular equilibrium that in zero approximation, can be considered as two balls connected by a massless and rigid bar of length $r_e$. In latter approximation B can be expressed as:

$$B \;=\; \frac{h}{8\pi^2 c I_e} \tag{3.6}$$

where I represents the classical inertia $\mu r_e^2$, with $r$ the distance between the two nuclei. $\alpha_e$ represents the change of the molecule inertia because of the vibrational motion and can be expressed as a function of the internuclear distance at equilibrium and of the anharmonic oscillator [53]. A more detailed discussion of these parameters can be found in Herzberg's book "Spectra of Diatomic molecules" [53].

**Walk through example:** The upper state of the $C_2$ molecular transition shown in figure 3.1 will be used as example. For the time it will be named $C_2$(upper state). The $C_2$(upper state) has an $\omega_e$ = 1788.45 cm$^{-1}$, $\omega_e x_e$ = 16.87 cm$^{-1}$ $\omega_e y_e$ = -0.259 cm$^{-1}$ [61], which allows calculating the energy of the vibrational levels (with respect to the minimum of the potential curve) using equation 3.3, E($\nu = 0$) = 889.97 cm$^{-1}$, E($\nu = 1$) = 2643.84 cm$^{-1}$, E($\nu = 2$) = 4361.64 cm$^{-1}$ etc. The first vibrational level has $B_\nu$=1.7455 cm$^{-1}$, which can be used to derive the rotational energies from equation 3.4. However, in this work another methods is used to calculate the rotational energy levels, which accounts also for the interaction between the nuclear motion and the electron motion. It will be explained in the following sections.

### 3.1.2 Electronic structure

The potential curves of a molecule depend on the electronic configuration. Not only the energy of the electronic state (the minimum of the potential curves) but also the shape of the potential curve itself (dissociation limit, the existence of one or more minima etc.) is influenced by the electronic configuration. Hereby the electronic states will be only classified in terms of properties involved in the calculation of the energy levels of the diatomic molecule and symmetry of the eigenfunction. The electrons in the molecular orbitals have a defined orbital angular momentum L. A diatomic molecule has a natural axis of symmetry: the inter-nuclear axis. Thus the natural constant of the motion for an electron in a molecular orbital is the projection of its

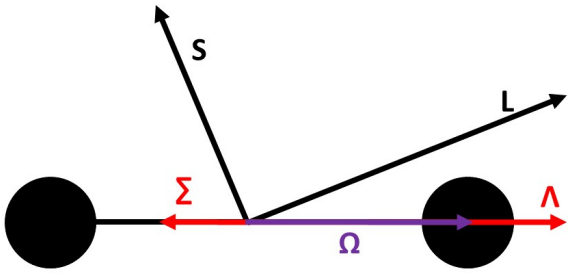


Figure 3.3: Diagram of the projection of the electronic angular momenta onto the molecular axis.

angular momentum (L) onto the molecular axis, indicated by the quantum number $M_L$, with $-L<M_L<L$. The module of the projection of the angular momentum (called $\Lambda$) onto the molecular axis is used to classified the electronic state. According to the component of the electronic orbital angular momentum along the inter-nuclear axis 0, 1, 2, etc. the corresponding molecular state is identified as $\Sigma$, $\Pi$, $\Delta$. Molecular states with $\Lambda \neq \Sigma$ are double degenerate since $M_L$ can be rather positive or negative, without affecting the energy of the molecule in first approximation (a splitting in the energy level is introduced by the lambda doubling, later discussed in this section). The electrons in the molecular orbital has also a spin whose projection onto the molecular axis can be used to define the quantum numbers $\Sigma$. Similarly to $\Lambda$, $\Sigma$ is the quantum number $M_s$, the component of the electronic spin along the internuclear axis. $\Sigma$ brings a degeneracy of 2S+1. The total electronic angular momentum projection onto the inter-nuclear axis is defined as:

$$\Omega = |\Lambda + \Sigma| \tag{3.7}$$

Figure 3.3 shows a diagram of the projection of the different momenta of the electron onto the molecular axis of symmetry.

**Walk through example:** The potential curve of the $C_2$(upper state) is shown in figure 3.2 (black), and its electronic configuration is $1\sigma_g^2 1\sigma_u^2 2\sigma_g^2 2\sigma_u^1 1\pi_u^3 3\sigma_g^2$ [62]. The total electronic angular momentum projection onto the molecular axis $M_L$ is equal to $\pm 1$ since $\Lambda = 1$ it is a $\Pi$ state. The potential curve represents the configuration in which the projection of the electron spin onto the molecular axis $\Sigma = 1$, it follows that the spin degeneracy is 3.

It has been said so far that the energy of the electronic state can be treated separately from the nuclear part. However, the electronic motion can couple with the nuclear motion. The effect of the quantum numbers hereby discussed on the energy

levels of the molecules lays in the coupling between the electrons motion, the total electron spin and the motion of the nuclei.

### 3.1.3 Coupling effects

On top of the energy of the nuclear motion and the electronic state energy, each ro-vibrational state has the contribution of the interaction between the different electronic motions: spin-orbit coupling, spin-rotation, lambda doubling and spin-spin coupling. The effect of the interactions between the different motions is represented graphically in figure 3.4.

#### Spin-orbit

The motion of the electrons generates a magnetic field along the molecular axis proportional to $\Lambda$. The internal magnetic field of the molecule causes precession of the nuclear spin about the molecular axis. The interaction causes a splitting of the energy levels of a molecule accordingly to the total angular momentum including electron spin $\Omega$, the energy of the split levels can be written as [53]:

$$E_e \;=\; E_0 + A\Lambda\Sigma \tag{3.8}$$

where $E_0$ is the energy of the electronic state and A is a constant for the given electronic state. From equation 3.8 follows that coupling between orbit and rotation can occur only if $\Lambda \neq 0$ and $\Sigma \neq 0$.

#### Spin-rotation

The electron spin can couple with the nuclei rotation, whose motion generates a magnetic field along the resultant between the molecular rotation and the projection of the electronic angular momentum onto the molecular axis. These couplings create a splitting of the energy levels of the molecule proportional to its rotation. When $\Lambda = 0$ but $S \neq 0$ the electron spin does not couple with the rotation of the electrons so there is a 2S+1 degeneracy, but the spin-rotation coupling produces a splitting of the energy levels accordingly to the total angular momentum including electron spin (S+N+$\Lambda$). As a result, 2S+1 energy levels result from this coupling.

#### Spin-spin

When two or more electrons are present an additional shift of the energy levels can occur due to the mutual coupling of the electron spins. This shift is independent of the nuclear rotation and typically is described through a variable, named $\lambda$.

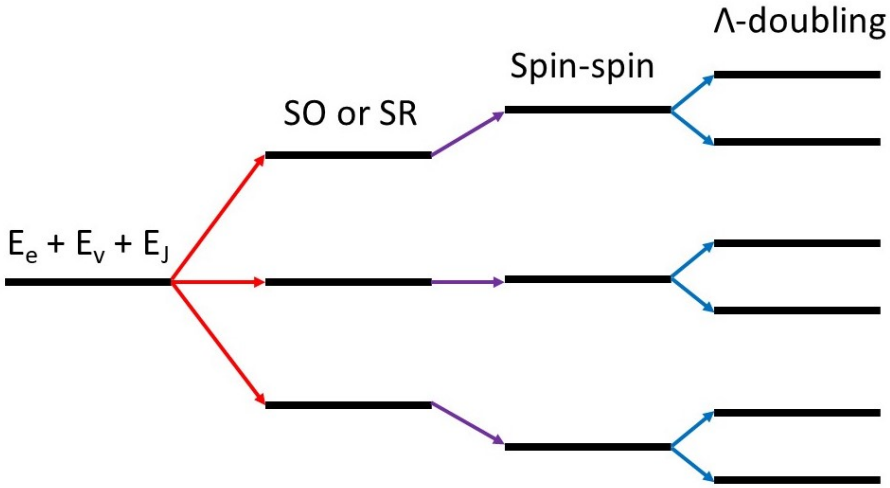


Figure 3.4: Scheme of the splitting and shift of the energy levels induced by the different interactions. $E_e$+$E_\nu$+$E_J$ represent the sum of the electron energy, vibrational energy and rotational energy. SO and SR stand for spin-orbit and spin-rotation. The example is valid for a case with S=1, $\Lambda = 1$.

### $\Lambda$ doubling

The electron angular momentum can also couple with the nuclear-rotation, producing an additional splitting of the energy levels. Every rotational level is split into two components. These two components are not related to the value of $M_L$ of the molecule, but rather to the parity of the electronic state (see section 3.1.4). The lambda doubling is described through the spectroscopic constants q, p, o (first-order approximation). The lambda doubling is typically a minor effect and often can be neglected, however, it increases at higher rotational energy (high J), thus it should be taken in account when high rotational levels are investigated.

### Hund's cases

Different cases are distinguished accordingly to which coupling can be neglected in the calculation of the energy of the molecule. Molecular states in which the coupling between the electron motion and the molecular rotation is (very) weak and the electronic motion is (strongly) coupled to the inter-nuclear axis are called Hund's case (a). In other words, the spin-orbit coupling is dominant with respect to the coupling of the electron spin with the molecular rotation. In such cases, the total angular momentum projection onto the inter-nuclear axis $\Omega$ is well defined (thus $\Sigma$ state cannot be Hund's case (a). In Hund's case (a) state $\Omega$ is a good quantum number for the Hamiltonian, each eigenfunction has a defined $\Omega$ value.

The so-called Hund's case (b) represents the situation in which the electron motion is weakly coupled to the inter-nuclear axis. The interaction between the electronic motion and the molecular rotation is dominant in determining the energy levels of the molecule. When S≠0 the rotational energy level of the molecules separates, because of the coupling between spin and molecular rotation, in sub-components named F1, F2, ... Fn with n being the spin degeneracy.

Most of the cases that can be found in nature are Hund's case (a) or (b) or a combination of both. Other types of coupling are Hund's case (c) and (d), these are rarely found in nature and their discussion is out of the scope of this work, a completer description can be found in the Herzberg's book "Spectra of diatomic molecules" [53].

**Walk through example:** The $C_2$(upper state) is a Hund's case (a) for the first few rotational levels (J<3) and becomes a Hund's case (b) for higher J numbers. The $C_2$(upper state) has $\Lambda = 1$ and $\Sigma = 1$, the total energy levels that can expect to form are three from spin-orbit interactions (named F1, F2, F3). Since $\Sigma = 1$ the spin-spin interaction is also present. Moreover, the Λ-doubling split again the energy levels and a total of 6 energy levels can be expected for each total rotational quantum number J.

### 3.1.4 Symmetry of the eigenfunction

The symmetry of an energy level of a linear molecule is often important in the calculation of the transition probability (selection rules, see section 3.2.1) and the perturbations in the energy levels (see section 3.1.7).

Figure 3.5 shows a graphical representation of the symmetry property of the total eigenfunction and electronic eigenfunction. With symmetry of the system, it is meant the behaviour of the total eigenfunction upon change of coordinate (of all particle in the systems electrons and nuclei) from $\vec{x} \rightarrow -\vec{x}$. If the total eigenfunction remains unchanged it is called positive, if it changes sign it is called negative. Often the property of being negative or positive of an eigenfunction is called parity. The total eigenfunction is the product of three components rotational, vibrational and electronic component (3.1.1). The vibrational part of the eigenfunction depends only on r (the magnitude of inter-nuclear distance, that can be always expressed as $x^2 + y^2 + z^2$), thus it remains unchanged upon reflection of the coordinate system. The symmetry of the rotational part depends on the N value (rotational quantum number) and it can be demonstrated that is positive for even N and negative for odd N [60]. The electronic eigenfunction symmetry is defined only for cases in which Λ=0, in such cases the electronic eigenfunction can change the sign or remain unchanged when a

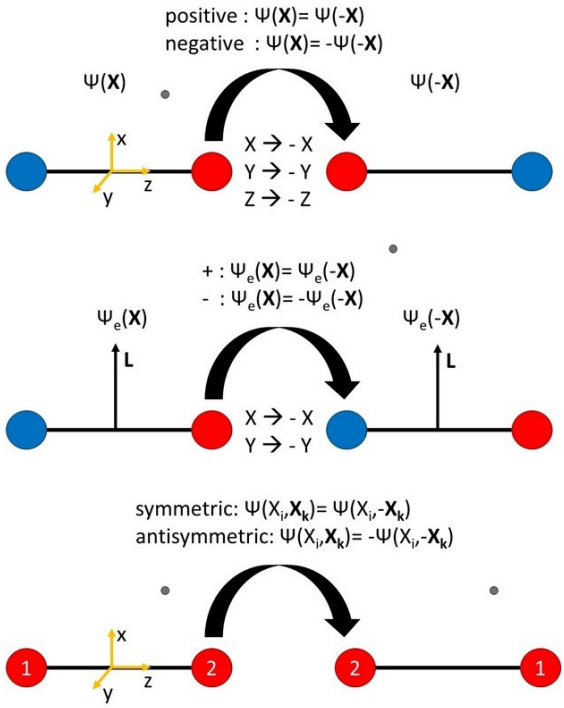


Figure 3.5: Schematic representation of the symmetry propriety of the total eigenfunction ($\Psi$), the electronic eigenfunction ($\Psi_e$) and the symmetry property of homo-nuclear molecule. The index i indicates the electrons, while k the nuclei.

reflection with respect to a plane passing to both nuclei is performed. It should be noted that the eigenfunction stays always unchanged for a transformation $z \rightarrow -z$, since $\Lambda$=0, but change sign or not upon transformation $(x, y) \rightarrow (-x, -y)$ where the nuclei lay on the z plane. When $\Lambda \neq 0$ two eigenfunctions exist a positive and a negative one. As discussed in section 3.1.2 $\Lambda = |M_L|$ thus a degeneracy is always present for every $\Lambda \neq 0$. It can be shown that the two eigenfunctions ($\pm$M$_L$) are not associated with $\pm M_L$, but rather it is a linear combination of the two possible orientation of $M_L$ having one a positive symmetry and one negative symmetry [53]. The total eigenfunction symmetry will result from the product of the symmetry of the rotational, vibrational and electronic (and nuclear) part. A molecular state with is called positive or negative accordingly to the total eigenfunction symmetry.

### The homo-nuclear molecules

In the case of homo-nuclear molecule the symmetry or anti-symmetry propriety of the total eigenfunction can be defined. If the total eigenfunction remain unchanged upon exchange of position of the two nuclei, the molecule is symmetric if it changes is anti-symmetric. It can be shown that in a homo-nuclear molecule all positive rotational levels (i.e. $\Psi_r(\vec{x}) = \Psi_r(-\vec{x})$) are symmetric (s) and all negative rotational level (i.e.

$\Psi_r(\vec{x}) = -\Psi_r(-\vec{x})$) are anti-symmetric (a) if the electronic state is even (g) or *vice versa* if the electronic state is odd (u) [53]. In the case of homo-nuclear molecules, the nuclear spin statistics influence the energy level that can occur in the molecule and in particular their degeneracy. Two nuclei of nuclear spin I form a molecule of total nuclear spin T $\in 2I, 2I-1, ....$ Every T value has a degeneracy 2T+1 associate with the quantum number $M_T$ (projection of T onto an arbitrary axis). The total eigenfunction is the product of the molecular eigenfunction excluding the nuclear spin and the nuclear spin function itself:

$$\Psi' \ = \ \Psi\beta \tag{3.9}$$

Where $\Psi'$ is the total eigenfunction including nuclear spin, $\Psi$ has been defined in equation 3.2 and $\beta$ is the nuclear spin part. It follows that for I$\neq$0, $\beta$ can be both symmetric or anti-symmetric. Thus the total eigenfunction can be made symmetric or anti-symmetric by choosing the correct combination of $\Psi$ and $\beta$. The number of possible combination of nuclear spin that leads to symmetric spin eigenfunction is (2I+1)(I+1) and anti-symmetric is I(2I+1). A homo-nuclear molecule either follow a Bose statistic (integral nuclei spins) or a Fermi statistic (half-integral nuclei spins), which implies that the total eigenfunction can be rather symmetric or anti-symmetric respectively. As consequence, the rotational level in a homo-nuclear molecule has a different degeneracy accordingly to its parity. For homo-nuclear molecules whose nuclear spin is 0 (e.g. $He_2$, $C_2$ etc) the total eigenfunction must be symmetric upon exchange of nuclei and only symmetric nuclear spin eigenfunctions are possible, thus all the anti-symmetric rotational levels cannot exist.

**Walk through example:** The C atom has nuclear spin 0, thus the total nuclear spin of the $C_2$(upper state) is also 0. The $C_2$(upper state) is a g state. Thus, Positive rotational levels are symmetric in a nuclei exchange, however, the nuclear spin is 0 and the total eigenfunction including the nuclear spin must be symmetric. It follows that thus all rotational levels must be positive and one of the branches of the $\Lambda$-doubling is lost.

### 3.1.5 Classification of the electronic states

The classification of the electronic states allows to describe the possible electronic transitions (see section 3.2). In section 3.1.2 and 3.1.3 the quantum numbers that characterize the electronic motion in the molecular orbital. An electronic state of a molecule is generally indicated as:

$$^{2S+1}\Lambda^{+/-}_{g/u} \tag{3.10}$$

where S is the electron spin, $\Lambda$ the projection of the electron angular momentum onto the molecular axis, +/- indicates the parity of the electronic eigenfunction upon reflection at a plane passing through both nuclei (a reflection with respect to the symmetry plane of a linear molecule) and g/u indicates the symmetry or anti-symmetry in homo-nuclear molecules, thus the behaviour of the electronic eigenfunction upon change of coordinates $\vec{x} \rightarrow -\vec{x}$ (a reflection with respect to the center of symmetry).

**Walk through example:** the $C_2$(upper state) discussed so far can be classified as a $^3\Pi_g$ state. However, several electronic configurations of the $C_2$ molecule can be described by this symbol, to distinguish it from the other a "d" is added. The $C_2$(upper state) is known in literature as the $C_2(d^3\Pi_g)$ state.

### 3.1.6 Calculation of the energy level

The calculation of the energy levels of a molecule can be carried out by calculating the contribution of each energy component discussed so far (neglecting the small contribution accordingly to the so-called Hund's cases) or by writing the Hamiltonian of the system and diagonalizing it. The matrix diagonalization can be carried out numerically, for this purpose the program PGOPHER [63] is used in this work. Among many other options, PGOPHER can calculate the energy levels of a diatomic molecule when the molecular constants (see sections 3.1.2 and 3.1.2) are provided.

The single electronic and vibrational level can be treated separately and the energy of the electronic state and vibrational state treated as additive constants. Thus, only the contribution of the molecular rotation and its coupling with the electronic motion should be taken into account in the calculations. The single interaction terms can be written as:

- Rotational Energy: $B_\nu \hat{N}^2$
- Spin-orbit coupling: $AL_zS_z$
- Spin-spin coupling: $\frac{3}{2}\lambda(3S_z - \hat{S}^2)$
- $\Lambda$ Doubling $q\frac{1}{2}[\hat{N}_+e^{-2i\phi} + \hat{N}_-e^{-2i\phi}]$

where the $\hat{}$ represent an operator, N represents total angular momentum excluding spin (i.e. J-S), $L_z$ and $S_z$ the projection of the electronic angular momentum and the electronic spin onto the inter-nuclear axis, S the electron spin, $N_\pm$ the operator that connects the N level with the $N \pm 1$ level, q is the constant used to describe the $\Lambda$ doubling and is effectively the energy difference between the two energy levels

produced by this coupling. The Hamiltonian terms written here are only a first-order approximation a higher-order expansion can be found in [63]. The Hamiltonian is expressed in terms of the spectroscopic constants that can be commonly found in literature. A complete base for a linear molecule is a set of all possible combination of the quantum numbers J, $M_L$ and $M_S$+$M_L$. For example in a $^3\Sigma$ (meaning $\Lambda = 0$ and S=1) state the complete basis for a vibrational state $\eta$ (it includes also the information on symmetry, parity, etc..) and J is: $|\eta J 0 - 1\rangle$, $|\eta J 00\rangle$, $|\eta J 01\rangle$. In this basis it is possible to calculate the matrix element, but they do not have a defined parity it is necessary to take linear combination of them in order to obtain eigenfunction that are parity defined:

$$|\eta J \Lambda \pm \Omega\rangle = \begin{cases} \frac{1}{\sqrt{2}}(|\eta J \Lambda \Omega\rangle \pm |\eta J - \Lambda - \Omega\rangle) & if\ \Lambda \neq 0 \text{ or } \Sigma \neq 0 \\ |\eta J \Lambda \pm \Omega\rangle & if\ \Lambda\ =\ \Sigma\ =\ 0 \end{cases} \tag{3.11}$$

for the aforementioned $^3\Sigma$ the new base is $\frac{1}{\sqrt{2}}(|\eta J 01\rangle \pm |\eta J 0 - 1\rangle)$ and $|\eta J 00\rangle$. The matrix obtained $\langle \eta J, \pm, \Lambda, \Omega | \hat{H} | \eta J, \pm, \Lambda, \Omega \rangle$ can be diagonalized to find the energy levels and the eigenfunction expressed as function of the basis used to write the Hamiltonian [63]. The negative and positive combination are orthogonal (their matrix element is 0) this implies that the two symmetry can be treated separately. An advantage of this approach is the fact that the Hund's cases (a) and (b) can be treated in the same way. In fact, that base chosen to write the Hamiltonian is complete for both cases. In general, the eigenvalue of each energy level can be written as:

$$|\Psi_E\rangle\ =\ \sum_{\Omega} C_i |\eta J \Lambda \Omega\rangle \tag{3.12}$$

The Hund's case (a) or (b) character of a molecular state will be visible in the energy level eigenfunction, Hund's case (a) will have a dominant contribution from one of the $|J, \Lambda, \Omega\rangle$, while Hund's case (b) eigenvalues will be a combination of several $|J, \Lambda, \Omega\rangle$ without a dominant character. It follows that is possible to treat correctly also cases in which the coupling changes at increasing J.

**Walk through example:** Considering the $\nu$-th, J-th rotational level of the $C_2(d^3\Pi_g)$ state, a complete basis is the $|\eta J, M_L = \pm 1, M_L + \Sigma = \pm 0/1/2\rangle$. Which can be combined as in 3.11 to $|\eta J, 1, \pm, \Omega\ =\ 0/1/2\rangle$. The energy levels with J=10 and $\nu = 0$ have an Hamiltonian:

$$\begin{array}{c} \\ |J,-,2\rangle \\ |J,-,1\rangle \\ |J,-,0\rangle \end{array} \begin{array}{c} \begin{array}{ccc} |J,-,2\rangle & |J,-,1\rangle & |J,-,0\rangle \end{array} \\ \begin{pmatrix} 19552.98 & -25.63 & 0.04076 \\ -25.63 & 19573.88 & -25.84 \\ 0.04076 & -25.84 & 19587.23 \end{pmatrix} \end{array} \tag{3.13}$$

where the basis is written in the form $|J, \pm, \Omega\rangle$ the matrix elements are expressed in $cm^{-1}$ and the + combination component are missing because of the nuclear spin of the $C_2$ molecule being 0. The vibrational and electronic energies contribute only to the matrix diagonal. The diagonalization of the matrix gives the energy level and the eigenfunction of the single energy levels.

$$\begin{cases} \Psi_1(E = 19531.44\,\mathrm{cm}^{-1}) &= 0.73|J,-,2\rangle + 0.62|J,-,1\rangle + 0.28|J,-,0\rangle \\ \Psi_2(E = 19570.64\,\mathrm{cm}^{-1}) &= -0.61|J,-,2\rangle + 0.42|J,-,1\rangle + 0.66|J,-,0\rangle \\ \Psi_3(E = 19612.01\,\mathrm{cm}^{-1}) &= 0.29|J,-,2\rangle - 0.66|J,-,1\rangle + 0.69|J,-,0\rangle \end{cases} \quad (3.14)$$

The $\Psi_{3,2,1}$ represents the F1, F2 and F3 components of the $C_2(d^3\Pi_g)$ state with J=10 and $\nu = 0$. The fact that there is no dominant component in any of the eigenfunction of the energy levels reflects the fact that the $C_2(d^3\Pi_g)$ state has a Hund's case (b) character.

### 3.1.7 Perturbations

The procedure presented so far to calculate the energy levels of diatomic molecules is assuming that every electronic state is not interacting with any of the others. However, it is possible that a non zero interaction between energy levels belonging to different electronic configuration takes place. Perturbations can be separated into three groups: rotational perturbations, vibrational perturbations and electronic perturbations. Electronic perturbations typically affects the potential curve shape, one strong example of electronic perturbation is the avoided crossing rule. This rule says that the potential curves of two electronic configurations with the same $\Lambda$ and symmetry propriety cannot cross [64]. Electronic perturbations are taken into account for the calculation of the electronic energy and the vibrational energy. However, these are treated as constants in the calculation of the energy levels of the molecule that is described in this chapter. The same is valid for vibrational perturbations, these influence only the vibrational energy, thus their effect can be considered in the calculation by appropriately changing the vibrational energy constants. For this reason, such perturbations will not be discussed here.

Rotational perturbation, on the other hand, influences only some of the rotational energy levels, but they can significantly modify an emission spectrum since they do not only influence the energy levels but also the eigenfunction and consequently the transition probability. Rotational energy levels belonging to the different electronic configuration can mix producing a hybrid state. Rotational state belonging to different electronic states can mix only if 3 conditions are strictly respected:

1. $\Delta$J = 0.

2. $a \leftrightarrow a$ and $s \leftrightarrow s$

3. $+ \leftrightarrow +$ and $- \leftrightarrow -$

to have a mixing between two rotational levels they must have the same J, the same parity and the same symmetry (if defined). In addition, other two conditions can be found:

1. $\Delta\Lambda = 0,\pm 1$.

2. $\Delta$S = 0

these conditions do not hold rigorously, the first is valid only for Hund's case (a) and (b) (thus for the majority of the cases). The second rule is not strict [53]. The perturbation can be taken into account in the calculations performed so far, by extending the basis used to describe a given ro-vibrational state adding the perturbing states. At the same time, the so-called perturbation strength must be given, this is de facto the matrix element between the perturbing state. Diagonalizing the Hamiltonian extended to the perturbing states it is possible to find the energy of the perturbed level and the mixing between the levels. A sufficient amount of spectroscopic data must be available in literature to properly calculate perturbations for a given state, using this method. A comprehensive overview of how perturbations in a diatomic molecule are treated can be found in the Lefebvre-Brion's book "Perturbation in the spectra of diatomic molecules" [65].

## 3.2 Electronic transition

In this section is discussed when a radiative decay of an electronic state to another can take place in electric dipole approximation (selection rules) and how the probability of decay can be calculated. Note that if the transition probability is 0 in electric dipole approximation this is typically called *forbidden transition*.

### 3.2.1 Transition probability

The interaction between a molecular Hamiltonian and an electromagnetic field gives the probability of decay from an energy state E'$_{J'\nu'\Omega'}$ to a lower energy E"$_{J''\nu''\Omega''}$ emitting a photon of energy E'$_{J'\nu'\Omega'}$-E"$_{J''\nu''\Omega''}$. The stronger interaction is between

the electric dipole and the electric field. The single components of the electric dipole are define as:

$$M_{x/y/z} \;=\; \sum e_k x/y/z_k \tag{3.15}$$

where M is the electric dipole, e the charge of the k-th particle and x/y/z the position of the particle. If the interaction term E·M is included in the Hamiltonian it can be found that the transition probability between the two states is proportional to:

$$R_{J'J''\nu'\nu''\Omega'\Omega''} \;=\; \int \bar{\Psi}'_{J'\nu'\Omega'} \vec{M} \Psi''_{J''\nu''\Omega''} d\tau \tag{3.16}$$

$R$ is the transition dipole moment, $\Psi$ are the total eigenfunctions of the initial molecular state ' and final molecular states ", $\vec{M}$ is a vector of the three components of the electric dipole. The integration should be performed over the whole domain. The electric dipole of a molecule can be written as the sum of an electronic and a nuclear part $M \;=\; M_e + M_n$. The total eigenfunction (see equation 3.2) consists of an electronic part and a nuclear part. The rotational part can be neglected since it introduces only a constant term for a given combination of J' (the total rotational angular momentum of the upper state) and J" (the total rotational angular momentum of the lower state) that respect the selection rule $\Delta$J = $\pm$ 1,0 (see equation 3.18). The transition dipole moment can be written as:

$$R_{\nu'\nu''} \;=\; \int \Psi'_{\nu'} \Psi''_{\nu''} dr \int \vec{M} \bar{\Psi}'_e \Psi''_e d\tau_e \;=\; \int \Psi'_{\nu'} \Psi''_{\nu''} R_e dr \tag{3.17}$$

$R_e$ is the electronic transition moment. The electronic transition moments can be obtained from *ab initio* calculations [59] or from experimental measurements [66]. From the potential curves the (ro-)vibrational eigenfunction can be obtained [67]. The transition dipole moment TDM can then be obtained numerically. Once the TDM (i.e. $R_{\nu'\nu''}$) are known the Einstein coefficient is calculated as:

$$\begin{aligned} A_{J'J''\nu'\nu''\Omega'\Omega''} \;=\; 10^{-43} \cdot \frac{64\pi^4\nu^3}{3h} & \\ \cdot (2 - \delta_{0\Lambda'}\delta_{0\Lambda''}) \sqrt{(2J'+1)(2J+1)} & \begin{pmatrix} J' & 1 & J'' \\ -\Lambda' & \Lambda' - \Lambda'' & \Lambda'' \end{pmatrix} \\ \cdot |R_{\nu'\nu''}|^2 \frac{1}{(2J'+1)} & \left[\frac{cm^3}{Debay^2 \cdot s}\right] \end{aligned} \tag{3.18}$$

where $\nu$ is the transition frequency in cm$^{-1}$ $\frac{(E'_{J'\nu'\Omega'} - E''_{J''\nu''\Omega''})}{hc}$, $\delta_{0\Lambda''}$ the Dirac delta and $10^{-43}$ a re-scaling factor. The second line of the equation is the so-called Hönl-London factors, coming from the integration of the rotational eigenfunction, expressed

in the formalism of [68], $R_{\nu'\nu''}$ has been defined in equation 3.17 and is expressed in Debye (i.e. $3.336{\cdot}10^{-30}$ C·m ), (2J'+1) is the degeneracy of the upper state. The calculation 3.18 is carried out between states with defined J, $\Omega$, $\Lambda$, the symmetry adapted bases given in equation 3.11. However, the final energy states eigenfunction are a linear combination of those states (and eventually perturbing state), it follows that the Einstein coefficient in a transition between two final states is as well a weighted sum.

**Walk through example:** Considering the $C_2$ emission shown in figure 3.1, which is between the $C_2(d^3\Pi_g)$ state and the $C_2(a^3\Pi_u)$ state. Considering the energy levels $\Psi_{1,2,3}$ (see 3.14) calculated in section 3.1.6. The transition probability between F2 the F2 energy level of the $C_2(a^3\Pi_u)$ state with J=9 and $\nu = 0$ can be calculated as:

$$\langle \Psi_2^{a^3\Pi_u}(E = 146.52\,\mathrm{cm}^{-1})|T(1)|\Psi_2^{d^3\Pi_g}(E = 19570.64\,\mathrm{cm}^{-1})\rangle \tag{3.19}$$

where T(1) represents the electric dipole interaction and

$$\Psi_2^{a^3\Pi_u}(E'' = 146.52\mathrm{cm}^{-1}) \;=\; -0.57|J'', -, 2\rangle + 0.50|J'', -, 1\rangle + -0.64|J'', -, 0\rangle \tag{3.20}$$

and

$$\Psi_2^{g^3\Pi_g}(E' = 19570.64\,\mathrm{cm}^{-1}) \;=\; -0.61|J', -, 2\rangle + 0.42|J', -, 1\rangle + 0.66|J', -, 0\rangle \tag{3.21}$$

where J"=9, J"=10 the base elements are expressed in the form $|J, \pm \text{ combination}, \Omega, \rangle$. With the eigenfunction of the two states expressed in term of the symmetry adapted basis the single matrix element can be solved using the second line of equation 3.18, where $R_{\nu'\nu''} = 1.82$ Debye [61]. The Einstein coefficient than is obtained summing all the contributions and with $\nu = 19570.64 - 146.52$ cm$^{-1}$. The transition probability is $3.5 \cdot 10^6$ s$^{-1}$.

In reality, a system is composed of many molecules in a given energy state ($N_{J'\nu'\Omega'}$) and the amount of photons produced by a transition $' \rightarrow''$ must be proportional to $N_{J'\nu'\Omega'}$. The photons produced in a decay of $N_{J'\nu'\Omega'}$ into an energy state $E''_{J''\nu''\Omega''}$ can be written as:

$$N_{Ph} \;=\; N_{J'\nu'\Omega'} A_{J'J''\nu'\nu''\Omega'\Omega''} \tag{3.22}$$

where $A_{J'J''\nu'\nu''\Omega'\Omega''}$ is the Einstein coefficient for the transition $J'\nu'\Omega' \rightarrow J''\nu''\Omega''$

**Selection rules**

An electric dipole transition is possible whenever the transition dipole is $\neq 0$. General selection rules can be derived from the symmetry of the total eigenfunction. Shortly, the general selection rules are:

1. $\Delta$J = $\pm$ 1,0. Generally in spectroscopy transition in which $\Delta$J = 0 as Q band, $\Delta$J = -1 as P and $\Delta$J = +1 as R.

2. negative rotational levels combine only with positive rotational levels.

3. anti-symmetric levels combine only with anti-symmetric levels and symmetric levels combines only with symmetric levels.

The proof of the first rule involves the properties of the rotational eigenfunction and explanation of it can be found in [69]. The explanation of the second and third rule is easy to obtain from equation 3.17. The integral $R = \int \bar{\Psi}' \vec{M} \Psi'' d\tau$ is performed over the complete domain, the electric dipole change sign upon transformation $\vec{x} \rightarrow -\vec{x}$, so it is anti-symmetric with respect to the center of the integration. If both $\Psi'$ and $\Psi''$ are positive or negative, the integrating function is anti-symmetric with respect to the center of integration, thus its integral is 0, so the transition is not possible in electric dipole approximation. Similarly, the third selection rule can be derived by considering that the electric dipole does not change sign upon nuclei exchange and therefore the integral is not 0 only if the two functions are both anti-symmetric or both symmetric. Since in homo-nuclear molecules the negative states are always anti-symmetric and positive states are always symmetric if the molecule is symmetric in an exchange of nuclei (g) and vice versa if the molecule is anti-symmetric (u). It follows that in a homo-nuclear molecule the symmetric states (g) couple only with anti-symmetric states (u). Additional selection rules can be found for Hund's case (a) and (b). Those coupling cases are the most commonly found in nature, thus these selection rules are commonly holding.

1. $\Delta$S = 0.

2. $\Delta\Lambda = \pm 1,0$.

3. $\Sigma^+ \rightarrow \Sigma^+$ and $\Sigma^- \rightarrow \Sigma^-$

A discussion of these selection rules can be found in [53].

## 3.3 Ro-vibrational population distribution

In sections 3.1 and 3.2 it was discussed how to obtain the energy levels of an electronic state of a molecule and the transition probability between two states has been discussed. However, the final observed spectra depends on the amount of particles that decay from a state m to a state n. In general these are not known, but in case that the ro-vibrational states follows a Boltzmann distribution, the number of molecules in a ro-vibrational state is:

$$N_{e,\nu',J'} = N_e \frac{1}{\sum_{\nu'} e^{-\frac{E_{\nu'}}{kT_{vib}}}} \frac{1}{\sum_{J'} (2J'+1) e^{-\frac{E_{J'}}{kT_{rot}}}} (2J'+1) e^{-\frac{E_{J'}}{kT_{rot}}} e^{-\frac{E_{\nu'}}{kT_{vib}}} \tag{3.23}$$

where $N_{\nu' J'}$ represent the number of molecule in a vibrational state $\nu'$ with vibrational energy $E_{\nu'}$, and a rotational state J' with rotational energy $E_{J'}$ (note that J is the total angular momentum including electron spin) for a electronic state e that has a total number of molecules $N_e$. $T_{vib}$ and $T_{rot}$ are the vibrational temperature and rotational temperatures associated with the population distribution. The terms $\sum_{\nu'} e^{-\frac{E_{\nu'}}{kT_{vib}}} = Q_{vib}$ and $\sum_{J'} (2J'+1) e^{-\frac{E_{J'}}{kT_{rot}}} = Q_{rot}$ are called vibrational and rotational partition functions. These are normalization parameters to ensure that the sum over all possible ro-vibrational states is equal to the number of molecule in that electronic state.

## 3.4 Calculation and fit of emission spectra

In this work, the program MassiveOES [70] is used to calculate synthetic emission spectra and fit the experimental spectra and get the rotational and vibrational temperatures. MassiveOES takes as input a SQLite database which includes, line by line, all the information needed to simulate an electronic transition: the wavelength each transition, its respective Einstein coefficients, the energy levels of the upper and lower state of the transition. In the standard case, MassiveOES suppose a Boltzmann population distribution of the rotational and vibrational levels in the emitting state, thus the partition function can be written as:

$$Q = \sum_{\nu',J',\Omega'} e^{-\frac{E(\nu')}{k_b T_{vib}}} \cdot (2J'+1) e^{-\frac{E(J')}{k_b T_{rot}}} \tag{3.24}$$

where $\nu'$, J', and $\Omega'$ are the vibrational quantum number, the rotational quantum number, and the fine structure quantum numbers of the upper state respectively.

$E(\nu')$ and $E(J')$ are the vibrational and rotational energy of the $\nu', J'$ state, stored in the input database. $T_{vib}$ and $T_{rot}$ are the rotational and vibrational temperature of the upper state. The database must include a sufficient number of rotational and vibrational states (accordingly to the rotational and vibrational temperature) in order to properly calculate the partition function. The photon produced by an ensemble of molecule in the electronic excited state $N_e$, whose ro-vibrational excitation follows a Boltzmann distribution can be written combining equation 3.22 and 3.23. If $N_e$, $T_{rot}$ and $T_{vib}$ are known it is possible to predict theoretically the emission that can be measured from the plasma. The expected intensity of a line is:

$$I(\nu', \nu'', j', j'', \Omega', \Omega'') \;=\; \frac{N_{excited}}{Q} \cdot e^{-\frac{E(\nu)}{k_b T_{vib}}} \cdot (2J'+1) e^{-\frac{E(J',\Omega')}{k_b T_{rot}}} \cdot A_{\nu'\nu''J'J'\Omega'\Omega'''} \quad (3.25)$$

where $I$ represents the intensity of a single transition, $N_{excited}$ the density of molecule in the excited state of the transition, $Q$ the ro-vibrational partition function. $\nu''$ and $J''$ are the vibrational quantum number and the total angular momentum of the ground state. $A_{\nu'\nu''J'J''\Omega'\Omega''}$ stands for the transition probability and it is given in the database. Each line is convoluted with a Voigt profile defined by a Gaussian and a Lorentzian width, to take into account the instrumental profile. A polynomial baseline, of order 0 or 1, can be added to the spectra to correct for the baseline. To properly reproduce an experimental spectrum the spectra is convoluted also with a pixel-like profile (a rectangle) of width determined by the experimental spectra.

### 3.4.1 Fitting procedure

The experimental spectra is imported in massiveOES as function of pixel number and the wavelength is imported as:

$$\lambda \;=\; \lambda_{start} + \Delta\lambda i + \Delta\lambda^2 i^2 \quad (3.26)$$

where i represent the pixel number, $\lambda_{start}$, $\Delta\lambda i$, and $\Delta\lambda^2 i^2$ are fitting parameters that allow matching experimental spectra and synthetic spectra. Such approach allows to correct both misplacements at one and match the synthetic and experimental spectra. If a mismatch is present the fit is not possible at all the error on the line position must be negligible to be able to fit the experimental spectra.

The simulated spectra is used to fit the experimental one by least square minimization method. The total amount of fit parameter is shown in table 3.1:

| Parameter | meaning |
|---|---|
| N | excited specie density |
| $T_{rot}$ | rotational temperature |
| $T_{vib}$ | vibrational temperature |
| Baseline | constant baseline |
| Linear baseline | baseline slope |
| $\sigma_G$ | Gaussian width of the Voigt profile |
| $\sigma_L$ | Lorentzian width of the Voigt profile |
| $\lambda_{start}$ | wavelength of the first point in the spectra |
| $\Delta\lambda$ | distance between two points in the spectra |
| $\Delta\lambda^2$ | quadratic correction of the position of a point in the spectra |

Table 3.1: Total amount of fitting parameters in a Boltzmann population fit.

### 3.4.2 State by state fitting

MassiveOES offers also the possibility to treat each energy level as fitting parameter independently. Such procedure allows to determine the population of each rovibrational level. In such case a line intensity is given:

$$I(\nu', \nu'', j', j'', \Omega', \Omega'') \;=\; N_{J'\nu'\Omega'} \cdot e^{-\frac{E(\nu)}{k_b T_{vib}}} \cdot (2J'+1) e^{-\frac{E(J',\Omega')}{k_b T_{rot}}} \cdot A_{\nu'\nu'' J' J' \Omega' \Omega'''} \quad (3.27)$$

where $N_{J'\nu'\Omega'}$ is the density of molecules in the energy level define by the quantum numbers: $J', \nu', \Omega'$. To have a good result the emission lines must be well separated in order to reduce to the minimum the correlation between the population of different emitting states.

# 4 Experimental apparatus

## 4.1 Experimental setups

## 4.2 2.45 GHz microwave plasma torch

The experimental setup used in this work is shown in figure 4.1 *(a)*. The plasma torch used in this work has been modified from the original design of University of Stuttgart [71] so that it can be operated, in a fully enclosed environment, near atmospheric pressure but also at lower pressures. It consists of a cylindrical $TE_{10}$ cavity (cylindrical resonator) and a coaxial resonator. The coaxial resonator placed at the bottom of the quartz tube consists of two elements: a $\lambda$ quarter resonator and a tip in its center. The tip consists of two geometrical parts: a cylinder of height 12 mm with a diameter of 15 mm and a cone of 8 mm height with a base diameter of 15 mm. The tip position can be adjusted to enhance the electric field at its top for a given microwave frequency [33]. The enhanced electric field allows ignition in the pressure range 10-1000 mbar. A quartz tube of 30 mm outer diameter and 26 mm inner diameter is mounted in the center of the cylindrical resonator to confine the gas as can be seen in figure 4.1. At the bottom of the coaxial resonator, the gas is injected in the quartz tube by four tangential gas inlets of 4.3 mm inner diameter. The cylindrical cavity has three vertical slits of width 5.5 mm and height 43 mm (that corresponds to the cylindrical resonator height) which allow optical access to the plasma in the resonator.

The 2.45 GHz microwaves are generated by a magnetron MH3000S-213BB powered by a 3 kW power supply ML3000D-111TC, from Muegge GmbH components. The power supply can be operated with a microwave power output that ranges between 300 W and 3000 W. The magnetron is connected to the microwave cavity via a three steps tuner and a bi-directional coupler. The three steps tuner allows adjusting the impedance of the waveguide to the plasma impedance, to maximize the amount of

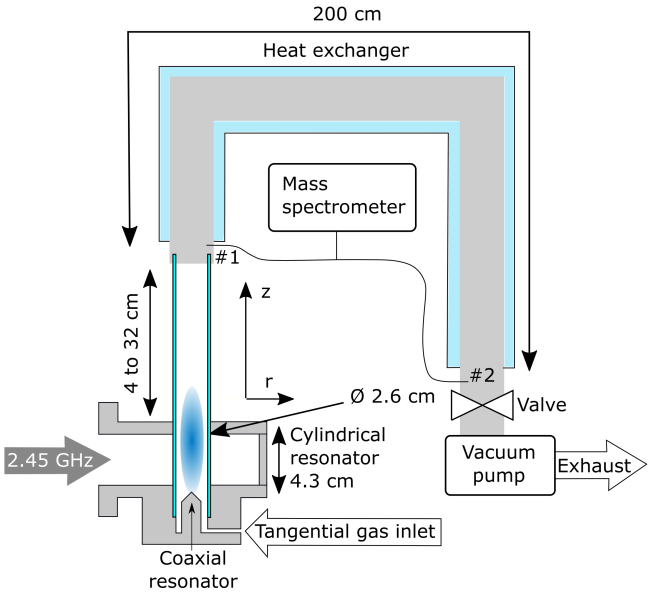


Figure 4.1: Schematic of the plasma torch and its exhaust system. The reference axis typically used and the mass spectrometer sampling position are indicated in figure.

power coupled to the plasma. The bi-directional coupler allows measuring the power produced by the magnetron and the power reflected by the plasma.

The plasma is ignited and confined in the quartz tube. The end of the quartz tube is connected to a double wall pipe, cooled by water. The quartz tube length can be varied between 8.5 cm (limited by the minimum length needed to connect the heat exchanger) up to 40 cm (limited by the holding system). The plasma effluent is pumped away by a vacuum pump with variable pumping speed. The system is operated at pressures between 30 mbar and 1000 mbar with $CO_2$ flow rate between 1 and 100 L/min. A $CO_2$ flow below 5 L/min typically generates unstable plasma at pressures above 100 mbar. At pressures below 100 mbar, a plasma generated with a $CO_2$ flow below 5 L/min and microwave powers above 1 kW typically heats the quartz tube above the acceptable level.

The system exhaust is provided with 2 connections with a mass spectrometer, one is positioned 8 cm above the quartz tube end (called position 1), the second is positioned after the heat exchanger, 2 m away from the end of the quartz tube (called position 2). The gas sampled in position 1 is the hot effluent of the plasma, while the gas sampled in position 2 is already at room temperature.

### 4.2.1 Magnetron operational modes

The magnetron used can be operated in pulsed mode or continuous mode. In continuous mode (or CW) the microwaves are continuously produced and coupled to the plasma. In pulsed mode, the microwaves are generated following a trigger signal. The

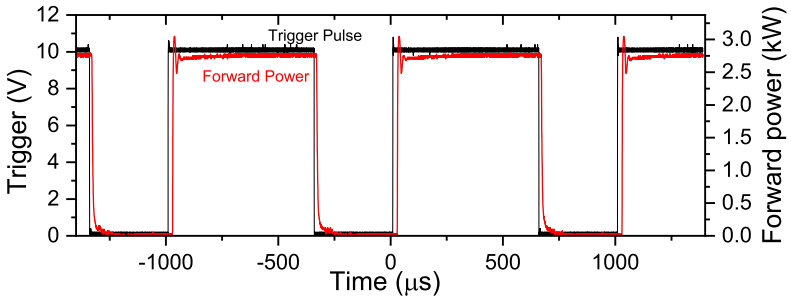


Figure 4.2: The trigger pulse (black) and the microwave power produced in response to it (red). Frequency of 1 kHz and duty cycle 65 %.

microwave power supply is fed with a square pulse of 10 V amplitude. Nominally the magnetron can be pulsed from 500 Hz to 18 kHz, however, a minimum pulsing rate of 20 Hz is used in this thesis. The duty cycle can range from 1 % up to 99 %. The minimum duty cycle achievable is limited by the plasma, which burns only if a minimum amount of power is coupled into it. Figure 4.2 shows the typical trigger signal and the microwave power generated by the magnetron, measured with a bi-directional coupler (which attenuate the signal of 50 dB) with a Muegge GmbH microwave detector MM1001B-111AB. The repetition rate of the pulse is 1 kHz, thus every 1 ms a new on-off cycle is repeated. The pulse is characterized by a duty cycle, which is defined as the ratio between ON time and total pulse time $\frac{t_{on}}{t_{on}+t_{off}}$. Figure 4.2 also shows the typical delay between the trigger pulse and the magnetron response that is *ca.* 20 $\mu$s. The microwave power e-raise time is 1.5 $\mu$s and the e-fall time is 5 $\mu$s, these values do not change significantly with frequency.

### 4.2.2 Additional experimental setup: the surfaguide

The plasma torch described in section 4.2 has a minimum pressure of 30 mbar with a $CO_2$ flow of 1 L/min. To extended the operating range to lower pressures (down to 0.5 mbar) and flow (down to 0.05 L/min) another experimental setup is used. Such device has shown to be qualitatively and quantitatively identical to the plasma torch at the same conditions, namely same input flow, power and pressure [72].

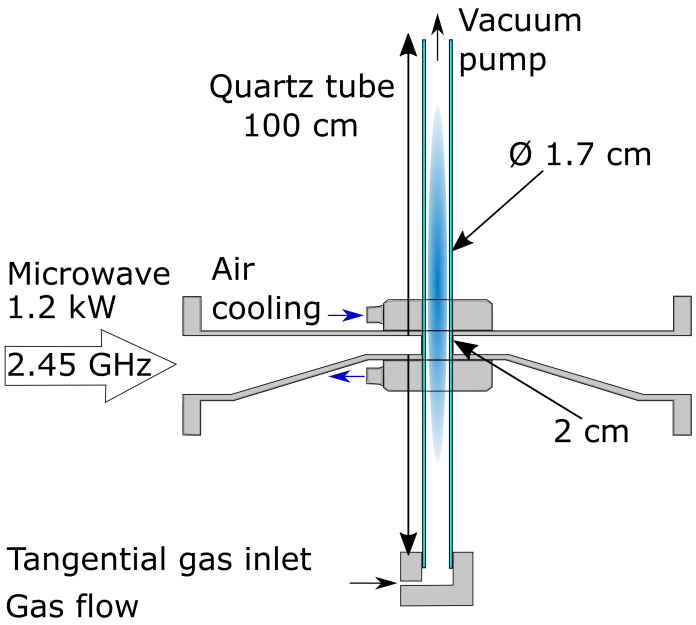


Figure 4.3: Schematic of the surfaguide used for the low pressure experiments (see text for geometrical details).

A scheme of the used setup is shown in figure 4.3, the setup used is a surfaguide plasma reactor [73]. Such setup is comparable to the one used by Britun et al. [34]. The power is delivered by a 2.45 GHz solid-state microwave generator that is connected to a tapered waveguide, with a three steps tuner used to adjust the waveguide impedance to the plasma impedance. The tapered waveguide is provided with a 32 mm hole, in which a 17 mm inner diameter quartz tube is inserted. The gas is injected on one side of the quartz tube via 4 tangential. The flow range can be varied between 0.05 L/min and 3 L/min, which results in a minimum pressure achievable of 0.5 mbar. The solid-state power supply can generate a maximum microwave power of 300 W, both continuous and pulsed modes. In case of pulsed operation, the minimum frequency is 5 kHz and the maximum 10 MHz, the OFF and ON-times can be set independently, and duty cycle down to $10^{-4}$ can be achieved.

## 4.3 Diagnostics setup

### 4.3.1 Mass spectrometry analysis of the plasma effluent

Mass spectrometry is a technique that allows measuring the charge-mass ratio of an ion. The mass spectrometer is used to measure the concentration of the stable species in the plasma effluent (i.e. CO, $CO_2$ and $O_2$).

A mass spectrometer typically consists of three parts: a sampling system, an ionization chamber and a mass-charge selector. The sampling system leads the sampled

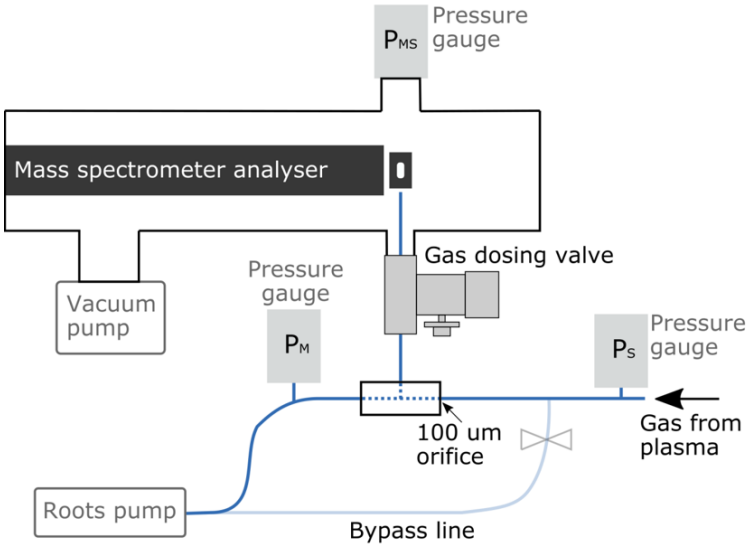


Figure 4.4: A scheme of the mass spectrometer system used in this work [75].

mixture to the ionization chamber and it reduces the pressure (of the gas sample) to the ionization chamber working pressure (typically below $10^{-5}$ mbar). The sampling system changes significantly according to the application: a capillary, a nozzle and (or) differential pumping are typically employed to sufficiently reduce the pressure. In the ionization chamber, the electrons emitted from a filament accelerate under the influence of a potential difference and ionize the sampled gas mixture. A mass spectrometer typically allows to tune the acceleration potential and the current of electrons emitted from the filament, such parameters can be adjusted to optimize the products of the ionization. The ensemble of possible products of an electron-molecule collision are called cracking patterns and they typically change accordingly to the electron energy (e.g. $CO + e \rightarrow C^+ + O + e$, $CO + e \rightarrow CO^+ + e$, $CO + e \rightarrow C + O^+ + e$ , etc.). The ionized products are extracted from the ionization chamber using a potential difference and pass through a charge-mass selector (in the present case a quadrupole mass analyzer [74]). Finally, the ions are measured by a detector (e.g. Faraday cup, SEM detector). Calibration of a mass spectrometer with known mixtures is necessary to measure the concentration of species in the sampled gas.

Figures 4.1 *(a)* shows the position where the plasma effluent is analyzed with the mass spectrometer. The gas can be sampled after the heat exchanger (cold gas is sampled) *ca.* 2 m after the end of the plasma or 8 cm (hot gas is sampled) above the end of the quartz tube. By changing the length of the quartz tube it is possible to measure closer to the resonator. Figure 4.4 shows the scheme of the mass spectrometer setup. The gas is sampled using a 0.9 mm diameter tube. To reduce the pressure from atmospheric to the mass spectrometer working pressure (in this work the mas

spectrometer ionization chamber is kept constant at $1{\cdot}10^{-6}$ mbar) two orifices are used. A 100 $\mu$m orifice connects the 0.9 mm sampling tube with an intermediate T-shaped chamber kept at the constant pressure of 1 mbar. The T-shaped chamber is connected to the ionization chamber of the mass spectrometer via a variable orifice that allows controlling the pressure in the ionization chamber. An electron current of 0.5 mA is generated to ionize the sampled gas and the electrons are accelerated by a potential difference of 40 V, thus the electron energy is *ca.* 40 eV.

The mass spectrometer is calibrated to measure the concentration of CO, $CO_2$, $O_2$ using known gas mixtures. The calibration of the mass spectrometer allows to determine the response of the diagnostics relative to a known gas. The diagnostic has been calibrated using Ar gas as reference. Ar is chosen because its main peak 40 ($Ar^+$) and 20 ($Ar^{++}$) do not overlap with the main peaks of $O_2$, CO and $CO_2$. The calibration is performed by sampling a mixture of Ar and the investigated gases ($O_2$, $CO_2$, CO). The calibration factors can be derived from the measured current and the concentrations, the equations for a Ar/CO mixture are:

$$\begin{cases} \frac{I_{28}}{I_{40}} = \frac{C_{CO}^{28}}{C_{Ar}^{40}} \frac{[CO]}{[Ar]} \\ \\ \frac{I_{12}}{I_{40}} = \frac{C_{CO}^{12}}{C_{Ar}^{40}} \frac{[CO]}{[Ar]} \\ \\ \frac{I_{16}}{I_{40}} = \frac{C_{CO}^{16}}{C_{Ar}^{40}} \frac{[CO]}{[Ar]} \end{cases} \tag{4.1}$$

where $C_i^m$ is the cracking pattern coefficient for a specie i on a mass m. $I_m$ represents the measured current on a mass m, [CO] and [Ar] are the (known) concentration of Ar and CO in the sampled gas. The calibration factors of the mass spectrometer are the ration $\frac{C_i^m}{C_{Ar}^{40}}$ where $C_{Ar}^{40} = 1$ is the reference peak. The typical calibration factor matrix is given in table 4.1:

| mass/species | CO | $CO_2$ | $O_2$ | $N_2$ |
|---|---|---|---|---|
| 12 | 0.11 | 0.01 | 0 | 0 |
| 14 | 0 | 0 | 0 | 0.083 |
| 16 | 0.02 | 0.15 | 0.38 | 0 |
| 28 | 1.11 | 0.18 | 0 | 0.87 |
| 32 | 0 | 0.001 | 0.665 | 0 |
| 44 | 0 | 0.82 | 0 | 0 |

Table 4.1: Typical calibration factors measured for the mass spectrometer used in this work, with electron energy 40 eV at ionization chamber pressure of $10^{-6}$ mbar [75].

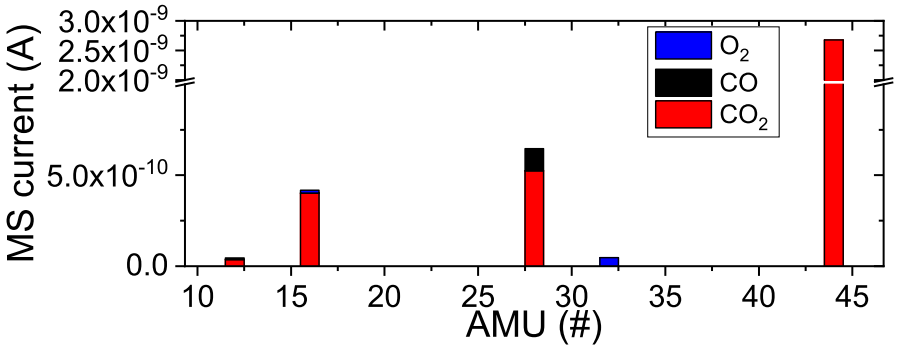


Figure 4.5: Signals recorded in the mass spectrometer for masses 12, 16, 28, 32 and 44. The fraction of signals attributed to $O_2$, $CO_2$ and CO are shown in blue, red and black respectively.

At the working pressure, the important contribution on a given mass-charge ratio is predominantly produced by dissociative ionization. The only exception is the contribution of $CO_2$ to mass-charge ratio m=32, this is originated by two steps reaction formation of molecular oxygen from carbon dioxide: $CO_2 + e \rightarrow C^+ + O_2 + e$, $CO_2 + e \rightarrow C + O_2 + e$ and ionization of the molecular oxygen $O_2 + e \rightarrow O_2^+ + e$. Although the relative contribution of this process is small it cannot be neglected since the concentration of $CO_2$ is often much larger than the concentration of $O_2$, thus the contribution of $CO_2$ to the signal measured on the mass 32 can be significant.

The analysis of the system behaviour shows that the calibration is valid, for $CO_2$ conversion measurements, in the pressure range 5-1000 mbar and no significant gas de-mixing takes place [75]. The determination of the gas composition has been carried out by calculating a synthetic mass spectrum and using a least square minimization routine (python library scypy.optimize method L-BFGS-B) on the experimental data to determine the particle concentration in the gas [76]. A synthetic mass spectrum is calculated as:

$$I(m) = \sum_i \beta_i n_i c_i^m \tag{4.2}$$

where I(m) is the peak intensity at mass m, $\beta_i$ the MS calibration parameter for the specie i, $n_i$ is the species relative density of species i and $c_i^m$ is the contribution (cracking pattern) to mass m of the species i. Figure 4.5 shows a graphical representation of the analysis performed on the mass signals. The contribution of different species to each mass/charge ratio can be distinguished.

The concentration obtained from the mass spectrometer analysis are used in equation 2.13 to calculate the conversion. From the conversion, the energy efficiency is

derived as in equation 2.14, where to calculate the specific energy input the experimental $CO_2$ flow and power are used.

The $CO_2$ conversion is known within $\pm$ 1.6 %, because of systematic errors in the calibration procedure and background subtraction as discussed in [75]. The error on the energy efficiency is obtained by propagating the uncertainty on the conversion:

$$\sigma_\eta = \sigma_\chi \frac{\Delta H}{SEI} \tag{4.3}$$

where $\sigma_\eta$ and $\sigma_\chi$ represents the errors on the energy efficiency and conversion respectively. Since the error on the conversion is constant, the error on the energy efficiency increases at decreasing SEI.

### 4.3.2 Absolute calibration of a spectrometer

A spectrometer is used to analyze the light emitted by the plasma separating its spectral components. Figure 4.6 shows the schematics of a Czerny-Turner monochromator, with the collected light passing through a slit and reflected by the first mirror onto a plane grating. The diffracted light is then reflected by a second mirror onto the exit slit (which acts as a wavelength selector) and there, it is measured by a photo-detector. By changing the angle between the grating and the mirrors, it is possible to change the wavelength that is reflected by the second mirror in the detector. The diffracted wavelength follows the equation [77]:

$$sin(\alpha) + sin(\beta) = kn\lambda \tag{4.4}$$

where $\alpha$ is the angle between the incident light and the grating normal, $\beta$ is the angle between the normal to the grating plane and the diffracted light, k is the order of diffraction, n is the groove density of the grating (typically expressed in grove/mm) and $\lambda$ is the wavelength of the diffracted light. A monochromator measures only the photons with the selected energy (thus with wavelength $\lambda$), while in a spectrometer the photo-detector is replaced with an array of detectors, these detectors allow to measure at the same time the photons in a given wavelength range (e.g. between 500 nm and 530 nm) with spectral resolution. In a spectrometer, the detector can be a charge coupled device (CCD) [78] or an intensified charge coupled device (iCCD). The CCD and iCCD detectors convert photons into electrical current that is then measured. The main difference between the two devices is the time resolution: with the same signal intensity an iCCD can measure down to a few ns while a CCD needs tens of ms. Typically CCD chips offer a better signal to noise ratio with respect to

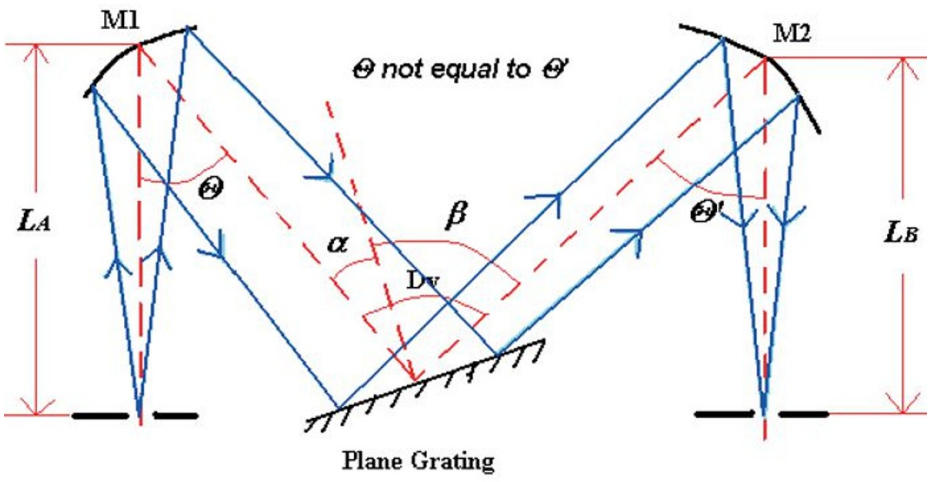


Figure 4.6: Scheme of a Czerny-Turner monochromator, adopted from [79]

iCCD chips. The CCD chips are matrices of photo-detector (pixels) with a given size (typically of the order of $\mu$m), each pixel measures the photons with wavelength $\lambda + \Delta\lambda$. The spectral range imaged on a chip as well as the dispersion $\Delta\lambda$ depends on several factors: the measured wavelength, the grating grove density, the spectrometer focal length and the pixel size.

A spectrometer is characterized by an instrumental function: therefore even only if photons at a single wavelength $\lambda_0$ are collected, the spectrometer measures a signal with a certain apparent spectral dispersion characterized by a FWHM, which is the instrumental profile.

Typically the instrumental function of a spectrometer can be described by a Voigt profile (i.e. a convolution of a Gaussian and a Lorentzian) and FWHM is the full width at half maximum of the Voigt profile. The light emitted by a source (e.g. the $C_2$ molecular emission) is convoluted with the instrumental profile, therefore it is necessary to know the instrumental profile to correctly interpreter the measured spectra. The signal intensity per pixel decreases at increasing resolution (i. e. lower FWHM). To determine the instrumental function of a spectrometer it is sufficient to measure with a spectrometer the emission from a source of light with a natural broadening much smaller than the (expected) instrumental broadening. Typically the atomic emission of a single state is sufficient, for the most spectrometer to obtain a Dirac-like emission. The emission of a low pressure mercury lamp is used to evaluate the instrumental profile.

Figure 4.7 shows a scheme of the resonator and the early effluent region, the slit

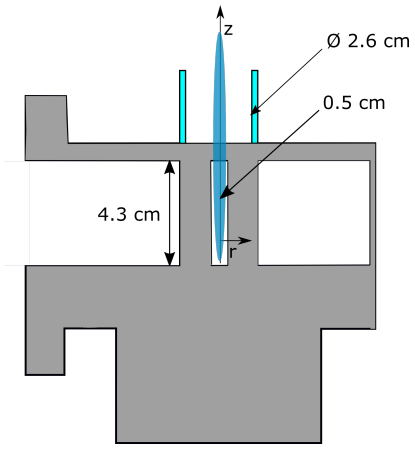


Figure 4.7: A scheme of the resonator with the slit.

in the resonator allows to have optical access to the plasma. The plasma emission is collected via a double iris system that reduces the collection area to about 1 $mm^2$, to obtain a good spatial resolution. The optics are mounted on a two rails system that allows to vary the height (z position) and the radial position of the measure. In this work two spectrometers are used to analyze the plasma emission: a SPEX-1000 spectrometer of 1 m focal length (with a 1800 l/mm grating) provided with an Andor AK420-OE CCD camera and an ANDOR shamrock SR 303i-A of 33 cm focal length equipped with 300 l/mm, 1200 l/mm and 2400 l/mm gratings, an ANDOR iStar iCCD camera is used as a detector. The SPEX-1000 spectrometer has a resolution of about 20 pm at 546 nm. At the same wavelength, the resolution of the ANDOR spectrometer is *ca.* 0.8 nm with the 300 l/mm grating, 120 pm with the 1200 l/mm grating and 50 pm with the 2400 l/mm grating. Figure 4.8 shows the instrumental profiles obtained with these spectrometers: a 1800 l/mm grating and a 1 m focal length (SPEX-1000), a 1200 l/mm grating and 0.33 m focal length (ANDOR) and 2400 l/mm grating and 0.33 m focal length (ANDOR). The instrumental profile of the ANDOR spectrometer is not symmetric, this distortion is due to the spectrometer optics, which slightly distort the image.

### Intensity calibration

The signal measured using a spectrometer is proportional to the amount of light emitted. However, the ratio between signals measured at different wavelength is not corresponding to the emitted photon flux. The sensitivity of the optical component used to measure the optical emission must be taken into account. Indeed the optics, the optical fiber and the spectrometer employed in the measurements transmit a different fraction of light accordingly to the wavelength. Additionally, bandpass filters (high pass 280 nm; high pass 400 nm; high pass 500 nm) are used to filter the second

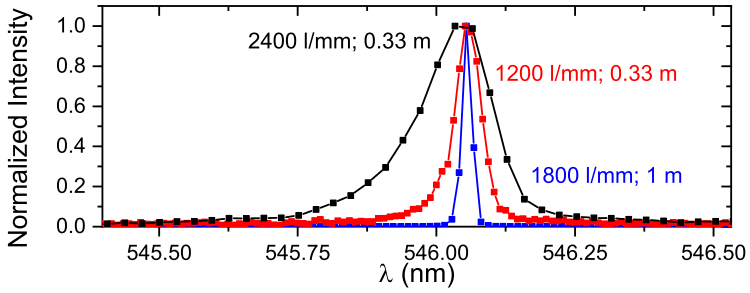


Figure 4.8: The instrumental function of a SPEX-1000 spectrometer equipped with a 1800 l/mm grating (blue curve) and an ANDOR shamrock SR 303i-A equipped with a 2400 l/mm grating or 1200 l/mm grating. The measured light is the Hg atomic emission at 546 nm.

order light (photons at 400 nm are reflected at the same angle as photons at 200 nm with m=2). Moreover, the sensitivity of the CCD (or iCCD) chip depends on the photon energy. In the AK420-OE CCD chips, the sensitivity (i.e. the fraction of incident photons measured) of the chip changes between 10 % for wavelength below 250 nm up to 80 % in the visible.

The correction of the optics sensitivity is called relative intensity calibration. Relative (as well as absolute) calibration are performed by using reference sources of light, to evaluate the proportionality factor between the measured and emitted light. The SPEX-1000 optics have been absolute calibrated between 400 nm and 850 nm with an Ulbricht sphere (Labsphere USS-800C-100R in combination with a LPS-100 power supply). The absolute calibration is extended in the wavelength range between 250 nm and 400 nm, using the overlap with a Deuterium lamp. The calibration factors can be calculated as:

$$C(\lambda) = \frac{I(\lambda)4\pi}{m(\lambda)} \tag{4.5}$$

where $C(\lambda)$ is the proportionality factor, $I(\lambda)$ the lamp emission in $\frac{photons}{s\,m^2\ \ nm\,sr}$ and $m(\lambda)$ the signal measured in $\frac{counts}{s\ \ nm}$. When $I(\lambda)$ is the absolute photon "flux" emitted from the lamp, the spectrometer is absolute calibrated (under the assumption that the solid angle is the same in the calibration and the experiments), if $I(\lambda)$ the lamp emission normalized to a reference wavelength, the spectrometer is relatively calibrated. The ANDOR shamrock spectrometer has been relatively calibrated using a deuterium-halogen mini lamp.

An absolute calibrated emission spectra can be used to calculate the excited species density as well as the rotational and vibrational population distribution. If the ab-

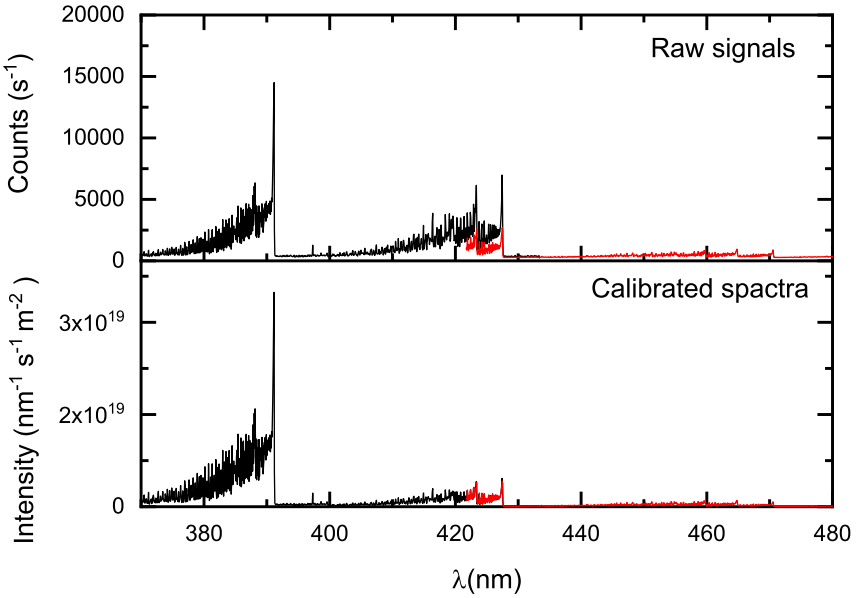


Figure 4.9: A comparison between a the raw signal recorded by the CCD camera and the calibrated spectra. The spectra is the $N_2^+$ first negative band recorded by a pure nitrogen plasma at atmospheric pressure.

solute photon flux is used the N parameter in equation 3.25 is the density of the emitting molecular state. However, the rotational and vibrational population distribution can be obtained also from relative calibrated spectra, since the rotational and vibrational temperature defines the fraction of molecule in a ro-vibrational energy level (see equation 3.25), independently of the absolute amount of molecule in that state. Figure 4.9 shows the effect of the (absolute) calibration on two spectra recorded with the ANDOR spectrometer using the 1200 l/mm grating. The first negative band of $N_2^+$ is measured in one spectrum between 370 nm and 430 nm and between 420 nm and 480 nm. The top graph shows the raw signals (in counts per second), while the bottom graph the calibrated spectra. The mismatch, due to two the optics sensitivity, between the two raw spectra is corrected by the calibration.

### 4.3.3 Imaging setup

Imaging is a technique, which allows measuring the spatial distribution of the plasma emission by using an iCCD camera. The imaging in the z direction is possible thanks to the slit present in the microwave resonator that is shown in figure 4.7. The axial integrated plasma emission to be performed requires modifications to the original setup. Figure 4.10 shows the modifications of the experimental setup for measuring the plasma emission integrated along the axial direction (i.e. gas stream direction)

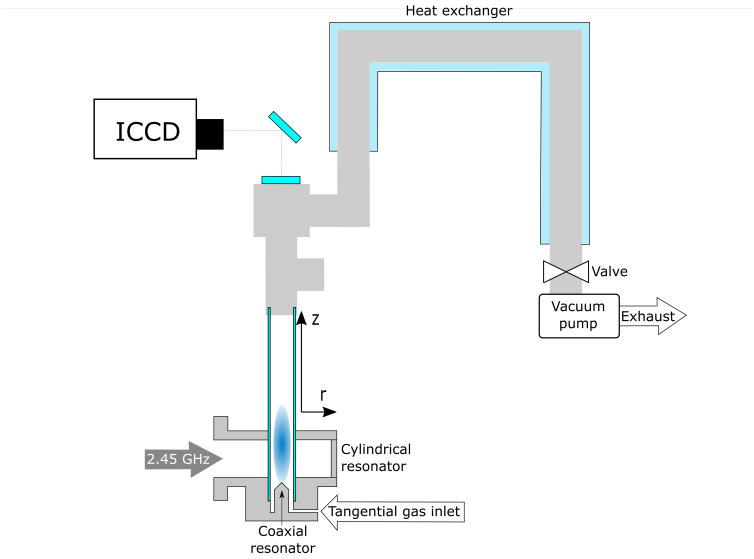


Figure 4.10: Figure shows the modified setup to measure the axial integrated optical emission.

and determining its radial cross section: a CF40 cube is introduced on top of the plasma torch, a quartz Thorlabs window WG42012 is mounted on the top side of the CF40 cube. A Thorlabs mirror PF20-03-01 reflects the emitted light that is then measured with an ANDOR iStar iCCD camera with 2048x512 pixels of 13 $\mu$m size and a squared intensifier of size 18 mm, equipped with a Nikon lens of 35 mm focal length.

# 5 Spectral characteristics of $CO_2$ microwave based plasmas

In this chapter, the typical emission characteristics of $CO_2$ microwave plasmas will be discussed, and the calculations performed to analyze the measured spectra will be presented. In section 5.1 the typical emission spectrum of a $CO_2$ microwave discharge in the pressure range 1-1000 mbar is discussed. In section 5.2, 5.3 and 5.4 the simulation and analysis of the $C_2$ Swan band, CO Ångström and third positive bands and CN Violet band are presented.

## 5.1 Optical emission in $CO_2$ microwave plasma

The emission spectra of a $CO_2$ microwave plasma can be grouped accordingly to the pressure range: at pressures below *ca.* 120 mbar the plasma uniformly fill the quartz tube and the spectrum is dominated by a continuum emission and several CO bands; at pressures above *ca.* 120 mbar the plasma is contracted and confined in the center of the quartz tube and the spectrum is dominated by the $C_2$ emission along with atomic emission of carbon and oxygen. The former case is called "expanded regime", while the second case is called "contracted regime" (a detailed discussion of the two regimes is presented in chapter 6). The aim of $CO_2$ decomposition by microwave plasma is the formation of CO molecules, whose concentration in the system varies between few per cent and 50 % (see chapter 6 for more information about the $CO_2$ dissociation).

Figure 5.1 *(a)* shows a typical emission spectrum, recorded in the resonator in the two different regimes, measured with the SPEX-1000 spectrometer (only the part with the relevant emission are shown in figure). In the contracted at 900 mbar regime, the spectrum is dominated by the $C_2$ Swan ($d^3\Pi_g \rightarrow a^3\Pi_u$) band (visible in the range between 460 nm and 570 nm) similarly to what is observed in several works [80], [81], [82], [83]. In addition, some typical carbon (*ca.* 248 nm, 906 nm,

907 nm, 908 nm, 909 nm, 911 nm, 940 nm and 960 nm) and oxygen (at *ca.* 777 nm and 844 nm) atomic lines can be identified.

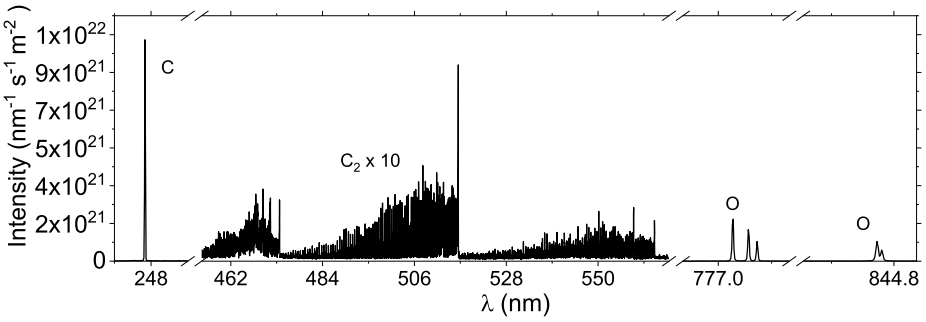


(a) *920 mbar*

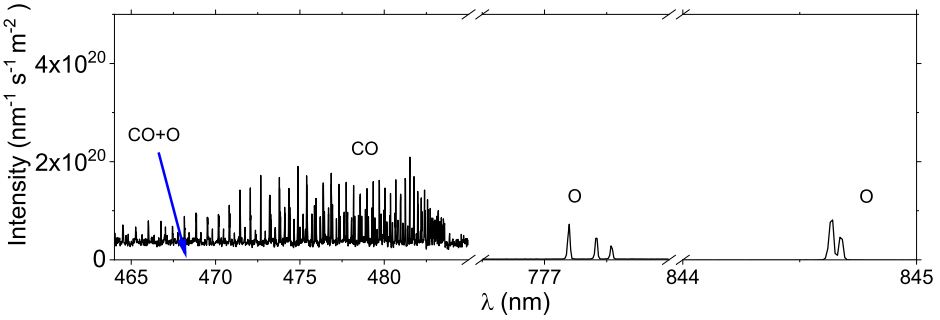


(b) *60 mbar*

Figure 5.1: *(a)* typical emission spectra absolutely calibrated recorded at 920 mbar, 10 L/min and 900 W. The emission was recorded in the center of the resonator. The spectra region between 460 nm and 567 nm ($C_2$ emission) has been multiplied by 10. *(b)* typical emission spectra absolutely calibrated recorded at 60 mbar, 10 L/min and 900 W. The emission is recorded in the center of the resonator. Both spectra are absolutely calibrated.

A broadband continuum (emission extending in the range 300-700 nm) is present also in the contracted regime, but it is typically less intense (in term of signal per pixel) than the $C_2$ Swan band or the atomic lines (its contribution can be distinguished in the baseline). Its origin is attributed to recombination processes of oxygen atoms via $O + O \rightarrow O_2 + h\nu$ and $CO + O + M \rightarrow CO_2 + M + h\nu$ reactions [84]. The latter is known to take place in atomic oxygen and carbon monoxide mixtures [85], [86] and in the current setup, it is an indication of CO losses. In the expanded regime at 60 mbar, the $C_2$ emission is no longer visible and other molecular structures appear: the spectrum is dominated by the continuum emission, on top of which can be identified some CO emission bands: the CO Ångström band in the region 420 nm - 600 nm and the

CO third positive system between 240 nm and 300 nm (not seen in figure 5.1). The atomic oxygen lines can be observed at 777 nm and 844 nm, but no atomic carbon lines are detected.

## 5.2 Analysis of the $C_2$ Swan Band

### 5.2.1 Formation mechanisms of $C_2$

$C_2$ is a homo-nuclear diatomic molecule and the Swan band is an electronically allowed dipole transition between its electronic excited states $C_2(d^3\Pi_g)$ and the $C_2(a^3\Pi_u)$ . Figure 5.2 shows the potential curves of the $a^3\Pi_u$, $d^3\Pi_g$, $c^3\Sigma_u^+$, $b^3\Sigma^-$, $e^3\Pi_g$ triplet states and the $1^5\Pi_g$ of the $C_2$ molecule [54]. The formation of the $C_2$ molecule in $CO_2$ microwave plasmas originates from atomic carbon [54]. Two main mechanisms can lead to the formation of $C_2$: one is the three body recombination of atomic carbon [87] and one involves the formation of the $C_2O$ molecule [88]. The three body process can be written as the following:

$$C + C + M \rightarrow C_2^* + M \tag{5.1}$$

where M is a third body and * represents an electronic excitation of $C_2$. The carbon atoms are in the electronic configuration $2s^22p^2$ ($^3P_J$, $^1D$, $^1S_0$). The dissociation asymptote and the dissociation fragments are shown in figure 5.2.

Little et al. [89] have shown that reaction 5.1 favours the formation of the $C_2(1^5\Pi)$ with respect to the other possible electronically excited states [87], however, no information on the branching ratio can be found in the literature.

The $C_2O$ molecule in $CO/CO_2$ mixture can be generated from two vibrationally excited CO molecules (CO + CO $\leftrightarrow$ $C_2O$ + O) or from a carbon atom reacting with a CO molecule [54]. The so-formed $C_2O$ molecule can then react with a carbon atom forming $C_2$ in a vibrationally excited state. The reaction chain mentioned so far are the following:

$$CO(X^1\Sigma, \nu) + CO(X^1\Sigma, \omega) + M \rightarrow C_2O + M \tag{5.2}$$

$$C(^3P_J) + CO(X^1\Sigma, \nu) + M \rightarrow C_2O + M \tag{5.3}$$

$$C(^3P_J) + C_2O \rightarrow C_2^* + CO \tag{5.4}$$

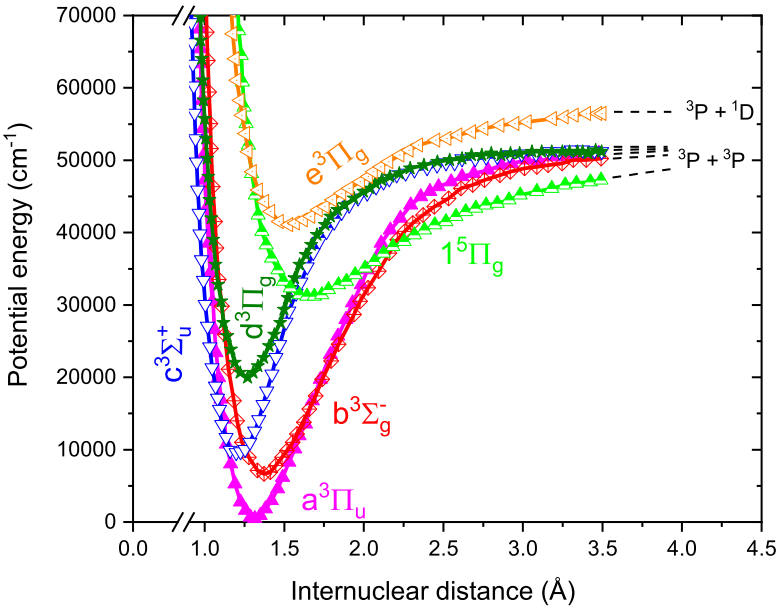


Figure 5.2: Potential curves of $a^3\Pi_u$, $d^3\Pi_g$, $c^3\Sigma_u^+$, $b^3\Sigma^-$, $e^3\Pi_g$ triplet states of the $C_2$ molecule and the $1^5\Pi_g$ state. The minimum of the $a^3\Pi_u$ potential curve is taken as 0 energy reference.

where the $C(^3P_J)$ states are the lowest electronic configurations of the carbon atom in the ground electronic configuration $2s^22p^2$. Caubet et al. [88] have shown that two of the possible electronically excited products of reaction 5.4 are the $C_2(d^3\Pi_g)$ and the $C_2(1^5\Pi)$ states. They found that this reaction favours the formation of the $C_2(d^3\Pi_g)$ state with respect to the $C_2(1^5\Pi)$ state.

The $C_2(1^5\Pi)$ state is of particular importance since it can lead to the formation of the so-called *high pressure band* [90] of the $C_2$ molecule. In fact, the $1^5\Pi$ state undergoes to selective collisional energy transfer with the seventh vibrational level of the $C_2(d^3\Pi_g)$ state:

$$C_2(^5\Pi, \nu = 0) + M \rightarrow C_2(d^3\Pi_g, \nu = 6) + M \tag{5.5}$$

Therefore, the $1^5\Pi$ overpopulates the $C_2(d^3\Pi_g, \nu = 6)$. The latter can decay radiatively and can produce the high pressure band (reaction 5.6) or its population can be quickly collisionally redistributed (reaction 5.7).

$$C_2(d^3\Pi_g, \nu = 6) \rightarrow C_2(a^3\Pi_u) + h\nu \tag{5.6}$$

$$C_2(d^3\Pi_g, \nu = 6) + M \rightarrow C_2(d^3\Pi_g, \nu') + M \tag{5.7}$$

Reactions 5.6 and 5.7 are concurrent processes, when the collisional redistribution is fast enough, the emission of the $C_2(d^3\Pi_g)$ state does not present evidence of overpopulated $\nu = 6$. Vibrational-electronic energy transfer (V-E) between CO and $C_2$ has been postulated by Rich and Bergman [91] and confirmed by Wallart [92], [93]. Direct electronic excitation from vibrational excited CO has been observed at low pressure by laser pumping the vibrational excitation of $CO(X^1\Sigma)$ by Grigorian and Cenian [94]. They found that ground state vibrationally excited ($\nu > 10$) CO molecules can pump several electronic excited states of $C_2$. In particular, the observed the excitation of the $C_2(d^3\Pi_g)$ , the $C_2(e^3\Pi_g)$ and the $C_2(C^1\Pi_g)$ states. A similar observation was already carried out by Wallart et al. [92], [93], however, they concluded that direct V-E transfer is not likely to happen. Their observations have been explained by assuming the formation of a non radiative state in reaction 5.4 that is the precursor of the radiative states.

In conclusion, in $CO_2$ plasmas the $C_2$ molecules (or their precursors) are formed in three body processes that involve at least a carbon atom. Moreover, the radiative $C_2(d^3\Pi_g)$ state is formed preferentially (directly or by energy redistribution).

### 5.2.2 Simulation of the emission spectra

The upper state of the $C_2$ Swan band is the $C_2(d^3\Pi_g)$ state that is a triplet, thus 3 sub-levels exist because of the spin-orbit interaction $\Omega = 0, 1, 2$. It should be noted that the $C_2$ molecule has a Hund's case (a) character at low J and a Hund's case (b) character at high J, thus $\Omega$ is not a good quantum number (although it is very useful to explain the band structure). When $\Lambda$ doubling is considered each level would split into two sub-levels (accordingly to the parity of the eigenfunction). However, since $C_2$ is a homonuclear molecule with nuclear spin equal to zero half of them are missing (see section 3.1.4). The ground state has the same number of sub-levels for each rotational level. The Q branch ($\Delta J = 0$) is missing for the transition $\Pi_0 - \Pi_0$ (see [53] for further discussions), while for the $\Pi_1 - \Pi_1$, $\Pi_2 - \Pi_2$ the Q-branch is weak. The R ($\Delta J = +1$) and P ($\Delta J = -1$) branches represent the strongest branches of the three sub-transition $\Pi_0 - \Pi_0$, $\Pi_1 - \Pi_1$, $\Pi_2 - \Pi_2$. Finally, satellites branches $\Pi_0 - \Pi_1$, $\Pi_0 - \Pi_2$, etc. are present although with a much lower transition probability.

The calculation of the energy levels of the $C_2(a^3\Pi_u)$ and $C_2(d^3\Pi_g)$ states and the transition probability used to analyze the spectra in this work have been taken

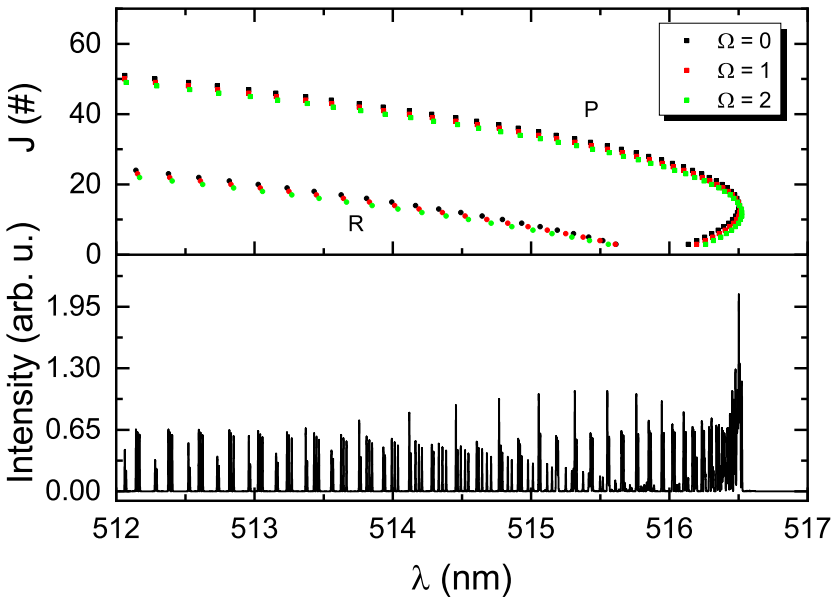


Figure 5.3: Simulated 0-0 transition of the $d^3\Pi_g \rightarrow a^3\Pi_u$transition on the bottom part of the graph. The Fortrat plot is shown on the top part of the graph, where only the transitions with Einstein coefficient above $10^6$ $s^{-1}$ are shown.

from Brooke et al. [61]. They re-investigated the molecular constants of the $C_2(d^3\Pi_g)$ and $C_2(a^3\Pi_u)$ states using the program PGOPHER [63]. Those were used to compute RKR potential curves, using the program RKR [58]. The recalculated potential curves have been used along with the electronic transition dipole moments [61] as inputs of LEVEL [67]: LEVEL calculates the eigenvalues of a one-dimensional potential for diatomic molecules and computes the matrix elements between different eigenvalues LEVEL has been used by Brooke et al. [61] to recalculate the transition dipole moments. The calculations of PGOPHER are imported into MassiveOES in order to analyze the experimental spectra. The calculation of the vibrational energy levels is up to the ninth level of the $C_2(d^3\Pi_g)$ state and the tenth level of the $C_2(a^3\Pi_u)$ state, while the maximum J number included in the calculation is J = 300.

Typically, the measured emission of the $C_2$ Swan band consists of three vibrational transition groups $\Delta\nu = 0, \pm 1$, while the other vibrational groups ($\Delta\nu = \pm 2$, etc.) are too weak to be observed at high resolution. The typical emission is shown in figure 3.1 *(b)*: the $\Delta\nu = +1$ transition group is observed between 450 nm and 480 nm, $\Delta\nu = 0$ between 480 nm and 517 nm, $\Delta\nu = -1$ between 517 nm and 567 nm. Figure 5.3 shows a simulation of the transition from the $\nu' = 0$ to the $\nu'' = 0$ of the $C_2$ Swan band between 517 nm and 512 nm. The top part of the graph shows a Fortrat plot, where the P and R progressions can be seen. In particular, the P branch forms the

band head at *ca.* 516.5 nm, and this region the overlap between the lines is such that is not possible to resolve them with the spectrometer used in this work. Only the P transition of the higher rotational levels (J > 30) can be distinguished. The R progression starts at *ca.* 515.5 nm and at high rotational temperatures (>3000 K) produce a long rotational tail that reaches wavelength down to 480 nm (visible in figure 5.4).

### 5.2.3 $C_2(d^3\Pi_g)$ ro-vibrational population distribution

As discussed in section 2.1.1, in a plasma, rotational and vibrational population distributions are not always Boltzmann distributions, thus not necessarily a (single) rotational and vibrational temperature can be defined. Therefore, before assuming a Boltzmann population distribution, it is necessary to assess if there are deviations from it.

Figure 5.4 (I) shows a state by state fitting of a typical high resolution Swan band spectrum measured in the plasma torch resonator. The spectrum was recorded at 920 mbar and 10 L/min $CO_2$ and microwave power of 900 W. The emission has been fitted using a state by state fit between 485 nm and 517 nm, corresponding to the $\Delta\nu = 0$ transition group. A state by state fitting does not make any assumption on the population distribution, and the population of each energy level of the upper state is fitted, hence determined, independently from the others. The rotational population distribution of the first, second and third vibrational level ($\nu = 0, 1, 2$) obtained from the fit is shown in figure 5.5 *(a)*. The population of the three sub-components of each rotational level has been summed in order to reduce the noise (note that there is no temperature information in the population distribution of the fine structure). From the plot 5.5 *(a)* it can be concluded that the rotational population of these three levels follows a Boltzmann distribution (the logarithm of the population is linear with the energy of the level, see equation 3.23).

The population of the high energy rotational levels is not well determined for the vibrational level 1 and 2. As it can be seen in 5.4 (II), the 1-1 and the 2-2 transitions have a much lower intensity with respect to the 0-0 transition. Since the rotational levels are Boltzmann distributed, their population decreases with increasing energy, thus the intensity of the lines generated from these energy levels is not sufficient to determine correctly their population. Moreover, the overlapping of different lines generated from different energy levels leads to additional uncertainties, since the underpopulation of a level can be compensated by the overpopulation of the other. A clear example of this can be seen in the low rotational energy levels (that are strongly

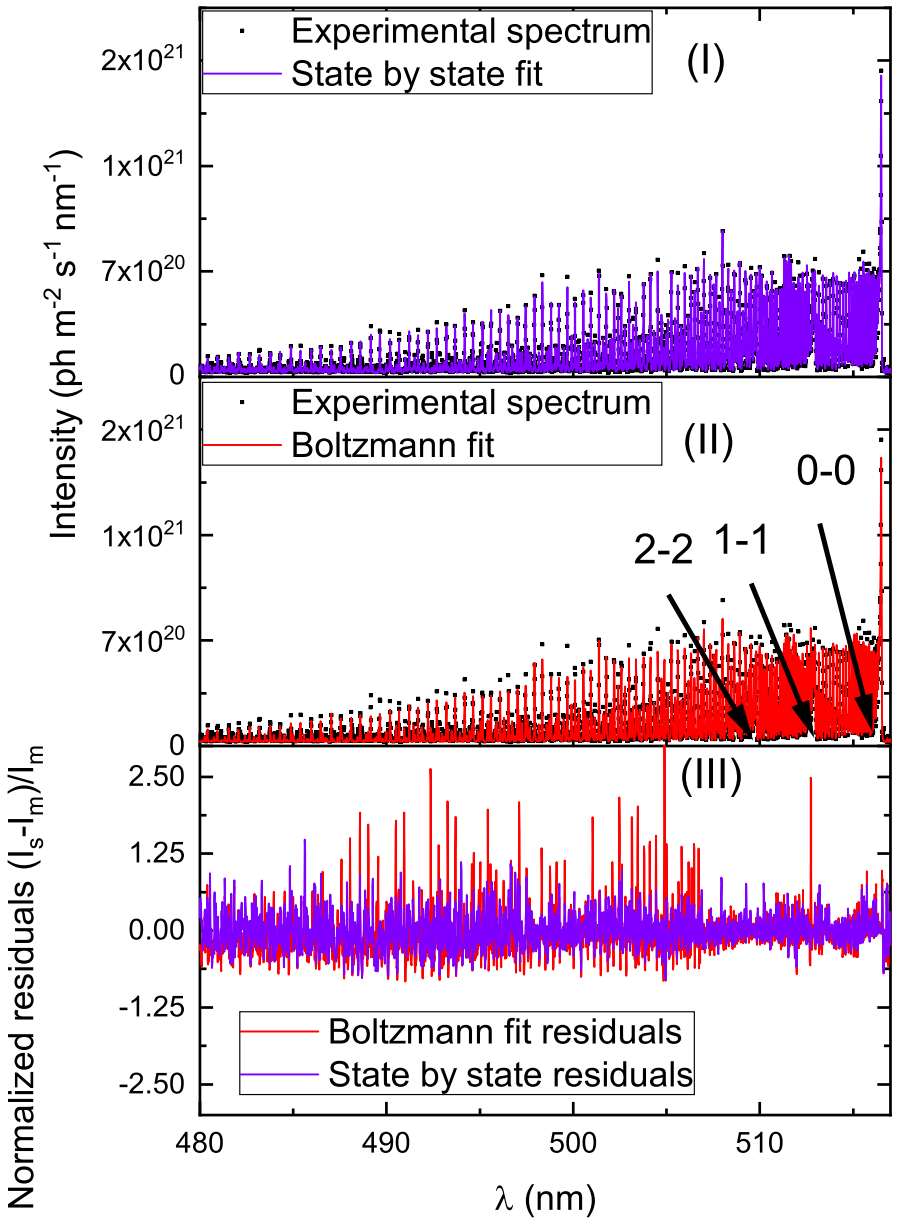


Figure 5.4: (I) state by state fit of the $\Delta\nu = 0$ transition group. (II) fit performed assuming a Boltzmann distribution of vibrational and rotational levels. (III) normalized residuals of the two fits.

overlapped in the band head) and whose population is determined with a high error. In fact, they appear as scattered as the high energy levels in the Boltzmann plot shown in figure 5.5 *(a)*.

Figure 5.5 *(b)* shows the natural logarithm of the vibrational population as a function of the vibrational energy levels. The population of each vibrational level has been obtained by summing the population of the rotational levels from J'=10 to J'=50. The distribution obtained seems to deviate from a Boltzmann distribution (two vibrational temperatures seems to exist one for the levels 0, 1, 2 and one for the levels 3, 4, 5, 6). However, this is originated from the state by state fitting, since every rotational level population is fitted independently, the population of the high vibrational levels (whose emission is strongly overlapped) is poorly determined. Figure 5.5 *(c)* shows the Boltzmann plot of the vibrational states obtained assuming a Boltzmann distribution of the rotational states, using a rotational temperature of 6000 K. Such analysis reveals that the population of the vibrational states follows a Boltzmann distribution, therefore a temperature can be defined. Since both vibrational and rotational levels are Boltzmann distributed, the fit of the $C_2$ emission is performed with Boltzmann distributed rotational and vibrational energy levels. Figure 5.4 (II) shows the results of a fit of the $\Delta\nu = 0$ transition group under the assumption of Boltzmann distributed vibrational and rotational levels. Figure 5.4 (III) shows a comparison of the residuals resulting from the two fits. Although the state by state fit has lower residuals (as expected since the number of fitting parameters is significantly larger), the difference with the residuals resulting under the assumption of Boltzmann distribution is not significant. This is an additional indication that a Boltzmann distribution of the rotational and vibrational states is applicable.

The error associated with the rotational and vibrational temperatures is of $\pm$ 500 K, as estimated in [54]. The errors on the determination of $T_{rot}$ and $T_{vib}$ are mostly systematic. Moreover, the $\Delta\nu = 0$ transition group is precise in the determination of the rotational temperature, but not in the determination of the vibrational temperature, whose value is better determined by fitting the $\Delta\nu = +1$ transition group.

### 5.2.4 $C_2(d^3\Pi_g)$ as thermometric species

The nascent rotational population distribution of a molecule can rather present an overpopulation of the high rotational levels (because of energy exchange during the formation process) or be a thermal distribution. As observed in the previous section, the distribution of the rotational levels in a typical $CO_2$ microwave discharge at the current setup can be considered as a Boltzmann distribution. At the same time the

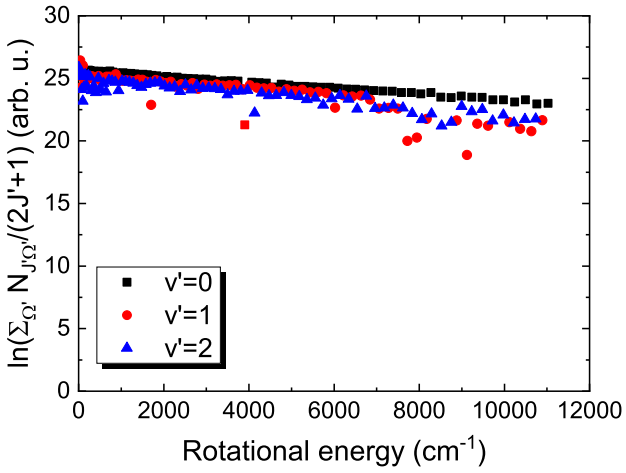


(a)

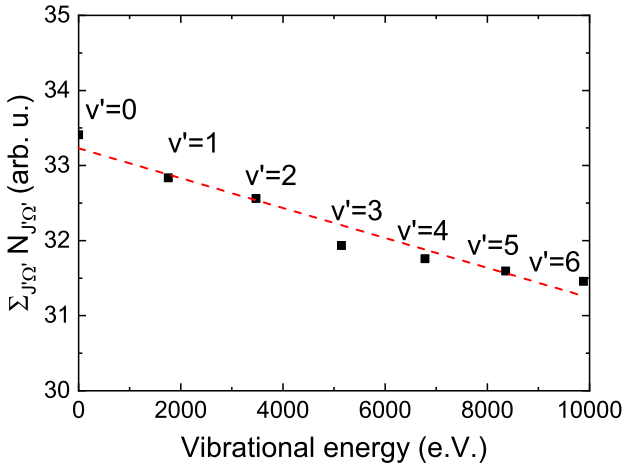


(b)

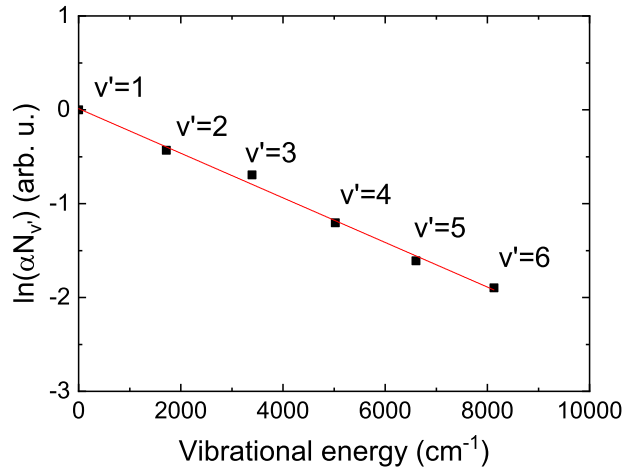


(c)

Figure 5.5: *(a)* rotational Boltzmann plot of the first, second and third vibrational levels ($\nu'$ = 0,1,2). *(b)* vibrational Boltzmann plot obtained from the state by state fitting of the $\Delta\nu$ = -1,0,1. *(c)* Boltzmann plot obtained from the analysis of the $\Delta\nu$ = +1 transition group under the assumption of rotational Boltzmann distribution.

$C_2(d^3\Pi_g)$ rotational energy transfer time between the different rotational levels (RET) measured by Brockhinke et al. [95] in an oxyacetylene flame at 2200 K are in the order of $4{\cdot}10^{-9}$ s, thus much shorter than the radiative lifetime of 100 ns [96]. Therefore, it can be concluded that the temperature associated with the rotational population distribution is representative of the gas temperature.

The nascent vibrational population distribution can deviate from Boltzmann distribution because of the selective population mechanism of the $C_2(d^3\Pi_g, \nu = 6)$ (discussed in section 5.2.1). Nevertheless, the vibrational population distribution of the $C_2(d^3\Pi_g)$ is found to follow a Boltzmann population distribution as well, as observed in the previous section. The vibrational relaxation time was investigated by Bondybey [97], revealing that the vibrational relaxation time of the $C_2(d^3\Pi_g)$ in an Ar solid matrix (4.2 K) is faster than the radiative lifetime for high vibrational levels ($\nu \geq 3$) and much slower (few $\mu s$) for the other vibrational levels. Therefore, it is surprising to observe that the vibrational population distribution thermalizes despite the selective population of the $C_2(d^3\Pi_g)$ $\nu = 6$ associate with the formation mechanisms (5.1 and 5.4). However, in $CO_2$ plasma, the presence of vibrationally excited CO (that exchange vibrational energy with $C_2$, see section 5.2.1 ), and $CO_2$ may lead to faster thermalization of the $C_2(d^3\Pi_g)$ [54]. Moreover, Xuechu and Nanquan [98] performed the analysis of the Swan band in the chemi-luminescence of Na+$CCl_4$ in Ar at a temperature below 900 K. The $C_2(d^3\Pi_g)$ state is formed preferentially in the $\nu = 6$ vibrational level and they deduced a vibrational relaxation of the $C_2(d^3\Pi_g)$ by Ar in the order of $1.5{\cdot}10^6$ $mbar^{-1}s^{-1}$ ($2{\cdot}10^6$ $Torr^{-1}$ $s^{-1}$). Such rate is sufficiently fast (at the typical working temperatures) to explain the thermalized vibrational distribution. A more detailed discussion of the vibrational and rotational relaxation of the $C_2(d^3\Pi_g)$ state in $CO_2$ microwave plasma can be found in the work of Carbone et al. [54].

## 5.3 CO emission

The CO emission observed in $CO_2$ microwave plasmas at low pressure (< 120 mbar) mainly originates from the transitions $CO(B^1\Sigma^+) \rightarrow CO(A^1\Pi)$, i.e. *Ångström* band, $CO(b^3\Sigma^+) \rightarrow CO(a^3\Pi)$, i.e. third positive band. Emission is also observed in the range between 230 and 250 nm whose origin can be linked to the $CO(a^3\Pi) \rightarrow CO(X^1\Sigma^+)$, i.e. Cameron band or the $CO(A^1\Pi) \rightarrow CO(X^1\Sigma^+)$, i.e. fourth positive system. Only the *Ångström* band is used to infer the gas temperature. Preliminary studies on the third positive system and on the emission in the UV range will be discussed. Figure 5.6 *(a)* shows *ab initio* calculations of the singlet states' potential curves of

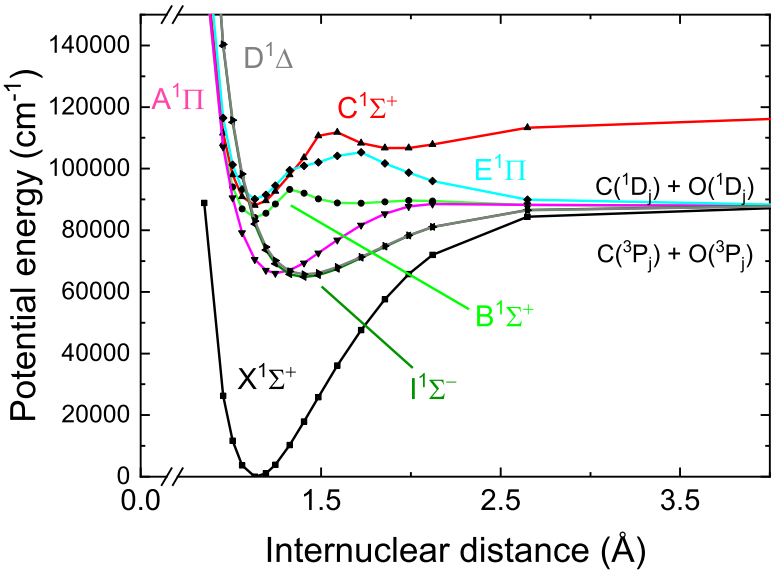


(a) *Singlet states*

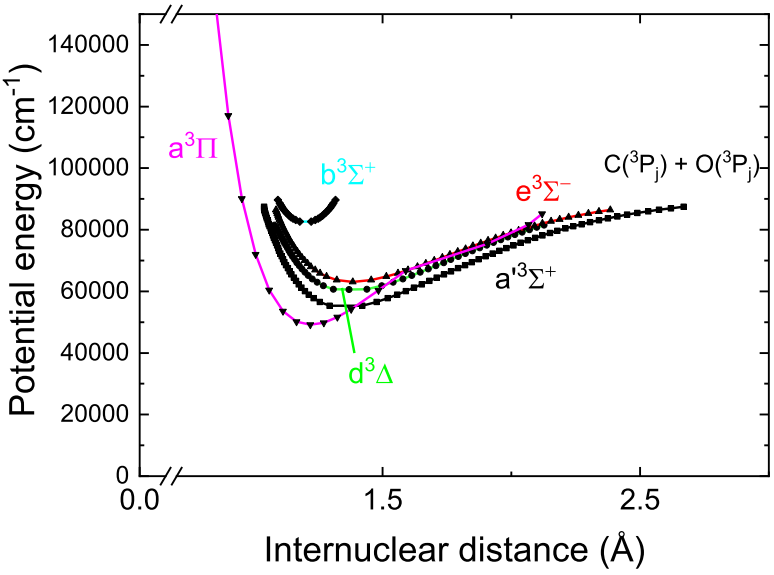


(b) *Triplet states*

Figure 5.6: *(a) ab initio* potential curves of the singlet CO bound states. *(b)* RKR potential curves of the triplets CO bound states.

the CO molecule. The analytic curve of the CO($X^1\Sigma^+$), CO($B^1\Sigma^+$), CO($C^1\Sigma^+$), CO($A^1\Pi$) and CO($E^1\Pi$) states obtained from Cooper and Kirby [99], while the analytic curves of the CO($D^1\Delta$) and CO($I^1\Sigma^-$) states from the work of Rosenkrantz and Kirby [100]. Figure 5.6 *(b)* shows RKR calculations of the CO(a'$^3\Sigma^+$), CO($e^3\Sigma^-$), CO($d^3\Delta$) triplet states of the CO molecule from [101]. The potential curve of the CO($a^3\Pi$) has been calculated *ab initio* by Peterson et al. [102], while the potential curves of the CO($b^3\Sigma^+$) is an RKR calculation performed with the program RKR [58] using the molecular constants of Prasad et al. [103]. All the potential curves are shifted in energy to have a dissociation limit consistent to the one of [99]. The dissociation products are given accordingly to S. V. O'neil and H. F. Schaefer [104].

### 5.3.1 CO *Å*ngström band and its perturbations

The simulation of the *Å*ngström band is carried out using PGOPHER in combination with LEVEL. The *Å*ngström emission is commonly used to determine the rotational temperature in various types of CO containing plasmas [105–108]. These works focus on the investigation of the Q-band of the 0-1 vibrational transition to determine the rotational distribution of the CO($B^1\Sigma^+$,$\nu = 0$) state. A complete simulation of the CO *Å*ngström band has been carried out, through a recalculation of the transition dipole moments and taking into account the known perturbation on the CO($A^1\Pi$) state.

To obtain absolute transition probabilities it is necessary to calculate the transition dipole moments ($R_{\nu'\nu''}$ in equation 3.17). The computer program LEVEL [67] is used to calculate the transition dipole moments. The potential curves of the CO($A^1\Pi$) and CO($B^1\Sigma^+$) states are shown in figure 5.6 and have been calculated by Cooper and Kirby [99]. The electronic transition moment ($R_e$ in equation 3.17) between the two states has been calculated also by Kirby and Cooper [109] and are shown in figure 5.7.

The calculation of the ro-vibrational energy levels of the CO($A^1\Pi$), CO($B^1\Sigma^+$) states and the Einstein coefficient of the transition between them has been carried out using the program PGOPHER [63]. The calculation of the transition probabilities and transition frequency has been performed between the CO($B^1\Sigma^+$,$\nu' = 0, 1$) and the CO($A^1\Pi$,$\nu' = 0, ..., 9$) states. The resulting lifetime for the CO($B^1\Sigma^+$,$\nu' = 0$) and CO($B^1\Sigma^+$,$\nu = 1$) decays to all the possible vibrational levels of the CO($A^1\Pi$) state are shown and compared with experimental results in table 5.1.

| | $A_{B\to A}$ | $A^a_{B\to A}$ | $A^b_{B\to A}$ |
|---|---|---|---|
| $\nu$=0 | $16\cdot 10^6$ s$^{-1}$ | $14.5\cdot 10^6$ s$^{-1}$ | $13 \pm 2\cdot 10^6$ s$^{-1}$ |
| $\nu$=1 | $15.7\cdot 10^6$ s$^{-1}$ | | |

Table 5.1: Einstein coefficients for the Ångström transition calculated by using PGOPHER (first column) in comparison with the values of $^a$ values from [110], $^b$ from [111].

The CO($A^1\Pi$) state of CO interacts with several neighboring states [112] and several of its vibrational levels are perturbed [113–115]. Compared to the $C_2$ Swan band, which is only weakly perturbed, the perturbations on the CO($A^1\Pi$) state influence strongly the band head shape and should be taken into account when simulating a high resolution spectrum of the CO Ångström band. The perturbation on the first vibrational level ($\nu$=0) has been studied by Field and Wicke [115], Le Floch et al. [113] and Niu et al. [114]. They found out that the first vibrational level is perturbed by the CO($e^3\Sigma^-$,$\nu = 1, 2$), CO($d^3\Delta$,$\nu = 4, 5$), CO(a'$^3\Sigma^+$,$\nu = 9$), CO($D^1\Delta$,$\nu = 0$) and CO($I^1\Sigma^-$,$\nu = 1, 2$) states. Field and Wicke [115] and Niu et al. [114] investigated the perturbation on the second vibration level ($\nu = 1$) and found it to be perturbed by the $e^3\Sigma^-(\nu = 3)$, $d^3\Delta(\nu = 5, 6)$, a'$^3\Sigma^+(\nu = 10, 11)$, $D^1\Delta(\nu = 1)$ and $I^1\Sigma^-(\nu = 2, 3)$ sates. Field and Wicke [115] have also investigated the perturbation on the high vibrational levels of the $A^1\Pi$ ($0 \leq \nu \leq 18$) state. In all cases, de-perturbed molecular constants are calculated, with these constants and the perturbation coefficient have been used to simulate the CO Ångström emission in this work. An overview of the perturbation parameters and molecular constants is given in appendix A.2.1.

**Emission spectrum**

The Ångström emission is originated from two singlet states, hence it is not required to make a distinction between Hund's case (a) or (b) is meaningless. The CO($B^1\Sigma^+$) $\rightarrow$ CO($A^1\Pi$) transition is characterized by a dominant Q-band, with an Einstein coefficient about 2-3 time higher than the R and P branches. Figure 5.8 shows a Fortrat plot of the CO Ångström band in the wavelength 460-485 nm, corresponding to the 0-1 vibrational transition. There are few lines missing in the Fortrat plot for the R and P branches, due to their low transition probability, which is below $10^6\, s^{-1}$ because of the perturbations. The other vibrational transition groups (e.g. 0-0, 0-2, 0-3 etc.) calculated present a similar structure. The CO($B^1\Sigma^+$) state has only two vibrational levels active in emission, the electronic state, in fact, pre-dissociate above the $\nu = 1$ level [116], [117]. Eidelberg et al. [116] observed as last emitting

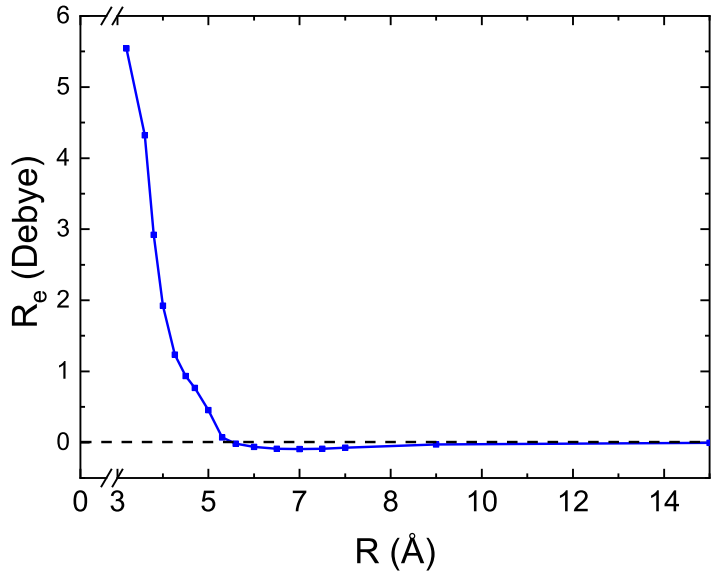


Figure 5.7: Electronic transition dipole between CO($A^1\Pi$) and CO($B^1\Sigma^+$) state [109].

rotational levels J = 64 for the $\nu = 0$ level and J = 36 for the $\nu = 1$, while all the rotational levels of the $\nu = 2$ vibrational level pre-dissociate.

### CO($B^1\Sigma^+$) as thermometric species

The first vibrational level of the CO($B^1\Sigma^+$) state lies 10.7 eV above the first vibrational level of the ground state of the CO molecule [118]. This state undergoes to two main radiative transitions: the CO($B^1\Sigma^+$) $\rightarrow$ CO($A^1\Pi$) and the CO($B^1\Sigma^+$) $\rightarrow$ CO($X^1\Sigma^+$). The emission spectrum of the second transition lies around 115 nm and is strongly influenced by radiation trapping for gas pressures above 0.1 mbar [119] (hence, for all the cases investigated in this thesis). The radiative lifetime of the CO($B^1\Sigma^+$) state is 22 ns. However, at pressures above 30 mbar (the minimum working pressure of the experimental apparatus described in chapter 4) the only radiative decay occurring is the CO($B^1\Sigma^+$) $\rightarrow$ CO($A^1\Pi$) transition and the effective radiative lifetime is between 90 and 60 ns [120].

The formation of the CO($B^1\Sigma^+$) state can occur by electron impact excitation of the ground state (reaction 5.8), via atomic carbon and oxygen recombination (reaction 5.9, the recombination asymptote are shown in figure 5.6).

$$CO + e \rightarrow CO(B^1\Sigma^+) + e \tag{5.8}$$

$$C + O + M \rightarrow CO(B^1\Sigma^+) + M \tag{5.9}$$

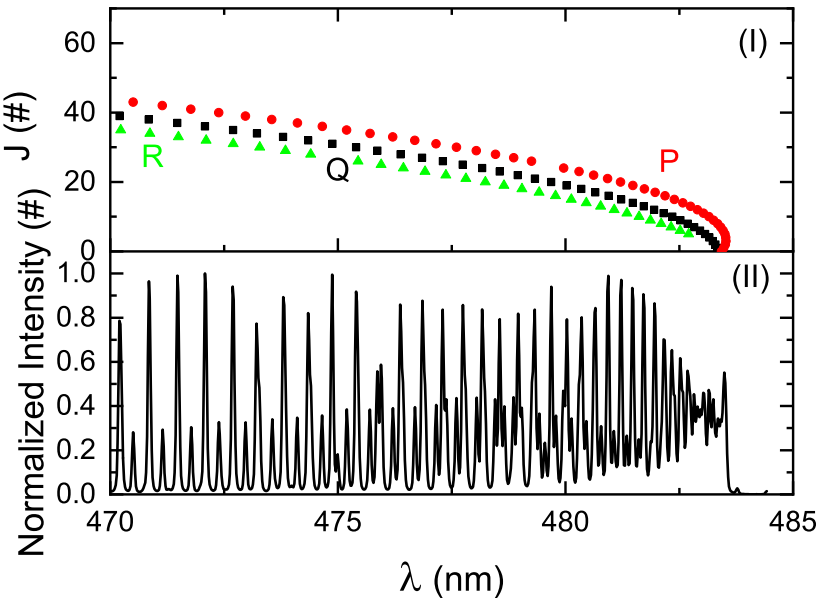


Figure 5.8: (I) Fortrat plot of the $\nu' = 0 \rightarrow \nu'' = 1$ vibrational transition between 470 nm and 485 nm, with transitions having Einstein coefficients above $10^6\ s^{-1}$. (II) simulation of the $\nu' = 0 \rightarrow \nu'' = 1$ vibrational transition between 470 nm and 485 nm at rotational temperature of 2000 K. The emission intensity has been normalized to the maximum intensity.

Production from recombination of carbon and oxygen is (likely) not the origin of the $CO(B^1\Sigma^+)$ state since no carbon or $C_2$ emission is observed and there are no other indications that atomic carbon forms in $CO_2$ microwave discharges at pressures between 35 mbar and 100 mbar. In addition, 3-body process (as reaction 5.9) are less efficient at low pressure. On the contrary, in the investigated setup an increase of the $CO(B^1\Sigma^+)$ emission is observed while reducing the pressure. Moreover, the pulsed measurements show an instantaneous ($< 1\mu s$) decay of the Ångström band emission (see chapter 7), while the reaction 5.9 would have a slower decay rate since it is a heavy particle interaction. It is thus concluded that the $CO(B^1\Sigma^+)$ state is produced as a result of electron driven processes.

An overview of the electron impact cross sections with the ground state of the CO molecule [121, 122] is shown in figure 5.9. The direct electron excitation of the $CO(B^1\Sigma^+)$ state from the ground state of CO is less favourable than the excitation of the $CO(a^3\Pi)$ state. Moreover, such state is also produced in the electron impact dissociation of $CO_2$ (in reaction 2.19). The $CO(a^3\Pi)$ state is a metastable state (i.e. it has a long radiative lifetime), it is thus possible that the source of the $CO(B^1\Sigma^+)$ state is the electron excitation of the $CO(a^3\Pi)$ . In addition, the $CO(B^1\Sigma^+)$ state can also be produced from electron impact excitation of the $CO(A^1\Pi)$ state. The

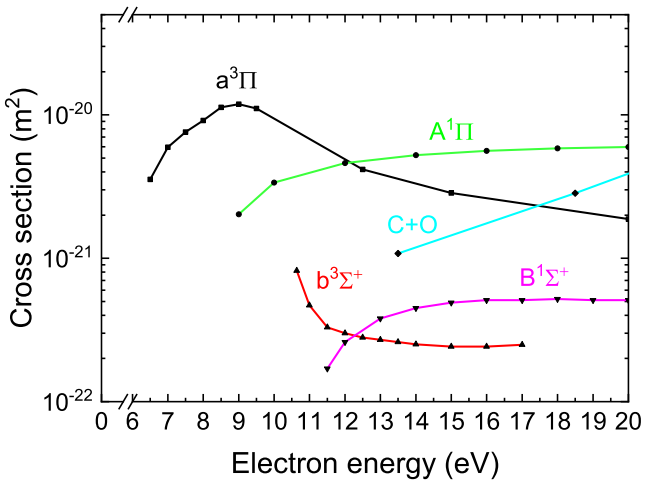


Figure 5.9: Electron impact cross section for the formation of the CO($a^3\Pi$), CO($A^1\Pi$), CO($b^3\Sigma^+$) and CO($B^1\Sigma^+$) electronic exciting states from the ground state of the CO molecule. The electron impact dissociation of CO into C + O cross section is also indicated [121, 122].

cross sections of these processes are not available, nevertheless, the electron energy threshold for both processes is *ca.* 6 eV (i.e. the energy gap between the CO($a^3\Pi$) and the CO($B^1\Sigma^+$) state), significantly lower than the 11.6 eV, which is the energy required for excitation from the ground state (see figure 5.6).

It is expected that the electron temperature in $CO_2$ microwave plasmas below 120 mbar is 2-3 eV, as estimated by Groen et al. [29], who performed plasma impedance simulations in order to calculate the electron temperature in $CO_2$ microwave plasmas. With such electron temperature, the fraction of electrons that have sufficient energy to excite the CO($B^1\Sigma^+$) state is small. Thus, both excitation from the ground state and from CO($a^3\Pi$) into the CO($B^1\Sigma^+$) state can occur. However, to conclude which of them is the precursor (or precursors) a collisional radiative model is required. The construction of such a model would be challenging since most of the necessary data are not available in the literature.

The CO($B^1\Sigma^+$) electronic excited state of CO is known to be efficiently quenched by CO, $CO_2$ and $O_2$ and O [111, 123]. In a $CO_2$ plasma, the main quenchers are the $CO_2$ and CO molecules (the $O_2$ molecule is hardly present because of the high gas temperature, see chapter 6) and the oxygen atoms. Settersten et al. [123] investigated the quenching rate of the CO($B^1\Sigma^+$,$\nu$=0) by CO and $CO_2$ as a function of the temperature. The CO($B^1\Sigma^+$) loss frequency due to collisional quenching varies from 0.1 GHz at 2000 K and 35 mbar to 0.4 GHz at 3000 K and 100 mbar (the quenching frequency are calculated in the conditions where CO emission is observed in this work). Collisional transfer between the CO($B^1\Sigma^+$) and CO($b^3\Sigma^+$) states has also been observed in two photons laser excitation experiments [124]. The collisional transfer reaction is:

$$CO(B^1\Sigma^+) + CO \rightarrow CO(b^3\Sigma^+) + CO \tag{5.10}$$

The effective lifetime of the CO($B^1\Sigma^+$) state can be expected to be shorter than the rotational relaxation time, that has been calculated by Du et al. to be *ca.* 100 ns at pressures of *ca.* 70 mbar [125]. The CO($B^1\Sigma^+$) state is formed via electron excitation from a lower lying state, thus the rotational population distribution reflects the one of the precursor state (the CO ground state, accordingly to Du et al. [125] and Silva et al. [105]). If the rotational population distribution of the precursor state is out of equilibrium, the CO($B^1\Sigma^+$) state has no time to equilibrate before radiative decay.

The use of the CO($B^1\Sigma^+$) state as thermometric species has been discussed by Du et al. [125]. They investigated the CO($B^1\Sigma^+$) rotational population distribution in a DBD discharge at 70 mbar and compared the gas temperature measured by thermography with the rotational temperature associated with the rotational population distribution of the CO($B^1\Sigma^+$) state and found them in good agreement. Silva et al. [105], [106] performed the rotational population distribution analysis of the CO($B^1\Sigma^+$) state in a microwave discharge, concluding that the rotational population distribution of the CO($B^1\Sigma^+$) state is in equilibrium with the gas temperature by assuming direct impact excitation from the ground state of CO (that is necessarily in equilibrium with the gas temperature and has the same rotational structure of the CO($B^1\Sigma^+$) state) and a radiative lifetime much shorter than the collision frequency. It is concluded that the analysis of the CO($B^1\Sigma^+$) state rotational distribution is a good tool to determine the gas temperature in microwave and low temperature DBD discharges at pressures above 10 mbar.

### 5.3.2 CO third positive Band

The transition observed between 260 and 320 nm is identified as the third positive system of CO that corresponds to the CO($b^3\Sigma^+$) $\rightarrow$ CO($a^3\Pi$) transition. The CO($b^3\Sigma^+$) state can be formed via different reactions. One possibility is the electron impact excitation of the ground state of CO, with threshold energy of 10.4 eV (reaction 5.11). Similarly to CO($B^1\Sigma^+$) also the CO($b^3\Sigma^+$) state can be produced from electron excitation of the metastable CO($a^3\Pi$) state (reaction 5.12) with threshold energy of *ca.* 6 eV. The CO($b^3\Sigma^+$) can also be directly formed from $CO_2$ dissociation with a threshold energy of 15.84 eV (reaction 5.13) [36]. Finally, collisions induced crossing between the CO($B^1\Sigma^+$) and CO($b^3\Sigma^+$) state have also been reported (reaction 5.14) [124]. Loge et al. [124] discussed that the CO($b^3\Sigma^+$,$\nu = 0$) state is faster

quenched with respect to the CO($b^3\Sigma^+$,$\nu = 1$). Reaction 5.14, can explain why the Ångström band disappears at lower pressures (above 120 mbar, at the plasma contraction) with respect to the third positive system, which disappears at pressures above 300 mbar.

$$CO(X^1\Sigma^+) + e \rightarrow CO(b^3\Sigma^+) \tag{5.11}$$

$$CO(a^3\Pi+) + e \rightarrow CO(b^3\Sigma^+) \tag{5.12}$$

$$CO_2 + e \rightarrow CO(b^3\Sigma^+) + O(^3P) \tag{5.13}$$

$$CO(B^1\Sigma^+) + CO \rightarrow CO(b^3\Sigma^+) + CO \tag{5.14}$$

The investigations of quenching rates of the CO($b^3\Sigma^+$) carried out by twist et al. [126], they found a quenching cross section of the CO($b^3\Sigma^+$,$\nu = 0$) state of $7.7{\cdot}10^{-19}$m$^2$, which multiplied for the gas density and the thermal velocity gives a quenching rate faster than the radiative lifetime at the typical working pressure ($>$ 30 mbar) and temperature ($>$ 1000 K).

Perturbation on the CO($b^3\Sigma^+$) state arises from the high vibrational levels of the CO(a'$^3\Sigma^+$) state. The CO($b^3\Sigma^+$) state lays close to the dissociation limit of the CO(a'$^3\Sigma^+$) and the rotational progression of the CO($b^3\Sigma^+, \nu = 0$) level is repeatedly perturbed at increasing J number. In this work, simulations of the third positive band of CO have been performed to confirm the assignation and to prove that the perturbations are the origin of the observed shape of the CO third positive system. Since the data available are not sufficient to properly calculate the emission of the CO($b^3\Sigma^+$) level at high gas temperature. In fact, perturbation analysis of the CO($b^3\Sigma^+$) state has been carried out only at low gas temperature [103, 127, 128]. Thus, the emission of the CO($b^3\Sigma^+$) state cannot be properly analyzed to calculate the gas temperature because of the strong perturbation that affects the rotational tail.

The type of perturbations that are used to describe the interaction between the CO($b^3\Sigma^+$) and the CO(a'$^3\Sigma^+$) sates are *homogeneous perturbations*. They are modelled as constant off-diagonal elements in the Hamiltonian matrix of each rovibrational level of the CO($b^3\Sigma^+$) state. The information gathered from literature allows calculating the emission spectrum of the CO($b^3\Sigma^+$) state only to certain extend. *Ab initio* electronic transition moment for the CO($b^3\Sigma^+$) $\rightarrow$ CO($a^3\Pi$) are not available in the literature and relative experimental TDM are used [66] to calculate

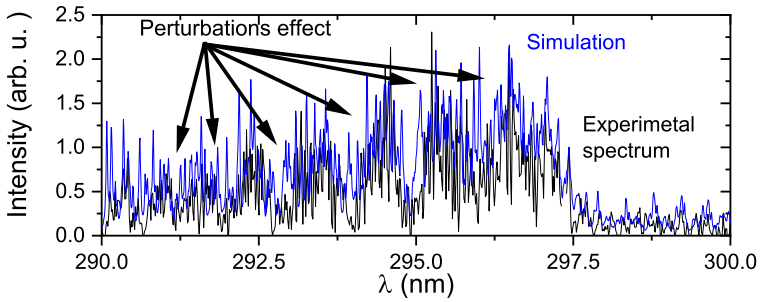


Figure 5.10: Comparison between the experimental spectrum and simulated emission. The effect of the perturbation is seen in the strong depletion of the rotational tail indicated by the arrows in figure.

the Einstein coefficient. The used parameters for the simulation can be found in appendix A.2.2. The measured spectrum is shown in figure 5.10 along with the simulation performed. As it can be seen in the plot, the perturbations alter enormously the emission spectrum. The magnitude of the perturbations on the CO($b^3\Sigma^+$, $\nu = 0$) are known, to the best of the author's knowledge, up to the CO($a'^3\Sigma^+$, $\nu \leq 34$). To prove that the perturbations are the origin of the spectra distortion also at high J number, the perturbation between CO($a'^3\Sigma^+$, $34 < \nu < 37$) states are included in the simulation with arbitrary perturbation magnitude.

It can be concluded that the optical emission measured at a wavelength between 260 and 310 nm is indeed the emission from the CO third positive. Whose rotational tail is distorted by the perturbations of the CO($a'^3\Sigma^+$, $\nu > 34$).

### 5.3.3 Emission in the UV range

The recorded spectra show emission in the region 230-260 nm as well (the sensitivity of the camera is too low to detect emission below 230 nm). A few candidates might be responsible for such emission: the so-called first negative band of $CO^+(B^2\Sigma^+) \rightarrow CO(X^2\Sigma^+)$, the high vibrational transition group $\Delta\nu = -9, -10, -11$ of the fourth positive system $CO(A^1\pi) \rightarrow CO(X^1\Sigma^+)$ and the Cameron band $CO(a^3\Pi) \rightarrow CO(X^1\Sigma^+)$ with $\Delta\nu = -2, -3, -4$. The band heads of the first negative band of $CO^+$, although being in the analyzed region, do not match with the measured ones. Instead, both the CO fourth positive [129] and Cameron bands [130] seem to have the bands heads in a compatible position with the measured spectra.

Figure 5.11 shows an emission spectrum in the region 235-267 nm. The spectrum has been recorded in a surfaguide setup (described in chapter 4). The spectrum was recorded at 1.1 mbar, with a $CO_2$ flow of 0.1 L/min and microwave power of 720 W.

At these parameters, the UV emission is significantly more intense than in the plasma torch. In fact, the features of the spectra discussed in this section, although always visible in the expanded regime of the plasma torch, are stronger at lower pressure where the signal to noise ratio is better, as in the surfaguide. The spectrum visible in figure 5.11, is exemplary for all the spectra measured in $CO_2$ microwave plasma at pressures lower than 30 mbar. Contrarily to the plasma torch (where pressures higher than 30 mbar are achieved), the carbon line at 248 mbar is instead visible in the surfaguide spectra, which achieve lower pressures.

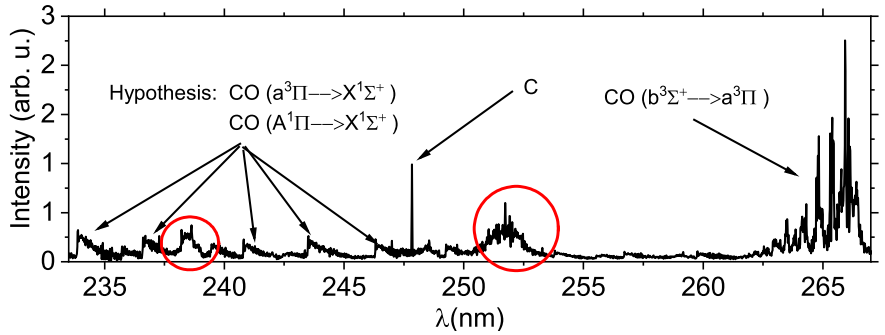


Figure 5.11: Emission between 235 nm and 270 nm at 1.1 mbar, $CO_2$ flow of 100 sccm and microwave power of 720 W. The bands highlighted in red at 252 nm and 237 nm have not been assigned.

The density of the CO($a^3\Pi$) (third positive upper state) excited state is expected to be higher with respect to the CO($A^1\Pi$) ($4^+$ band upper state) state since the vibrational levels involved in the Cameron band ($\nu \geq 0$) are lower with respect to the vibrational levels involved in the fourth positive band ($\nu \geq 6$). As a consequence, if the vibrational levels are Boltzmann distributed, the fraction of molecules in the excited states that contribute to the fourth positive band is lower.

The electron impact excitation, with electron energy below 12 eV, favours the formation of the CO($a^3\Pi$) state compared to CO($A^1\Pi$) (see figure 5.9). The expected electron temperature is *ca.* 2-3 eV [29], thus the fraction of electrons with energy above 12 eV is low. Moreover, both states can be formed via electron impact dissociation of the $CO_2$ molecule, via the reactions 5.15 and 5.16. The first one has a peak at 40 eV, reaching values of $2.6 \cdot 10^{-22}$ m$^2$, [131], while the lower limit of the cross section for the second reaction is *ca.* $1 \cdot 10^{-20}$ m$^2$ at 11 eV [132]. Additionally, both the CO($a^3\Pi$) and CO($A^1\Pi$) states can be produced by vibrationally excited CO molecule in V-E energy transfer [92].

$$CO_2 + e \rightarrow CO(A^1\Pi) + O \tag{5.15}$$

$$CO_2 + e \rightarrow CO(a^3\Pi) + O \tag{5.16}$$

The quenching rates constants of the CO($a^3\Pi$) state with $O_2$, $CO_2$ and CO are $1.1{\cdot}10^{-16}$ $s^{-1}$ $m^{-3}$, $1.1{\cdot}10^{-17}$ $s^{-1}$ $m^{-3}$ and $1.4{\cdot}10^{-16}$ $s^{-1}$ $m^{-3}$, respectively [133]. The self quenching of the CO($A^1\Pi$) state was estimated for the third vibrational level to be in the order of $1{\cdot}10^{-15}$ $s^{-1}$ $m^{-3}$ [134], one order of magnitude larger than the self quenching of the CO($a^3\Pi$). The formation processes and the comparison of the known quenching rates seem to favour the formation of the CO($a^3\Pi$) state.

The $\Delta\nu = -9, -10, -11$ of the CO fourth positive band transition group have a transition probability in the order of $10^5$ $s^{-1}$ [135], three order of magnitude higher than the Einstein coefficient of the Cameron band $\Delta\nu = -2, -3, -4$ [136] ($A_{0\rightarrow2}$= 122 $s^{-1}$, $A_{0\rightarrow3}$= 33 $s^{-1}$, $A_{0\rightarrow4}$= 4 $s^{-1}$). Hence, a strong conclusion about the origin of the UV emission measured in the expanded regime cannot be made.

Both the Cameron band and the fourth positive system are compatible with the observed emission, the measurements must be extended at least at about 200 nm in order to safely identify the origin of the emission since the shape of the two bands significantly changes at a lower wavelength. However, McGuire et al. [135] observed in an ICP torch at atmospheric pressure forth positive emission. This suggests that also in this context the emission observed is originated from the CO($A^1\Pi$) state.

The analysis of the UV emission may lead to relevant information since the CO($a^3\Pi$) state can be directly involved in the $CO_2$ dissociation process (see reaction 2.20), while the emission of highly vibrational excited CO($A^1\Pi$) levels, can be used to estimate the vibrational population distribution of the excited state of the CO molecule. The CO($A^1\Pi$) emission allows measuring the density of highly vibrational excited levels, which may deviate from equilibrium. Such deviations can be relevant for the $CO_2$ dissociation and the plasma kinetics.

## 5.4 CN molecule

The CN($B^2\Sigma^+$) emission is stronger with respect to the one of the $C_2(d^3\Pi_g)$ state. The analysis of the CN($B^2\Sigma^+$) emission not only provides a comparison for the gas temperature measured with $C_2$ rotational population distribution, but also a more efficient species to measure the gas temperature at pressures higher than *ca.* 120 mbar in microwave pulsed experiments. The addition of a small amount of nitrogen (below 5 %) to the $CO_2$ results in the contracted regime in the formation of the CN violet band. The CN Violet bands correspond to the transition CN($B^2\Sigma^+$) $\rightarrow$ CN($X^2\Sigma^+$).

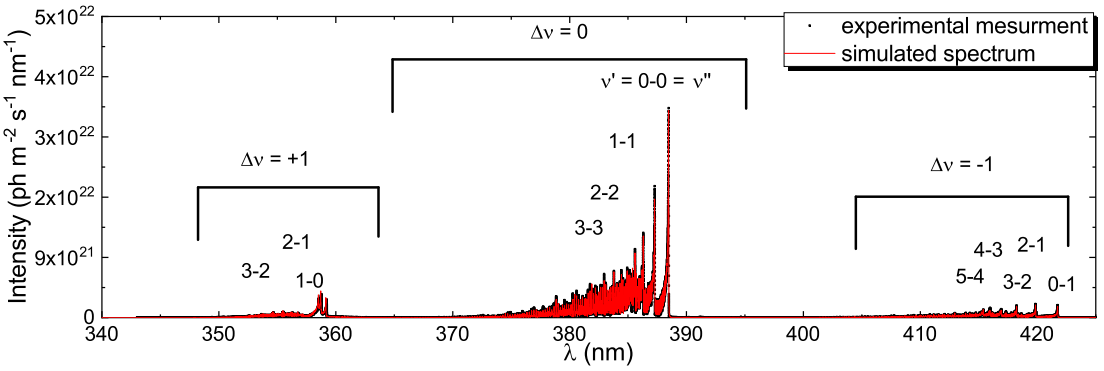


Figure 5.12: CN violet band emission between 340 nm and 430 nm recorded at 930 mbar, 10 L/min $CO_2$ and 0.3 L/min $N_2$ and microwave power of 900 W. The experimental results are shown in black, while the fit using $T_{rot}$=$T_{vib}$=6000 ± 500 K and assuming a Boltzmann distribution is shown in red.

Along with the CN violet band formation, a strong decrease of the $C_2$ Swan band can be observed. Such behaviour is commonly observed in microwave discharges at both atmospheric and reduced pressures [83, 137, 138] as well as in RF discharges at high pressure [139, 140]. At pressures lower than *ca.* 100 mbar, however, an addition of nitrogen does not result in the emission of the CN violet band, but in the emission of the second positive band of the nitrogen molecule [141]. The CN molecule is of no relevance for $CO_2$ conversion but it is a convenient byproduct of nitrogen addition to the plasma. The addition of a small fraction of $N_2$ to a $CO_2$ plasma does not alter significantly the electron properties and neutral particles energy balance of the plasma as argued by Carbone et al. [54].

The anti-correlation between the emission of the $C_2$ Swan band and the CN Violet band can be explained by the competition between the formation mechanisms of the two molecules. Dong et al. [142] showed that the CN molecule is not formed from $C_2$, but rather from atomic carbon. The atomic carbon is, in the case of $CO_2$ microwave plasmas, a precursor for both $C_2$ and CN. The reaction rates favour the formation of CN, and this explains the observed anti-correlation between the two emission bands. The CN violet system has been used to measure the gas temperature in several experiments [26, 83, 139, 143, 144].

The simulation of the transition has been carried out using PGOPHER [63]. The required molecular constants for the CN($B^2\Sigma^+$) and CN($X^2\Sigma^+$) are taken from S. Ram et al. [145]. The square of transition dipole moments ($\int \Psi_\nu(r) R_e(r) \Psi_{\nu'}(r)$) are exported in arbitrary units from the program LIFBASE [146]. The transition dipole moments used in LIFBASE are calculated using the RKR potential curves

obtained from the work of Ito et al. [147] and Cerny et al. [148] with the electronic transition dipole function calculated by Ito et al. [149]. To ensure the completeness of the partition function, the calculation of PGOPHER has been performed up to J=180. For the CN violet system, some perturbations also exist [150] but these are not included in the calculations as they do not affect significantly the spectra. The constants used in the calculation are given in appendix A.3. The spectra simulated with PGOPHER and MassiveOES are cross checked with LIFBASE calculations. They yield the same results both in terms of line positions and intensities, ensuring the correctness of the calculations.

Figure 5.12 shows the CN emission in the plasma torch at atmospheric pressure obtained with 10 L/min $CO_2$ and 0.3 L/min of nitrogen and 900 W. In the figure, the band heads of the vibrational transitions of the CN Violet band are indicated and grouped accordingly to their transition groups. A spectrum (red line) is simulated under the assumption of Boltzmann distribution for both vibrational and rotational population distributions. No significant deviation between the experimental spectrum and simulated one can be observed.

# 6 $CO_2$ conversion in a continuous plasma torch

Two microwave frequencies are mainly used to generate plasma to investigate $CO_2$ dissociation: in microwave sources of frequency 915 MHz values of energy efficiencies up to 50 % and conversion up to 80 % have been obtained, although not simultaneously [82]. Typically energy efficiency and conversion anti-correlates, an high value of conversion implies low energy efficiency and *vice versa*.

In the 2.45 GHz sources, the highest energy efficiency is measured by Kurchatov institute [22]. Energy efficiency up to 80 % are reported. However, in more recent experiments an energy efficiency between few percent and 50 % is obtained [52, 82, 151–153]. The measured energy efficiencies are maximum 50 % which is much lower than the 80% reported by Butylkin et al. [47], where vibrational ladder climbing was identified as a mechanism for $CO_2$ dissociation. Belov et. al. [151] investigated a 2.45 GHz microwave plasma torch in a pressure range between 200 mbar and 900 mbar, with variable flow injection geometry (i.e. direct, tangential and inverse), concluding that the flow dynamics strongly influences the overall $CO_2$ conversion. They reported an increase in energy efficiency while using larger gas flows. The experimental setup used in this work is different from the one used by Belov et al. [151], particularly in terms of plasma cross section (the quartz tube has a diameter of 140 mm in Belov et al. compared to 30 mm in the present setup) and gas injection configurations (the injection is placed in the center of the quartz tube). Recent work by van den Bekerom et al. [152] at pressures below 100 mbar have shown that most of the literature results do not outperform the best possible thermal efficiencies and that in microwave plasma thermal dissociation and the plasma volume (heated fraction) leads to much higher effective specific energy input (SEI) locally in the plasma. B. Wolf et al. [31] measured, in a 2.45 GHz microwave plasma torch, the electron density as a function of the pressure in a 2.45 GHz plasma torch using a microwave interferometer. The resulting electron density was found to be $10^{18}$ $m^{-3}$ at pressures below 100 mbar, it increases rapidly at a pressure of 120 mbar to $10^{19}$ $m^{-3}$ and then increases linearly

with pressure. The ionization degree shows a similar behaviour it is in the order of $10^{-5}$ at pressures between 50 and 100 mbar, increases rapidly at 120 mbar to a value of $10^{-4}$and then is constant up to atmospheric pressure. B. Wolf et al. [31] concluded that the plasma size is skin depth limited at pressures above *ca.* 120 mbar. Moreover, B. Wolf et al. [154] identify a homogeneous mode and two contracted modes between 50 mbar and atmospheric pressure. They measured the gas temperature as a function of the pressure through doppler broadening of oxygen and observed a gas temperature increasing from 3000 to 6000 K increasing the pressure from 50 to *ca.* 200 mbar and constant (=6000 K) at higher pressures.

In this chapter, an overview of the performances of the microwave plasma torch described in chapter 4 is given. In the first part of the chapter in which the gas temperature, plasma volume and $CO_2$ conversion observed in the plasma torch are systematically investigated. The second part focuses on explaining the physical mechanism driving the $CO_2$ conversion and the observed trend.

## 6.1 Gas temperature

The gas temperature is studied using optical emission spectroscopy. The analysis and interpretation of the rotational population distribution are discussed in chapter 5. The gas temperature in the contracted regime is determined from the Swan band emission of the $C_2(d^3\Pi_g)$ molecule and, upon nitrogen addition, from the Violet band of the $CN(B^2\Sigma^+)$; in the expanded regime the gas temperature is obtained from the Ångström band of the $CO(B^1\Sigma^+)$ molecule. The optical emission used to determine the temperature is integrated over the line of sight (LOS), thus the gas temperature obtained from the analysis is averaged over the emission region. Figures 6.1 *(a)* and *(b)* show the gas temperature and line integrated particle density evolution along the plasma radial and axial direction at quasi-atmospheric pressure (i.e.880-1000 mbar in this work; the precision was limited by mechanical precision of the regulation valve). The LOS area is *ca.* 1 $mm^2$ (see chapter 4). Since the double iris system is moved by a $\mu$m translator whose precision is much smaller than the LOS size, the precision on the measurement position is assumed to be *ca.* $\pm$0.5 mm. The measurements are performed with a $CO_2$ flow of 10 L/min, at quasi-atmospheric pressure and a microwave power of 900 W. The radial analysis is performed at a fixed height of 58 mm above the bottom of the resonator. The total height of the resonator, including the waveguide wall, is 53 mm, thus the measurements are performed in the early effluent. The slit in the microwave resonator is only 5 mm wide (see chapter 4),

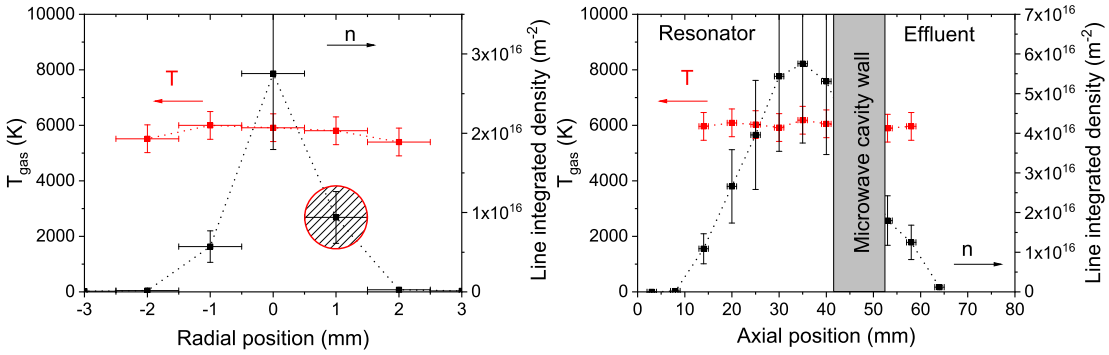


(a) (b)

Figure 6.1: *(a)* gas temperature evolution and line integrated population density of the $C_2(d^3\Pi_g)$ state in the radial direction, red and black dots respectively. The measurements were performed at a height of 58 mm from the resonator bottom. *(b)* gas temperature evolution and population density of the $C_2$ $(d^3\Pi_g)$ in the axial direction, red and black dots respectively. The measurements are performed in the center of the quartz tube, r=0. In both cases the $CO_2$ flow is 10 L/min, at quasi-atmospheric pressure. The analysis of the $C_2$ emission has been performed on the $\Delta\nu = 0$ transition group.

which is not enough to investigate the plasma emission variations in the radial direction. The axial measurements are taken along the axis of the quartz tube inside the microwave resonator. In both cases, the gas temperature measured from the $C_2$ rotational population distribution does not exhibit any dependence on the axial or radial positions, with a value of *ca.* 6000 $\pm$ 500 K. The axial analysis shows that the $C_2(d^3\Pi_g)$ state (line integrated) density peaks in the upper part of the resonator and it decays in the effluent. The upward shift of the plasma in the resonator is probably due to a combination of effects related to the gas flow and the distribution of the electromagnetic field inside the cylindrical cavity. The radial scan shows that the hot region (where $C_2$ emits) occupies only a small portion of the quartz tube. This is in accordance with the volume measurements reported in section 6.2. No temperature gradients are measured in the radial direction but this can be explained by the fact that only a small region is probed. Moreover, the gas temperature is averaged over the radial profile. Indeed, the $C_2$ molecules emit only in the core of the plasma where the gas temperature is 6000 K. The formation process of $C_2$ involves carbon atoms (as discussed in section 5.2.1) that can form (thermally) from CO dissociation only at temperatures above *ca.* 5000 K (see section 2.3.4). Groen et al. [29] and Wolf et al. [154] reported similar values and temperature profiles by O line Doppler broad-

ening measurements in a pure $CO_2$ microwave discharge in the constricted regime. The expanded regime the plasma does not extend above the resonator, thus it is not possible to perform properly an investigation of the gas temperature variation in the radial direction. Indeed a radial profile of the gas temperature is expected as measured by Bekerom et al. [155]. Figure 6.2 *(a)* shows the gas temperature in the microwave resonator as a function of the $CO_2$ flow at 900 W and quasi-atmospheric pressure. At these conditions, no variation of the temperature can be observed over the flow range 5-100 L/min. Figure 6.2 *(b)* shows the variation of the gas temperature and vibrational temperature of the $C_2(d^3\Pi_g)$ state by changing the power between 900 W and 3 kW at 10 L/min and quasi-atmospheric pressure. Figure 6.2 *(c)* shows a comparison of the vibrational and rotational temperatures of the $C_2(d^3\Pi_g)$ and $CN(B^2\Sigma^+)$ states as functions of the pressure (in the contracted regime) at 10 L/min, 900 W. All measurements of figures 6.2 are performed at z = 20 mm and r = 0 mm. The gas temperature does not show any spatial variation, hence the measurements performed in the center of the resonator are representative of the average gas temperature in the emitting region. The measured rotational and vibrational temperatures are constant within error-bars and equal to each other in the contracted regime with a value of 6000 K ± 500 K.

As mentioned in chapter 5 and discussed in more detail in section 6.2, the plasma is either diffuse or contracted, with a sharp transition between the two regimes at *ca.* 120 mbar. The transition reflects also a change of the main emitting species, which are (mostly) the $CO(B^1\Sigma^+)$, $CO(b^3\Sigma^+)$ states in the expanded regime and $C_2(d^3\Pi_g)$ state in the contracted regime. Figure 6.3 shows the measured gas temperature determined from the $CO(B^1\Sigma^+)$ and $C_2(d^3\Pi_g)$ emission spectra as a function of the pressure. The transition is stable and no oscillations of the plasma between the two states (namely contracted and expanded) can be observed, not even close to the transition pressure. The measurements of the $C_2$ Swan band are carried out at a constant $CO_2$ flow of 10 L/min and a microwave power of 900 W. The emission of the CO molecule is investigated for two conditions: $CO_2$ flow of 5 L/min and microwave power of 900 W and $CO_2$ flow of 10 L/min and microwave power of 1500 W. In the expanded regime the gas temperature is about 2000 K ± 200 K at 30 mbar and increases with pressure up to 2800 K ± 280 K.

Right before the transition from expanded to the contracted regime, the measured gas temperature is 2800 K ± 280 K at a pressure of 125 mbar. Such measurement agrees with the values measured using Raman scattering at the center of a similar plasma torch by van den Bekerom et al. [152]. In opposition to that Wolf et al. [154]

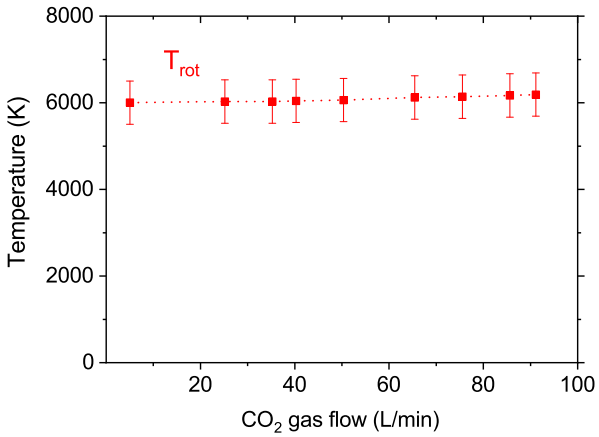


(a)

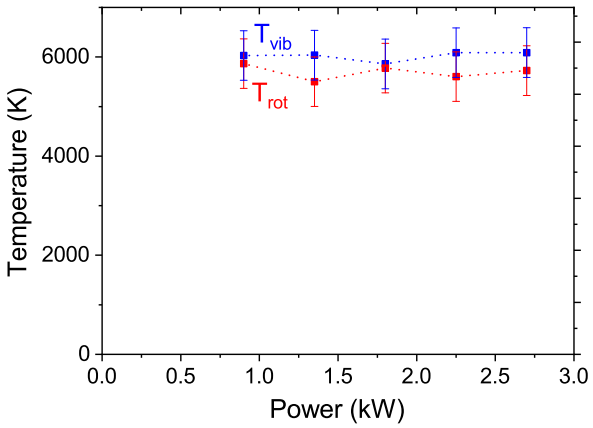


(b)

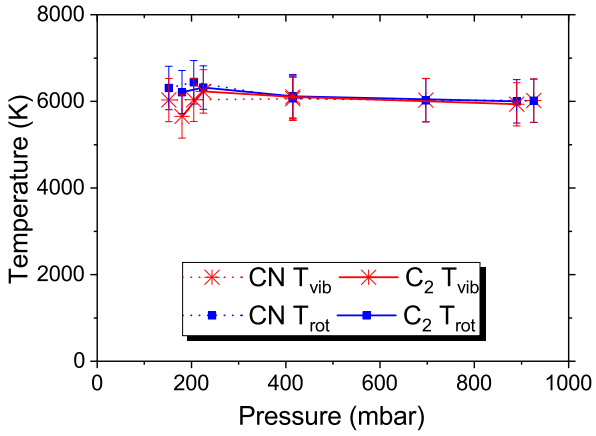


(c)

Figure 6.2: *(a)* variation of the gas temperature as a function of the flow in the center of the resonator at quasi-atmospheric pressure and 900 W. *(b)* gas temperature variation at quasi-atmospheric pressure and 10 L/min as a function of the power coupled to the plasma. *(c)* comparison of the rotational and vibrational temperatures determined from the CN (measured with a $N_2$ addition of 0.3 L/min) and $C_2$ emission as function of the pressure at 900 W and 10 L/min.

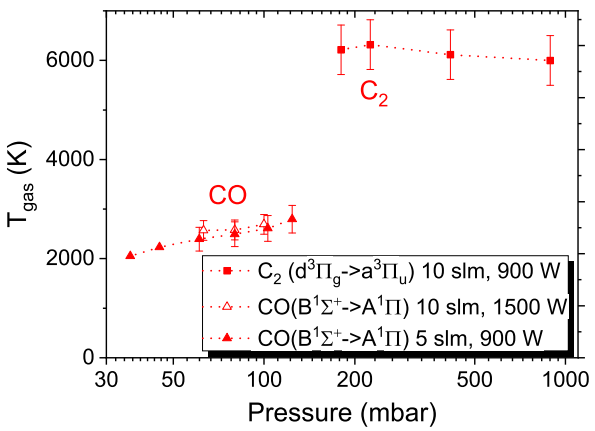


Figure 6.3: Gas temperature (=$T_{rot}$) as a function of the pressure is represented by the red triangles and red squares. The red triangles represent the rotational temperature associated with the population distribution of the CO($B^1\Sigma^+$. The red squares represent the rotational temperature calculated from the rotational population distribution of the $C_2(d^3\Pi_g)$ state.

observed an intermediate pressure plasma using oxygen broadening measurement. We do not observe such intermediate gas temperature values. However, the pin used in this work to ignite the plasma may affect the transition between the expanded and contracted regime, which is more abrupt with respect to what observed by Wolf et al. [154]. When the contraction of the plasma takes place, the gas temperature abruptly increases to 6000 ± 500 K and remains constant within error-bars up to 1000 mbar. In $CO_2$ microwave plasmas, in the pressure range of the contracted regime (from *ca.* 120 mbar up to 1000 mbar), similar gas temperatures values have been measured by Babou et al. [83], Spencer et al. [81], Mitsingas et al. [80], Bongers et al. [82] and Groen et al. [29]. In this study, The vibrational temperature of the $C_2(d^3\Pi_g)$ state is repeatedly observed to be in equilibrium with the gas temperature, suggesting that the heavy particles in the plasma are in equilibrium when the plasma is contracted. A vibrational temperature in equilibrium with the gas temperature is also measured by Babou et al. [83], while Spencer et al. [81] and Mitsingas et al. measured a higher vibrational temperature 7700 K and Bongers et al. [82] measured an even higher vibrational temperature 9000 K. The reason for such differences in the vibrational temperature can be related to the low sensitivity of the $C_2$ Swan band $\Delta\nu$=0 transition to the vibrational temperature as discussed in Carbone et al. [54], implying the need of using a higher resolution spectrometer [54].

To summarize the observations: the plasma transition from expanded to the contracted regime is abrupt and the plasma appears to be stable also close to the contraction pressure (no oscillations can be observed). No intermediate temperature can be measured around the transition. The abrupt temperature variation correlates with the abrupt change of the plasma size and hence the abrupt change in power density

(see section 6.2). In the contracted regime the vibrational temperature is observed to be equal to the gas temperature.

## 6.2 Plasma volume

The axial integrated light emission has been acquired by iCCD imaging using the experimental setup shown in figure 4.1 *(b)*. From this measurement, the maximum plasma radial cross section can be defined. The analysis of the plasma emission cannot be carried out using a single bi-dimensional Gaussian profile but rather using a sum of two bi-dimensional Gaussian profiles. Figure 6.4 shows a diameter cut of the plasma emission measured with the iCCD camera at quasi-atmospheric pressure. The total emission consists of a broad and a peaked component. The broad component contribution to the total intensity is generally smaller than the peaked one. A systematic analysis shows that the broad component size increases with the pressure, but the ratio with the peaked component reduces with the pressure to a value below 0.05. Such a low ratio makes it difficult to distinguish if the broad component is produced by a real photon flux or it is noise. Moreover, the separation of the plasma emission into two components (*a priori*) has no strong physical basis.

To reduce the systematic errors in its determination of the plasma region has been defined as the region in which the light intensity is above 15 % of its maximum. *De facto* such method determines the peak component size. The diameters obtained with the two methods coincide if the size at 10 % of the Gaussian height is used. This is sufficient, with a good signal to noise ratio, to identify the region where the $C_2$ molecule in the contracted regime and the CO molecule in the expanded regime emit light. The gas temperature can be determined from the emission of these molecules, therefore the identified region corresponds to the region where the gas temperature is the one discussed in section 3.2. Since the energy of the microwaves is coupled to the electrons and transferred by collisions to the heavy species [156], the presence of hot gas (i.e. emission from CO or $C_2$) is assumed to be a trace of the presence of electrons, thus of plasma. The $C_2$ emission, as well as the CO emission, is always observed along with the atomic oxygen emission, which was postulated to be representative of the electron density spatial profile by Wolf et al. [31, 154]. Moreover, the oxygen emission profile measured using a bandpass filter (840 $\pm$ 5 nm) is found to be equal (within 5 % of difference with random variation) to the emission profile measured without a filter. The emission intensity of the $C_2$ Swan band is much higher than the atomic oxygen lines emission, which gives a better signal to noise (i.e. the recombination

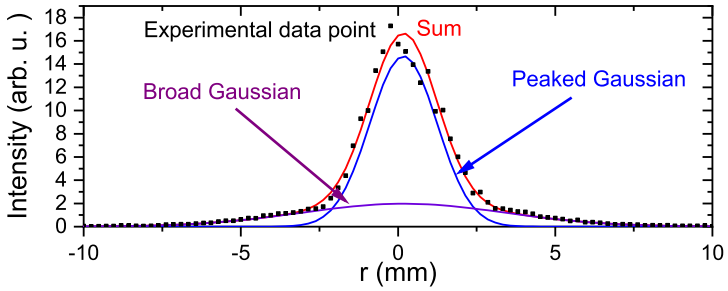


Figure 6.4: Plasma emission along a diameter of the quartz tube measured with the iCCD camera at quasi-atmospheric pressure, 20 L/min and 900 W of power. The two Gaussian components of the performed fit and their sum are shown.

continuum) ratio. Therefore measurements without filter, which include both the $C_2$ Swan band emission (or CO emission) and the atomic oxygen lines, are preferred.

Figure 6.5 shows a measurement of the axially integrated light emission performed with the iCCD camera in a case with $CO_2$ flow of 10 L/min and microwave power of 2400 W, in the pressure range from 60 to 110 mbar. At 60 and 80 mbar (figure 6.5 *(a),(b)*) the plasma emission shows a hollow profile, whereas at 100 mbar the plasma emission peaks in the center of the quartz tube (figure 6.5 *(c)*). The transition depends also on the power coupled to the plasma: at 60 mbar, for example, the plasma emission peaks in the center of the quartz tube for any power below *ca.* 1500 W.

At the transition to a contracted regime, the plasma cross section abruptly and drastically reduces the plasma diameter changes from about 20 mm in the expanded regime to values below 10 mm. Figure 6.6 *(a)* shows the changes of plasma diameter with power at different flows and constant pressure of *ca.* 900 mbar. Figure 6.6 *(b)* shows the changes of the plasma diameter as a function of power at pressures of 200, 500 and 900 mbar at a constant flow of 20 L/min. The cross section of the plasma weakly decreases while increasing the pressure. The dominant parameter that defines the plasma cross section, after the plasma contraction takes place, is the microwave power coupled into the plasma.

The plasma extension in the axial direction is recorded with the iCCD camera mounted on the side of the microwave resonator (see figure 4.7). In the resonator, the light emission is limited by the slit width (5.5 mm). Figure 6.7 *(a)* shows a picture of the plasma taken by a photo camera from the side in which the masking due the waveguide wall is visible. Similarly to the cross section, the plasma extension in the axial direction (plasma length) is defined as the region where the emission is above

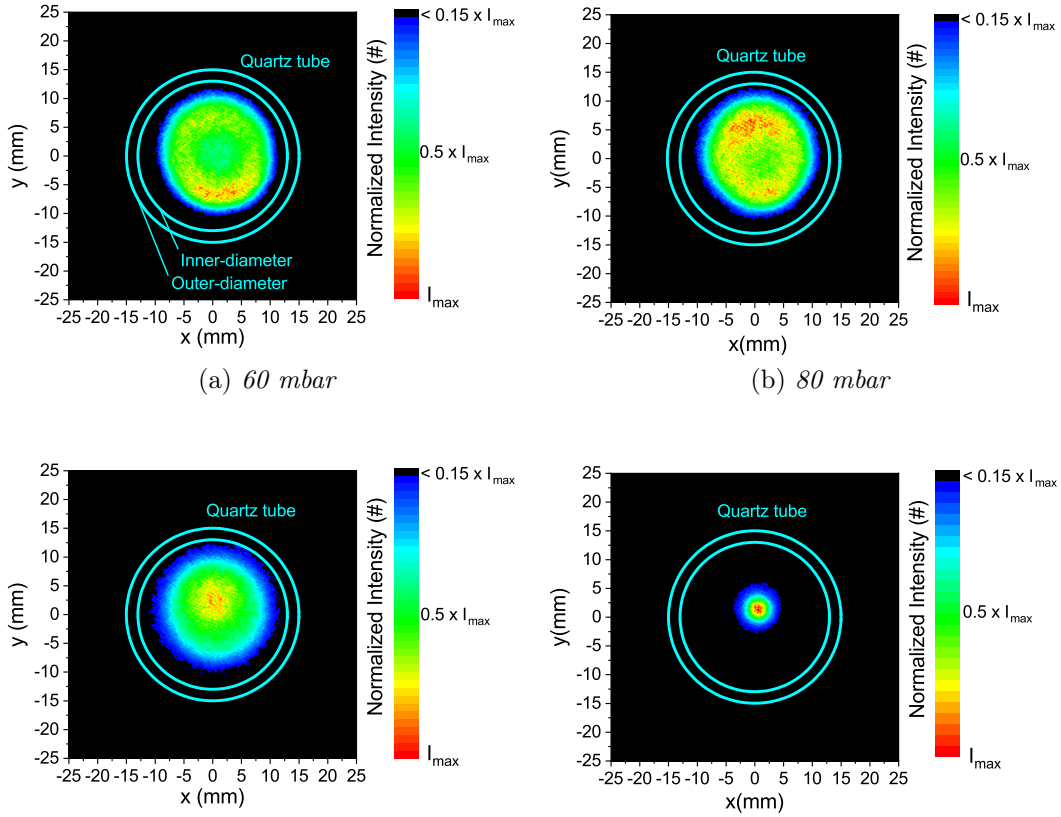


(a) *60 mbar* (b) *80 mbar*

(c) *100 mbar* (d) *110 mbar*

Figure 6.5: Radial extension of the plasma for a power of 2400 W and a $CO_2$ flow of 10 L/min at the pressures of 60, 80, 100, 110 mbar. The microwave waveguide is positioned at the right side of the picture.

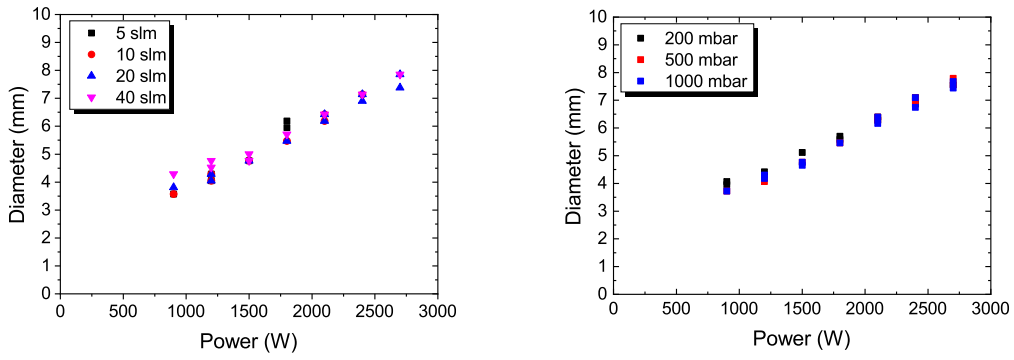


(a) (b)

Figure 6.6: *(a)* plasma cross section variation as a function of the power at quasi-atmospheric pressure and different flows. Figure *(b)* shows the effect of the pressure on the plasma cross section at a constant flow of 20 L/min.

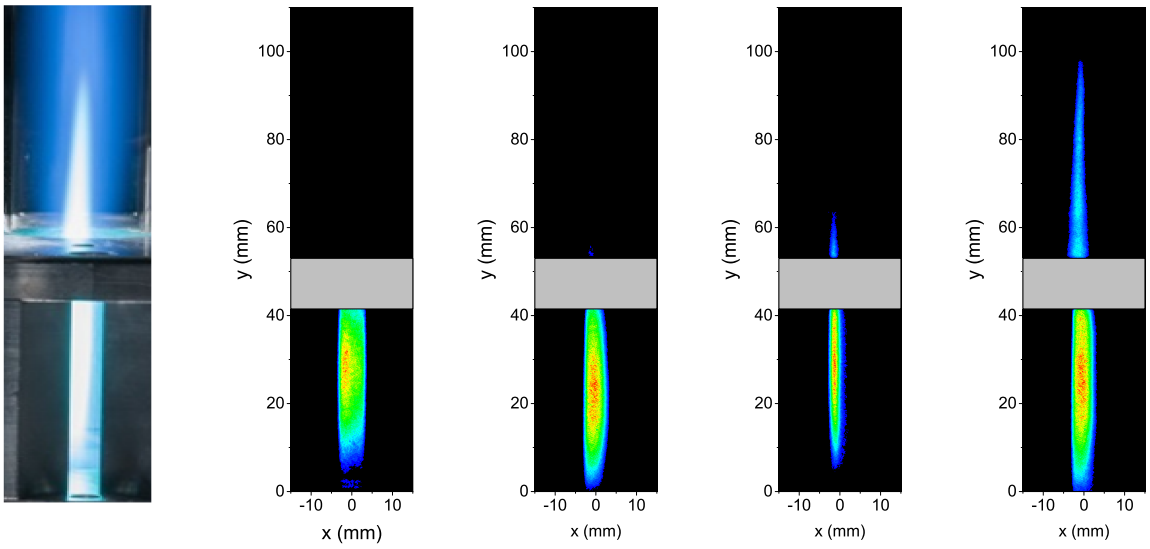


(a) *Plasma* (b) *60 mbar, 2700 W* (c) *200 mbar, 2700 W* (d) *920 mbar, 900 W* (e) *920 mbar, 2700 W*

Figure 6.7: *(a)* photo of the plasma torch (plasma burning in the microwave cavity). Axial iCCD images of the plasma with a $CO_2$ flow of 10 L/min and at a pressure of 60 mbar and microwave power of 2700 W *(b)*, 200 mbar and 2700 W *(c)*, quasi-atmospheric pressure 900 W *(d)* and 2700 W *(e)*.

15 % of its maximum. In figure 6.7, some typical plasma optical emission profiles, integrated along the waveguide direction, are shown for different pairs of pressure and power. The plasma extends in the effluent at atmospheric pressure (see figures *(d), (e)*) and at low powers, it does not fill the bottom of the resonator *(c)*. Reducing the pressure, the plasma extends much less in the effluent, as it can be seen by comparing figures 6.7 *(c)* and *(e)*. Figure 6.7 *(b)* shows, on the other hand, that in the expanded regime the plasma fills the resonator without extending above it.

The variation of the plasma length as a function of the pressure, flow and input power are summarized in figures 6.8. The plasma length as a function of power and for several flows is reported in figure 6.8 *(a)* for quasi-atmospheric pressure conditions. Figure 6.8 *(b)* shows the effect of the power at different pressures and constant flow of 20 L/min. The flow only weakly influences the plasma length while the plasma length significantly increases with power. The plasma length also increases with pressure. In the investigated power range at 200 mbar, the axial elongation is mostly not visible because the microwave waveguide edge covers the variation of plasma emission length.

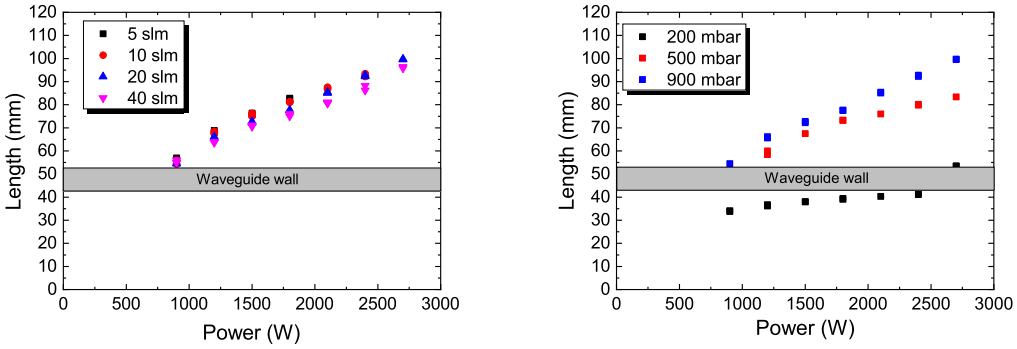


(a) (b)

Figure 6.8: *(a)* plasma length as function of power for several $CO_2$ flows at quasi-atmospheric pressure. *(b)* plasma axial extension at different pressures and a constant flow of 20 L/min. In both figures, the horizontal lines indicate the upper and lower positions of the metallic waveguide wall in the axial direction.

At pressures below 200 mbar, the plasma mostly expands radially, increasing its cross section. At higher pressures, the plasma mostly elongates axially (but the radial extension is comparable to the ones observed at 200 mbar). The total plasma volume can be calculated as the volume of the cylinder having the measured cross section and length. In this approximation, the plasma volume depends (mostly) on the changes of plasma radius rather than plasma length. At pressures below 100 mbar, the plasma appears to fill the quartz tube, although some small variation of the diameter can be observed (18-22 mm). The diameter variation at this pressure is the only responsible for the volume change. The SEI (see equation 2.15) used in section 6.3 is calculated using the total $CO_2$ flow and microwave power coupled into the plasma. However, not all the gas interacts with the plasma: the gas injected at the bottom of the resonator swirls around the plasma region (this is evident from the fact that the quartz tube is not damaged, despite a gas temperature of several thousands of Kelvin in the core of the discharge). A scheme of the gas dynamics in the plasma torch is shown in figure 6.9. The plasma emission can also be used as a measure of the plasma volume (the hot region) around which the rest of the gas swirls. In this case, the local SEI for the molecules entering the plasma region is significantly higher than the global SEI based on the total gas flow entering the quartz tube. For the present setup, the typical local specific energy input calculated, as the global SEI divided by the fraction of volume occupied by the plasma, as suggested by van den Bekerom [152]. The local specif energy input is always (much) above 10 eV/molecule in the contracted regime.

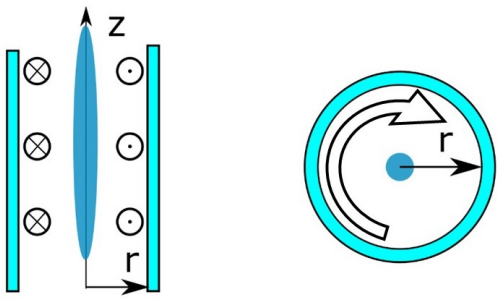


Figure 6.9: Schemes of the swirling flow in the plasma torch.

## 6.3 Steady state conversion

In this section, the $CO_2$ conversion obtained in the microwave plasma torch will be investigated as a function of the pressure, power and flow. The discussion of the physical mechanism causing the observed trends will be given in sections 6.4 and 6.5.

### 6.3.1 Impact of the measurement position on the conversion

The experimental setup is provided with two measurement positions, one before and after the heat exchanger (see figure 4.1 in chapter 4). The two measurement positions are compared to assess the impact of the CO recombination into $CO_2$ on the plasma CO yield. This allows evaluating if the mixture is stable and the amount of CO lost in the heat exchanger. The CO recombination can occur via two different reactions:

$$CO + O + M \rightarrow CO_2 + M \tag{6.1}$$

$$CO + O_2 \rightarrow CO_2 + O \tag{6.2}$$

Figure 6.10 *(a)* shows the $CO_2$ conversion measured before the heat exchanger, at *ca.* 38 cm after the quartz tube end (named position 1) and after the heat exchanger, 2 m after the end of the quartz tube end (named position 2). The measurements are performed at 200 mbar at 40 and 10 L/min of $CO_2$ as a function of the power. In most of the conditions, the sampling position does not affect the results, the fraction of CO does not change between position 1 and 2, indicating that the recombination of CO into $CO_2$ between these two positions is negligible. Only a small deviation is observed at SEI above 3.4 eV/molecule, where the conversion measured close to the resonator is lower than the one measured with cold gas. Such effect might be related to poor gas mixing [75].

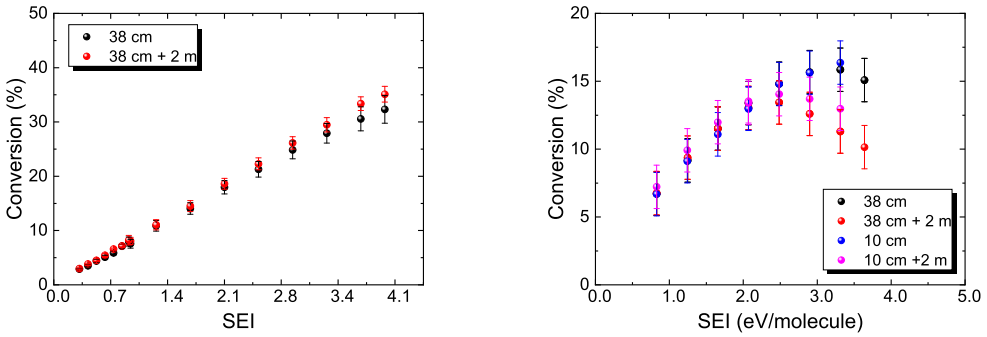


(a) *200* mbar (b) *900 mbar*

Figure 6.10: Comparison of the conversion measured 38 cm after the resonator and 2 m after the first measurement point. The measurements shown in figure *(a)* are performed at 200 mbar with 10 or 40 L/min and with a power between 600-3000 W, the ones in figure *(b)* at quasi-atmospheric pressure with a power between 600-3000 W and a flow of 10 L/min.

Figure 6.10 *(b)* shows the conversion measured at quasi-atmospheric pressure and flows of 10 L/min in positions 1 and 2. Figure 6.10 *(b)* also shows the effect of using a shorter quartz tube, which allows measuring 10 cm after the resonator. A shorter tube (thus a heat exchanger closer to the quartz tube) does not significantly affect the measured conversion (i.e. it is equal to the one measured with the longer quartz tube). At SEI above 2 eV/molecule a difference between the conversion measured with the two tube lengths and between the two measurement positions. The conversion is higher if measured closer to the plasma. Such behaviour is most likely related to the average gas temperature, which increases with increasing SEI. At quasi-atmospheric pressure a SEI above *ca.* 2 eV/molecule favours the recombination.

Figures 6.10 show that the gas sampled at 38 cm (or less) above the resonator is not always in a steady state condition (namely some recombination reactions can still occur). The mixture concentration is measured with the goal of characterizing the plasma torch performances. For this purpose, the measurements performed close to the resonator are misleading, since (at quasi-atmospheric pressure and SEI above 2 eV/molecule) some of the CO is lost because of recombination. Two meters away from the resonator the gas is at room temperature. At room temperature all the atomic oxygen must be already recombined into $O_2$ and only the reaction 6.2 can take place, which is slow at room temperature [157], the gas mixture is stable in this conditions and representative of the torch performances. The conversion from here on is measured only in position 2.

### 6.3.2 Plasma torch performances in CW operation

Figures 6.11 *(a)* and *(b)* show the conversion and energy efficiency as functions of the microwave power at different pressures and a constant flow of 10 L/min. The different behaviour between 200 mbar and quasi-atmospheric pressure can clearly be distinguished. At pressures lower than 900 mbar, the decrease of conversion observed at SEI above *ca.* 2 eV/molecule is not present. At 500 mbar the conversion reaches a saturation point at *ca.* 2 eV/molecule, while it increases linearly with SEI (i.e. the power) at 200 mbar and 60 mbar. Figure 6.11 *(b)* shows the energy efficiency corresponding to the conversion shown in figure 6.11 *(a)*. At lower pressures, the energy efficiency decreases less at increasing power. At 60 mbar the opposite trend is observed: the energy efficiency increases with power, although its value does not exceed the energy efficiency of *ca* 30 % measured at 200 mbar. The qualitative difference between energy efficiency as a function of power at 60 mbar compared to higher pressures correlates with the change of regime (expanded to contracted), which takes place at 120 mbar.

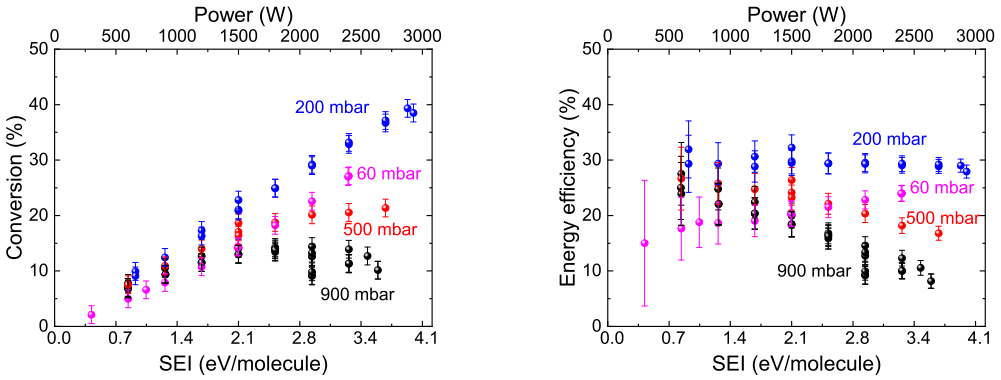


(a) (b)

Figure 6.11: *(a)* conversion and *(b)* energy efficiency observed at the pump inlet as functions of the SEI at constant flow of 10 L/min. Black, red, blue and magenta spheres represent measurements performed at quasi-atmospheric pressure, 500 mbar, 200 mbar and 60 mbar, respectively.

Figures 6.12 show that the amount of $CO_2$ converted typically depends on the SEI: the higher the energy per molecule, the higher the conversion. At 60 mbar (figure *(d)*) the conversion increases from values of *ca.* 1 % at SEI *ca.* 0.4 eV/molecule up to *ca.* 30 % at SEI *ca.* 4 eV/molecule. At 200 mbar (figure *(c)*) the increase obtained by increasing the SEI is stronger: a conversion of *ca.* 3 % is measured at *ca.* 0.3 eV/molecule and a conversion of *ca.* 40 % at *ca.* 4 eV/molecule. At 500 mbar

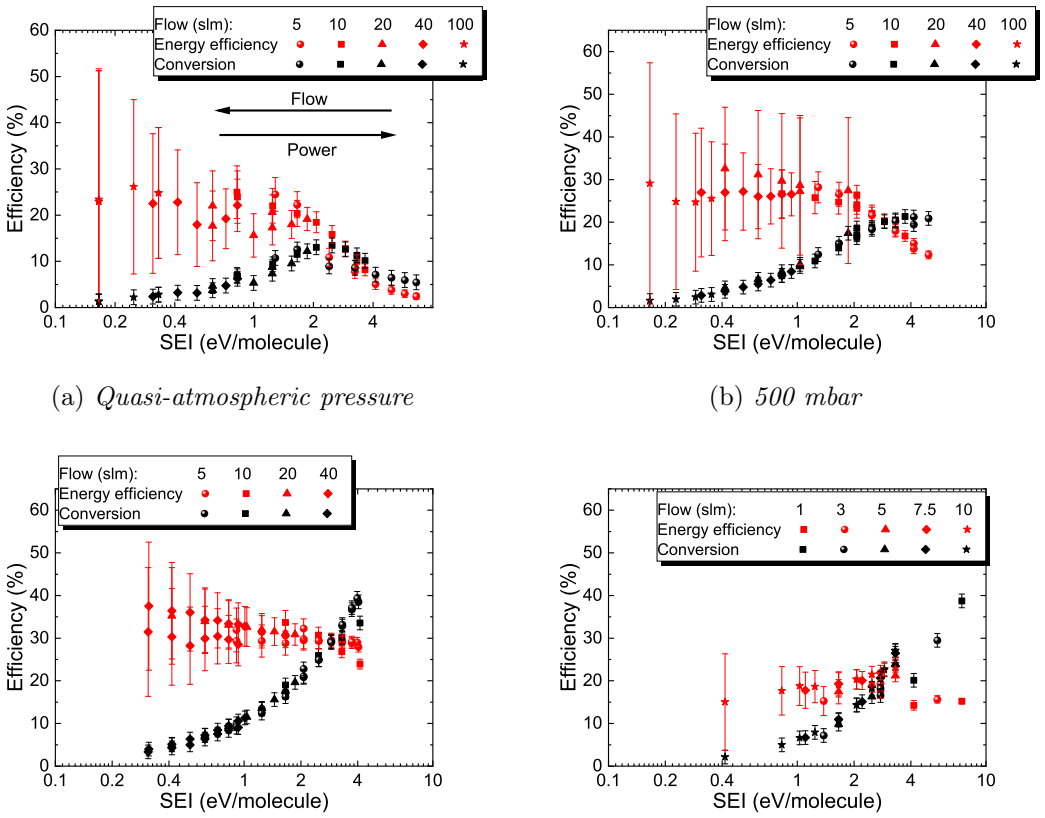


(a) *Quasi-atmospheric pressure*

(b) *500 mbar*

(c) *200 mbar*

(d) *60 mbar*

Figure 6.12: Energy efficiency (red dots) and conversion (black dots) as functions of the SEI. Flow varies between 1 and 100 L/min (depending on the pump capacity) and the power between 900 and 2700 W. The effect of $CO_2$ flow and power on the SEI is indicated by the arrows in *(a)*.

(figure *(b)*) the conversion increases from *ca.* 2 % at *ca.* 0.2 eV/molecule up to 20 % at *ca.* 4 eV/molecule. A noticeable deviation from the established trends can be observed at SEI above 2 eV/molecule at 500 mbar, where the conversion saturates: an increase of power (i.e. SEI at fixed flow) does not produce a further increase of the fraction of $CO_2$ converted. At quasi-atmospheric pressure (figure *(a)*) an increase of SEI produces a decrease of conversion above 2 eV/molecule. In the latter case the conversion increases from *ca.* 1% at *ca.* 0.2 eV/molecule to *ca.* 13 % at *ca.* 2 eV/molecule and then decreases to 5 % at *ca.* 8 eV/molecule. The energy efficiency is weakly changing with the SEI and is observed (almost) constant within error-bars in most of the studied conditions as can be observed in figures 6.12 *(c)*, *(d)* and in figures 6.12 *(b)*, *(a)* at SEI below 2 eV/molecule. The energy efficiency changes with the pressure, the maximum of *ca.* 35 % measured at 200 mbar.

No flow effect on the energy efficiency can be detected, as opposed to what has been previously observed at pressures between 200 mbar and atmospheric pressure by Belov et al. [151]. Although the conversion and energy efficiency they observed are comparable to the ones measured in this work. However, the differences between the two setups may be the origin of the discrepancy. The measured conversion and energy efficiency are comparable to those obtained in a similar device at 100-500 mbar [82, 158]. At quasi-atmospheric pressure the conversion measured is comparable to the one obtained in similar microwave plasma configuration, ranging between few per cent up to 15 % [81, 159].

The conversion and energy efficiency depend only on the SEI, but at quasi-atmospheric pressure, with a $CO_2$ flow of 5 L/min, the observed conversion deviates from the trend observed at 10 L/min. The lower flow is (probably) the main responsible of the observed deviation, but the physical mechanism behind it is still unclear. Such a trend could also be present at lower pressures but shifted to higher SEI values. This hypothesis is supported by figure 6.12 *(b)* where the conversion is observed to saturate at SEI higher than *ca.* 2 eV/molecule. Further investigations in this direction are needed. Nevertheless carrying out measurements at SEI above 4 eV/molecule at pressures above 200 mbar is challenging, because of the limitations in the microwave power (max. 3000 W) and since the plasma is unstable at flows below 5 L/min and pressures above 200 mbar.

The conversion of $CO_2$ into CO is investigated as a function of the pressure at fixed flow and power and the results are shown in figure 6.13 *(a)* and *(b)* respectively. The contraction of the plasma takes place (see sections 6.1 6.2 for more details) at a pressure value that depends on the power coupled to the plasma: at 750 W the plasma contracts at 180 mbar, at 1500 W at 120 mbar and 2400 W at 110 mbar. In figure 6.13 the contraction pressure is indicated by vertical dashed lines. The amount of $CO_2$ dissociated increases until the plasma contracts. The energy efficiency before the plasma contraction increases rapidly with the pressure, it reaches an optimum at pressures near the contraction and then stays constant at low power and decreases at higher power. Interestingly, there are no abrupt changes in the conversion at the transition between contracted and expanded regimes which depends on the pressure and power input, but not on the input flow. Such an effect can be explained by considering the flow dynamics in the plasma torch but also that the plasma, in this gas temperature range, acts mainly as a heat source. This will be discussed in section 6.5 in more detail. These observations are in agreement with Fridman's overview and discussion of the results from the Kurchatov institute [22]. After the contraction

takes place the conversion of $CO_2$ reduces with increasing the pressure, with the trend of the higher the power the stronger is the reduction. The energy efficiency follows a similar trend as conversion. Similar observations were carried out also by Wolf et al. [158] who measured an energy efficiency and conversion comparable to the ones shown in figure 6.13. Notably, in a comparable device, Den Harder et al. [52] observed the same trend, but with higher maximum energy efficiency (up to 48 %). The reasons for the differences between those experiments are not clear.

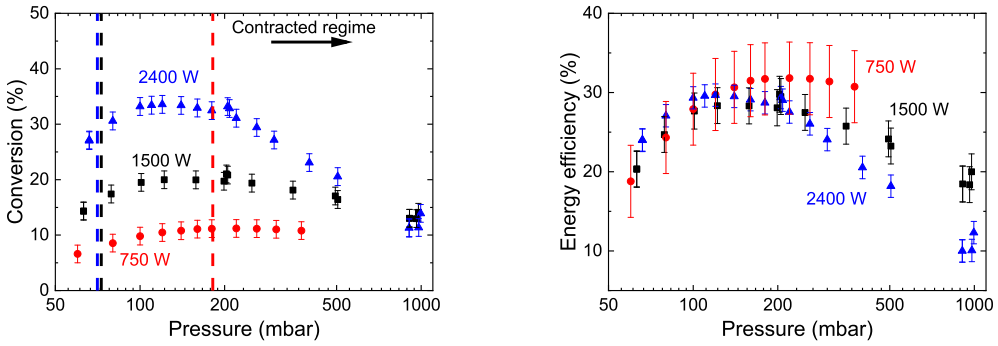


(a) (b)

Figure 6.13: *(a)* conversion and *(b)* energy efficiency as functions of pressure at a constant flow 10 L/min for the power values of 750 W, 1500 W and 2400 W represented in red, black and blue, respectively. In figure *(a)* the dashed lines mark the pressure at which the plasma contracts at the studied powers.

## 6.4 Thermal equilibrium considerations

To estimate the degree of $CO_2$ dissociation in the core of the plasma, thermal equilibrium calculations have been performed using the program CEA [49]. CEA calculates the thermal equilibrium composition at a fixed temperature and pressure minimizing the Gibbs free energy (see section 2.3.4). However, it does not include the gas dynamics, the recombination or the temperature gradients. Den Harder et al. [52] have shown that the thermalization time of the mixture is in the order of few microseconds at a temperature above 4000 K, thus much shorter than the global gas residence time in the reactor (a few ms for the total flow under the approximation of conservation of mass flux through the reactor). We note that re-circulation flow patterns may increase the residence time of the cold particles locally while the hot gas coming out of the plasma will expand rapidly. This means that, in the contracted regime, for

the fraction of $CO_2$ heated in the plasma core (i.e. at 6000 K), the thermal equilibrium composition is representative of the gas composition. At gas temperatures lower than 3000 K (thus lower pressure), the residence time is not sufficiently long to ensure (theoretically) a complete thermalization. However, the thermal calculation represents the maximum conversion that can be expected to be produced by thermal dissociation, whose importance in low pressure microwave plasmas has been also discussed by Van Bekerom et al. [152]. The purpose of this calculation is to serve as a starting point to evaluate the impact of thermal dissociation onto the $CO_2$ conversion, rather than predictive modelling of the $CO_2$ conversion.

Figure 2.5 shows the molar fractions of $CO_2$, CO, $O_2$, O and C as a function of gas temperature while heating a pure $CO_2$ gas. The molar fraction of $CO_2$ decreases rapidly above temperatures of about 3000 K with the formation of CO and $O_2$. Above this temperature $O_2$ dissociates and the gas becomes predominantly a CO+O mixture. At temperatures above 5500 K, CO starts dissociating and the gas becomes a mixture of C and O atoms. As recombination processes of the C atoms lead to the formation of the $C_2$ Swan bands in a $CO_2$ plasma (see section 5.2.1), the latter is observed only when the gas temperature exceeds 5000 K.

Figures 6.14 *(a)* and *(b)* show a comparison between the experimentally measured energy efficiency and conversion with the theoretical thermal conversion. The latter is calculated using the gas temperature and pressure of the experimental conditions. The calculated conversion (under the assumption that the measured gas temperature is representative of the whole plasma core) represents an upper limit to the conversion that can be obtained from solely thermal dissociation. Indeed the recombination processes and the temperature gradients (but also the limited plasma volume) can only produce a reduction of $CO_2$ conversion in the experiments. Instead, the thermal energy efficiency is meaningful only if all the $CO_2$ is converted at the measured gas temperature and there are no CO losses.

The conversion in the contracted regime is well below the thermal limit, which can be explained considering that not all the injected gas is heated to 6000 K. The conversion in the contracted regime is coherent with expected the thermal conversion down to *ca.* 60 mbar. At lower pressures, however, the measured conversion is higher than the one expected from only thermal contribution and it is expected to increase at higher powers. Thus, the observed conversion rates can be explained by invoking only thermal conversion in the pressure range 60-1000 mbar. However, at lower pressures, the electron driven processes start to play a role. These are more

relevant and easily identifiable at high specific energy inputs when the conversion rates exceed the thermal dissociation limit prescribed by the gas temperature.

The energy efficiency is always lower than the expected value. Notably, in the contracted regime the energy efficiency is consistent (in the lowest power case of 750 W) with a $CO_2$ conversion taking place at 6000 K, without significant losses.

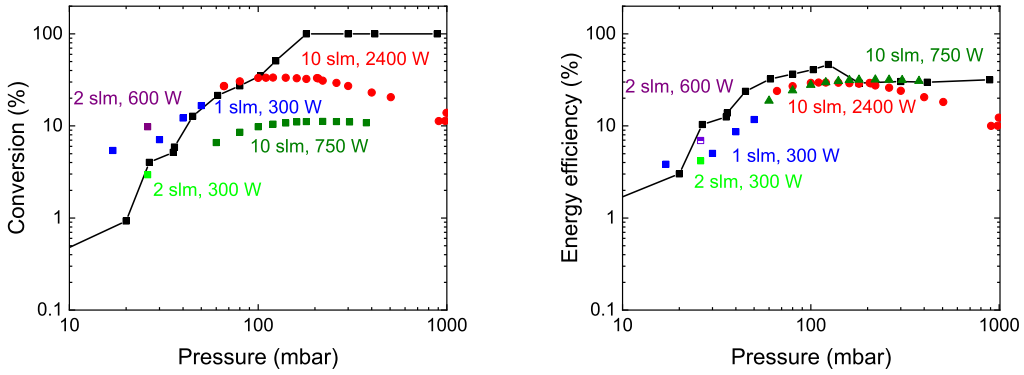


(a) (b)

Figure 6.14: A comparison between the expected conversion rate expected by heating $CO_2$ gas and the experimental measurements of the conversion *(a)* and energy efficiency *(b)* as functions of the pressure. Experimental measurements at 10 L/min 750 W (red circle), 10 L/min 2700 W (magenta down triangle) and 1 L/min 300 W (blue up triangle).

To observe in an experiment the thermal dissociation fractions shown by figure 6.14 *(a)*, the mixture composition needs to be cooled rapidly to avoid recombination of CO via:

$$CO + O + M \rightarrow CO_2 + M. \tag{6.3}$$

Den harder et al. predicted a loss fraction of 20 % if a $CO/O/CO_2$ mixture at an initial temperature of 3500 K is cool down at a rate of $10^6$ K/s [52]. The CO recombination process typically happens in the plasma itself, in the gas layer that surrounds the plasma and in the effluent as evidenced by its chemiluminescence continuum reported in section 5.1 and by the lack of difference in conversion between measurements in position 1 and 2. The increase of converted $CO_2$ with the pressure that can be observed in figure 6.13 *(a)* can be correlated with the observed increase of gas temperature that is measured with power for a non contracted plasma. As the pressure increases the gas temperature increases with a maximum of 2800 K

measured experimentally right before the transition to a contracted regime. Assuming a thermally driven dissociation process, thermal calculations do predict an increasing energy efficiency with gas temperature as seen in figure 2.6 *(b)*. The pressure has only a limited effect on the absolute value of the energy efficiency for thermal dissociation (as can be seen in figure 2.6), while the gas temperature has the strongest influence on the energy efficiency. The observed increase in conversion with power has to be also compared with the plasma size and low overall conversion rate. Moreover, a pressure increase at gas temperature below 3000 K (see figure 2.6 *(b)*) would actually reduce (slightly) the energy efficiency, while the energy efficiency increases here (see figure 6.13 *(a)*).

The plasma contraction increases the power density, that drives an abrupt increase of the gas temperature which reaches a value of 6000 K $\pm$ 500 K and remains constant at every investigated flow, power and pressure. Thermal calculations predict at such high gas temperatures that energy efficiency should increase with increasing pressure. However, the opposite trend is found experimentally (see figure 6.13). Losses of CO by recombination via reaction 6.3 is a pressure dependent process. Even if locally the conversion of $CO_2$ into CO can be high, the recombination process reduces the CO molar fraction measured downstream of the plasma reactor. At low gas flow rates (i.e. high specific energy input as shown in figure 6.12), one can expect a slower cooling rate meaning that a larger fraction of CO is lost. A decrease of the conversion and energy efficiency is indeed observed at low gas flows ($<$ 10 L/min) being more pronounced at high pressure. Moreover, in the contracted regime the plasma occupies only a small part of the tube and hydrodynamic effect between the cold swirling gas flow and hot plasma core should be additionally considered (this will be discussed in the next section).

It can be concluded that in the pressure range 60-1000 mbar thermal dissociation is the dominant process for $CO_2$ dissociation and the gas temperature is, therefore, the most important parameter for the conversion process. In particular, the plasma contraction does not produce a change in the mechanism driving the $CO_2$ conversion. The distinction between the two regimes involves only the power deposition rather than the conversion, where different mechanism are relevant only at pressures much lower than the transition pressure.

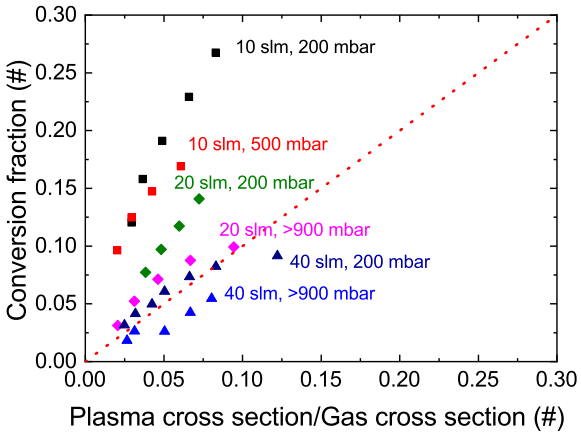


Figure 6.15: $CO_2$ conversion as a function of the ratio between plasma volume and gas volume. The red dashed line represents the equivalence between the fraction of $CO_2$ converted and the ratio of the plasma cross section and gas cross section.

## 6.5 Gas dynamics simulation

The conversion measured in the plasma torch in the contracted regime is significantly lower than the expected value, a fact that can be easily explained by the reduced plasma size. However, a comparison between the plasma cross section (measured in section 6.2) and the gas cross section, which is the cross section of the quartz tube from which the plasma cross section has been subtracted, in terms of conversion rate shows that there is no apparent correlation between the two quantities. The ratio between the gas cross section and the plasma cross section has a meaning only if the gas velocity in the axial direction is much higher than in the radial direction. Figure 6.15 shows the $CO_2$ conversion fraction as a function of the ratio between the plasma cross section and the gas cross section in several experimental conditions. The ratio between the plasma and gas cross sections does not show any direct correlation with the conversion.

Figures 6.16 *(a)* and *(b)* show the $CO_{out}$ (=$CO_2$*$\chi$) flow at quasi-atmospheric pressure and 200 mbar as a function of the power coupled into the plasma. Similar trend at 900 mbar is found for the 20 and 40 L/min conditions (figure 6.16 *(a)*) while for an input gas flow of 10 L/min a reduction in $CO_{out}$ flow is measured. Such reduction of conversion with pressure at the lowest input flow appears at 500 mbar and quasi-atmospheric pressure as seen in figure 6.12. The energy per CO molecule ($= \frac{0.0138 \cdot power}{CO_{out}}$) at 200 mbar results to be always between 9 and 12 eV/molecule, with no significant trend observable. At quasi-atmospheric pressure, the energy per CO molecule increases exponentially at high SEI from values between 9 and 12 eV/molecule up to values (the same observed at 200 mbar) even above 60 eV/molecule. CO losses are responsible for the reduction of conversion at

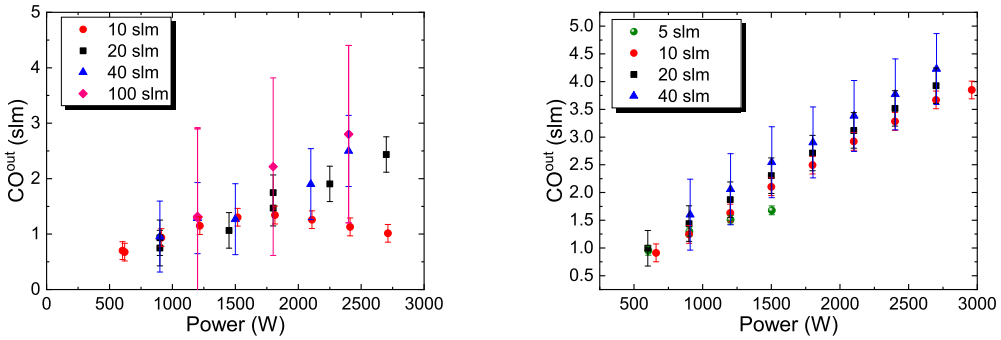


(a) *quasi-atmospheric pressure* (b) *200 mbar*

Figure 6.16: $CO_{out}$ flow as a function of the plasma surface at quasi-atmospheric pressure *(a)* and 200 mbar *(b)*.

high pressure and high SEI (>2 eV/molecule). The CO losses are driven by the reactions 2.27 and 2.28 and need a minimum SEI to be activated, the higher the pressure the lower is the SEI at which CO losses become important.

At fixed pressure, the output flow of CO appears to be a function of the microwave power only and weakly influenced by the input $CO_2$ gas flow. Following the assumption of local thermal equilibrium, the temperature profile in the quartz tube defines the region where $CO_2$ dissociation takes place. The observed conversion can be related to the mixing between the cold gas and the hot gas driven by the temperature gradient. The amount of $CO_2$ that flows from the cold region into the (hot) plasma should then be proportional to the surface (or volume) of the hot region itself. The turbulent mixing that drives the $CO_2$ gas into the plasma is not depending on the magnitude of the $CO_2$ flow, thus it is driven by the gas temperature gradient. This hypothesis is consistent with the observations carried out in sections 6.1 and 6.2: neither the plasma size nor the temperature are affected by the $CO_2$ input flow. As a result, the influx of cold gas into the plasma region is the same, thus the total $CO_{out}$ flow is constant at given pressure and power. On the other hand, a power variation changes the plasma dimensions (see section 6.2) and consequently the $CO_2$ flux into the plasma.

The flow dynamics therefore are proposed to be the limiting factor for the $CO_2$ conversion in microwave plasmas. Simulations of the flow dynamics in the source, in the presence of a heating element, have been performed using the Ansys fluent model [160]. The following simulations have been performed by Clément Brochet during an internship at Max Planck Institute for plasma physics [161]. In this work, the results

of the simulations are analyzed and their implications for the $CO_2$ dissociation in microwave plasma are discussed. A short introduction about the flow model used is presented in the appendix B. An external heating power is coupled to the system 5 cm above the gas injection (*ca.* the experimental height). The power density coupled is calculated considering the experimental power and the plasma size, which corresponds to the plasma volume measured in section 6.2. Inside the deposition volume, the power density is uniform. In other words, the power deposition profile is set up to reproduce in the simulation the power density observed in the experiments assuming that all the power is coupled to the plasma light emitting region.

The gas temperature measured experimentally is high (6000 K), therefore it is necessary to consider the chemistry to properly simulate the gas heating. The modelling of the chemistry using kinetic models is computationally expensive and the results depend on the model used. The $CO_2$ conversion observed in the contracted regime can be entirely explained by thermal conversion (see section 6.4). If the plasma chemistry is evolving at thermal equilibrium (at least in the vicinity of the power deposition profile), the simulation of the gas dynamics can be carried out under the approximation of a single fluid whose proprieties (molar mass, heat capacity, conductivity, viscosity) are the ones of the molecular mixture obtained by heating $CO_2$ gas (see figure 2.5). Figures 6.17 *(a)* and *(b)* show the heat capacity and the thermal conductivity of the thermal mixture as functions of the temperature at 60 mbar and 1000 mbar. These values are obtained using the CEA code. The double peak structure is related to the dissociation of the $CO_2$ molecule into CO that happens between 2000 and 3000 K and the CO molecule dissociation into C+O that occurs between 6000 and 9000 K (see figure 2.5).

Figures 6.18 *(a)*, *(b)* and *(c)* show the gas temperature, radial velocity and axial velocity resulting from the simulation of plasma at 1000 mbar, 20 L/min and 1500 W of microwave power. The radial velocity obtained in the simulation of the gas flow (figure 6.18 *(b)*) shows the existence of a radial flux towards the center of the plasma, the axial velocity increases consequently in the center to conserve the mass flux. The simulations performed using the experimental power density and the thermal equilibrium chemistry result in a simulated gas temperature corresponding to the experimentally measured one (figure 6.18 *(a)*). Such result is obtained if and only if the power is deposited in the experimentally measured volume, proving that the emitting region measured in section 6.2 is (approximately) the power deposition profile. Moreover, the consistency of the thermal description of the system is also proven. However, if the gas composition evolved always at thermal equilibrium, the

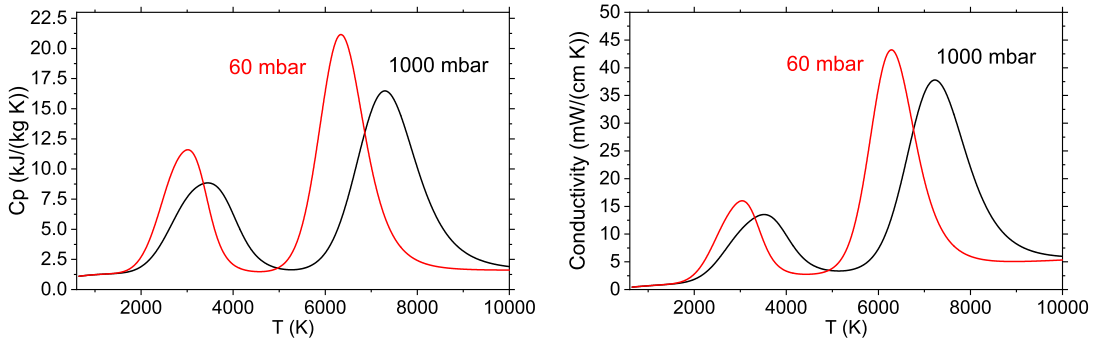


(a) $C_p$ (b) *heat conductivity*

Figure 6.17: Heat capacity *(a)* and heat conductivity *(b)* of the thermal mixture obtained by heating the $CO_2$ gas at 60 mbar and 1000 mbar.

CO fraction at the position of the measurements at about 2 m distance from the resonator would be zero (at 300 K the CO fraction in a $CO_2$ gas is 0). Therefore a non-equilibrium effect should take place to preserve the CO produced in the plasma. This effect can be identified as the strong mixing between cold and hot gas (radial velocity in the order of m/s, see figure 6.18 *(b)*) that takes place at the end of the plasma but also at the radial edges of the plasma. The efficiency of such mixing, the temperature and the pressure determine the fraction of CO that is preserved. However, it also implies that the gas temperature resulting from the simulation, after the mixing has taken place, are overestimated in the region at temperatures below 3000 K. In fact, in reality, part of the energy is stored in the CO molecule and does not contribute to the gas temperature, while in the simulation all the CO is lost (because of the thermal equilibrium evolution) leading to an overestimation of the gas temperature.

Figure 6.19 shows the gas temperature radial profile at z=100 mm (a cut of figure 6.18 *(a)*). Three regions can be defined: a cold region close to the quartz tube, a region at 3000 K and the power deposition profile at 6000 K. Such behaviour is related to the shape of the heat capacity and heat conductivity that peaks at *ca.* 7000 K and 3000 K. The heating (or cooling) of the mixture at temperatures above (or below) requires a significant amount of power (dissipation). This, in the experimental conditions, limits the hot region temperature to about 6000 K, the power is transmitted to the neighbouring regions, that can be heated up to 3000 K only. The existence of the 3000 K region around the plasma core is of particular interest because effectively the region in which the $CO_2$ dissociation happens, is significantly larger than the one

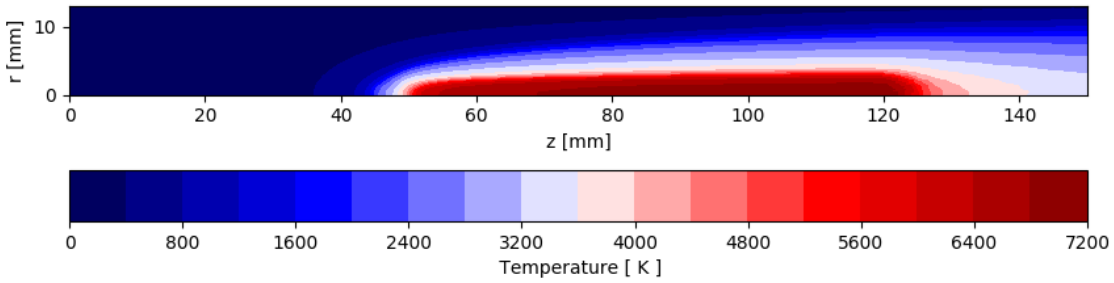


(a) $T_g$

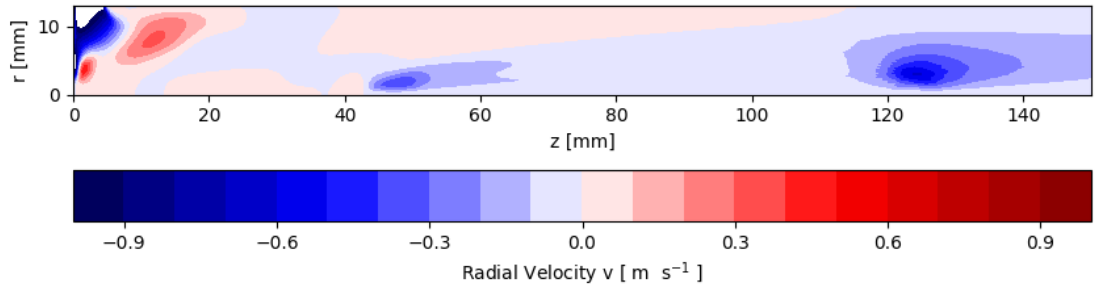


(b) $V_r$

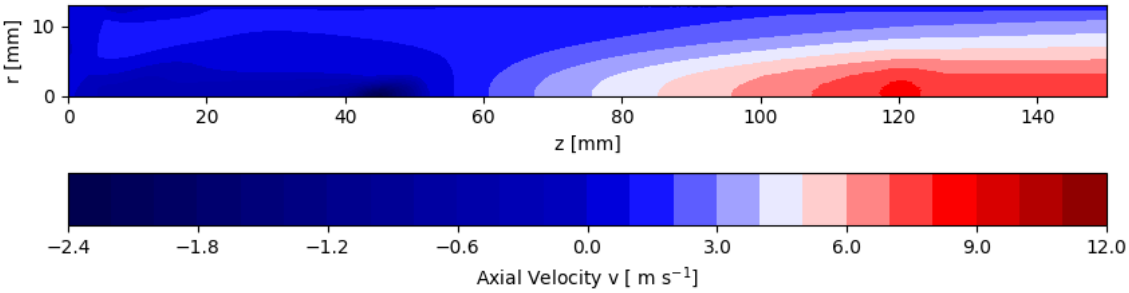


(c) $V_z$

Figure 6.18: Gas temperature *(a)*, radial velocity *(b)* and axial velocity *(c)* obtained in the simulation of the gas dynamics at 20 L/min, 1000 mbar and 1500 W. z=0 corresponds to the gas injection position.

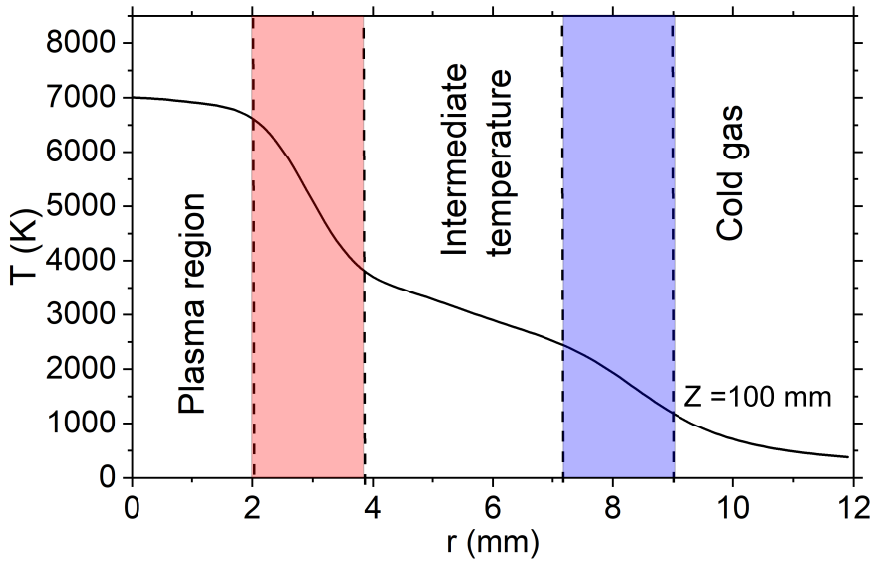


Figure 6.19: The gas temperature radial profile obtained from the simulation at z=100 mm. The three temperature region are separated by three strong gradients.

observed in section 6.1.

The simulated radial velocities and particle densities can be used to calculate the radial influx. The latter can be compared with the experimental $CO_{out}$ flux, to determine if the radial influx is sufficient to explain the measured conversions. The mass influx can be calculated from the radial velocity and the particle density. The plasma effluent is included in the calculation, thus the calculated inflow is slightly overestimated for temperature region below 3000 K, for the reason mentioned so far. The radial mass flux entering the region at 3000 K, 3500 K, 4000 K and 6000 K is 2.81, 1.53, 0.94 and 0.33 L/min, respectively. When heated at 4000 K is 95% of the $CO_2$ is thermally dissociated. The influx at 4000 K can be taken as a lower limit for the expected $CO_{out}$ flow under the assumption of no CO recombination. These values should be compared with the $CO_{out}$ flow measured experimentally in the simulated case, which is 1.1 L/min. The result is that the influx into the region where $CO_2$ is completely dissociated (0.94 L/min) is comparable with the $CO_{out}$ flux measured experimentally (1.1 L/min). The latter is however significantly smaller than the influx of $CO_2$ into the 3500 K region where dissociation of *ca.* 80 % is expected, with the optimum energy efficiency for thermal conversion (*ca.* 50 %, see figure 2.6).

The $CO_2$ flow into the 6000 K region (0.37 L/min) is much smaller than the $CO_{out}$ flow and not all the $CO_2$ is heated to 6000 K before being dissociated. However,

experimentally the energy efficiency results to be limited by the expected energy efficiency at 6000 K (see figure 6.14). It can be concluded that this fact is purely coincidental. Indeed the $CO_{out}$ flow is lower with respect to the $CO_2$ inflow into the thermally active region ($T_{gas} > 3000$ K at 1000 mbar). Such an effect could be due to the CO recombination into $CO_2$, which limits the $CO_{out}$ flux and causes an energy efficiency loss. The energy efficiency of the simulated case is 1 eV/molecule, well below the 2 eV/molecule, above which (at quasi-atmospheric pressure) there is experimental evidence of CO recombination. It can be concluded that a significant fraction of CO is lost in all experimental conditions. Thus it is possible to significantly improve the energy efficiency and conversion by reducing the CO recombination. However, the CO recombines within the discharge zone or in the early effluent (no significant differences between the CO concentration at 12 cm and at 2 m after the plasma is observed, see section 6.3.1), which makes challenging to mitigate the CO recombination. At pressures lower than atmospheric, but still, in the contracted regime, the thermally active region can be expected to be large. The radial temperature gradient can be supposed to be the same at 200 and 900 mbar since the plasma cross section does not depend on the pressure (see section 6.2). At lower pressure the $CO_2$ dissociation starts at lower temperatures (see figure 2.6), thus a larger region contributes to the $CO_2$ dissociation. Simulations at lower pressures (i.e. 200 mbar as well as 500 mbar) should be performed to confirm this hypothesis.

## 6.6 Summary

The 2.45 GHz microwave $CO_2$ plasma torch is characterized using OES, iCCD imaging and mass spectrometry in the pressure range between 60 mbar and quasi-atmospheric pressure (*ca.* 900 mbar). At pressures below *ca.* 120 mbar, the plasma is observed to fill the tube while at higher pressures the plasma contracts, occupying less than 10 % of the quartz tube cross section. The pressure at which the contraction occurs varies between 110 mbar at 2400 W of input power and 170 mbar at 750 W of input power. The gas temperature increases from 2000 K up to 3000 K between 30 mbar and *ca.* 110 mbar. At the contraction point, the gas temperature abruptly increases to 6000 K and remains constant at this value up to quasi-atmospheric pressure. For the gas temperatures reported in this study, the observed $CO_2$ conversion rates into CO can be explained through invoking thermal dissociation at pressures above 30 mbar. Moreover, the appearance of the $C_2$ Swan band is correlated with the formation of carbon atoms from CO dissociation that takes place thermally only at temperatures

above 5000 K. The highest energy efficiency (*ca.* 33 %) is measured at *ca.* 120 mbar concurrently with the plasma contraction.

Through the modelling of the gas dynamics (performed by Brochet et al. [161] and analyzed in this work), under the assumption of chemical composition in thermal equilibrium it has been possible to prove that the volume measured by optical emission spectroscopy is the region in which (most) of the microwave power is deposited. Such simulations predict (in the contracted regime) a gas temperature consistent with the experimentally measured values. The gas dynamics simulations performed under the assumption of single fluid evolving at thermal equilibrium allow the identification of a radial influx, driven by the temperature gradient, which determines the fraction of $CO_2$ converted into CO. The dominant effect of radial inward flux for $CO_2$ conversion is also consistent with the observation that at higher power more $CO_2$ is converted. The gas cooling dynamics are (likely) the most important limiting factor for avoiding CO losses due to recombination at high SEI (i.e. low flow and high power).

# 7 Temporal effects on $CO_2$ conversion in microwave plasma

In section 6 the dominant mechanism of $CO_2$ conversion to CO has been identified as thermal dissociation. The factors limiting the energy efficiency and conversion are the heating of the gas (that goes up to 6000 K) far above the optimum for thermal dissociation or electron impact dissociation and the flow dynamics driven by it, which are responsible for the inward flow of $CO_2$. The latter is the fraction of $CO_2$ converted and it can be influenced only by changing its driving force: the temperature gradients. The pulsing of the power source in microwave $CO_2$ plasma is investigated in section 7.1 as possible means to access different dissociation mechanism than the thermal dissociation and to improve the energy efficiency.

In previous experiments, van den Bekerom et al. [152] found for a microwave plasma torch, in the expanded regime, an improvement of the energy efficiency of the conversion (less than a factor 2). The power pulsing was performed at 5 kHz frequency in pressure range 30-160 mbar of the microwave with a duty cycle 20-90 %. The experiments were performed at fixed average power (80 W) and varying the duty cycle and the peak power accordingly. In the same setup, the investigation of the rotational and vibrational temperature of the $CO_2$ molecule via Raman scattering performed in a pulsed microwave discharge by Van den Bekerom et al. [162] shows that at 25 mbar a non-equilibrium condition between the vibrational temperature and gas temperature is achieved. In DC pulsed discharges at even lower pressure (1-7 mbar), a strong non-equilibrium between the vibrational temperature and gas temperature can be sustained for even longer times up to 5 ms [163, 164]. Moreover Klarenaar et al. [163] observed that the non-equilibrium decreases at higher pressure. However, Klerenaar et al. [163] were not able to directly relate the increase of conversion with the increase of non-equilibrium. No systematic investigations of the effect of pulsing the microwave power in the contracted regime are so far available in the literature. Verreycken et al. [165] investigated the influence of the microwave ON-time in pulsed experiments in a microwave plasma torch. In these experiments, carried out at 160 mbar, the

ON-time of the microwave pulses was varied between 50 ns and 50 $\mu$s, the measured conversion and energy efficiency are within the accuracy of the measurements, they are comparable with the CW conversion and energy efficiency. An investigation of the effect of pulsing the power in the pressure range 200-1000 mbar have been performed in this work and it is presented in section 7.1.

Britun et al. [34] measured an improvement of the conversion and energy efficiency in a surfaguide in pressure range 1-30 mbar when pulsing a microwave with the frequency of few kHz. The observed improvement has been explained by the synchronization of the flow with the microwave pulse. Theoretically, such an effect could also improve the energy efficiency at higher pressure, where increasing the $CO_2$ conversion is much more challenging (and relevant). Our investigation in this direction (performed at 200 mbar) are presented in section 7.1.1.

Vermeiren and Bogaerts [166] modelled a discharge at 100 mbar and with SEI of 1 eV/molecule with an ionization degree of $10^{-6}$ and a reduced electric field of 50 Td, focusing on the investigation of the effect of the OFF-time (i.e. inter-pulse time) and the ON-time. Increasing the inter-pulse time at fixed ON-time increases the energy efficiency of the discharge, for ON-time longer than 10 $\mu$s. In the model used by Vermeiren and Bogaerts [166], the effect is explained by a higher impact of vibrationally induced dissociation ($CO_2$ + M $\rightarrow$ CO + O + M , $CO_2$ + O $\rightarrow$ CO + $O_2$) due to a higher population of the highly vibrational excited $CO_2$ state in case $t_{off} \gg t_{on}$. In section 7.1.2 the effect of changing independently, the ON and OFF-time from 50 ns up to 200 $\mu$s are investigated at 20 mbar. To understand if, also in pulse mode, the conversion and energy efficiency are determined by the gas temperature and its gradients, the plasma volume (section 7.2) and gas temperature (section 7.3) are investigated.

## 7.1 $CO_2$ conversion in a pulsed microwave discharge

To evaluate the energy efficiency of the conversion in pulse experiments, but also to characterize the pulse, it is critical to determine the power coupled to the plasma. During a pulse, the total amount of power coupled into the plasma is determined by the pulse power shape and the duty cycle as:

$$P_{eff} = \int_0^{1/\nu} P_F(s) - P_R(s) ds \tag{7.1}$$

where $P_{eff}$ is the effective power coupled to the plasma, $\nu$ is the pulse frequency, $P_F$ the forward power and $P_R$ the reflected power. In case of square pulses equation 7.1

| Pressure/flow | 10 L/min | 20 L/min | 40 L/min |
|---|---|---|---|
| 200 mbar | 50% | 25% | 25% |
| >900 mbar | 82% | 60% | 55% |

Table 7.1: Minimum duty cycle that can be used to sustain a plasma at 1 kHz depending on pressure and flow.

is:

$$P_{eff} = DC(P_F - P_R) \tag{7.2}$$

where DC is the duty cycle. Differently to continuous operation, the microwaves power coupling to the plasma changes during the pulse. Thus, equation 7.2 is only an estimation of the power effectively coupled to the plasma. The reflected power shows a strong variation at the beginning of the pulse, during the build-up phase of the electron density. The fraction of microwave power reflected can be significant at a low duty cycle. The reflected power, as well as the forward power, have been measured using the bidirectional coupler and microwave diodes. The reported average powers in pulse mode are the effective mean power coupled to the plasma. In all cases at the beginning of the pulse, a peak of reflected power can be observed (see figure 7.5 for instance), such behaviour is expected: at the beginning of the discharge the electron density and temperature profiles evolve quickly, causing a change in the plasma impedance [29]. The impedance of the waveguide is matched to the steady state plasma impedance (reached after *ca.* 100 $\mu$s) thus there is a mismatch between the waveguide impedance and the impedance of the plasma during the build-up phase (the first 100 $\mu$s). This way of matching the power maximizes the power deposited into the plasma.

The duty cycle is changed to investigate the conversion as a function of the SEI. The minimum duty cycle that can be used is a function of the flow and pressure. Table 7.1 shows the minimum duty cycle at different flows and pressure at a repetition rate of 1 kHz. The higher the flow the lower the duty cycle that can be achieved. The minimum duty cycle cannot be correlated to a minimum power needed to sustain a $CO_2$ microwave plasma that typically increases at higher flows. The reason for this behaviour is not understood.

Figure 7.1 *(a)* and *(b)* show the comparison between the conversion measured in pulsed microwave regime and continuous mode plotted as a function of the specific energy input. The latter is calculated using the effective power defined by equation 7.2. The measurements are performed at the frequency of 1 kHz. The pulse measurements are performed at flows of 10 L/min, 20 L/min and 40 L/min and fixed pulsed power

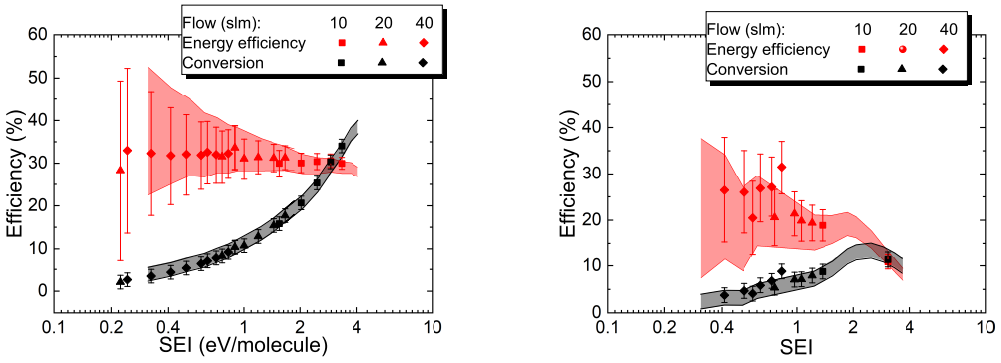


(a) *200 mbar* (b) *900 mbar*

Figure 7.1: Energy efficiency (red dots) and conversion (black dots) measured with a pulse frequency of 1 kHz at quasi-atmospheric pressure *(a)* and at 200 mbar *(b)*. The dashed lines represent the conversion and energy efficiency measured in CW mode. The pulse power is kept at 2700 W and the duty cycle has been varied to change the effective power coupled into the plasma. The SEI is calculated using the effective power.

of 2700 W. The measured conversion and energy efficiencies (shown in chapter 6) in the continuous mode are shown by the dashed lines. The conversion measured and energy efficiency are equal within the error-bars in pulsed and CW modes.

In conclusion, no beneficial effect on the conversion or energy efficiency is observed for the investigated parameter range.

### 7.1.1 Plasma-flow synchronization

The $CO_2$ injected at the bottom of the resonator has an axial velocity that can vary from sub m/s velocity up to a few m/s depending on the flow and pressure (this velocity can be obtained by considering flux conservation and the quartz tube cross section, detailed simulations of gas flow dynamics are presented in section 6.5). The time the incoming gas needs to axially cross the resonator is in the order of a few ms for the conditions investigated in this work.

The time needed to dissociate $CO_2$ is significantly lower (*ca.* $\mu$s), and it follows that energy is spent to keep the gas mixture hot without producing additional CO from $CO_2$ dissociation. If the microwave pulse can be synchronized with the gas flow the energy efficiency can be improved as demonstrated by Britun et al. [34] although at significantly lower pressures and in conditions of electron impact dissociation. Even if in the investigated regime thermal dissociation is dominant, the power deposition can be optimized to treat only once the injected gas. With a gas velocity of about few m/s

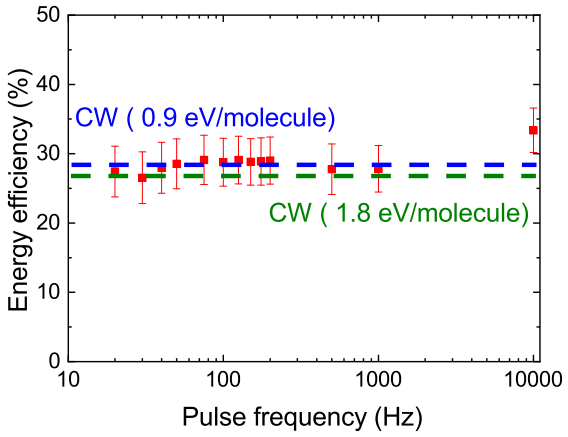


Figure 7.2: Energy efficiency as a function of the pulsing frequency, between 20 Hz and 10 kHz with a duty cycle was fixed to 50 % and the peak power 2700 W. Measurements are carried out at 200 mbar, 20 L/min $CO_2$ flow. The energy efficiency obtained in CW mode is indicated by the dashed lines at SEI equivalent to the peak power (1.8 eV/molecule) or average power (0.9 eV/molecule).

the optimal pulsing frequency is in the order of hundreds of Hz. Figure 7.2 shows the energy efficiency measured at 200 mbar, and 20 L/min of $CO_2$ flow. The conversion depends on the power coupled to the plasma, which changes with the frequency, because of the different impedance matching. It follows that comparing the changes of conversion with the frequency is misleading since the changes in conversion are due to the different power coupled to the plasma and not to a frequency effect. The pulse power was kept constant at 2700 W and the duty cycle was fixed at 50 %. The axial gas velocity in this condition is 3.14 m/s, the resulting refreshment rate in the resonator is *ca.* 80 Hz. The microwave pulse frequency is changed from 20 Hz up to 10 kHz. The energy efficiency is found to be constants *ca.* 30 % and independent from the frequency used.

It can be concluded that synchronizing the microwave pulse with the gas flow does not lead to any improvement of the torch performances.

### 7.1.2 Effect of fast pulsing on the conversion

To have a complete overview of the effect of pulsing on $CO_2$ microwave discharges, ns short pulses should be investigated. Such short pulses should favour the vibrational excitation of the $CO_2$ molecule, avoiding excessive gas heating. The effect of ns scale pulsing is investigated in the surfaguide experimental setup described in section 4.2.2. The experiments have been carried out in collaboration with the Karlsruhe Institute of Technology. Such choice is made because the experiments were carried out using a solid-state power supply, which has a maximum peak power of 300 W, too low to sustain a plasma in the plasma torch described in chapter 4.2.

Figure 7.3 *(a)* shows the frequency variation performed at pressures of 20 and 60 mbar with a total $CO_2$ flow of 0.05 L/min. The peak power is 300 W and the duty cycle is 50 %. The energy efficiency does not show any (significant) variation with the frequency at a fixed duty cycle. They are comparable to the ones measured in continuous mode. The flow induced refreshment rate (i.e. a synchronization between flow and microwave pulse) invoked by Britun et al. [34] to explain the increase of energy efficiency and conversion at low repetition rate is not observed in our setup. However, the axial gas velocity at 0.05 L/min is 0.83 m/s, which results in a refreshing rate of 40 Hz. Therefore, a sufficiently low repetition rate to observe an increase in energy efficiency cannot be achieved with the used power supply, which has a minimum repetition rate of 5 kHz.

Figure 7.3 *(b)* shows an independent variation of the ON/OFF-time at 5 mbar and 0.05 L/min. The ON-time is fixed at 2 $\mu$s and the OFF-time varied between 100 ns and 200 $\mu$s (red dots). Similarly, the OFF-time is fixed to 200 $\mu$s and the ON-time changed between 200 ns and 200 $\mu$s (magenta dots). In both cases, 300 W of peak power have been used. The observed increase is about a factor 2 in energy efficiency (it should be noted that the conversion decreases at increasing energy efficiencies). Vermeiren and Bogaerts [166] modelled a discharge at 100 mbar and with SEI of 1 eV/molecule with an ionization degree of $10^{-6}$ and a reducing electric field of 50 Td, focusing on the investigation of the effect of the OFF-time (i.e. inter-pulse time) and the ON-time. Increasing the inter-pulse time at fixed ON-time results in an increase of the energy efficiency of the discharge, for ON-time longer than 10 $\mu$s. A similar effect is observed in this work: the energy efficiency is increased at lower duty cycle (higher OFF-time at fixed ON-time). The source of such increase have been identified, in the model used by Vermeiren and Bogaerts [166], as a higher impact of vibrationally induced dissociation ($CO_2 + M \rightarrow CO + O + M$ , $CO_2 + O \rightarrow CO + O_2$) due to an higher population of the highly vibrational excited $CO_2$ state in case $t_{off} \gg t_{on}$. The observed trends are consistent with the observation of van den Bekerom et al. [155]: they observed that the lower the duty cycle, the higher the energy efficiency. Moreover, at lower pressure, the energy efficiency is less sensitive to the duty cycle. At 5 mbar the energy efficiency has been observed to increase from 2 % in CW mode to 4 % at duty cycle 0.2 (see figure 7.3 *(b)*), the same change that is observed by van den Bekerom et al. at 30 mbar.

In the expanded regime of the microwave plasma torch (i.e. at low pressure) improvement of the energy efficiency is expected when an OFF-time much longer than the ON-time is used, similarly to what it is observed in the surfaguide. On the

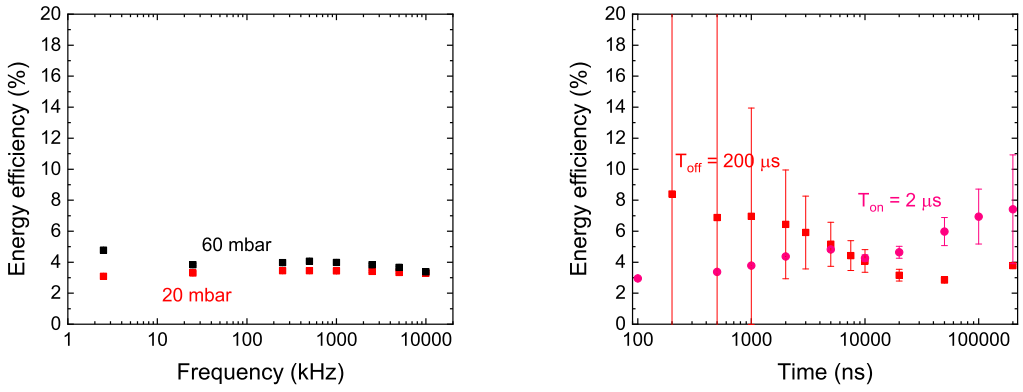


(a) (b)

Figure 7.3: *(a)* energy efficiency as a function of the frequency at fixed duty cycle of 50 % at 0.05 L/min and 20 mbar (red dots) and 60 mbar (black dots). The error-bars are below 0.5 % to small to be appreciated on such scale. *(b)* variation of the ON-time at fixed OFF-time (red dots) and the variation of the OFF-time at fixed ON-time (magenta dots). All measurements are performed on the surfaguide setup.

other hand, in the contracted regime (high pressure) pulsing the microwave does not have any beneficial effect on energy efficiency. Indeed, the gas dynamics simulations show that the $CO_2$ inflow is driven by the temperature gradient (see section 6.1). If the position of the gradients (i.e. the plasma volume) and their magnitude (i.e. the gas temperature) does not change the influx is the same. The fraction of gas that interacts with the plasma per unit of time is not directly correlated with the axial gas velocity, but rather with the plasma size and the gas temperature. Indeed, in CW a change of axial velocity (higher $CO_2$ flow) does not produce a change in the $CO_{out}$ flow. Even at relatively slow pulse rate, these are not changed and the fraction of injected flow driven into the plasma depends, at a fixed pressure, just on the average power, which determines the position of the temperature gradients (namely the power deposition volume, see section 6.2). In a microwave plasma torch pulsing the microwave does not have any beneficial effect on the energy efficiency when the plasma is in the contracted regime, since the gas flow dynamics, which determines the conversion, is driven by the temperature gradients established by the plasma itself.

The results obtained by pulsing the plasma strengthen the distinction between the two regimes observed in chapter 6: in the contracted regime it is not possible to influence strongly the $CO_2$ conversion (thus the flow dynamics) by pulsing the microwave, while at low pressure (in the expanded regime) pulsing can improve the energy efficiency.

## 7.2 Plasma volume variation in pulsed mode

In sections 6.2 and 6.5 the effect and the relation between plasma volume and $CO_2$ influx into the plasma of the power to plasma volume have been discussed. The $CO_{out}$ flow, which is found to depend only on the power at a fixed pressure, is closely linked to the inward flow of $CO_2$. Thus, whenever (at the same pressure) the same $CO_{out}$ is observed (i.e. same conversion) the same inflow into the plasma volume can be expected. In this view, the equivalence between the conversion obtained in pulsed measurements and CW mode at high pressure (see section 7.1) can be explained by an equivalence between the influx of $CO_2$, for the power coupled into the plasma, which requires an equivalence between the hot region in CW and pulsed regime. In this section, the evolution of the plasma volume during a pulse is investigated using iCCD imaging. As in section 6.2 both plasma diameter and length are measured. However, the iCCD camera cannot be used at quasi-atmospheric pressure to measure the plasma diameter, because of the microwave power radiated into the room during microwave pulsing experiments is significant ($> 100 \mu W cm^{-2}$) and at quasi-atmospheric pressure, it represents a threat to the iCCD camera (far from being dangerous). For this reason, the plasma cross section is measured only at reduced pressures (500 mbar and 200 mbar). The plasma length is measured at a higher distance from the setup and also at quasi-atmospheric pressure measurements can be performed without damaging the iCCD camera.

The measurements of the emission using an iCCD camera during a pulse allow to distinguish two different sources of light: the $C_2$ emission (which is the only one measured in CW) and the continuum recombination radiation. The $C_2$ emission decays in the pulse afterglow within the first few hundreds of $\mu$s (see figure 7.14), the atomic carbon and oxygen atoms follow the $C_2$ emission decay. Plasma emission can be still measured using the iCCD at the end of the pulse. Figure 7.4 shows the emission measured in the resonator at 900 $\mu$s from the beginning of the pulse at 200 mbar, with a duty cycle of 55 % and peak power of 2700 W. No emission from the $C_2$ molecule can be detected but a continuum emission can be measured. This emission is identified as the continuum emission originated from CO and O recombination (see section 5.1). In particular, most of the light collected originates from CO and O recombination, since the objective used (standard glass) filters out all wavelength below 380 nm. As discussed by Peeters et al. [84] in the visible the continuum emission is mostly originated from CO recombination rather than O recombination. As a result, two different radii and length can be identified: one is the power deposition profile, visible

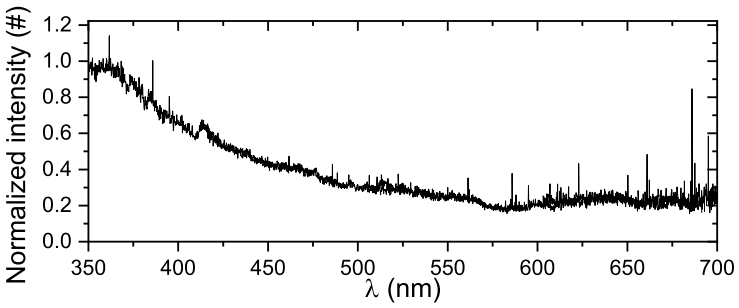


Figure 7.4: Optical emission measured in the resonator at 900 $\mu$s from the beginning of the pulse. The measurements are performed at a pressure of 200 mbar, 55 % duty cycle and 1 kHz repetition frequency, peak power 2700 W and 20 L/min of $CO_2$ flow. The peaks that can be seen in the spectrum are due to the noise of the iCCD camera.

during the pulse ON-phase, and the other is the recombination region, visible during the OFF-phase. The width and length of the continuous emission are generally wider than the power deposition profile, however, the continuous emission has a much lower intensity than the $C_2$ emission. It follows that the plasma diameter and length are narrower and shorter during a pulse.

Figures 7.5 *(a)* and *(b)* show the time evolution of the length and diameter during a pulse at 200 mbar and 20 L/min. The (set) peak power is 2700 W, two duty cycles are investigated 55 % (figure *(a)*) and 75 % (figure *(b)*). The evolution of the forward and reflected power during the pulse is shown in the top section of the plots. To compare the plasma size in CW and pulsed mode the plasma lengths and diameters measured in continuous operation are represented by the dashed lines in figure 7.5 *(a)* and *(b)*. The continuous mode measurements are performed at the same pressure and flow. In figure *(a)* two values of length measured in CW are compared with the pulse length: at a power of 1356 W, the average power coupled to the plasma in pulsed mode and at a power of 2456 W, the peak power used in pulse mode. The peak power is estimated from the measurements of the forward power via the relation peak power $= \frac{AveragePower}{DutyCycle}$. The plasma diameter converges in pulsed mode to the CW diameter value measured in CW operation at the peak power. On the other hand, the length of the pulsed plasma corresponds to the CW length associated with the average pulsed power. The same correspondence can be observed in figure 7.5 *(b)*. As consequence, the length of the plasma correlates with the measured conversion (which corresponds to the conversion measure in CW at power equivalent to the average power) and the diameter does not. The diameter reaches its steady state value faster than the length, in the case of duty cycle 55 % (figure 7.5 *(b)*), the diameter has already reached its equilibrium position after 200 $\mu$s, while the plasma

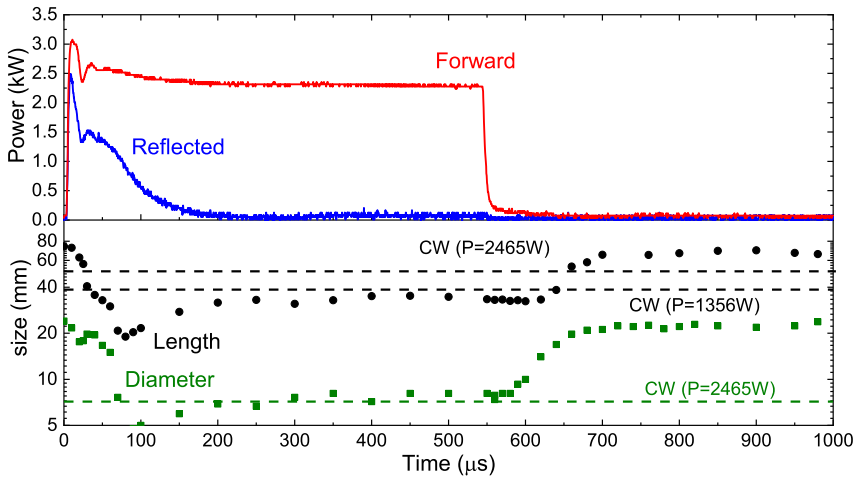


(a) *200 mbar, Duty Cycle = 55 %*

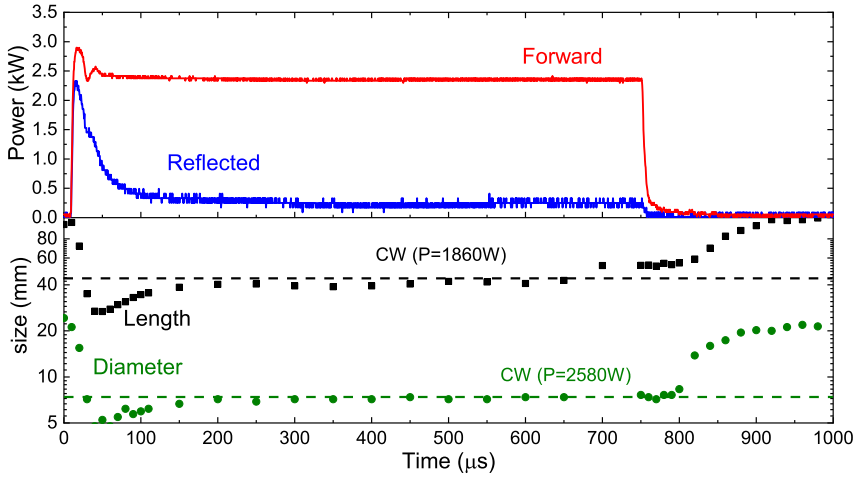


(b) *200 mbar, Duty Cycle = 75 %*

Figure 7.5: Evolution of the plasma diameter (green dots) and the plasma length (black dots) during a pulse. The forward (red line) and reflected (blue line) power are shown in the top part of the graph. The frequency of the pulse is 1 kHz, the set peak power is 2700 W and the duty cycle is 55 % *(a)* and 75 % *(b)*. The measurements are performed at a pressure of 200 mbar with an injected $CO_2$ flow of 20 L/min. The CW values of the diameter and length are indicated by the dashed lines, the powers are specified in the plots.

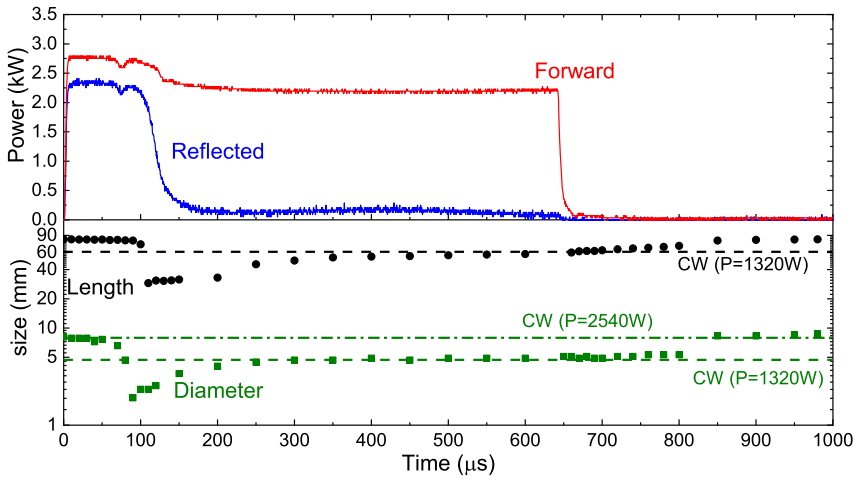


(a) *500 mbar, Duty Cycle = 65 %*

Figure 7.6: Evolution of the plasma diameter (green dots) and the plasma length (black dots) during a pulse. The forward (red line) and reflected (blue line) power are shown in the top part of the graph. The set peak power is 2700 W, the duty cycle is 65 %. The measurements are performed at a pressure of 500 mbar with an injected $CO_2$ flow of 20 L/min. The CW value of the diameter and length are indicated by the dashed lines. In the case of the diameter two values are shown the peak power (2540 W) and the average power (1320 W).

length is still growing, until 300 $\mu$s. Such an effect is not understood and should be further investigated.

The size of the recombination region is significantly larger than the power deposition zone. The recombination of the CO into $CO_2$ takes place up to the wall of the quartz tube (the maximum diameter measured is about 24 mm against an inner diameter of 26 mm, see figure 7.5) and the maximum size is independent of the average power coupled into the plasma. A possibility is that, similarly to the diameter of the power deposition profile, the recombination zone diameter depends on the peak power. The length of the recombination zone instead depends on the average power coupled to the plasma, as the latter increases, the recombining plasma length also increases. Such behaviour is reasonable: when more power is coupled into the plasma a the cooling is slower due to the mixing between the hot core and the cold $CO_2$ swirling gas in the outer region.

Figure 7.6 *(a)* shows the behaviour of the diameter and the length during the pulsed at 500 mbar, 20 L/min. The (set) peak power is 2700 W and the duty cycle 65 % (the minimum achievable). The measured forward power is *ca.* 1640 W which results in peak power of 2540 W, the average power coupled to the plasma after having

subtracted the reflected power is *ca.* 1320 W. The behaviour of the reflected power, that is shown in the top part of the figure is reproducible and corresponds to delayed ignition of the plasma, that happens at *ca.* 90 $\mu$s after the application of the power. The plasma length is found also at 500 mbar to converge to the one measured in CW at the average power. However, the measured diameter converges to a value slightly higher than the one expected for the average power of 1320 W.

Since the measurement are made with different alignment the systematic errors differ, thus the comparison carried out in figures 7.6 and 7.5 may be misleading. The measurements of the plasma diameter may be affected by significant systematic errors due to several factors: the camera alignment, the calibration of the pixel size and the oscillation of the light intensity. An error of *ca.* 1 mm on the diameter (= 4 pixels) is possible (although it can be even more in some condition). For such reason, additional experiments have been carried out: CW and pulsed measurements are carried out with the same camera alignment to eliminate the systematic errors. The results are shown in table 7.2, where the diameter in pulsed measurements is measured at the end of the ON-time, after the equilibrium is reached. The CW experiments are performed at the set peak power (2700 W), thus an additional uncertainty (on the real peak power) is originated here. The trends observed in figures 7.5 *(a)* and *(b)* are confirmed: at 500 mbar however the diameter converges to a value between the peak power and the average power. In conclusion in pulse mode, the plasma diameter in the plasma phase is equivalent to the plasma diameter in the continuous mode at a power equal to the peak power.

| Pressure | DC | CW at Peak Power | CW at average Power | Pulse mode |
|---|---|---|---|---|
| 200 mbar | 55 % | 7.1± 0.5 mm | 4.3± 0.5 mm | 7.2± 0.5 mm |
| 200 mbar | 75 % | 7.1± 0.5 mm | 5.6± 0.5 mm | 6.8± 0.5 mm |
| 500 mbar | 65 % | 7.2± 0.5 mm | 4.2± 0.5 mm | 5.6± 0.5 mm |

Table 7.2: Comparison between the plasma diameter in pulsed mode at 2700 W and in CW mode.

Figure 7.7 *(a)* shows the behaviour of the plasma length during the pulse at 900 mbar, 20 L/min. The (set) peak power is 2700 W and the duty cycle 65 % (the minimum achievable). The measured forward power is *ca.* 1640 W which results in a peak power of *ca.* 2540 W, the average power coupled to the plasma after having subtracted the reflected power is *ca.* 1605 W. The evolution of the length of the power deposition zone at 900 mbar displays the same behaviour such as at 500 and 200 mbar (figures 7.5 and 7.6).

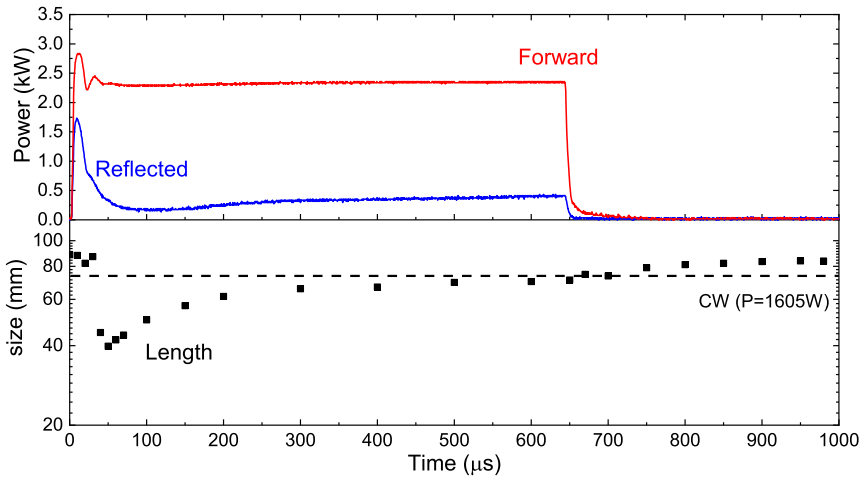


(a) *900 mbar, Duty Cycle = 65 %*

Figure 7.7: Evolution of the plasma length (black dots) during a pulse. The forward (red line) and reflected (blue line) power are shown in the top part of the graph. The set peak power is 2700 W, the duty cycle is 65 %. The measurements are performed at a pressure of 900 mbar with an injected flow of 20 L/min. The CW value of the length is indicated by the dashed lines, the power is specified in the plots.

The analysis of the recombination volume, visible during the OFF-phase and determined in the same way as the power deposition volume, reveals that its diameter decreases for increasing pressures (see figure 7.8). To have significant emission from the recombination reaction $CO+O+M \rightarrow CO_2^* + M \rightarrow CO_2 + h\nu$, two conditions must be fulfilled: atomic oxygen and CO must be present and the temperature should be higher than 1500 K [84]. The thermal dissociation of $CO_2$ into CO takes place (with a significant dissociation degree) at a gas temperature above 2000 K. Therefore, the region where the recombination continuum is not observed is also inactive for the $CO_2$ dissociation. Therefore, the region where recombination continuum is observed represents an upper limit for the region where thermal dissociation can take place, which is larger than the power deposition profile. During the OFF-phase of the pulse, the recombination radius is observed to reach a steady value, indicating that the volume in which the recombination takes place does not change throughout the OFF-phase. The slow increase of diameter observed at the end of the pulse is an artefact of the analysis method the $C_2$ emission starts to decay at the end of the pulse, which causes the ratio between the continuum emission and the $C_2$ emission to change. In fact, the lower the $C_2$ emission the more the continuum contributes to total intensity and eventually it affects the calculations of the plasma diameter. This is supported by the fact that the decay time of the $C_2$ emission is consistent with the rise time

| Pressure | DC | Power deposition | Recombination |
|---|---|---|---|
| 200 mbar | 55 % | 35 mm | 70 mm |
| 500 mbar | 65 % | 58 mm | 81 mm |
| 900 mbar | 65 % | 71 mm | 83 mm |

Table 7.3: Comparison between the length of the recombination zone and the plasma length.

of the diameter. Table 7.3 shows that the recombination zone is longer at higher pressure, however also the power deposition region elongates at higher pressure. The difference of length between the power deposition profile and the recombination zone reduces at increasing pressures. This can be explained considering that the cooling in the effluent is driven by the mixing between the hot and cold gas and the end of the plasma. The main mechanism for gas cooling is the turbulent mixing between hot and cold gas, which is expected to be less efficient at lower pressure, leading to a slower cooling and consequentially to a longer recombination region. This picture is consistent with the measurements of Belov et al. [151], where a thermocouple was used to measure the gas temperature in the effluent of a $CO_2$ microwave plasma, finding a lower gas temperature at lower pressure.

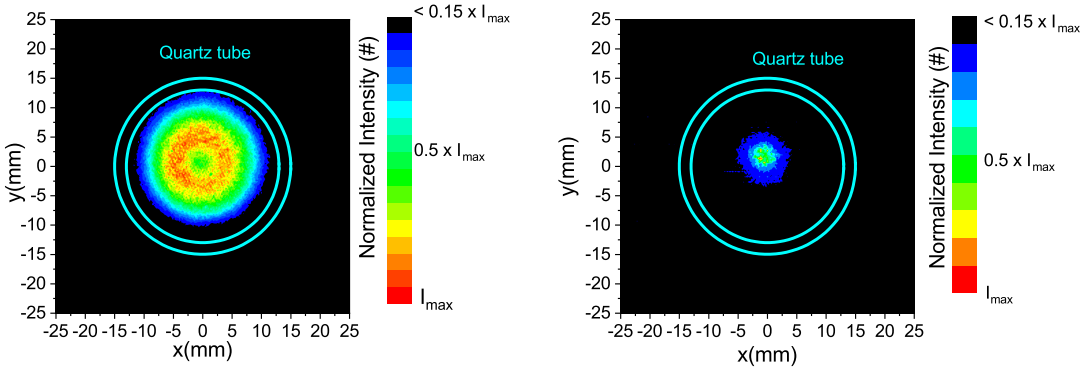


(a) *200 mbar* (b) *500 mbar*

Figure 7.8: iCCD image of the plasma cross section at a delay of 980 $\mu$s, thus at the end of the afterglow. The measurements are performed at 1 kHz frequency, peak power of 2700 W and with a $CO_2$ flow of 20 L/min. Figure *(a)* is acquired at 200 mbar and duty cycle 55 %. Figure *(b)* is acquired at 500 mbar and duty cycle 65 %. Note that the emission intensity between the two figures cannot be compared.

The recombination zone shrinks from a diameter of 24 mm at 200 mbar to 10 mm at 500 mbar. Thus, the inactive zone of the plasma is enlarging at higher pressure. This can explain the better plasma performance of the torch at lower pressure.

Figures 7.8 *(a)* (200 mbar, 20 L/min, 1356 W) and *(b)* (500 mbar, 20 L/min, 1320 W) shows the radial imaging of the light emission at the end of the pulse (i.e. 980 $\mu$s). The continuum emission observed in figure 7.8 *(b)*, presents a depletion in the center, that can be explained as a lower CO and O density in the center. This is caused by faster recombination of CO and O at the beginning of the afterglow, that will results in a lower emission from the center in the recombination continuum. At 550 $\mu$s the temperature in the center of the quartz tube is *ca.* 6000 K. Right after the end of the ON-phase (550 $\mu$s), the continuum emission is Gaussian like and only after few hundreds of $\mu$s it becomes hollow, indicating a quicker loss of CO in the center.

The pulsed measurements suggest that the plasma emission measured in CW by iCCD imaging is a superimposition of the CO recombination continuum and the molecular ro-vibrational spectrum (this would also justify the fit of the axially integrated plasma emission via two 2D Gaussian functions). The CO emission is weaker than the $C_2$ emission, therefore when measuring the plasma cross section in the expanded regime, the contribution of the recombination continuum may be significant (if not dominant). The recombination continuum measured at the end of the pulse at 200 mbar fills the quartz tube as the plasma volume in the expanded regime (see section 6.1). Such observation implies than the active zone of the plasma does not change (significantly) at the transition between the expanded regime (i.e. below 110 mbar) and the contracted regime (i.e. above 120 mbar) and decreases at higher pressures consistently with the behaviour of the conversion, that does not present any abrupt change at the regime transition.

Similarly to the radial extension of the recombination at the end of the pulse also the axial extension of the recombination is visible. Figures 7.9 *(a)*, *(b)*, *(c)* shows the axial distribution of the continuum emission at 200, 500 and 900 mbar respectively. The recombination of CO into $CO_2$ is a three body process, as such its rate increases strongly increasing the pressure. Indeed, the plasma emission is observed to increase at the pulse end with pressure: at 200 mbar (figure 7.9 *(a)*) it is 0.1 counts/ns, at 500 mbar (figure 7.9 *(b)*) it is 0.3 counts/ns and at 900 mbar (figure 7.9 *(c)*) 1.8 counts/ns. However, the magnitude of the recombination from figures 7.9 *(a)*, *(b)*, *(c)* are not comparable, since the recombination emission is wavelength dependent and its shape changes with the temperatures of the CO and O [84] and the iCCD camera is not calibrated. The picture serves to compare the recombination region size as function of the pressure. As mention previously the turbulent cooling is the main mechanism for the gas cooling and at 200 mbar is expected to be less efficient than at high pressure, which results in a longer recombination region than the power

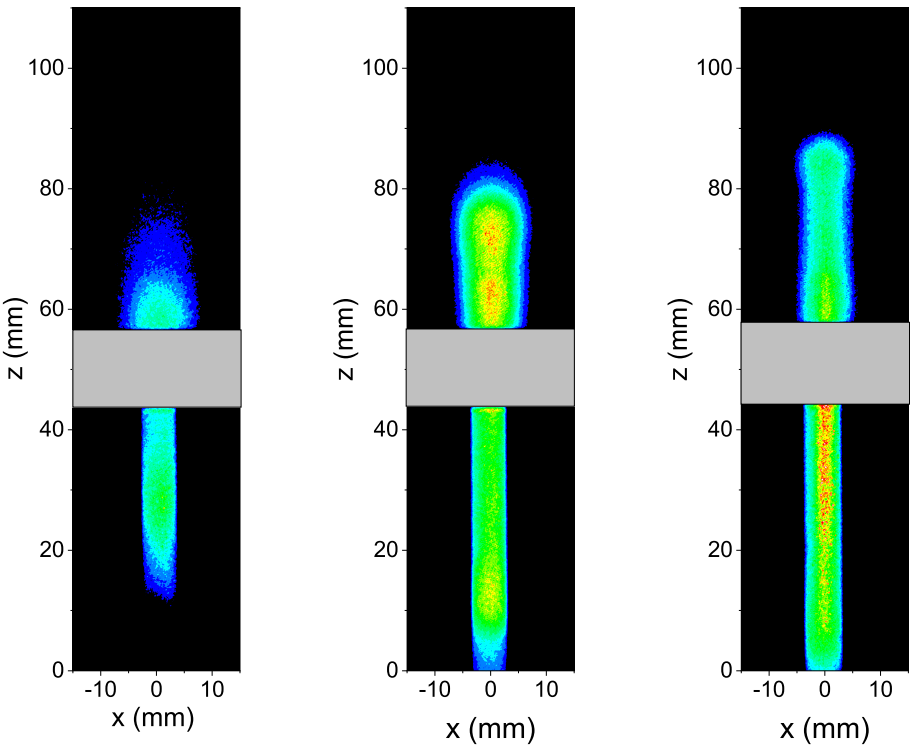


(a) *200 mbar* (b) *500 mbar* (c) *900 mbar*

Figure 7.9: iCCD image of the plasma axial elongation at a delay of 980 $\mu$s. The measurements are performed at 1 kHz frequency, peak power of 2700 W and with a $CO_2$ flow of 20 L/min. Figure *(a)* is acquired at 200 mbar and duty cycle 55 %. Figure *(b)* is acquired at 500 mbar and duty cycle 65 %. Figure *(c)* is acquired at 900 mbar and duty cycle 65 %. Note that the emission intensity between the three figures cannot be compared.

deposition zone. The cooling of the effluent gas should not be confused with the cooling rates measured in section 7.3, which are the cooling rate of the plasma core. Although the cooling of the gas in the effluent is faster at higher pressure (that is why the recombination zone approaches the plasma zone at higher pressures), the CO recombination reactions are slower at lower pressure, since CO recombination is a 3-body process. On the other hand, the faster cooling reduces the region in which thermal dissociation of $CO_2$ happens, lowering the efficiency.

## 7.3 Cooling rates

The pulsing of the plasma allows investigating the time scales of the plasma evolution through the investigation of the optical emission decay. The measured emission allows to calculate the temperature evolution in the region where the molecular emission is generated and to obtain information on the gas cooling dynamics. The emission of the $C_2$ Swan band is analyzed in the contracted regime. In the contracted regime 0.3 L/min of $N_2$ are also added to measure the CN violet band in addition to the $C_2$ Swan band, whose higher intensity allows to measure better the temperature decay in the afterglow compared to the $C_2$ Swan band.

All spectra are acquired in the center of the quartz tube (r=0 mm) resonator at about 35 mm height (z=35 mm), the collection area is a circle of *ca.* 5 mm diameter. This choice is done to measure the maximum possible signal, which is critical in the pulse afterglow. In the contracted regime all the spectra have been acquired using the iCCD and the ANDOR spectrometer with 1200 l/mm grating. The analysis of the Swan band has been carried out only on the $\Delta\nu = 0$ transition group between 485 nm and 517 nm. As discussed by Carbone et al. [54] this band allows to properly determine the rotational temperature but results insufficient to determine the vibrational temperature. The latter is fixed to 6000 K as determined from the CW operation. This transition group is so weakly dependent on the vibrational temperature that the set value is not influencing the final gas temperature resulting from the analysis [54]. The CN violet band emission has been analyzed between 360 and 400 nm. In this region, there is a sufficient number of vibrational transitions to determine also the vibrational temperature. The analyzed part of the CO Ångström band is the 0-1 transition, between 470 and 484 nm, which is sufficient to measure the rotational temperature. The observed temperature decay is generally small and comparable to the error-bars. However, the errors on the temperature determination are mostly systematic [54]. If the analysis is carried out consistently between different spectra,

only the statistical errors are relevant for calculating the temperature decay, those are only a few tens of kelvin smaller than the systematic errors on the temperature determination. Using the temperature decay in the afterglow it is possible to estimate the initial cooling rate of the central region of the plasma by fitting the linear decay of temperature observed.

### 7.3.1 Gas temperature decay in the plasma afterglow

Figure 7.10 shows the gas temperature evolution during a pulse at 28 mbar and 2 L/min, the set peak power is 1800 W with a duty cycle of 30 %. At higher peak power the heat losses to the quartz tube are large and the risk of damages are high. The gas temperature is observed to increase during the pulse from 1500 K up to 2300 K, and at the end of the pulse, the measured gas temperature is comparable to the 2000 K measured in similar condition in CW, although higher. Comparatively van den Bekerom et al. [155] observed an increase of the gas temperature of *ca.* 200 K (from an initial value of 1700 K) when the plasma is pulsed at 30 mbar and with an average microwave power of 80 W. Although the power used (in figure 7.10) is 10 times higher than the one used by van den Bekerom [155] the gas temperature measured are comparable. This indicates that most of the power is spent in $CO_2$ dissociation by enlarging the plasma, rather than in increasing the gas temperature. The observation of the temperature decay in the afterglow is not possible since the *Å*ngström band is not visible any longer as soon as the microwave generation is stopped. Such behaviour is expected since the $CO(B^1\Sigma^+)$ state is originated from electron impact collisions. Electrons recombine in a time scales in the order of ns as soon as the microwave power is switched off.

Figure 7.11 shows the normalized intensity and rotational and vibrational temperature behaviour at 900 mbar, 20 L/min during a pulse with 2700 W of (set) peak power and a duty cycle 65 %. A delay of *ca.* 20 $\mu$s between the trigger signal (i.e. the reference time) and the microwave power pulse is observed due to the microwave power supply electronics. At the beginning of the pulse, the $C_2$ rotational distribution is observed already at a temperature above 5000 K and reaches the equilibrium temperature 6000 K within the first 60 $\mu$s from the pulse beginning. Such observation is consistent with the fact that $C_2$ forms thermally in a significant amount only at a temperature above 5000 K (using CEA as in chapter 6). Den Harder et al. [52] calculates the equilibration time of the CO molecule at different gas temperatures, at a temperature above 4500 K an equilibration time shorter than 10 $\mu$s is expected, which is consistent with the picture of $C_2$ emission occurring at thermal equilibrium.

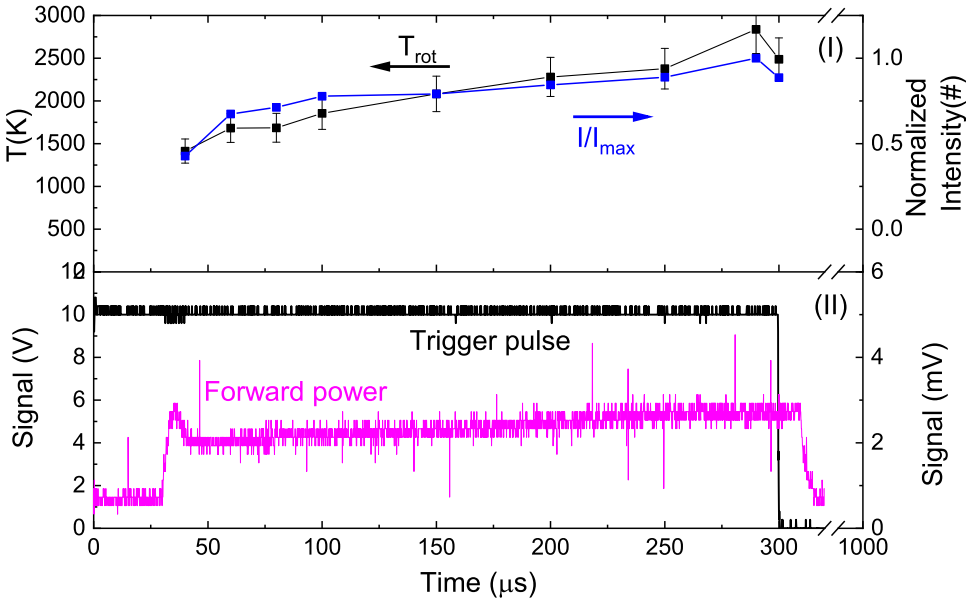


Figure 7.10: Evolution of the gas temperature, determined from the emission of the $CO(B^1\Sigma^+)$ state, during a pulsed microwave discharge with peak power of 1800 W and duty cycle of 30 % at 28 mbar, 3 L/min (expanded regime). Forward and reflected power are indicated in the bottom plot.

Van de Steeg et al. [167] observed experimentally an equilibration time of 60 $\mu$s for the gas temperature in $CO_2$ microwave discharges at 25 mbar using Raman scattering as diagnostic. A much faster equilibration is expected at atmospheric pressure because of the much faster collision frequency due to the higher density.

The temperature stays constant during the pulse at *ca.* 6000 K, the same temperature observed in the CW regime. In the afterglow, the gas temperature decay can be observed for the first 200 $\mu$s. The $C_2$ emission intensity decays as well and after *ca.* 200 $\mu$s the $C_2$ emission cannot be detected any longer. The intensity decay in the afterglow is not linked to a reduction of the plasma size, as confirmed by iCCD imaging, but to a real decrease in the emissivity. Using the temperature decay in the afterglow it is possible to estimate the initial cooling rate of the central region of the plasma.

To confirm that the measured decay rate is not an artefact, nitrogen is added to the $CO_2$ gas to measure the CN violet band. The rotational temperature of the CN band is a few hundreds of degree higher than the $C_2$ (5800 K vs 6300 K), however, they are within the systematic error-bars. The temperature decay rate measured in the effluent for the CN and $C_2$ emission is $3.0 \pm 0.2 \cdot 10^6$ K/s and $2.8 \pm 0.55 \cdot 10^6$ K/s respectively. The rotational temperature and vibrational temperatures of the $CN(B^2\Sigma^+)$ states

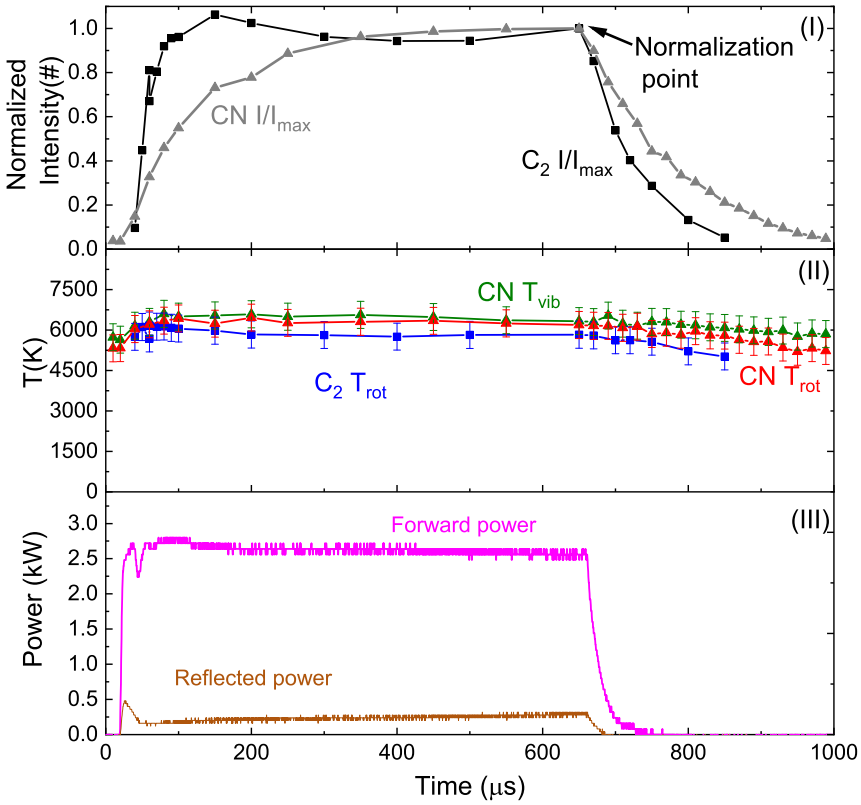


Figure 7.11: Evolution of the gas temperature during a pulse at atmospheric pressure, 20 L/min (+0.3 L/min $N_2$ in the CN emission case), the peak power of 2700 W and duty cycle of 65 %. Plot I shows the normalized particle density of the $C_2(d^3\Pi_g)$ (black square) and $CN(B^2\Sigma^+)$ (grey triangles). Plot II shows the measurement of the gas temperature (= rotational temperature) from the $C_2$ (blue square) and CN (red and triangle) emission band. The vibrational temperature measured for the CN $B^2\Sigma^+$ is shown by the green triangles. Plot III shows the forward and reflected power.

are equal within error-bars during the pulse. During the OFF-time, the vibrational temperature decays slower than the rotational temperature, but it remains within uncertainties. The difference in the increase rate of the $C_2$ and CN emission intensity is due to the different shape of the power coupled to the plasma, because of the different impedance matching, between the two experiments.

In conclusion, the gas temperature decay can be observed only in the contracted regime using optical emission spectroscopy.

### 7.3.2 Cooling rates in the contracted regime

A systematic investigation of the cooling of the central region of the plasma in the contracted regime has been carried out. All the measurements is carried out with a pulse frequency of 1 kHz. Figure 7.12 shows an investigation of the cooling rates as a function of the average power (i.e. duty cycle and peak power variation) at atmospheric pressure, which does not show any significant variation of the cooling rates. A small systematic trend can be observed: the cooling rates are slower at pulse average power. This might be an indication of a larger fraction of power spent into heating. However, all the measured values are equal within error-bars and the observed trend might be artificial. The cooling rates obtained from the CN and $C_2$ emission are also compared in this figure and they result equal within error-bars.

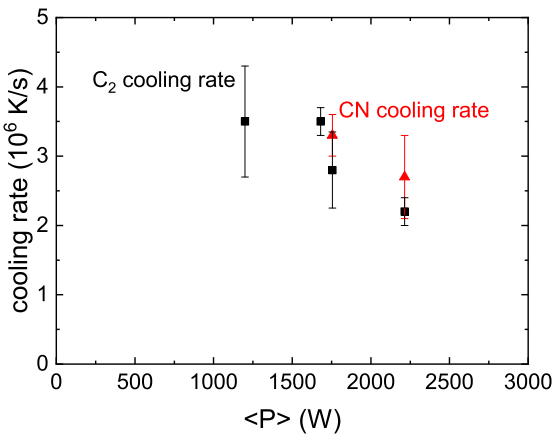


Figure 7.12: Cooling rates as function of the average power coupled to the plasma at atmospheric pressure, 20 L/min (+ 0.5 L/min $N_2$ in case the CN emission is measured). The cooling rates obtained from CN emission are shown in red, the ones obtained from the $C_2$ emission in black.

Figures 7.13 *(a)* shows the measured cooling rate as function of the $CO_2$ flow at atmospheric pressure and at 200 mbar. The cooling rates are rather independent on the gas flow rate in the order of $3 \cdot 10^6$ K/s. Figure 7.13 *(b)* shows the gas cooling rates as function of the pressures, at 200 mbar a cooling rate of $9 \cdot 10^6$ K/s is observed, higher than the $3 \cdot 10^6$ K/s observed at 900 mbar, meaning that the plasma core

cools more rapidly at lower pressures. At 200 mbar the plasma volume is smaller than at atmospheric pressure (the diameter is the same but the length is lower, see section 6.2). The cooling rate describes the time in which the energy stored in the plasma volume is dissipated, since the plasma is smaller and the particle density lower at 200 mbar the amount of energy stored in the plasma volume is lower and dissipated faster.

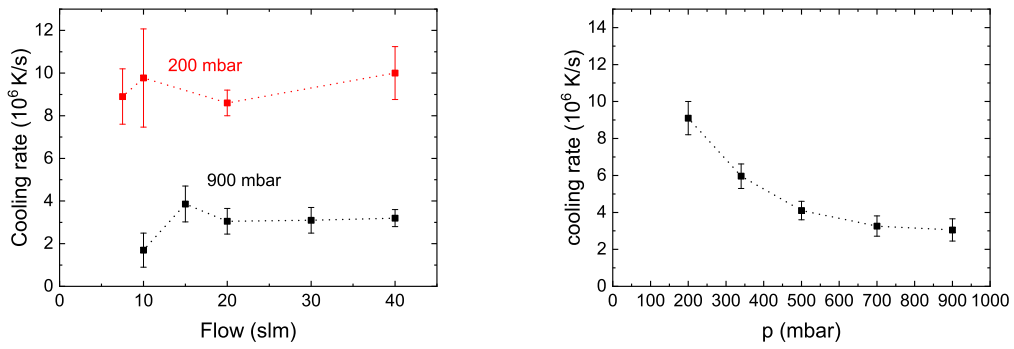


(a) *Flow scan* (b) *pressure scan*

Figure 7.13: Figure *(a)* shows the cooling rates evolution as function of the injected flow at quasi-atmospheric pressure and 200 mbar. Figure *(b)* the cooling rate as function of the pressure.

The cooling rates measured in the contracted regime are higher than $10^6$ K/s. Such value is sufficiently high, accordingly to den Harder et al. [52], to preserve (most of) the CO formed in the plasma. Nevertheless, the measured cooling rates refers to the core of the discharge and they are not necessarily correlated with the recombination of the CO in the effluent.

### 7.3.3 Correlation gas temperature and emission intensity

In the following section, the emission intensity decay is linked to the gas temperature decay in the afterglow. In thermal condition the $C_2$ molar fraction increases strongly from $7.5{\cdot}10^{-9}$ $mol^{-1}$ at 5000 K to $1.6{\cdot}10^{-4}$ $mol^{-1}$ at 7000 K. The $C_2$ density in the plasma changes of five orders by increasing the gas temperature of 2000 K. It can be hypothesized that the intensity decay in the plasma afterglow is driven by the gas cooling itself. The decay rate of the intensity assuming quasi-thermal equilibrium can be derived by computing the $C_2$ density at thermal equilibrium at each time of the pulse afterglow. To make a comparison between the density decay and emission intensity decay of the $C_2$ Swan band, both are normalized to their respective values at

the beginning of the afterglow. Figures 7.14 shows a comparison between the normalized density decay assuming thermal equilibrium and using experimental $T_{gas}$ and the normalized intensity decay. The measurements are carried out at 200 mbar (figure *(a)*), 500 mbar (figure *(b)*) and 900 mbar (figure *(c)*). The shape of the normalized density decay strongly depends on three parameters: the temperature decay rate, the initial temperature and the time at which the pulse ends. The time at which the pulse ends (relatively to the trigger signal) can be determined by the measurements of the forward and reflected power as can be seen in figure 7.11. The decay rates are measured experimentally and they are indicated in the figures. Setting the initial gas temperature is more challenging since the absolute value is affected by systematic errors. For this reason in the figures *(a)*, *(b)* and *(c)* three density decays are given with initial temperature of 5500 K (magenta dashed line), 6000 K (red dashed line) and 6500 K (olive dashed line). At all investigated pressures the temperature decay can be used, under the assumption of thermal evolution, to describe the $C_2$ emission intensity decay in the plasma afterglow. This is possible not only because the plasma is thermally evolving, but also the formation processes of the $C_2$ favours the formation of the $C_2(d^3\Pi_g)$ state (see section 5.2.1). Thus, the emission decay is then proportional to the $C_2$ formation.

### 7.3.4 Physical interpretation of the cooling rates

The gas dynamics simulations are shown in chapter 6 shows that the thermal conduction contributes negligibly to the gas cooling. The source of cooling in the central region can be interpreted as an effect of the influx of particles from the outer region to the center of the plasma (note that an equivalent outflow must compensate). The new particles entering in the center of the plasma equilibrate with the surrounding gas reducing the average gas temperature. This description of the gas cooling in the afterglow is also supported by the evolution of the $C_2$ emission in the afterglow, that follows the gas temperature (see figure 7.14). Under this assumption, the influx of particle can be calculated by knowing the gas temperature and the heated mass of particles at the end of the ON-time. At thermal equilibrium (indeed the plasma afterglow evolves at thermal equilibrium as seen in the previous section) the energy required to heat a given mass of $CO_2$ is given by the enthalpy. With the plasma volume and the gas temperature (measured experimentally), the mass influx needed to produce the observed cooling at thermal equilibrium can be calculated as:

$$m_{in} = \frac{H(T_{core}) - H(T - \frac{\partial T}{\partial t} \cdot t)}{H(T_{core}) - H(T_0)} m_{core} \tag{7.3}$$

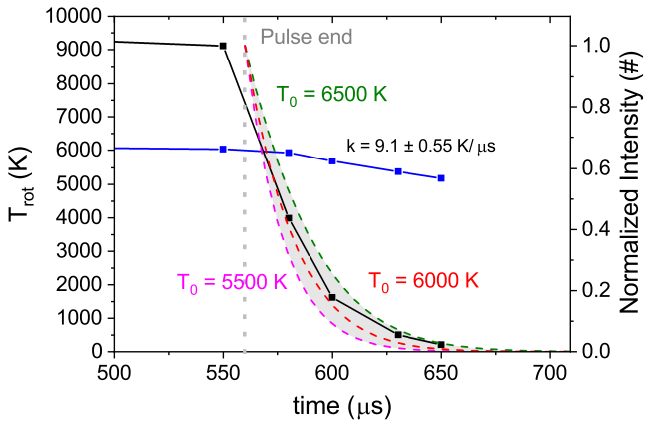


(a) *200 mbar*

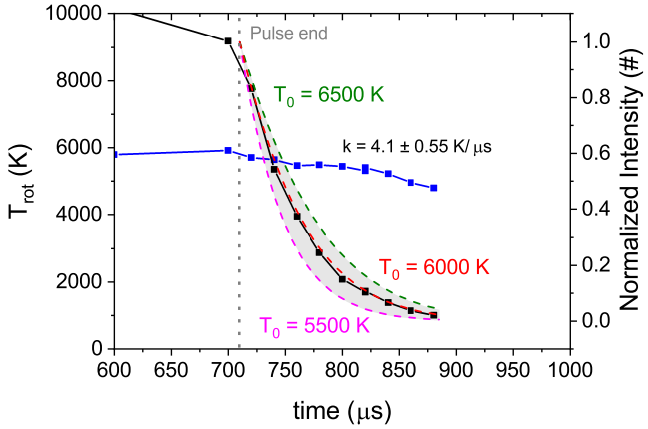


(b) *500 mbar*

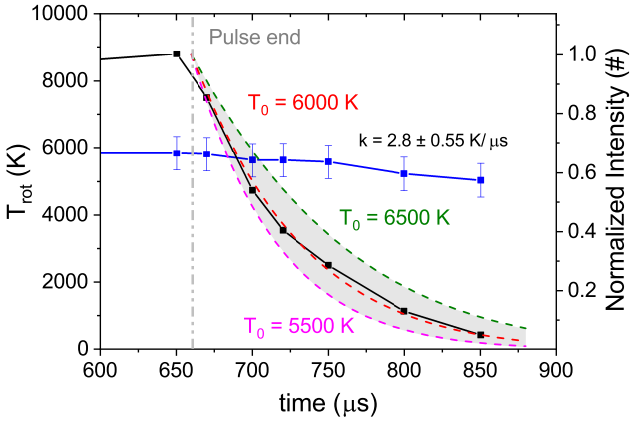


(c) *900 mbar*

Figure 7.14: Comparison of the evolution of the normalized density of the $C_2(d^3\Pi_g)$ molecule, with the expected evolution at thermal equilibrium for a cooling rate consistent with the measured one. The measurements were carried out at 200 mbar, 20 L/min with (set) peak power of 2700 W and a duty cycle of 55 % are shown in figure *(a)*; at 500 mbar, 20 L/min with (set) peak power of 2700 W and a duty cycle of 65 % are shown in figure *(b)*; at 900 mbar, 20 L/min with (set) peak power of 2700 W and a duty cycle of 65 % are shown in figure *(c)*. The dashed lines describe the decay of $C_2$ density at thermal equilibrium normalized to the initial temperature of 5500, 6000 and 6500 K. The measured temperature decay is indicated in the figures.

where $m_{in}$ is the $CO_2$ mass that enters the core in the time t, $\frac{\partial T}{\partial t}$ the cooling rates, H the enthalpy of the mixture at temperature T, $T_0$ the initial temperature of the mass that enters the core, $T_{core}$ the core temperature and $m_{core}$ the mass heated to $T_{core}$. The plasma being in quasi-steady state, the mass of the particle in the plasma does not change in time, which corresponds to $m_{in} = m_{out}$. The temperature of the cooling mass (i.e. the mass entering in the hot core) is a quite important parameter, the gas dynamics simulation highlights that two temperature gradients established in the plasma and the influx in the center should come from the neighbouring region at the temperature of about 3000 K. At this temperature, however, the $CO_2$ is almost completely dissociated and the influx is mostly composed of CO and O particles. The resulting mass influx for the cooling rates and volumes measured in section 7.2 and 7.3 are summarized in table 7.4: two equivalent mass influx are calculated assuming an initial temperature of 3000 K and 300 K. The mass influx is scaled to an equivalent volume of $CO_2$ influx in standard liter per minute by dividing the calculated mass influx by the $CO_2$ density in standard conditions 1.98 kg/m$^3$.

| Pressure | Average power | Cooling rate | influx at 300 K | influx at 3000 K | $CO_{out}$ |
|---|---|---|---|---|---|
| 900 mbar | 1755 W | 3 K/$\mu$s | 0.83 L/min | 1.3 L/min | 1.42 L/min |
| 500 mbar | 1380 W | 4 K/$\mu$s | 0.65 L/min | 1.1 L/min | 1.54 L/min |
| 200 mbar | 1455 W | 9 K/$\mu$s | 0.71 L/min | 1.2 L/min | 1.64 L/min |

Table 7.4: Inward flow needed to explain the observed cooling rates calculated with an initial gas temperature of 300 and 3000 K at different pressure and power.

The simulation of the gas dynamics (discussed in section 6.5) in the plasma shows that at 200 mbar the radial velocity at the edge of the power deposition profile is comparable to the one at 900 and 500 mbar, therefore a lower influx is expected also because of the lower particle density at 200 mbar [161]. The constant cooling rates measured at different powers imply that the mass influx is higher at higher power. In fact, at high powers, the region at 6000 K enlarges, therefore to have the same gas cooling a higher influx is needed. The cooling rates are consistent also with the measured $CO_{out}$ flux, that does not depend on the $CO_2$ flow as the observed cooling rates. The influx that explains the cooling rates measured experimentally is typically lower than the experimental $CO_{out}$ flow and the inflow obtained in the 2D simulation.

The calculated inflow is affected by severe systematic errors: the assumption on the gas temperature of the influx strongly influences the resulting in flux. The initial mass of gas is determined from the measured plasma volume and gas temperature (perfect gas law), therefore any experimental error in their determination propagates

to the determined influx. However, the interpretation of the cooling rates as the results of a temperature equilibration between a cold gas and a central hot core allows calculating an influx of the same order of magnitude as predicted from the gas dynamics simulation, confirming experimentally its existence and magnitude.

## 7.4 Summary

In a microwave plasma torch pulsing the microwave does not have any beneficial effect on the energy efficiency when the plasma is in the contracted regime, since the gas flow dynamics, which determines the conversion, are driven by the temperature gradients established by the plasma itself. On the other hand, in the surfaguide, it is observed that the energy efficiency increases when the OFF-time is much longer than the ON-time. Similar behaviour is expected in the expanded regime of the plasma torch.

During a pulse two volumes can be distinguished: the power deposition volume, visible at the beginning of a pulse and the recombination volume, visible during the OFF-phase of a pulse. The power deposition volume has a length is determined by the average power coupled to the plasma during a pulse. The diameter instead is not correlated with the average nor with the peak power. The recombination region allows determining the inactive zone of the plasma, which is observed to be a circular corona 2 mm thick at 200 mbar and expand radially at higher pressure. The recombination zone is significantly longer than the power deposition zone at 200 mbar, but it becomes comparable to the length of the power deposition zone at higher pressures, which is explained by slower recombination at lower pressure [151].

The investigation of the emission decay during the afterglow of a pulse allows measuring the cooling rate of the gas in the plasma core. The $C_2$ emission in the afterglow is found to evolve at thermal equilibrium consistently with the gas temperature and cooling rates measured. The cooling rates increases at decreasing pressures from $9 \cdot 10^6$ K/s at 200 mbar to $3 \cdot 10^6$ K/s at 900 mbar and they are weakly sensitive to the flow and power. The physical mechanism driving the gas cooling is assigned to an inward flow of cold $CO_2$, which cools the gas in the core. The cooling rates are the first experimental indications of the existence of a radial inflow.

# 8 Conclusion

In this work, a 2.45 GHz plasma torch is investigated as a possible means of $CO_2$ conversion into CO and $O_2$. The characterization of the plasma is performed using mass spectrometry, which allows determining energy efficiency and the fraction of $CO_2$ converted; optical emission spectroscopy used to determine the gas temperature; and iCCD imaging, which gives the plasma volume.

The $CO_2$ decomposition in a 2.45 GHz microwave plasma torch is investigated in a wide pressure, 30-1000 mbar, flow, 1-100 L/min, and power range, 600-3000 W. Two different regimes of the plasma torch, depending on the operating pressure and microwave input power, are described: at pressures below 120 mbar the plasma fills most of the plasma torch volume whereas at pressures of about 120 mbar an abrupt contraction of the plasma in the center of the resonator is observed along with an increase of the gas temperature from 3000 K to 6000 K. In the expanded regime the gas temperature is observed to increase with pressure: at 30 mbar the measure gas temperature is 2000 $\pm$ 200 K and at 100 mbar 3000 $\pm$ 300 K. In the contracted regime the gas temperature is constant and equal to 6000 $\pm$ 500 K up to 1000 mbar. In both regimes, neither the flow nor power is observed to influence the gas temperature.

The conversion and the energy efficiency are found to have an optimum at *ca.* 120 mbar, where a plasma contraction takes place. The maximum conversion obtained is *ca.* 40 % with an energy efficiency of 35 %. At every pressure the energy efficiency and the conversion increase almost linearly with the SEI up to 2 eV/molecule. Above this value the conversion and energy efficiency decrease at atmospheric pressure and saturates at 500 mbar. At 200 mbar, neither the energy efficiency nor the conversion decreases at SEIs higher 2 eV/molecule. These results are of particular relevance for the up-scaling of a microwave plasma torch, since increasing the power leads to a reduction of the $CO_2$ decomposition performances at pressures higher or equal to 500 mbar. Such reduction may occur even at lower pressures at powers higher than 3 kW, which is the maximum used in this work. The $CO_2$ conversion measured experimentally in the plasma torch is lower than the thermal limit at pressures above

30 mbar. In this pressure range, the thermal decomposition of $CO_2$ (and CO losses) is sufficient to explain the conversion and energy efficiency measured in the plasma torch. Below 30 mbar the conversion exceeds the thermal limit and it is driven by electron processes. However, the measured conversion and energy efficiency are low and not relevant for any application.

Through the analysis of the gas flow dynamics simulations [161] it is possible to identify the volume measured by ICCD imaging as the region in which the microwave power is deposited. Three temperature regions form in the tube: one in contact with quartz tube at a temperature between 300-2000 K that is thermally inactive, an intermediate zone at a temperature between 3000-3500 K and a core region at a temperature above 5000 K. The regions can be distinguished because of the strong temperature gradients that separate them. A $CO_2$ inflow is driven by the position and magnitude of the temperature gradients. The gas dynamics simulation shows the radial influx at 3500 K (temperature above which thermal decomposition of $CO_2$ is above 50 % at 1000 mbar) is comparable, but higher, with the measured $CO_{out}$. The conversion depends on the inflow into this second gradient, whose radial position is not influenced directly by the size of the power deposition region, namely the plasma volume. The experimental observation of a radial inflow can be obtained from the cooling rate of the plasma during the plasma afterglow. The simulations also highlight that significant CO losses take place close to the plasma since the $CO_{out}$ is lower than the inflow in the thermally active region.

The experiments performed show that pulsing the microwave from 20 Hz up to 10 kHz does not influence the $CO_2$ conversion in the contracted regime. The conversion is observed to follow the average power coupled into the plasma at constant energy efficiency. A different result is obtained at a pressure between *ca.* 5-20 mbar using a surfaguide, where pulsing the microwave with a long OFF-time improves the energy efficiency of factor 2, although the energy efficiency is below 10%. The determination, in the contracted regime, of the plasma cross-section and length evolution during a pulse highlight that the latter directly correlates with the average power coupled to the plasma (thus also to the conversion), while the plasma cross-section follows the peak power.

The $CO_2$ decomposition in the investigated microwave plasma torch is driven by the gas temperature; the energy efficiency and the conversion are limited by the gas dynamics, which determines the fraction of the injected $CO_2$ gas that interacts with the plasma volume. The thermal conversion limit cannot be exceeded in this setup without major changes in the power deposition or the flow dynamics (e.g. supersonic

expansion). However, the setup can be optimized to increase the fraction of $CO_2$ converted and energy efficiency since the theoretical thermal limit is not matched for the total gas flow.

The improvements of the plasma torch performances can take two directions: reducing the CO losses and improving the gas mixing. The reduction of CO losses can be achieved by actively cooling the effluent gas or with the dilution of the gas in the afterglow. The enhancement of gas mixing is significantly more challenging since the gas dynamics are governed mostly by the temperature gradient. Moreover, the swirl gas configuration is used to protect the quartz tube from heating and a change of configuration should take into account the necessity of keeping the quartz tube temperature below 1000 K.

# A Molecular constants

## A.1 Molecular constants used to calculate the $C_2$ Swan band system

| $\nu$ | Origin | A | $A_D$ | $B_\nu$ | $10^6 \cdot D_\nu$ | $\lambda$ | o | p | q |
|---|---|---|---|---|---|---|---|---|---|
| 0 | 19 378.46749(51) | -14.00139(63) | 0.0005068(83) | 1.7455663(43) | 6.8205(16) | 0.03301(47) | 0.61076(52) | 0.003973(43) | -0.0007752(43) |
| 1 | 21 132.14977(25) | -13.87513(49) | 0.0005740(83) | 1.7254062(53) | 7.0194(77) | 0.02972(38) | 0.61713(36) | 0.004133(44) | -0.0008171(43) |
| 2 | 22 848.3877(21) | -13.8205(23) | 0.000600(43) | 1.704516(21) | 7.308(22) | 0.0253(41) | 0.6208(32) | 0.00624(38) | -0.000835(14) |
| 3 | 24 524.2201(19) | -13.5361(28) | 0.000775(17) | 1.681437(16) | 7.438(24) | 0.0470(26) | 0.5827(26) | 0.00579(17) | -0.0008568(85) |
| 4 | 26 155.0448(29) | -13.3892(50) | 0.001451(14) | 1.656859(26) | 7.684(43) | 0.0219(38) | 0.6313(32) | 0.00954(29) | -0.000923(21) |
| 5 | 27 735.6720(43) | -13.0324(66) | 0.000723(37) | 1.630205(23) | 8.573(32) | 0.0601(28) | 0.6161(23) | 0.00685(32) | -0.000912(15) |
| 6 | 29 259.3548(36) | -12.820(10) | 0.001203(56) | 1.599876(31) | 8.998(44) | 0.0529(71) | 0.5773(71) | 0.00874(47) | -0.000986(22) |
| 7 | 30 717.9011(46) | -12.3458(71) | 0.000814(41) | 1.566047(32) | 10.044(66) | 0.0960(34) | 0.5532(31) | 0.00936(35) | -0.001175(17) |
| 8 | 32 102.655(22) | -12.107(22) | 0.00076(fixed) | 1.52675(31) | 9.60(97) | 0.095(fixed) | 0.546(22) | 0.0055(21) | -0.00088(21) |
| 9 | 33 406.230(22) | -11.698(39) | 0.00076(fixed) | 1.485755(96) | 11.85(10) | 0.172(26) | 0.498(28) | 0.0097(14) | -0.002062(44) |
| 10 | 34 626.7860(94) | -11.297(15) | 0.00076(fixed) | 1.441138(72) | 12.837(73) | 0.115(16) | 0.399(12) | 0.00745(90) | -0.000977(30) |

Table A.1: Molecular constants (in $cm^{-1}$) for the $d^3\Pi_g$ electronic state used in the calculations performed by Brooke et al. [61]. The uncertainties are given in parenthesis (i.e. one standard deviation to the last significant digits of the constants). For the vibrational level $\nu$=1 the additional constant H= $2.14(30) \cdot 10^{-11}$ is used.

| $\nu$ | Origin | A | $A_D$ | $B_\nu$ | $10^6 \cdot D_\nu$ | $\lambda$ | o | p | q |
|---|---|---|---|---|---|---|---|---|---|
| 0 | 0 | -15.26986(43) | 0.0002634(71) | 1.6240452(44) | 6.4506(19) | -0.15450(36) | 0.67525(35) | 0.002537(42) | -0.0005281(44) |
| 1 | 1618.02244(53) | -15.25197(61) | 0.0002266(73) | 1.6074266(44) | 6.4439(21) | -0.15373(51) | 0.67017(51) | 0.002705(44) | -0.0005772(42) |
| 2 | 3212.72793(96) | -15.2328(15) | 0.0001996(94) | 1.5907513(61) | 6.4527(44) | -0.1526(12) | 0.6649(14) | 0.003132(77) | -0.0006457(48) |
| 3 | 4784.0688(31) | -15.1972(39) | 0.000186(42) | 1.574088(24) | 6.455(24) | -0.1333(61) | 0.6815(51) | 0.00488(42) | -0.000618(17) |
| 4 | 6332.1364(51) | -15.2043(65) | 0.000318(36) | 1.557117(31) | 6.338(39) | -0.1551(72) | 0.6674(67) | 0.00632(36) | -0.000894(16) |
| 5 | 7856.8175(32) | -15.2096(35) | 0.00025(fixed) | 1.540139(24) | 6.312(35) | -0.1492(36) | 0.6546(37) | 0.00734(25) | -0.001246(12) |
| 6 | 9358.1565(40) | -15.1646(60) | 0.000355(33) | 1.523439(26) | 6.034(38) | -0.1551(46) | 0.6886(38) | 0.00504(32) | -0.000676(16) |
| 7 | 10 836.1430(92) | -15.085(11) | 0.00025(fixed) | 1.50869(25) | 3.51(92) | -0.1641(90) | 0.704(14) | -0.0244(23) | 0.00632(49) |
| 8 | 12 290.7997(29) | -15.1702(46) | 0.00025(fixed) | 1.488684(28) | 5.329(52) | -0.1665(36) | 0.6742(30) | 0.01449(29) | -0.002053(23) |
| 9 | 13 722.0897(43) | -15.0980(61) | 0.000419(31) | 1.472818(24) | 6.066(35) | -0.1584(27) | 0.6926(23) | 0.00303(33) | -0.000081(16) |

Table A.2: Molecular constants (in $cm^{-1}$) for the $a^3\Pi_u$ electronic state used in the calculations performed by Brooke et al. [61]. The uncertainties are given in parenthesis (i.e. one standard deviation to the last signficant digits of the constants). For the vibrational level $\nu$=0 the additional constants H= $6.73(16) \cdot 10^{-11}$, $o_D = -6.86(114) \cdot 10^{-6}$ and $q_D = -9.61(41) \cdot 10^{-9}$ are used.

| $v' - v''$ | | $d^3\Pi_g$ | | | | | | | | | | |
|---|---|---|---|---|---|---|---|---|---|---|---|---|
| | | 0 | 1 | 2 | 3 | 4 | 5 | 6 | 7 | 8 | 9 | 10 |
| $a^3\Pi_u$ | 0 | $7.626\ 10^{+6}$ | $2.814\ 10^{+6}$ | $2.809\ 10^{+5}$ | $4.333\ 10^{+3}$ | $2.033\ 10^{+2}$ | $3.642\ 10^{+1}$ | $2.470\ 10^{-2}$ | $2.140\ 10^{-1}$ | $9.989\ 10^{-4}$ | $3.827\ 10^{-3}$ | $3.140\ 10^{-9}$ |
| | 1 | $2.135\ 10^{+6}$ | $3.427\ 10^{+6}$ | $4.072\ 10^{+6}$ | $6.429\ 10^{+5}$ | $8.720\ 10^{+3}$ | $1.608\ 10^{+3}$ | $1.591\ 10^{+2}$ | $4.744\ 10^{+0}$ | $1.822\ 10^{+0}$ | $4.947\ 10^{-2}$ | $3.540\ 10^{-2}$ |
| | 2 | $3.832\ 10^{+5}$ | $2.746\ 10^{+6}$ | $1.270\ 10^{+6}$ | $4.422\ 10^{+6}$ | $9.615\ 10^{+5}$ | $7.432\ 10^{+3}$ | $6.154\ 10^{+3}$ | $3.223\ 10^{+2}$ | $6.379\ 10^{+1}$ | $4.108\ 10^{+0}$ | $1.567\ 10^{+0}$ |
| | 3 | $5.590\ 10^{+4}$ | $8.273\ 10^{+5}$ | $2.568\ 10^{+6}$ | $3.236\ 10^{+5}$ | $4.301\ 10^{+6}$ | $1.168\ 10^{+6}$ | $1.085\ 10^{+3}$ | $1.805\ 10^{+4}$ | $1.707\ 10^{+2}$ | $3.472\ 10^{+2}$ | $1.346\ 10^{-2}$ |
| | 4 | $7.224\ 10^{+3}$ | $1.710\ 10^{+5}$ | $1.169\ 10^{+6}$ | $2.066\ 10^{+6}$ | $2.505\ 10^{+4}$ | $4.005\ 10^{+6}$ | $1.149\ 10^{+6}$ | $4.993\ 10^{+3}$ | $3.581\ 10^{+4}$ | $1.535\ 10^{+2}$ | $9.452\ 10^{+2}$ |
| | 5 | $8.592\ 10^{+2}$ | $2.886\ 10^{+4}$ | $3.215\ 10^{+5}$ | $1.352\ 10^{+6}$ | $1.510\ 10^{+6}$ | $1.513\ 10^{+4}$ | $3.459\ 10^{+6}$ | $1.120\ 10^{+6}$ | $5.272\ 10^{+4}$ | $4.975\ 10^{+4}$ | $4.445\ 10^{+3}$ |
| | 6 | $9.574\ 10^{+1}$ | $4.280\ 10^{+3}$ | $6.793\ 10^{+4}$ | $4.745\ 10^{+5}$ | $1.381\ 10^{+6}$ | $1.038\ 10^{+6}$ | $8.028\ 10^{+4}$ | $3.438\ 10^{+6}$ | $8.558\ 10^{+5}$ | $1.863\ 10^{+5}$ | $4.075\ 10^{+4}$ |
| | 7 | $1.006\ 10^{+1}$ | $5.775\ 10^{+2}$ | $1.218\ 10^{+4}$ | $1.218\ 10^{+5}$ | $6.009\ 10^{+5}$ | $1.302\ 10^{+6}$ | $6.443\ 10^{+5}$ | $1.343\ 10^{+5}$ | $3.253\ 10^{+6}$ | $4.834\ 10^{+5}$ | $4.111\ 10^{+5}$ |
| | 8 | $9.931\ 10^{-1}$ | $7.206\ 10^{+1}$ | $1.945\ 10^{+3}$ | $2.582\ 10^{+4}$ | $1.830\ 10^{+5}$ | $6.840\ 10^{+5}$ | $1.087\ 10^{+6}$ | $4.546\ 10^{+5}$ | $1.285\ 10^{+5}$ | $3.081\ 10^{+6}$ | $1.342\ 10^{+5}$ |
| | 9 | $9.005\ 10^{-2}$ | $8.335\ 10^{+0}$ | $2.828\ 10^{+2}$ | $4.785\ 10^{+3}$ | $4.495\ 10^{+4}$ | $2.421\ 10^{+5}$ | $6.721\ 10^{+5}$ | $9.993\ 10^{+5}$ | $3.120\ 10^{+5}$ | $8.080\ 10^{+4}$ | $2.824\ 10^{+6}$ |

Table A.3: Vibrational transition probabilities (in $s^{-1}$) calculated by Brooke at al. [61] for the $d^3\Pi_g$-$a^3\Pi_u$ transition. The transition probabilities are calculated as the sum of all the possible transition from a J'=1,$\Omega'$ =0 energy level.

## A.2 Molecular constants for the calculations of the CO emission

### A.2.1 The Ångström band

| $B^1\Sigma^+$ | | | |
|---|---|---|---|
| $\nu$ | Origin | $B_\nu$ | $10^6\cdot D_\nu$ |
| 0 | 86916.198(3)[a] | 1.94808(16)[b] | 6.33 (17)[b] |
| 1 | 88988.359(6)[a] | 1.921835(77)[b] | 7.31(22)[b] |

Table A.4: Molecular constants (in $cm^{-1}$) for the $B^1\Sigma^+$ used in the calculations (in $cm^{-1}$). The uncertainties are given in parenthesis (i.e. one standard deviation to the last significant digits of the constants). [a] from reference [118], [b] from reference [168].

| $A^1\Pi$ | | | | | |
|---|---|---|---|---|---|
| $\nu$ | Origin | $B_\nu$ | $10^6\cdot D_\nu$ | $10^{12}\cdot H_\nu$ | $10^5\cdot q_\nu$ |
| 0[a] | 64746.742(4) | 1.604069(8) | 7.348(8) | -9(2) | 3.1(6) |
| 1[a] | 66228.201(3) | 1.58126(1) | 7.41(1) | -22(2) | 2.6(5) |
| 2[b] | 67675.26(12) | 1.55738(3) | 7.526 | - | - |
| 3[b] | 69088.4(7) | 1.53454(2) | 7.62 | - | - |
| 4[b] | 70465.91(12) | 1.5112(2) | 7.07 | - | - |
| 5[b] | 71809.04(12) | 1.487653(3) | 8.015 | - | - |
| 6[b] | 73117.54(12) | 1.4616(3) | 6.97 | - | - |
| 7[b] | 74391.76(9) | 1.43978(3) | 8.24 | - | - |
| 8[b] | 75631.63(10) | 1.41495(3) | 9.31 | - | - |
| 9[b] | 76837.28(9) | 1.39096(3) | 8.46 | - | - |

Table A.5: Molecular constants (in $cm^{-1}$) for the $A^1\Pi$ used in the calculations (in $cm^{-1}$). The uncertainties are given in parenthesis (i.e. one standard deviation to the last significant digits of the constants). [a] from reference [114], [b] from reference [115].

The list of perturbation included in the calculation for each vibrational level of the CO($A^1\Pi$) state:

- $\langle A^1\Pi(\nu=0)|\hat{N}_+\hat{L}_- + \hat{N}_- + \hat{L}_+|\ I^1\Sigma^-(\nu=1)\rangle = 0.103\ cm^{-1}$
- $\langle A^1\Pi(\nu=0)|\hat{N}_+\hat{L}_- + \hat{N}_- + \hat{L}_+|\ I^1\Sigma^-(\nu=2)\rangle = 0.1242\ cm^{-1}$
- $\langle A^1\Pi(\nu=0)|\hat{N}_+\hat{L}_- + \hat{N}_- + \hat{L}_+|\ D^1\Delta(\nu=1)\rangle = 0.0303\ cm^{-1}$
- $\langle A^1\Pi(\nu=0)|\hat{N}_+\hat{L}_- + \hat{N}_- + \hat{L}_+|\ D^1\Delta(\nu=2)\rangle = 0.0395\ cm^{-1}$
- $\langle A^1\Pi(\nu=0)|\ \hat{H}_{SO}|\ d^3\Delta(\nu=4)\rangle$ = -21.7 $cm^{-1}$

- $\langle A^1\Pi(\nu=0)|\ \hat{H}_{SO}|\ d^3\Delta(\nu=5)\rangle$ = 17.82 cm$^{-1}$
- $\langle A^1\Pi(\nu=0)|\ \hat{H}_{SO}|\ e^3\Sigma^-(\nu=1)\rangle$ = -15.103 cm$^{-1}$
- $\langle A^1\Pi(\nu=0)|\ \hat{H}_{SO}|\ e^3\Sigma^-(\nu=2)\rangle$ = 17.4 cm$^{-1}$
- $\langle A^1\Pi(\nu=0)|\ \hat{H}_{SO}|\ e^3\Sigma^-(\nu=3)\rangle$ = -19.89 cm$^{-1}$
- $\langle A^1\Pi(\nu=0)|\ \hat{H}_{SO}|\ a'^3\Sigma^+(\nu=9)\rangle$ = 2.407 cm$^{-1}$
- $\langle A^1\Pi(\nu=1)|\hat{N}_+\hat{L}_- + \hat{N}_- + \hat{L}_+|\ I^1\Sigma^-(\nu=2)\rangle$ = 0.079 cm$^{-1}$
- $\langle A^1\Pi(\nu=1)|\hat{N}_+\hat{L}_- + \hat{N}_- + \hat{L}_+|\ I^1\Sigma^-(\nu=3)\rangle$ = 0.043 cm$^{-1}$
- $\langle A^1\Pi(\nu=1)|\hat{N}_+\hat{L}_- + \hat{N}_- + \hat{L}_+|\ D^1\Delta(\nu=1)\rangle$ = 0.073 cm$^{-1}$
- $\langle A^1\Pi(\nu=1)|\ \hat{H}_{SO}|\ d^3\Delta(\nu=5)\rangle$ = -16.92 cm$^{-1}$
- $\langle A^1\Pi(\nu=1)|\ \hat{H}_{SO}|\ d^3\Delta(\nu=6)\rangle$ = 18.6 cm$^{-1}$
- $\langle A^1\Pi(\nu=1)|\ \hat{H}_{SO}|\ e^3\Sigma^-(\nu=3)\rangle$ = 3 cm$^{-1}$
- $\langle A^1\Pi(\nu=1)|\ \hat{H}_{SO}|\ a'^3\Sigma^+(\nu=10)\rangle$ = 4.9 cm$^{-1}$
- $\langle A^1\Pi(\nu=1)|\ \hat{H}_{SO}|\ a'^3\Sigma^+(\nu=11)\rangle$ = 3.6 cm$^{-1}$
- $\langle A^1\Pi(\nu=2)|\ \hat{H}_{SO}|\ d^3\Delta(\nu=7)\rangle$ = 10.73 cm$^{-1}$
- $\langle A^1\Pi(\nu=2)|\ \hat{H}_{SO}|\ e^3\Sigma^-(\nu=4)\rangle$ = 12.83 cm$^{-1}$
- $\langle A^1\Pi(\nu=2)|\ \hat{H}_{SO}|\ a'^3\Sigma^+(\nu=11)\rangle$ = 5.87 cm$^{-1}$
- $\langle A^1\Pi(\nu=2)|\ \hat{H}_{SO}|\ d^3\Delta(\nu=7)\rangle$ = 10.73 cm$^{-1}$
- $\langle A^1\Pi(\nu=2)|\ \hat{H}_{SO}|\ e^3\Sigma^-(\nu=4)\rangle$ = 12.83 cm$^{-1}$
- $\langle A^1\Pi(\nu=4)|\ \hat{H}_{SO}|\ d^3\Delta(\nu=9)\rangle$ = -6.997 cm$^{-1}$
- $\langle A^1\Pi(\nu=6)|\ \hat{H}_{SO}|\ d^3\Delta(\nu=12)\rangle$ = 10.997 cm$^{-1}$
- $\langle A^1\Pi(\nu=8)|\ \hat{H}_{SO}|\ d^3\Delta(\nu=15)\rangle$ = -10.52 cm$^{-1}$

Perturbation matrix element and the perturbing state molecular constants are taken from [114] and [115].

| $v'' - v'$ | | $B^1\Sigma^+$ | |
|---|---|---|---|
| | | 0 | 1 |
| $A^1\Pi$ | 0 | 0.711371 | -1.04229 |
| | 1 | -1.10599 | 0.970457 |
| | 2 | 1.29745 | -0.458789 |
| | 3 | -1.31425 | -0.151908 |
| | 4 | 1.22523 | 0.647565 |
| | 5 | -1.08945 | -0.982578 |
| | 6 | 0.950648 | 1.17676 |
| | 7 | -0.774885 | -1.19995 |
| | 8 | 0.600987 | 1.1131 |
| | 9 | 0.471082 | -1.01257 |

Table A.6: Transition dipole moment calculated using the program LEVEL [67], the potential curve of the $A^1\Pi$ and $B^1\Sigma^+$ [99] and the transition dipole [109].

### A.2.2 The third positive band

| $b^3\Sigma^+$ | | | |
|---|---|---|---|
| $\nu$ | Origin | $B_\nu$ | $10^6 \cdot D_\nu$ |
| $0^a$ | 83823.927(14) | 1.950561(77) | -8.6(12) |
| $1^b$ | 86015.582(66) | 1.91485(66) | -3.75(80) |
| $2^b$ | 88103.721(168) | 1.90207(65) | -3.75(80) |

Table A.7: Molecular constants (in $cm^{-1}$) for the $b^3\Sigma^+$ used in the calculations (in $cm^{-1}$). The uncertainties are given in parenthesis (i.e. one standard deviation to the last significant digits of the constants). $^a$ from reference [127], the origin is calculated with respect to the $a^3\Pi(\nu = 1)$ level with energy 50189.34 $cm^{-1}$. $^b$ from reference [128] the origin is calculated with respect to the $a^3\Pi(\nu = 1)$ level with energy 48474.75 $cm^{-1}$.

| $a^3\Pi$ | | | | | | | |
|---|---|---|---|---|---|---|---|
| $\nu$ | Origin | $B_\nu$ | $10^6 \cdot D_\nu$ | $A_\nu$ | $10^3$ $A_{\nu D}$ | $10^3$ $q_\nu$ | $10^3$ $p_\nu$ |
| $0^a$ | 48474.75(6)$^b$ | 1.6816404(3) | 6.377(4) | 41.445(17) | -0.206(7) | 0.1278(6) | 8.4(3) |
| $1^a$ | 50189.34(6)$^b$ | 1.6625836(3) | 6.412(4) | 41.266(20) | -0.349(8) | 0.1255(8) | 8.0(4) |
| $2^a$ | 51874.82(6)$^b$ | 1.6434204(3) | 6.447(6) | 41.086(22) | -0.345(8) | 0.1205(6) | 8.0(3) |
| $3^a$ | 53530.84(6)$^b$ | 1.6241514(3) | 6.491(5) | 40.890(20) | -0.339(7) | 0.1188(5) | 7.8(3) |
| $4^a$ | 55157.88(4)$^b$ | 1.60477(4) | 6.53(3) | 40.685(16) | -0.337(5) | 0.113(1) | 7.8(6) |
| $5^a$ | 56755.88(6)$^b$ | 1.58507(5) | 6.57(4) | 40.474(96) | -0.30(3) | 0.112(4) | 8(1) |
| $6^a$ | 58323.65(7)$^b$ | 1.5657(2) | 6.5(1) | 40.28(223) | -0.22(8) | 0.040(3) | 10(2) |

Table A.8: Molecular constants (in $cm^{-1}$) for the $a^3\Pi$ used in the calculations (in $cm^{-1}$). The uncertainties are given in parenthesis (i.e. one standard deviation to the last significant digits of the constants). $^a$ from reference [169] values are converted in $cm^{-1}$. $^b$ from reference [170].

The list of perturbation included in the calculation for each vibrational level of the CO($b^3\Sigma^+$) state:

- $\langle b^3\Sigma^+(\nu=0)|\ \hat{H}_{Homog}|\ a'^3\Sigma^+(\nu=31)\rangle = 112.157\ cm^{-1}$
- $\langle b^3\Sigma^+(\nu=0)|\ \hat{H}_{Homog}|\ a'^3\Sigma^+(\nu=32)\rangle = 103.425\ cm^{-1}$
- $\langle b^3\Sigma^+(\nu=0)|\ \hat{H}_{Homog}|\ a'^3\Sigma^+(\nu=33)\rangle = 95.06\ cm^{-1}$
- $\langle b^3\Sigma^+(\nu=0)|\ \hat{H}_{Homog}|\ a'^3\Sigma^+(\nu=34)\rangle = 88.32\ cm^{-1}$
- $\langle b^3\Sigma^+(\nu=0)|\ \hat{H}_{Homog}|\ a'^3\Sigma^+(\nu=35)\rangle = 100^a\ cm^{-1}$
- $\langle b^3\Sigma^+(\nu=0)|\ \hat{H}_{Homog}|\ a'^3\Sigma^+(\nu=36)\rangle = 100^a\ cm^{-1}$
- $\langle b^3\Sigma^+(\nu=0)|\ \hat{H}_{Homog}|\ a'^3\Sigma^+(\nu=37)\rangle = 100^a\ cm^{-1}$

Perturbation matrix element and the perturbing state molecular constants are taken from [127] and adapted to the PGOPHER standard, $^a$ indicates arbitrary values chosen because any value could be found. Information on the known perturbations arising on the $b^3\Sigma^+(\nu=1)$ and $b^3\Sigma^+(\nu=2)$ can be found in [128] and [103]. The latter information are not included in the simulation performed.

| $\nu'' - \nu'$ | | $b^3\Sigma^+$ | | |
|---|---|---|---|---|
| | | 0 | 1 | 2 |
| $a^3\Pi$ | 0 | 0.43301 | 0.52384 | 0.35930 |
| | 1 | 0.57819 | 0.25451 | 0.22953 |
| | 2 | 0.57967 | 0.11775 | 0.37238 |
| | 3 | 0.49825 | 0.37370 | 0.16159 |
| | 4 | 0.38686 | 0.47956 | 0.12837 |
| | 5 | 0.28325 | 0.50710 | 0.34496 |
| | 6 | 0.19636 | 0.40210 | 0.44980 |
| | 7 | 0.13005 | 0.30883 | 0.43661 |
| | 8 | 0.08292 | 0.24299 | 0.38022 |
| | 9 | 0.05160 | 0.16016 | 0.30703 |

Table A.9: Transition dipole moment calculated in the R centroid approximation $\mathrm{R}_e^2 \approx \bar{R}_e^2(r_c) \cdot q_{\nu'\nu''}$, values obtained accordingly to the data of [66]. Note that the values are in arbitrary units.

## A.3 Molecular constants for the calculations of the CN violet system

| $X^2\Sigma^+$ | | | | |
|---|---|---|---|---|
| $\nu$ | Origin | $B_\nu$ | $10^6 \cdot D_\nu$ | $10^{-3} \cdot \gamma$ |
| 0 | 0.0 | 1.891089596(96) | 6.39726(64) | 7.25514(52) |
| 1 | 2042.42143(24) | 1.873665288(90) | 6.40576(60) | 7.17376(74) |
| 2 | 4058.54933(29) | 1.856186883(85) | 6.41672(60) | 7.0850(12) |
| 3 | 6048.34329(35) | 1.83865221(11) | 6.42731(56) | 6.9814(12) |
| 4 | 8011.76637(42) | 1.82105914(21) | 6.44121(73) | 6.8631(14) |
| 5 | 9948.77554(56) | 1.80340409(27) | 6.4530(38) | 6.7198(14) |
| 6 | 11859.32721(61) | 1.78568472(29) | 6.4651(44) | 6.5417(15) |
| 7 | 13743.37442(66) | 1.76789824(29) | 6.4812(46) | 6.3136(14) |
| 8 | 15600.86884(71) | 1.75004020(28) | 6.4835(64) | 6.0121(15) |
| 9 | 17431.75410(77) | 1.73210149(27) | 6.5334(85) | 5.6133(22) |

Table A.10: Molecular constants (in $cm^{-1}$) for the $X^2\Sigma^+$ used in the calculations (in $cm^{-1}$).The uncertainties are given in parenthesis (i.e. one standard deviation to the last significant digits of the constants).

| $B^2\Sigma^+$ | | | | |
|---|---|---|---|---|
| $\nu$ | Origin | $B_\nu$ | $10^6 \cdot D_\nu$ | $10^{-2} \cdot \gamma$ |
| 0 | 25797.86825(43) | 1.9587413(13) | 0.660855(81) | 1.7154(52) |
| 1 | 27921.46650(55) | 1.9380444(45) | 0.67324(29) | 1.8162(82) |
| 2 | 30004.90632(77) | 1.916503(10) | 0.7021(27) | 1.840(13) |
| 3 | 32045.94678(73) | 1.894180(15) | 0.7105(60) | 2.453(16) |
| 4 | 34041.97036(68) | 1.8704809(66) | 0.7448(15) | 2.1169(97) |
| 5 | 35990.0970(21) | 1.847108(24) | 0.9132(54) | 0.431(83) |
| 6 | 37887.42418(74) | 1.8193429(54) | 0.8092(11) | 2.5237(87) |
| 7 | 39730.53401(80) | 1.790761(12) | 1.1054(58) | 0.6126(58) |
| 8 | 41516.64296(84) | 1.7621417(59) | 0.9040(13) | 3.4942(98) |

Table A.11: Molecular constants (in $cm^{-1}$) for the $B^2\Sigma^+$ used in the calculations (in $cm^{-1}$). The uncertainties are given in parenthesis (i.e. one standard deviation to the last significant digits of the constants).

| $v'' - v'$ | | $B^2\Sigma^+$ | | | | | | | | |
|---|---|---|---|---|---|---|---|---|---|---|
| | | 0 | 1 | 2 | 3 | 4 | 5 | 6 | 7 | 8 |
| $X^2\Sigma^+$ | 0 | $4.1110^{-2}$ | $3.8010^{-3}$ | $4.0210^{-5}$ | $1.0610^{-6}$ | $4.3910^{-8}$ | $2.2710^{-9}$ | $1.1610^{-11}$ | $1.2210^{-11}$ | $2.9410^{-15}$ |
| | 1 | $3.6710^{-3}$ | $3.3610^{-2}$ | $6.5010^{-3}$ | $7.8310^{-5}$ | $5.1710^{-6}$ | $1.3910^{-7}$ | $1.5810^{-8}$ | $2.1110^{-12}$ | $5.3510^{-11}$ |
| | 2 | $2.4710^{-4}$ | $6.0410^{-3}$ | $2.8010^{-2}$ | $8.3810^{-3}$ | $9.4310^{-5}$ | $1.4910^{-5}$ | $2.3410^{-7}$ | $5.9810^{-8}$ | $2.3110^{-10}$ |
| | 3 | $1.2110^{-5}$ | $6.1710^{-4}$ | $7.5010^{-3}$ | $2.3710^{-2}$ | $9.6410^{-3}$ | $8.2810^{-5}$ | $3.2710^{-5}$ | $2.3210^{-7}$ | $1.7410^{-7}$ |
| | 4 | $3.2110^{-7}$ | $4.1410^{-5}$ | $1.0310^{-3}$ | $8.3210^{-3}$ | $2.0410^{-2}$ | $1.0410^{-2}$ | $5.0810^{-5}$ | $6.0210^{-5}$ | $7.8910^{-8}$ |
| | 5 | $1.9110^{-10}$ | $1.5010^{-6}$ | $8.8110^{-5}$ | $1.4310^{-3}$ | $8.6810^{-3}$ | $1.8010^{-2}$ | $1.0810^{-2}$ | $1.5410^{-5}$ | $9.6710^{-5}$ |
| | 6 | $1.6610^{-9}$ | $4.0010^{-9}$ | $4.1510^{-6}$ | $1.5010^{-4}$ | $1.7910^{-3}$ | $8.7210^{-3}$ | $1.6210^{-2}$ | $1.0810^{-2}$ | $1.8010^{-7}$ |
| | 7 | $5.4010^{-10}$ | $7.2110^{-9}$ | $2.7210^{-8}$ | $8.7910^{-6}$ | $2.2210^{-4}$ | $2.0910^{-3}$ | $8.5710^{-3}$ | $1.4810^{-2}$ | $1.0510^{-2}$ |
| | 8 | $7.2310^{-11}$ | $2.8910^{-9}$ | $1.7210^{-8}$ | $1.1210^{-7}$ | $1.5710^{-5}$ | $3.0110^{-4}$ | $2.3210^{-3}$ | $8.2610^{-3}$ | $1.3810^{-2}$ |
| | 9 | $2.7610^{-12}$ | $4.3910^{-10}$ | $8.6510^{-9}$ | $2.7510^{-8}$ | $3.2310^{-7}$ | $2.5310^{-5}$ | $3.8210^{-4}$ | $2.5010^{-3}$ | $7.8510^{-3}$ |

Table A.12: The table shows the transition probabilities extracted from LIFBASE [146] for the CN ($B^2\Sigma^+$-$X^2\Sigma^+$) transition.

# B Flow model

Whenever dealing with gas dynamics simulations the solution of the Navier-Stokes equations, which are the general conservation laws for mass, momentum, and energy, should be found. The system of equations is the general expression of the Navier-Stokes equations:

$$\begin{aligned} \partial_t \rho + \nabla \cdot (\rho \mathbf{u}) &= 0 \\ \partial_t (\rho \mathbf{u}) + \mathbf{u} \cdot \nabla (\rho \mathbf{u}) &= -\nabla p + \rho \mathbf{g} + \nabla \cdot \underline{\underline{\tau}} \\ \partial_t (\rho E + \nabla \cdot ((\rho E + p)\mathbf{u}) &= \nabla \cdot \left( \lambda_{eff} \nabla T + \underline{\underline{\tau_{\mathbf{eff}}}} \cdot \mathbf{u} \right) + P_{in} \end{aligned}$$

where $\rho$ is the fluid density, u the fluid velocity, p the pressure, g the gravitational acceleration, $\underline{\underline{\tau}}$ and $\underline{\underline{\tau_{\mathbf{eff}}}}$ are the stress tensor and the effective stress tensor account for the turbulence, $\lambda_{eff}$ is the effective heat conductivity accounting for the turbulence, $\rho E = \frac{1}{2}\mathbf{u}^2 + c_p(T)T - pT$ is the total energy density and $P_{in}$ is the power input in the system. In the case of turbulent flow, the treatment of the velocity and pressure as an average component and a turbulent component (the deviation from the mean value) $u_i = \overline{u_i} + u_i'$ [171]. The gas dynamics have been simulated using the Reynolds-averaged Navier-Stokes model [172], [173]. Such model, or better the closure applied in this model, is found to be the most appropriate to simulate the turbulent behaviour of the swirling gas in the plasma torch. The Reynolds stress model has been preferred to the k-$\epsilon$ model because the closure applied, the Boussinesq hypothesis [160], is often not valid in strong swirling configurations [174].

The geometry of the plasma torch naturally allows for bidimensional axis-symmetric modelling of the swirling flow. The simulations are carried out in a small segment of the axis-symmetric (i.e. the theta direction in the cylindrical symmetry of the quartz tube) portion of the plasma torch. Such approximation allows the computation of the tangential velocity under the assumption of axis-symmetric quantities ($\frac{\partial}{\partial \theta} = 0$). The axis-symmetric approximation implies the modelling of the four tangential gas inlets as an injection ring. The gas velocity at the inlets is scaled to reproduce the mass flux used in the experiments. Moreover, it is not possible, because of divergence in the mass flux, to simulate with only a tangential component in the injection velocity,

therefore an initial angle is used, that gives a small radial component. The simulation domain includes the quartz tube wall, whose temperature is fixed in the simulation at 300 K. The boundary condition is observed to influence only the gas temperature in the gas effluent. The simulation domain includes a tube of 2 m length, that is enough to reach a stable flow in the axial direction, at the end of the tube the flow is fixed (free-flow boundary conditions).

# Bibliography


[1] IEA. *Total $CO_2$ emission*. URL: https://www.iea.org.

[2] C. Le Quéré et al. "Global Carbon Budget 2015". In: *Earth System Science Data* 7.2 (Dec. 2015), pp. 349–396.

[3] Nosayaba Oka. "Sustainable development: 2015 climate change agreement and Nigeria's commitment to its nationally determined contributions". In: *Management of Sustainable Development* Volume 11 (June 2019), pp. 11–20.

[4] Joeri Rogelj et al. "Scenarios towards limiting global mean temperature increase below 1.5 °C". In: *Nature Climate Change* 8.4 (Mar. 2018), pp. 325–332.

[5] Pete Smith et al. "Biophysical and economic limits to negative $CO_2$ emissions". In: *Nature Climate Change* 6.1 (Dec. 2015), pp. 42–50.

[6] Phil Williamson. "Emissions reduction: Scrutinize $CO_2$ removal methods". In: *Nature* 530.7589 (2016), pp. 153–155.

[7] Ocean Studies Board, National Research Council, et al. *Climate Intervention: Carbon Dioxide Removal and Reliable Sequestration*. National Academies Press, 2015.

[8] Timothy M Lenton. "The global potential for carbon dioxide removal". In: *Geoengineering of the Climate System* (2014), pp. 52–79.

[9] IEA. *Putting $CO_2$ into use*. Research rep. Sept. 2019.

[10] Elsje Alessandra Quadrelli et al. "Carbon Dioxide Recycling: Emerging Large-Scale Technologies with Industrial Potential". In: *ChemSusChem* 4.9 (Sept. 2011), pp. 1194–1215.

[11] Michele Aresta et al. "Catalysis for the Valorization of Exhaust Carbon: from $CO_2$ to Chemicals, Materials, and Fuels. Technological Use of $CO_2$". In: *Chemical Reviews* 114.3 (Dec. 2013), pp. 1709–1742.

[12] Fraunhofer Institüte. *Power generation in germany*. URL: https://www.energy-charts.de/power.htm.

[13] *What Energy Sources Power the World?* https://www.visualcapitalist.com/energy-sources-power-world/.

[14] *Solar Renewable Energy – Is Solar Energy Renewable and Can it Meet our Energy Needs?* https://greenplanetethics.com/solar-renewable-energy-is-solar-energy-renewable-and-can-it-meet-our-energy-needs/.

[15] M. Sherwin and D. Blum. *Liquid-phase methanol. Final report*. Tech. rep. Chem Systems Inc. Fairfield, NJ (USA), 1979.

[16] Ibram Ganesh. "Conversion of carbon dioxide into methanol – a potential liquid fuel: Fundamental challenges and opportunities (a review)". In: *Renewable and Sustainable Energy Reviews* 31 (Mar. 2014), pp. 221–257.

[17] Pavlos Nikolaidis and Andreas Poullikkas. "A comparative overview of hydrogen production processes". In: *Renewable and Sustainable Energy Reviews* 67 (Jan. 2017), pp. 597–611.

[18] Robert Schlögl. "The solar refinery". In: *Chemical Energy Storage*. De Gruyter, 2013, pp. 1–34.

[19] Annemie Bogaerts and Erik C. Neyts. "Plasma Technology: An Emerging Technology for Energy Storage". In: *ACS Energy Letters* 3.4 (Mar. 2018), pp. 1013–1027.

[20] Philipp Furler et al. "Solar thermochemical $CO_2$ splitting utilizing a reticulated porous ceria redox system". In: *Energy & Fuels* 26.11 (Oct. 2012), pp. 7051–7059.

[21] Ramses Snoeckx and Annemie Bogaerts. "Plasma technology – a novel solution for $CO_2$ conversion?" In: *Chemical Society Reviews* 46.19 (2017), pp. 5805–5863.

[22] Alexander Fridman. *Plasma chemistry*. Cambridge university press, 2008.

[23] Khan Academy. *Heat and temperature*. Web. Retrieved 4 March 2020.

[24] Peter G. Nelson. "Statistical mechanical interpretation of temperature". In: *Foundations of Chemistry* 21.3 (Mar. 2019), pp. 325–331.

[25] Yuichi Setsuhara. "Low-temperature atmospheric-pressure plasma sources for plasma medicine". In: *Archives of Biochemistry and Biophysics* 605 (2016). Special Issue: Low-temperature plasma in biology and medicine, pp. 3–10. ISSN: 0003-9861.

[26] P. J. Bruggeman et al. "Gas temperature determination from rotational lines in non-equilibrium plasmas: a review". In: *Plasma Sources Science and Technology* 23.2 (Apr. 2014), p. 023001.

[27] Dorothée Szabó and Sabine Schlabach. "Microwave plasma synthesis of materials-from physics and chemistry to nanoparticles: a materials scientist's viewpoint". In: *Inorganics* 2.3 (Aug. 2014), pp. 468–507.

[28] André Anders. "Plasma and ion sources in large area coating: A review". In: *Surface and Coatings Technology* 200.5-6 (Nov. 2005), pp. 1893–1906.

[29] P. W. C. Groen et al. "Numerical model for the determination of the reduced electric field in a $CO_2$ microwave plasma derived by the principle of impedance matching". In: *Plasma Sources Science and Technology* 28.7 (July 2019), p. 075016.

[30] M. Jimenez-Diaz et al. "A two-dimensional Plasimo multiphysics model for the plasma-electromagnetic interaction in surface wave discharges: the surfatron source". In: *Journal of Physics D: Applied Physics* 45.33 (Aug. 2012), p. 335204.

[31] A. J. Wolf et al. "Characterization of $CO_2$ microwave plasma based on the phenomenon of skin-depth-limited contraction". In: *Plasma Sources Science and Technology* 28.11 (Nov. 2019), p. 115022.

[32] M Baeva et al. "Two- and three-dimensional simulation analysis of microwave excited plasma for deposition applications: operation with argon at atmospheric pressure". In: *Journal of Physics D: Applied Physics* 51.38 (Aug. 2018), p. 385202.

[33] Martina Leins. "Development and spectroscopic investigation of a microwave plasma source for the decomposition of waste gases". PhD thesis. Fakultät Mathematik und Physik der Universität Stuttgart, 2010.

[34] Nikolay Britun et al. "Plasma-assisted $CO_2$ conversion: optimizing performance via microwave power modulation". In: *Journal of Physics D: Applied Physics* 51.14 (Mar. 2018), p. 144002.

[35] T. Silva et al. "Modelling the input and relaxation of vibrational energy in $CO_2$ plasmas". In: *Journal of Physics D: Applied Physics* 51.46 (Sept. 2018), p. 464001.

[36] John C. McConnell and Michael B. McElroy. "Excitation processes for Martian dayglow". In: *Journal of Geophysical Research* 75.34 (Dec. 1970), pp. 7290–7293.

[37] A. S. Morillo-Candas et al. "Electron impact dissociation of $CO_2$". In: *Plasma Sources Science and Technology* 29.1 (Jan. 2020), 01LT01.

[38] L.S. Polak and D.I. Slovetsky. "Electron impact induced electronic excitation and molecular dissociation". In: *International Journal for Radiation Physics and Chemistry* 8.1-2 (Jan. 1976), pp. 257–282.

[39] Marija Grofulović et al. "Electron-neutral scattering cross sections for $CO_2$: a complete and consistent set and an assessment of dissociation". In: *Journal of Physics D: Applied Physics* 49.39 (Sept. 2016), p. 395207.

[40] A. Cenian et al. "Modeling of Plasma-Chemical Reactions in Gas Mixture of $CO_2$ Lasers I. Gas Decomposition in Pure $CO_2$ Glow Discharge". In: *Contributions to Plasma Physics* 34.1 (1994), pp. 25–37.

[41] Bo Zhou et al. "Topology of conical/surface intersections among five low-lying electronic states of $CO_2$: Multireference configuration interaction calculations". In: *The Journal of Chemical Physics* 139.15 (Oct. 2013), p. 154302.

[42] J. Blauer and G. Nickerson. "A survey of vibrational relaxation rate data for processes importantto $CO_2$-$N_2$-$H_2O$ infrared plume radiation". In: *7th Fluid and PlasmaDynamics Conference*. American Institute of Aeronautics and Astronautics, June 1974.

[43] T. Silva et al. "Kinetic study of low-temperature $CO_2$ plasmas under non-equilibrium conditions. I. Relaxation of vibrational energy". In: *Plasma Sources Science and Technology* 27.1 (Jan. 2018), p. 015019.

[44] V. D. Rusanov and A. A. Fridman. "The physics of a chemically active plasma". In: *Moscow Izdatel Nauka* (1984).

[45] V. A. Legasov et al. "Nonequilibrium plasma-chemical process of the decomposition of $CO_2$ in HF and UHF discharges". In: *Akademiia Nauk SSSR Doklady* 238 (Jan. 1978). Translation courtesy of Nicolay Britun, pp. 66–69.

[46] R. I. Azizov et al. "Nonequilibrium plasmachemical process of $CO_2$ decomposition in a supersonic microwave discharge". In: *Akademiia Nauk SSSR Doklady* 271 (Aug. 1983). Translation courtesy of Nicolay Britun, pp. 94–98.

[47] I. P. Butylkin et al. "Plasma-chemical process of $CO_2$ dissociation in a nonequilibrium microwave discharge". In: *Zhurnal Tekhnicheskoi Fiziki* 51 (May 1981), pp. 925–931.

[48] Frank J Zeleznik and Sanford Gordon. "Calculation of complex chemical equilibria". In: *Industrial & Engineering Chemistry* 60.6 (1968), pp. 27–57.

[49] Bonnie J. McBride and Sanford Gordon. "Computer program for calculation of complex chemical equilibrium compositions and applications ii users manual and program description. 2; users manual and program description". In: *NASA Lewis Research Center; Cleveland,OH United States* (1996).

[50] G. J. M. Hagelaar and L. C. Pitchford. "Solving the Boltzmann equation to obtain electron transport coefficients and rate coefficients for fluid models". In: *Plasma Sources Science and Technology* 14.4 (Oct. 2005), pp. 722–733.

[51] LXCat. *Morgan database*. URL: `www.lxcat.net`.

[52] Niek den Harder et al. "Homogeneous $CO_2$ conversion by microwave plasma: Wave propagation and diagnostics". In: *Plasma Processes and Polymers* 14.6 (Nov. 2016), p. 1600120.

[53] Gerhard Herzberg. *Molecular spectra and molecular structure: spectra of diatomic molecules*. Vol. 1. van Nostrand, 1950.

[54] Emile Carbone et al. "Analysis of the $C_2$ ($d^3\Pi_g$-$a^3\Pi_u$) Swan bands as a thermometric probe in $CO_2$ microwave plasmas". In: *Plasma Sources Science and Technology* (2020).

[55] Alexander Kramida and Yuri Ralchenko. *NIST Atomic Spectra Database, NIST Standard Reference Database 78*. eng. 1999.

[56] Philip M. Morse. "Diatomic molecules according to the wave mechanics II. Vibrational levels." In: *Physical Review* 34.1 (1929), p. 57.

[57] Antonio J. C. Varandas and José Dias da Silva. "Potential model for diatomic molecules including the united-atom limit and its use in a multiproperty fit for argon". In: *Journal of the Chemical Society, Faraday Transactions* 88.7 (1992), p. 941.

[58] Robert J. Le Roy. "RKR1: A computer program implementing the first-order RKR method for determining diatomic molecule potential energy functions". In: *Journal of Quantitative Spectroscopy and Radiative Transfer* 186 (Jan. 2017), pp. 158–166.

[59] Hans-Joachim Werner et al. "Molpro: a general-purpose quantum chemistry program package". In: *Wiley Interdisciplinary Reviews: Computational Molecular Science* 2.2 (July 2011), pp. 242–253.

[60] Claude Cohen-Tannoudji et al. *Claude Cohen-Tannoudji; Bernard Diu; Franck Laloë: Quantenmechanik*. Vol. 1. Walter de Gruyter, 2013.

[61] James S.A. Brooke et al. "Line strengths and updated molecular constants for the $C_2$ Swan system". In: *Journal of Quantitative Spectroscopy and Radiative Transfer* 124 (July 2013), pp. 11–20.

[62] Margarita Martin. "$C_2$ spectroscopy and kinetics". In: *Journal of Photochemistry and Photobiology A: Chemistry* 66.3 (June 1992), pp. 263–289.

[63] Colin M. Western. "PGOPHER: A program for simulating rotational, vibrational and electronic spectra". In: *Journal of Quantitative Spectroscopy and Radiative Transfer* 186 (Jan. 2017), pp. 221–242.

[64] J. Von Neumann and E. Wigner. "No crossing rule". In: *Z Phys* 30 (1929), pp. 467–470.

[65] Helene Lefebvre-Brion. *Perturbations in the spectra of diatomic molecules*. Elsevier, 2012.

[66] Thomas A. Carlson et al. "Correlation between perturbation and collisional transfers in the A, B, C and b states of CO as revealed by high resolution lifetime measurements". In: *Zeitschriftür Physik A Atoms and Nuclei* 287.2 (June 1978), pp. 123–136. ISSN: 0939-7922.

[67] Robert J. Le Roy. "LEVEL: A computer program for solving the radial Schrödinger equation for bound and quasibound levels". In: *Journal of Quantitative Spectroscopy and Radiative Transfer* 186 (Jan. 2017), pp. 167–178.

[68] Annie Hansson and James K.G. Watson. "A comment on Hönl-London factors". In: *Journal of Molecular Spectroscopy* 233.2 (Oct. 2005), pp. 169–173.

[69] E. U. Condon and G. H. Shortley. *The Theory of Atomic Spectra, Cambridge Univ.* 1935.

[70] Jan Voráč et al. "Batch processing of overlapping molecular spectra as a tool for spatio-temporal diagnostics of power modulated microwave plasma jet". In: *Plasma Sources Science and Technology* 26.2 (Jan. 2017), p. 025010.

[71] M. Leins et al. "Microwave Plasmas at Atmospheric Pressure". In: *Contributions to Plasma Physics* 54.1 (Nov. 2013), pp. 14–26.

[72] A. Hecimovic et al. "Characterisation and comparison of microwave plasma discharges for $CO_2$ conversion at sub-atmospheric pressure". In: *XXV ESCAMPIG Paris*. 2020.

[73] D. T. Tuma. "A quiet uniform microwave gas discharge for lasers". In: *Review of Scientific Instruments* 41.10 (Oct. 1970), pp. 1519–1520.

[74] Edmond De Hoffmann et al. *Mass Spectrometry: Principles and Applications*. 1997.

[75] Ante Hecimovic et al. "Gas composition analysis method for a wide pressure range up to atmospheric pressure - $CO_2$ case study". In: *Review of Scientific Instruments* (2019). To be submitted.

[76] Aleksander Drenik et al. "Detection of ammonia by residual gas analysis in AUG and JET". In: *Fusion Engineering and Design* 124 (Nov. 2017), pp. 239–243.

[77] Christopher A. Palmer and Erwin G. Loewen. *Diffraction grating handbook*. Vol. 5. Thermo RGL New York, 2002.

[78] M. F. Tompsett et al. "Charge coupled 8-bit shift register". In: *Applied Physics Letters* 17.3 (Aug. 1970), pp. 111–115.

[79] *Horiba monochromator and spectrograph*. `https://www.horiba.com/us/en/scientific/products/optics-tutorial/monochromators-spectrographs/`.

[80] Constandinos M. Mitsingas et al. "High energy efficiency plasma conversion of $CO_2$ at atmospheric pressure using a direct-coupled microwave plasma system". In: *IEEE Transactions on Plasma Science* 44.4 (Apr. 2016), pp. 651–656.

[81] L. F. Spencer and A. D. Gallimore. "$CO_2$ dissociation in an atmospheric pressure plasma/catalyst system: a study of efficiency". In: *Plasma Sources Science and Technology* 22.1 (Dec. 2012), p. 015019.

[82] Waldo Bongers et al. "Plasma-driven dissociation of $CO_2$ for fuel synthesis". In: *Plasma Processes and Polymers* 14.6 (Sept. 2016), p. 1600126.

[83] Yacine Babou et al. “Spectroscopic study of microwave plasmas of $CO_2$ and $CO_2$-$N_2$ mixtures at atmospheric pressure”. In: *Plasma Sources Science and Technology* 17.4 (Aug. 2008), p. 045010.

[84] Floran Peeters et al. “Chemiluminescence as a diagnostic tool in $CO_2$ microwave plasma”. In: *ISPC 24 Naples*. 2019.

[85] M. W. Feast. “Investigation of the spectrum of the high voltage arc in carbon dioxide: the CO flame spectrum”. In: *Proceedings of the Physical Society. Section A* 63.7 (July 1950), pp. 772–774.

[86] F. Kaufman et al. “The kinetics of the carbon monoxide flame bands”. In: *Symposium (International) on Combustion* 9.1 (Jan. 1963), pp. 177–183.

[87] E. A. Ballik and D. A. Ramsay. “An extension of the phillips system of $C_2$ and a survey of $C_2$ states.” In: *The Astrophysical Journal* 137 (Jan. 1963), p. 84.

[88] P. Caubet and G. Dorthe. “Origin of $C_2$ high-pressure bands observed in the pre-oducts of a microwave discharge through CO”. In: *Chemical Physics Letters* 218.5-6 (Feb. 1994), pp. 529–536.

[89] C. E. Little and P. G. Browne. “Origin of the high-pressure bands of $C_2$”. In: *Chemical Physics Letters* 134.6 (Mar. 1987), pp. 560–564.

[90] A. Fowler. “Investigations relating to the spectra of comets.: (plate 14.)” In: *Monthly Notices of the Royal Astronomical Society* 70.6 (Apr. 1910), pp. 484–490.

[91] J. William Rich and Richard C. Bergman. “$C_2$ and CN formation by optical pumping of CO/Ar and CO/$N_2$/Ar mixtures at room temperature”. In: *Chemical Physics* 44.1 (Nov. 1979), pp. 53–64.

[92] Hidde L. Wallaart et al. “Transfer of vibrational energy to electronic excited states and vibration enhanced carbon production in optically excited V-V pumped CO”. In: *Chemical Physics* 196.1-2 (June 1995), pp. 149–169.

[93] H. L. Wallaart et al. “$C_2$ formation in vibrationally excited CO”. In: *Chemical Physics Letters* 246.6 (Dec. 1995), pp. 587–593.

[94] G. Grigorian and A. Cenian. “Vibrational to electronic energy transfer from CO to $C_2$ molecules”. In: *Chemical Physics Letters* 469.4-6 (Feb. 2009), pp. 247–249.

[95] A. Brockhinke et al. “Energy Transfer in the $d^3\Pi_g$-$a^3\Pi_u$ (0-0) Swan Bands of $C_2$: Implications for Quantitative Measurements”. In: *The Journal of Physical Chemistry A* 110.9 (2006). PMID: 16509624, pp. 3028–3035.

[96] C. Naulin et al. “$C_2$ Radicals in a supersonic molecular beam. Radiative lifetime of the $d^3\Pi_g$ state measured by laser-induced fluorescence”. In: *Chemical Physics Letters* 143.5 (1988), pp. 496 –500. ISSN: 0009-2614.

[97] V. E. Bondybey. “Sequential two photon excitation of the $C_2$ Swan transitions and $C_2$ relaxation dynamics in rare gas solids”. In: *The Journal of Chemical Physics* 65.6 (Sept. 1976), pp. 2296–2304.

[98] Li Xuechu and Lou Nanquan. “The vibrational population inversion and relaxation kinetics of the $C_2$ $d^3\Pi_g$ state”. In: *Chemical Physics Letters* 75.1 (1980), pp. 110 –114. ISSN: 0009-2614.

[99] David L. Cooper and Kate Kirby. "Theoretical study of low-lying $^1\Sigma^+$ and $^1\Pi$ states of CO I. Potential energy curves and dipole moments." In: *The Journal of Chemical Physics* 87.1 (1987), pp. 424–432.

[100] M. E. Rosenkrantz and K. Kirby. "Theoretical study of low-lying $^1\Sigma^-$ and $^1\Delta$ states of CO". In: *The Journal of Chemical Physics* 90.11 (1989), pp. 6528–6532.

[101] S. G. Tilford and J. D. Simmons. "Atlas of the observed absorption spectrum of carbon monoxide between 1060 and 1900". In: 1.1 (Jan. 1972), pp. 147–188.

[102] Kirk A. Peterson and R. Claude Woods. "Theoretical dipole moment functions involving the $a^3\Pi$ and $a'^3\Sigma^+$ states of carbon monoxide". In: *The Journal of Chemical Physics* 93.7 (1990), pp. 5029–5036.

[103] C. V. V. Prasad et al. "The third positive ($b^3\Sigma^+$-$a^3\Pi_r$) system of CO: Observation of the $\nu = 2$ level of $b^3\Sigma^+$". In: *Journal of Molecular Spectroscopy* 121.2 (1987), pp. 261–269. ISSN: 0022-2852.

[104] Stephen V. O'Neil and Henry F. Schaefer. "Valence-excited states of carbon monoxide". In: *The Journal of Chemical Physics* 53.10 (Nov. 1970), pp. 3994–4004.

[105] Tiago Silva et al. "Optical characterization of a microwave pulsed discharge used for dissociation of $CO_2$". In: *Plasma Sources Science and Technology* 23.2 (Mar. 2014), p. 025009.

[106] Tiago Silva et al. "Simple method for gas temperature determination in $CO_2$-containing discharges". In: *Optics Letters* 39.21 (Oct. 2014), p. 6146.

[107] D. J. Drake et al. "Characterization of a $CO_2/N_2/Ar$ supersonic flowing discharge". In: *Journal of Applied Physics* 106.8 (Oct. 2009), p. 083305.

[108] Brett A. Cruden et al. "Neutral gas temperature estimates in an inductively coupled $CF_4$ plasma by fitting diatomic emission spectra". In: *Journal of Applied Physics* 91.11 (Jan. 2002), pp. 8955–8964.

[109] Kate Kirby and David L. Cooper. "Theoretical study of low-lying $^1\Sigma^+$ and $^1\Pi$ states of CO. II. Transition dipole moments, oscillator strengths, and radiative lifetimes". In: *The Journal of Chemical Physics* 90.9 (1989), pp. 4895–4902.

[110] Marcel Drabbels et al. "Determination of electric dipole moments and transition probabilities of low-lying singlet states of CO". In: *The Journal of Chemical Physics* 99.4 (Aug. 1993), pp. 2352–2358.

[111] F. Di Teodoro et al. "Collisional quenching of CO B $^1\Sigma$+(v'=0) probed by two-photon laser-induced fluorescence using a picosecond laser". In: *The Journal of Chemical Physics* 113.8 (2000), pp. 3046–3054.

[112] Bernhard Gemein and Sigrid D. Peyerimhoff. "Theoretical study of the vibronic interactions in the ground and first excited $a^3\Pi$ and $a'^3\Sigma^+$ states of the CO molecule". In: *Chemical physics letters* 184.1-3 (1991), pp. 45–52.

[113] A. C. Le Floch et al. "Reinvestigation of the CO $A^1\Pi$ state and its perturbations: the $\nu$= 0 level". In: *Journal of Molecular Spectroscopy* 121.2 (1987), pp. 337–379.

[114] M. L. Niu et al. "High resolution spectroscopy and perturbation analysis of the CO $A^1\Pi$-$X^1\Sigma^+$ (0,0) and (1,0) bands". In: *Molecular Physics* 111.14-15 (2013), pp. 2163–2174.

[115] R. W. Field et al. “Analysis of perturbations in the $a^3\Pi$ and $A^1\Pi$ states of CO”. In: *Journal of Molecular Spectroscopy* 44.2 (Nov. 1972), pp. 383–399.

[116] M. Eidelsberg et al. “Reinvestigation of the vacuum ultraviolet spectrum of CO and isotopic species: the $B^1\Sigma^+ \leftrightarrow X^1\Sigma^+$ transition”. In: *Journal of Molecular Spectroscopy* 121.2 (1987), pp. 309 –336. ISSN: 0022-2852.

[117] W.-Ü. L. Tchang-Brillet et al. “A model of the B $^1\Sigma^+$-D $'^1\Sigma^+$ Rydberg-valence predissociating interaction in the CO molecule”. In: *The Journal of Chemical Physics* 96.9 (1992), pp. 6735–6745.

[118] A. C. Le Floch and C. Amiot. “Fourier transform spectroscopy of the CO Ångström bands”. In: 97.2-3 (Aug. 1985), pp. 379–389.

[119] L. W. Dotchin et al. “Radiative lifetimes and pressure dependence of the relaxation rates of some vibronic levels in $N_2^+$, $N_2$, $CO^+$, and CO”. In: *The Journal of Chemical Physics* 59.8 (Oct. 1973), pp. 3960–3967.

[120] John H. Moore and Dean W. Robinson. “Study of Some Electronic Transition Probabilities in CO and CN”. In: *The Journal of Chemical Physics* 48.11 (June 1968), pp. 4870–4874.

[121] Yukikazu Itikawa. “Cross sections for electron collisions with carbon monoxide”. In: *Journal of Physical and Chemical Reference Data* 44.1 (2015), p. 013105.

[122] LXCat. *Itikawa database*. URL: `www.lxcat.net`.

[123] T. B. Settersten et al. “Temperature- and species-dependent quenching of CO $B^1\Sigma^+$ probed by two-photon laser-induced fluorescence using a picosecond laser”. In: *The Journal of Chemical Physics* 117.7 (Aug. 2002), pp. 3173–3179.

[124] G. W. Loge et al. “Multiphoton induced fluorescence and ionization of carbon monoxide (B $^1\Sigma^+$)”. In: *The Journal of Chemical Physics* 79.1 (1983), pp. 196–202.

[125] Yanjun Du et al. “CO($B^1\Sigma^+ \rightarrow A^1\Pi$) Ångström system for gas temperature measurements in $CO_2$ containing plasmas”. In: *Plasma Chemistry and Plasma Processing* 37.1 (Jan. 2017), pp. 29–41. ISSN: 1572-8986.

[126] J. R. Twist et al. “Low energy electron impact excitation of the b $^3\Sigma^+$ state of CO”. In: *The Journal of Chemical Physics* 71.6 (1979), pp. 2345–2351.

[127] Teresa Rytel. “Analysis of the multiple perturbation arising in the $b^3\Sigma^+$ ($\nu$=0) state of the CO molecule”. In: *Journal of Molecular Spectroscopy* 145.2 (1991), pp. 420 –428. ISSN: 0022-2852.

[128] T. Rytel. “The Third positive system of CO ($b^3\Sigma^+$-$a^3\Pi_r$): the 1-v" progression”. In: *Journal of Molecular Spectroscopy* 173.2 (1995), pp. 370 –379. ISSN: 0022-2852.

[129] Fabienne Poncin-Epaillard and Mohammed Aouinti. “Characterization of $CO_2$ Plasma and Interactions with Polypropylene Film”. In: *Plasmas and Polymers* 7.1 (Mar. 2002), pp. 1–17. ISSN: 1572-8978.

[130] Ch. Ottinger et al. “Molecular beam study of the collision-induced intramolecular energy transfer CO($a^3\Pi$, $a'^3\Sigma^+$, $d^3\Delta$)”. In: *The Journal of Physical Chemistry* 99.42 (Oct. 1995), pp. 15642–15654.

[131] M. J. Mumma et al. “Excitation of the CO fourth positive band system by electron impact on carbon monoxide and carbon dioxide”. In: *The Journal of Chemical Physics* 54.6 (Mar. 1971), pp. 2627–2634.

[132] Peter W. Erdman and Edward C. Zipf. "Electron-impact excitation of the Cameron system ($a^3\Pi \rightarrow X^1\Sigma$) of CO". In: *Planetary and Space Science* 31.3 (1983), pp. 317 –321. ISSN: 0032-0633.

[133] DW Setser and GW Taylor. "Comparison of the reactivities of the lowest excited states of nitrogen ($A^3\Sigma_u$) and of carbon monoxide ($a^3\Pi$)". In: *Journal of the American Chemical Society* 93.19 (1971), pp. 4930–4932.

[134] S. V. Filseth et al. "Two photon excitation of CO ($A^1\Pi$) and $N_2$ ($a\ ^1\Pi_g$)". In: *Optics Communications* 23.2 (1977), pp. 231 –235. ISSN: 0030-4018.

[135] Sean D. McGuire et al. "Measurements and modeling of CO $4^{th}$ positive (A-X) radiation". In: *Journal of Quantitative Spectroscopy and Radiative Transfer* 245 (Apr. 2020), p. 106855.

[136] Thomas C. James. "Transition moments, Franck-condon factors, and lifetimes of forbidden transitions. Calculation of the intensity of the Cameron system of CO". In: *The Journal of Chemical Physics* 55.8 (Oct. 1971), pp. 4118–4124.

[137] E.A.H Timmermans et al. "The behavior of molecules in microwave-induced plasmas studied by optical emission spectroscopy. 2: Plasmas at reduced pressure". In: *Spectrochimica Acta Part B: Atomic Spectroscopy* 54.7 (July 1999), pp. 1085–1098.

[138] E. A. H. Timmermans et al. "The behavior of molecules in microwave-induced plasmas studied by optical emission spectroscopy. 1. Plasmas at atmospheric pressure". In: *Spectrochimica Acta Part B: Atomic Spectroscopy* 53.11 (Oct. 1998), pp. 1553–1566.

[139] M. Lino da Silva et al. "Radiation from an equilibrium $CO_2$-$N_2$ plasma in the [250-850 nm] spectral region: II. Spectral modelling". In: *Plasma Sources Science and Technology* 17.3 (June 2008), p. 035013.

[140] D. Vacher et al. "Radiation from an equilibrium $CO_2$-$N_2$ plasma in the [250-850 nm] spectral region: I. Experiment". In: *Plasma Sources Science and Technology* 17.3 (July 2008), p. 035012.

[141] H. Nassar et al. "$N_2^+/N_2$ ratio and temperature measurements based on the first negative $N_2^+$ and second positive $N_2$ overlapped molecular emission spectra". In: *Journal of Physics D: Applied Physics* 37.14 (July 2004), pp. 1904–1916.

[142] Meirong Dong et al. "Elucidation of $C_2$ and CN formation mechanisms in laser-induced plasmas through correlation analysis of carbon isotopic ratio". In: *Spectrochimica Acta Part B: Atomic Spectroscopy* 100 (Oct. 2014), pp. 62–69.

[143] A. Ricard et al. "Torche à plasma à excitation micro-onde : deux configurations complémentaires". In: *Journal de Physique III* 5.8 (Aug. 1995), pp. 1269–1285.

[144] H. Nassar. "CN violet system spectrum used as a molecular pyrometer and the influence noise to signal ratio on the temperature values". In: *Journal of Physics: Conference Series* 370 (June 2012), p. 012050.

[145] R. S. Ram et al. "Fourier transform emission spectroscopy of the $B^2\Sigma^+$–$X^2\Sigma^+$ system of CN". In: *Journal of Molecular Spectroscopy* 237.2 (2006), pp. 225 –231. ISSN: 0022-2852.

[146] J. Luque and D.R. Crosley. "LIFBASE: Database and Spectral Simulation Program (Version 1.5)". In: *SRI International Report MP* 99 (1999), p. 009.

[147] Haruhiko Ito et al. "Analysis of the $B^2\Sigma^+$-$A^2\Pi_i$ perturbations in the CN($B^2\Sigma^+ \rightarrow X^2\Sigma^+$) main band system: I. Molecular constants for $B^2\Sigma^+$ and $A^2\Pi_i$". In: *Journal of Molecular Spectroscopy* 127.2 (1988), pp. 283 –303. ISSN: 0022-2852.

[148] D. Cerny et al. "Extensive analysis of the red system of the CN molecule with a high resolution Fourier Spectrometer". In: *Journal of Molecular Spectroscopy* 73.1 (Oct. 1978), pp. 154–167.

[149] Haruhiko Ito et al. "Electronic transition moment for the $B^2\Sigma^+ \rightarrow X^2\Sigma^+$ emission of CN. Analysis of dependence on the internuclear distance". In: *The Journal of Chemical Physics* 94.8 (1991), pp. 5353–5359.

[150] Haruhiko Ito et al. "Analysis of the $B^2\Sigma^+$-$A^2\Pi_i$ perturbations in the CN($B^2\Sigma^+ \rightarrow X^2\Sigma^+$) main band system: Electronic structures of $B^2\Sigma^+$ and $A^2\Pi_i$". In: *Journal of Molecular Spectroscopy* 127.1 (1988), pp. 143 –155. ISSN: 0022-2852.

[151] Igor Belov et al. "Carbon dioxide dissociation in a microwave plasma reactor operating in a wide pressure range and different gas inlet configurations". In: *Journal of $CO_2$ Utilization* 24 (Mar. 2018), pp. 386–397.

[152] D. C. M. van den Bekerom et al. "How the alternating degeneracy in rotational Raman spectra of $CO_2$ and $C_2H_2$ reveals the vibrational temperature". In: *Applied Optics* 57.20 (July 2018), p. 5694.

[153] G. J. van Rooij et al. "Taming microwave plasma to beat thermodynamics in $CO_2$ dissociation". In: *Faraday Discussions* 183 (2015), pp. 233–248.

[154] A. J. Wolf et al. "Implications of thermo-chemical instability on the contracted modes in $CO_2$ microwave plasmas". In: *Plasma Sources Science and Technology* 29.2 (Feb. 2020), p. 025005.

[155] D. C. M. van den Bekerom et al. "The importance of thermal dissociation in $CO_2$ microwave discharges investigated by power pulsing and rotational Raman scattering". In: *Plasma Sources Science and Technology* 28.5 (May 2019), p. 055015.

[156] A. Schulz et al. "Scalable Microwave Plasma Sources From Low to Atmospheric Pressure". In: *Contributions to Plasma Physics* 52.7 (Aug. 2012), pp. 607–614.

[157] W. Tsang and R. F. Hampson. "Chemical kinetic data base for combustion chemistry. Part I. Methane and related compounds". In: *Journal of Physical and Chemical Reference Data* 15.3 (July 1986), pp. 1087–1279.

[158] Abraham J. Wolf et al. "$CO_2$ Conversion in Non-Uniform Discharges: Disentangling Dissociation and Recombination Mechanisms". In: *The Journal of Physical Chemistry C* (July 2020).

[159] Han S. Uhm et al. "Carbon dioxide elimination and regeneration of resources in a microwave plasma torch". In: *Environmental Pollution* 211 (Apr. 2016), pp. 191–197.

[160] Inc ANSYS. *Theory reference 5.6*. 1999.

[161] Clemént Brochet et al. "Fluid modelling of a microwave $CO_2$ plasma". Report.

[162] D. C. M. van den Bekerom et al. "Mode resolved heating dynamics in pulsed microwave $CO_2$ plasma from laser Raman scattering". In: *Journal of Physics D: Applied Physics* 53.5 (Nov. 2019), p. 054002.

[163] B. L. M. Klarenaar et al. "Excitation and relaxation of the asymmetric stretch mode of $CO_2$ in a pulsed glow discharge". In: *Plasma Sources Science and Technology* 28.3 (Mar. 2019), p. 035011.

[164] B. L. M. Klarenaar et al. "A rotational Raman study under non-thermal conditions in a pulsed $CO_2$ glow discharge". In: *Plasma Sources Science and Technology* 27.4 (Apr. 2018), p. 045009.

[165] T. Verreycken et al. "Investigation of the effect of on and off time on the dissociation of $CO_2$ in a pulsed microwave discharge, submitted to EPJ AP". In: *15th High pressure low temperature plasma chemistry symposium, September*, pp. 11–16.

[166] Vincent Vermeiren and Annemie Bogaerts. "Improving the energy efficiency of $CO_2$ conversion in nonequilibrium plasmas through pulsing". In: *The Journal of Physical Chemistry C* 123.29 (July 2019), pp. 17650–17665.

[167] G. van Rooij A. van de Steeg T. Butterworth. "Vibrational and gas heating dynamics in molecular plasma assessed by Thomson and Raman scattering". In: *ISPC 24 Naples*. 2019.

[168] R. Kępa and M. Rytel. "The Ångstrom ($B^1\Sigma^+ - A^1\Pi$) system of the CO molecules: new observations and analyses". In: *Journal of Physics B: Atomic, Molecular and Optical Physics* 26.19 (1993), p. 3355.

[169] Akira Wada and Hideto Kanamori. "Submillimeter-wave spectroscopy of CO in the $a^3\Pi$ state". In: *Journal of Molecular Spectroscopy* 200.2 (2000), pp. 196 –202. ISSN: 0022-2852.

[170] Brian G. Wicke et al. "Fine structure, dipole moment, and perturbation analysis of $a^3\Pi$ CO". In: *The Journal of Chemical Physics* 56.12 (1972), pp. 5758–5770.

[171] Andrei Nikolaevich Kolmogorov. "The local structure of turbulence in incompressible viscous fluid for very large Reynolds numbers". In: *Proceedings of the Royal Society of London. Series A: Mathematical and Physical Sciences* 434.1890 (July 1991), pp. 9–13.

[172] B. E. Launder et al. "Progress in the development of a Reynolds-stress turbulence closure". In: *Journal of Fluid Mechanics* 68.3 (Apr. 1975), pp. 537–566.

[173] Brian E. Launder. "Second-moment closure: present and future?" In: *International Journal of Heat and Fluid Flow* 10.4 (Dec. 1989), pp. 282–300.

[174] François G. Schmitt. "About Boussinesq's turbulent viscosity hypothesis: historical remarks and a direct evaluation of its validity". In: *Comptes Rendus Mécanique* 335.9-10 (Sept. 2007), pp. 617–627.